Tor Vergata University, Rome, Italy

Department of Computer, Systems and
Production Engineering

GeoInformation Ph.D.

XXII Cycle

The Cloud Dynamics and Radiation Database (CDRD) approach for precipitation retrieval by means of satellite based microwave radiometry

Candidate: Paolo Sanò

Mentors: Prof Giovanni Schiavon Dr. Alberto Mugnai

June 2010

INDEX

INTRODUCTION

Clouds and their associated precipitation play a very important role in the global water and energy cycle. Accurate global measurements of precipitation are therefore important for the validation of global climate models and for understanding the natural variability of the earth's climate. Moreover, rainfall monitoring can serve as an important element for risk management in severe precipitation events.

Space-borne monitoring of clouds and precipitation all around the globe has been gaining a growing interest from the international scientific community as a primary factor in determining and detecting the global climatic changes. Therefore, passive microwave techniques for the estimation of rainfall have advanced considerably over the past years, due largely to an increased understanding of the propagation of microwave radiation through precipitating clouds.

Several techniques (empirical or physical) have been proposed and applied in the last two decades for estimating cloud and precipitation parameters from measurements taken by space-borne microwave radiometers. Important approaches have been based on multiple regression and Maximum Likelihood methods. Bayesian techniques have proven to have a large potential and flexibility for precipitation profiling.
Briefly, Bayesian techniques consist of two parts. The first (forward problem) is the generation of a database (the Cloud Radiation Database (CRD)) in which the simulated brightness temperatures (Tbs), that would be measured by a space-born radiometer, are associated with the various structures (hydrometeors and surface rain rate) generated by a cloud-resolving numerical model, to create “profiles” (the components of the database). The second (inverse problem) is the retrieval of atmospheric parameters, like surface rain rate, using the experimental data (brightness temperatures) of a microwave radiometer, and the probabilistic (Bayesian) analysis of the CRD. In this second part, the profiles used for retrieval are chosen and weights are given based on the proximity of the observed microwave radiances to those of the database.
The unique feature of these techniques is that they constitute a rigorous statistical framework for developing cloud model-based inversion methods. As opposed to empirical methods, where measurements of both Tbs and precipitation parameters are collected to train a retrieval algorithm, the model-based approaches are based on refined physical models to simulate the measurements. This point of view offers the possibility to avoid *in situ* measurements and to deepen the understanding of the problem. On the other hand, model-based approaches have to tackle the critical issues of tuning simulations to the measurement manifolds in order to be representative of real observations, as well as the difficulties of an accurate representation of the microphysical properties of the atmosphere.

In the evaluation of the complete process of retrieval, the sources of possible errors are manifold and distributed along all the steps of the algorithms. Fortunately, many experimental errors can be detected and corrected, or it can be proven that their effect on the retrieval is not relevant. On the contrary, the approximations in the forward model can be important sources of

error in the retrieval procedure. They can be responsible for the non-uniqueness of the CRD. This means that even if the database includes a full spectrum of possible cloud/precipitation profiles, the radiometer observations may be compatible with several different profiles, and so the actual profile may not be uniquely identified. In other words, hydrometeor profiles obtained as result of the retrieval algorithm are, in some cases, unrepresentative of the dynamical and thermodynamical state of the atmosphere under observation. For this reason, the current research activities on the algorithm consider that the utilization of further information on the state of the atmosphere, in addition to the brightness temperatures, can represent a suitable constraint in the selection of profiles of CRD, and can consequently reduce retrieval uncertainties.

The research we have carried out in this thesis is aimed at reducing the non-uniqueness of the database, also referred to as "ambiguity", which represents a severe limit for retrieval methodology.
In our work we have first implemented a complete retrieval algorithm (inverse problem) based on the Bayesian estimation theory (BAMPR – Bayesian Algorithm for Microwave-based Precipitation Retrieval), and then we have tackled the problem of non-uniqueness. To this end we have analyzed the potential new information to be included in the retrieval procedure in order to reduce uncertainties. A better definition of the atmospheric state, and the vertical structure of clouds and precipitation, should improve the information extracted from satellite observations. We have therefore introduced "dynamical tags" in the procedure. This includes dynamics information such as geostrophic forcing or frontal lifting, but also thermodynamic and geographical information.

This thesis is organized as follows. Chapter 1 recalls the importance of the monitoring activity and the continuous progress of passive microwave sensing of the atmosphere, and it mentions the present characteristics of some satellite-borne passive microwave sensors. It also describes the international research projects on remote sensing of the atmosphere in which the work of this thesis is included.
Chapter 2 concerns the process of radiative transfer in the atmosphere, and the radiative transfer equation. It analyzes the effects of emission and scattering processes of hydrometeors on precipitation measurements, and presents an example of methods used in empirical algorithms for measuring rain rate.
In chapter 3 several aspects of precipitation retrieval based on a physical approach are presented. In particular the algorithm we have developed, the BAMPR, and the microwave measurements from DMSP satellite are described. Particular attention has been paid to the "screening problem" - the problem of rejecting areas (pixels) without rain or with a very low probability of rain, and therefore not suitable for retrieval.
Chapter 4 deals with uncertainties in retrieval, and presents the new possible dynamical and thermodynamical variables that can be combined with the brightness temperatures in retrieval. It describes the main elements of the new BAMPR algorithm, that include the use of the dynamical and thermodynamical variables, and that we are currently developing. Moreover, it presents the application of the new BAMPR to some disturbances over Italy, and gives some evaluations of the effects of the new variables on retrieval. Finally, it presents the results of a comparison of the new BAMPR with the "NESDIS" algorithm of NOAA.

CHAPTER 1 – Precipitation and remote sensing

Knowledge of rainfall on a global basis is important in many areas of atmospheric science. In fact, precipitation is a key meteorological phenomenon and constitutes a major component in both the water and energy budgets of the weather and climate system.
Accurate global measurements of precipitation are therefore important for the validation of global climate models and for understanding the natural variability of the earth's climate.
There are different approaches to the measurement of precipitation, using surface-based and satellite-based instruments.
Surface-based weather radars provide measurement of rainfall with a relatively high spatial and temporal resolution. Although they represent a valuable source of information, their coverage is limited and significant problems are involved in the measurements (for example ground clutter, and natural barriers such as mountains).

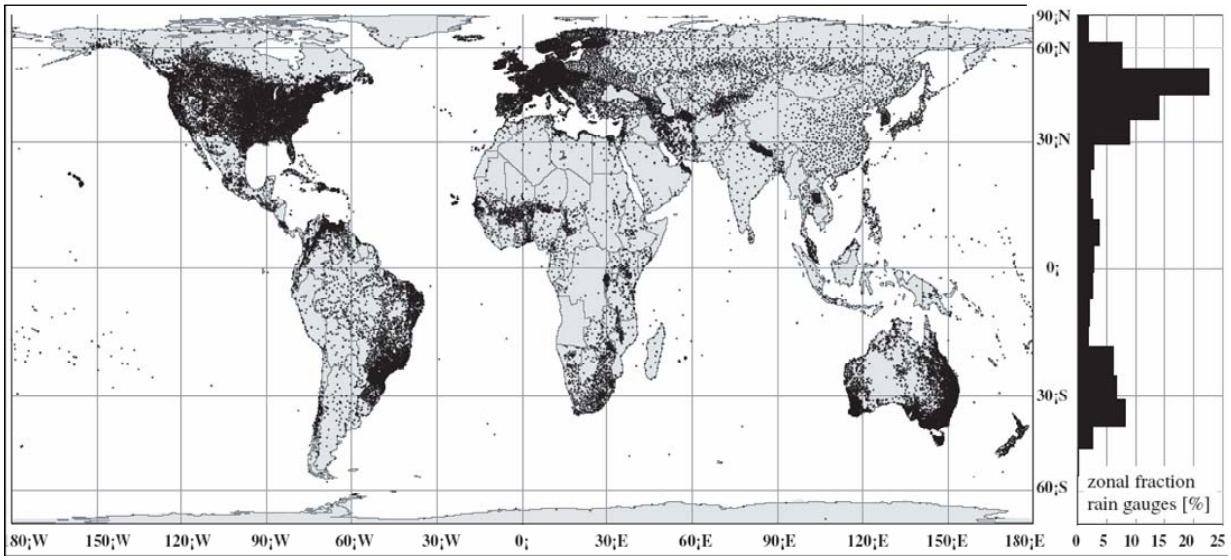

Fig. 1.1 - Distribution of about 40,000 stations of precipitation gauges utilized by the Global Precipitation Climatology Centre (GPCC). The histogram of the zonal fraction of stations depicts the non-uniform distribution with more than 60% of the precipitation gauges between 30°N and 60°N (Landolt-Börnstein 2006).

Rain gauges provide the only other ground-based source of rainfall measurement, but suffer from the fact that their distribution, particularly in developing countries, is not sufficiently dense to resolve the very large spatial variation of rainfall intensity. Moreover, their measurements suffer the effects of wind and evaporation. Figure 1.1 shows the distribution of about 40,000 stations utilized by the Global Precipitation Climatology Centre (Landolt-Börnstein 2006). The figure is a significant picture of the distribution of precipitation gauges in the different continents. The histogram on the right side of the figure points out the non-uniform distribution, with more than 60% of the precipitation gauges between 30°N and 60°N (Landolt-Börnstein 2006).

Over the oceans, radar coverage is virtually nonexistent except near the coasts, while ships provide only qualitative rainfall estimates (Petty 1995) because ship-borne rain gauge measurements are contaminated by sea spray and deflection of the wind by the ship's structure. In this context, satellites have the potential to give an important contribution to global rainfall monitoring. For this reason, space-borne microwave sensors have received, in recent years, several improvements in terms of ground resolution, number of microwave channels, and reliability. At the same time, considerable improvements in research activities on rain-rate retrieval algorithms have been made, as the relationships between the upwelling thermal radiation field and the underlying hydrometeor distribution have become better understood.

This chapter deals with different aspects of rainfall monitoring. It recalls the importance of the monitoring activity and the continuous progress of passive microwave sensing of the atmosphere, and it mentions the present characteristics of some satellite-borne passive microwave sensors. In particular, this chapter is organized as follows: Section 1.1 presents a few remarks on the relevance of clouds and precipitation on human life and the energy balance of the earth. Section 1.2 gives a short description of the evolution of precipitation measurements by satellites and of some existing problems. Section 1.3 describes the main characteristics of passive sensors widely utilized in rainfall estimation. Section 1.4 describes the participation of CNR-ISAC in international research projects on remote sensing of the atmosphere.

1.1 The importance of precipitation

Clouds are fundamental to most aspects of human life. Through production of precipitation, they are essential for supplying freshwater, upon which human life depends. Without rainfall most terrestrial forms of life would not exist and, in turn, the geology and chemistry of the planet would be quite different. Our planet is covered extensively by water, but the majority of it is salty. The actual freshwater resources are mainly composed of glaciers and permanent snow covers, and fresh ground water. However, only an extremely small fraction of the overall freshwater, coming from freshwater lakes and river storages, is completely renewable. The availability of freshwater is one of the greatest problems facing mankind at the beginning of the 21st century. Population growth, observed climatic instabilities, and the growing rate of global pollution have caused a drastic decrease in the availability of water. Over land, precipitation in all its forms is the ultimate source of freshwater.

There is another aspect concerning the importance of clouds. They have an essential influence on the planet’s energy balance. Figure 1.2 shows a simplified scheme of the annual mean global energy balance for the earth-atmosphere system. It is in clouds that latent heat is released through the process of condensation and the formation of precipitation. Latent energy transferred away from the earth's surface during evaporation is redistributed in the atmosphere through the formation of clouds. This form of heat is the basis for the development and evolution of the planet’s storm systems and, in turn, for the precipitation produced by these systems. Three-fourths of the energy that drives atmospheric wind circulation comes from the latent heat released by tropical precipitation.

Rainfall over land affects soil moisture and vegetation type, and then influences evaporation. On the other hand, a lack of rainfall leads to desertification and influences the radiation balance by altering the surface albedo.
Regarding the ocean, the salinity, and hence the stability, of the ocean surface layer is controlled by the freshwater input of precipitation and evaporation. Anomalous sea surface temperatures, such as those that occur in extreme events (for example El Niño), strongly affect global rainfall distribution producing floods in some areas and drought in others.

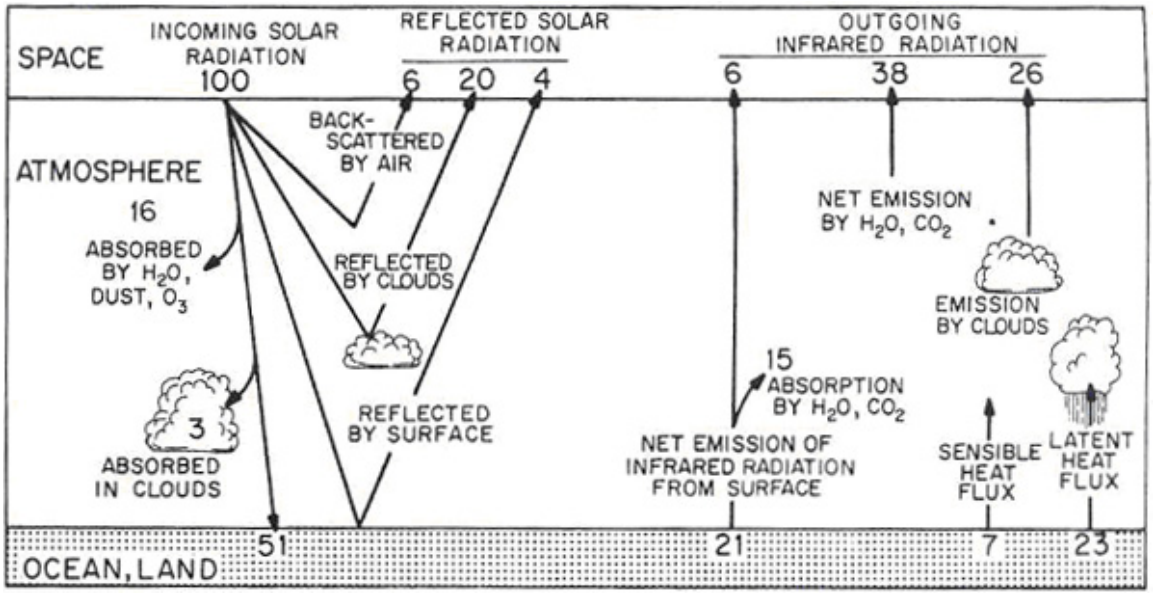

Fig. 1.2 – The annual mean global energy balance for the earth-atmosphere system (Wallace 1977)

There is still another aspect to consider. It concerns the importance of an accurate prediction of severe precipitation events. Adverse weather events, especially severe thunderstorms and floods, represent a serious problem for humans, social activities, and lands. Rainfall monitoring can serve as an important element for risk management in these extreme circumstances.

It is for such reasons that the need for information on the distribution and variability of the properties of clouds and precipitation has emerged as a priority in earth observations.
Moreover, the current emphasis on climate change has motivated an interest in geophysical parameters derived from satellite data, in order to better understand the degree of variability of the global climate system. One parameter of great interest is rainfall and its global distribution on a month-to-month and even a day-to-day basis.

1.2 Precipitation measurement from satellite

Space-borne monitoring of clouds and precipitation all around the globe has been gaining a growing interest from the international scientific community as a primary factor in determining and detecting the slow global climatic changes.

Space-borne passive instruments for rainfall and atmospheric observations may be divided essentially into two groups, depending on the wavelength of the measured radiation: visible-infrared (VIS-IR) and microwave (MW) sensors. VIS-IR sensors have the advantage of providing high-resolution measurements from very high altitudes. Thus, they are often placed aboard geo-stationary platforms allowing a continuous monitoring of (almost) a hemisphere. Visible to IR estimates of rainfall are only indirect because VIS-IR measurements are sensitive only to the uppermost layer of clouds. They infer the underlying cloud structure from the top-of-the-cloud appearance (from its brilliance or from its temperature), based on the optical and thermal properties of the clouds. Microwave sensors, on the contrary, have the great advantage of providing a more direct measurement of the internal structure of the cloud. Microwave wavelengths are not affected by the high level cirrus clouds, and thus are more capable of penetrating the upper portions of the cloud and directly sensing the precipitating layers (Mugnai et al. 1990).

Two different satellite systems are available for precipitation observation from space: first the meteorological geostationary satellites located at 36,000 km altitude (similar to the telecommunication satellites), and second the low level polar orbiting satellites (about 833 km altitude) of the US Defence Meteorological Satellite Program (DMSP is a meteorological long-term program of the Department of Defence, run by the Air Force Space and Missile Systems Center (Kramer 2002).
The system of five geostationary satellites (METEOSAT positioned at 0° longitude, GOES-East at 75°W, GOES-West at 135°W, GMS at 140°E and a second METEOSAT at 63°E) deliver full area-coverage of infrared radiation observations of a high spatial (4 km – GOES Imager) resolution in the belt between 65°S and 65°N (Kramer, 2002). Precipitation can empirically be estimated from infrared images.
The polar orbiting, sun-synchronous, DMSP satellites carry the Special Sensor Microwave / Imager (SSM/I), providing passive radiation measurements in seven channels. As previously mentioned, the physical interaction with precipitation is more direct for microwave channels than for visible or infrared channels. Microwave radiation has the ability to penetrate the clouds and offer insight into the structure of the rainfall itself. On the other hand, the spatial and temporal resolution of SSM/I is much lower than the IR sensors.

Passive microwave sensors have great potential for measuring precipitation from space, even though there are still some technological limits in their utilization. Looking at the history of satellite observation of precipitation, it becomes evident how technological innovations of sensors have marked the steps of the growth and diffusion of this technique.
In fact, the evolution of rainfall retrievals from passive microwave sensors closely followed the development and improvement of satellite sensors, starting with the Electronically Scanning Microwave Radiometer (ESMR) launched on *Nimbus-5* in December 1972. It was a single channel, 19-GHz radiometer, that allowed to map rainfall areas in a variety of tropical disturbances (Allison et al. 1974). *Nimbus-5* was followed by *Nimbus-6* in June of 1975, carrying an ESMR with a 37-GHz channel. Consequently, more quantitative approaches were developed by many investigators. It became clear then that more than one frequency was needed in order to properly retrieve the column water amounts. The first multichannel sensor, the Scanning Multichannel Microwave Radiometer (SMMR) on *Nimbus-7,* was launched in October 1978 and included frequencies ranging from 6.6 to 37 GHz, with spatial resolutions

ranging from 136 km × 89 km at 6.6 GHz to 22 km × 18 km at 37 GHz. SMMR measured both the horizontal and vertical polarizations (Shin and Kummerow 2003).
Following SMMR, the aforementioned DMSP low earth orbit (LEO) satellites carried the Special Sensor Microwave Imager (SSM/I), which was first flown on *DMSP-8* in August 1987. SSM/I is a conically scanning radiometer with seven channels, ranging from 19.3 to 85 GHz, and spatial resolutions ranging from 69 km × 43 km to 15 km × 13 km, respectively. The excellent calibration of the SSM/I, coupled with the data continuity provided by DMSP from 1987 to the present, led to a real improvement in the estimates of microwave rainfall.

The Tropical Rainfall Measuring Mission (TRMM) was launched in November 1997. It carries the TRMM Microwave Imager (TMI), which is based upon SSM/I technology, but with additional 10.7-GHz horizontal polarization and vertical polarization channels to expand the dynamic range of emission signals in the Tropics. The microwave observations cover the tropical belt from 30°S to 30°N on a 3-hourly basis. In addition to these channels, the TRMM satellite flies at a much lower altitude than the DMSP satellites (350 versus 833 km). This provides significantly improved spatial resolution for TMI (30 km × 18 km at 19.3 GHz) in comparison to what was previously available. TRMM is also the first satellite equipped with an active precipitation sensor (precipitation radar - PR). Its observation is used for calibration of the passive microwave based precipitation algorithms.

At the present, some technological questions still remain. Poor ground resolution, for example, represents the main drawback of the measurements, and it is determined by antenna diffraction. The linear dimensions of the footprints increase linearly with wavelength and satellite altitude, and decrease linearly with antenna size. Then, large antennas are required. Also the intermittent nature of the low-earth orbiting (LEO) satellite observations can represent a problem. When products on climatological scales are required (e.g., global monthly averages), insufficient temporal sampling may introduce large errors since every day only two local overpasses are available when only one satellite is operated.

1.3 Microwave remote sensors

1.3.1 The Special Sensor Microwave Imager (SSM/I)

The SSM/I is a seven-channel, four-frequency, orthogonally polarized, passive microwave radiometric system that measures atmospheric, ocean and terrain microwave brightness temperatures at 19.35, 22.2, 37.0, and 85.5 GHz. The data are used to obtain synoptic maps of critical atmospheric, oceanographic and selected land parameters on a global scale. The SSM/I archive data set consists of antenna temperatures recorded across a 1,400 km conical scan, satellite ephemeris, earth surface positions for each pixel and instrument calibration.
The SSM/I is flown aboard Defense Meteorological Satellite Program (DMSP) satellites F8, F10, F11, F12, F13, and F15.
Figure 1.3 shows a scheme of the radiometer and its scan geometry.
The SSM/I instrument consists of an offset parabolic reflector of dimensions 24 x 26 inches, fed by a corrugated, broad-band, seven-port horn antenna. The reflector and feed are mounted on a drum that contains the radiometers, digital data subsystem, mechanical scanning subsystem, and power subsystem. The reflector-feed-drum assembly is rotated about the axis

of the drum by a coaxially mounted bearing and power transfer assembly (BAPTA). All data, commands, timing and telemetry signals, and power pass through the BAPTA on slip ring connectors to the rotating assembly.
A small mirror and a hot reference absorber are mounted on the BAPTA and do not rotate with the drum assembly. They are positioned off axis so that they pass between the feed horn and the parabolic reflector, occulting the feed once each scan. The mirror reflects cold sky radiation into the feed, thus serving, along with the hot reference absorber, as calibration references for the SSM/I. This scheme provides an overall absolute calibration that includes the feed horn. Corrections for spillover and antenna pattern effects from the parabolic reflector are incorporated in the data processing algorithms.

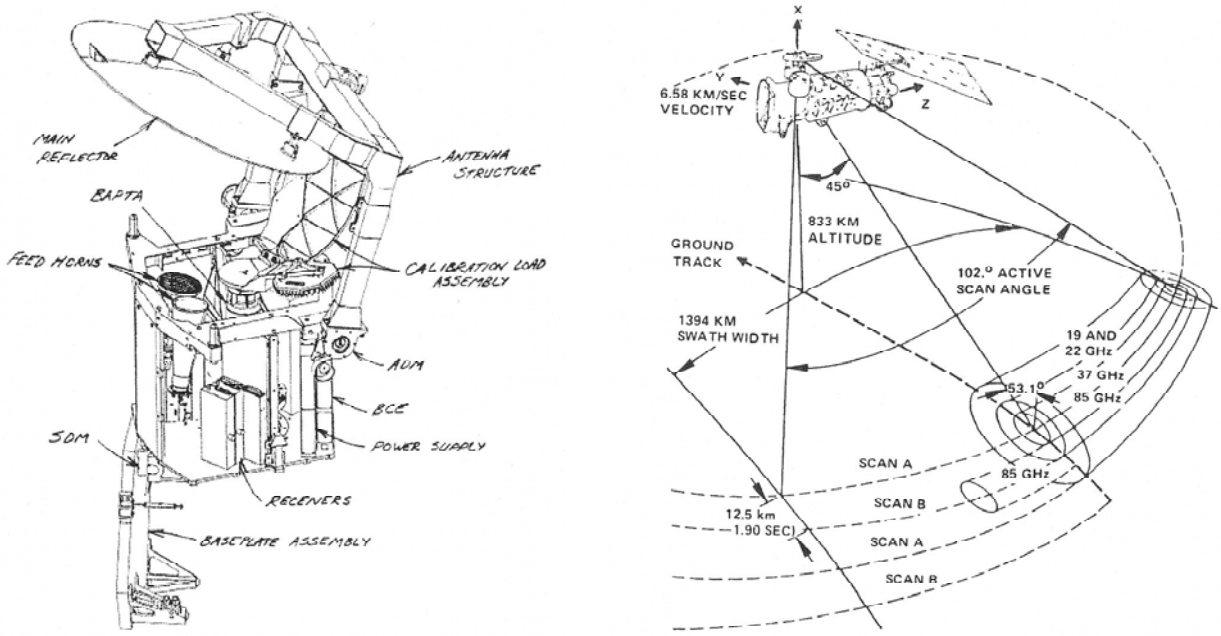

Fig. 1.3 Scheme of SSM/I radiometer (left) and of the scan geometry (right).

The SSM/I rotates continuously about an axis parallel to the local spacecraft vertical at 31.6 rpm and measures the upwelling scene brightness temperatures over an angular sector of 102.4 degrees about the sub-satellite track. The scan direction is from left to right when looking in the forward (F10, F11) or aft (F8) direction of the spacecraft. The active scene measurements lie ±51.2 degrees from the forward (F10, F11) or aft (F8) direction. This results in a swath width of approximately 1400 km. The spin rate provides a period of 1.9 sec during which the spacecraft sub-satellite point travels 12.5 km. During each scan, 128 discrete uniformly spaced radiometric samples are taken at the two 85 GHz channels and, on alternate scans, 64 discrete samples are taken at the remaining five lower frequency channels. The antenna beam intersects the Earth's surface at an incidence angle of 53.1 degrees (as measured from the local Earth normal). Table 1.1 shows the radiometric characteristics of SSM/I

Tab 1.1 Radiometric characteristics of the SSM/I

SSM/I	Special Sensor Microwave - IMAGER
Satellites	DMSP F 8, 10, 11, 13, 14 and 15
Status (June 2009)	Operational - Utilisation period: 1987 to ~ 2009
Mission	Multi-purpose MW imager
Instrument type	4-frequency, 7-channel MW radiometer
Scanning technique	Conical: 53.1° zenith angle, swath 1400 km – Scan rate: 31.9 scan/min = 12.5 km/scan
Coverage/cycle	Global coverage once/day
Resolution (constant)	Changing with frequency, consistent with an antenna diameter of 61 x 66 cm
Resources	Mass: 48.5 kg - Power: 45 W - Data rate: 6.0 kbps

Central frequency (GHz)	Bandwidth (MHz)	Polarisations	Accuracy (NEΔT)	IFOV	Pixel
19.35	400	V, H	0.43 K	45 x 68 km	25.0 x 12.5 km
22.235	400	V	0.73 K	40 x 60 km	25.0 x 12.5 km
37.0	1500	V, H	0.38 K	24 x 36 km	25.0 x 12.5 km
85.5	3000	V, H	0.71 K	11 x 16 km	12.5 x 12.5 km

1.3.2 The Special Sensor Microwave Imager/Sounder (SSMIS)

The Special Sensor Microwave Imager/Sounder (SSMIS) is a passive microwave radiometer with a 53.1 degree Earth incidence angle sensing upwelling microwave radiation at 24 channels covering a wide range of frequencies from 19 - 183 GHz. In common with its predecessor SSM/I, SSMIS employs conical scanning geometry that offers the advantage that the polarization of the measured radiances is invariant across the scan. In fact, these conical scanners provide images with a constant zenith angle, which implies a constant optical path in the atmosphere and homogeneous impact of the polarisation effects. In addition, the open design permits relatively large primary reflectors and consequently affords good horizontal resolution.

Additionally, conical scanning provides constant resolution across the image, though changing with frequency. It is noted that the IFOV is elliptical, with the major axis elongated along the viewing direction and the minor axis along-scan, approximately 2/3 of the major. Its size is dictated by the antenna diameter (actually, the antenna is slightly elliptical, to partially compensate for the panoramic distortion), but also by the portion of antenna effectively illuminated (this makes it possible to obtain the same IFOV for a group of different frequencies, if co-registration is a strong requirement).

SSMIS is the first conical scanner to be used for temperature sounding and it combines a range of temperature sounding channels (50 – 63 GHz) with humidity sounding channels (183 GHz) as well as a range of imaging channels (19 – 150 GHz).

With respect to SSM/I, SSMIS adds temperature and humidity sounding channels that, operating in absorption bands, are applicable over land. They also carry forward information on the atmospheric thermal-hygrometric structure, useful in the retrieval process.

Data are collected along an active scan of 144 degrees across track producing a swath width on the ground of 1707 km. The first of five sensors was launched on board DMSP F-16 on October 18, 2003.

The SSMIS is a joint US Air Force/Navy multi-channel passive microwave sensor that combines and extends the imaging and sounding capabilities of three separate DMSP microwave sensors including the SSM/T, SSM/T2, and SSM/I.
Table 1.2 shows the radiometric characteristics of SSMIS.

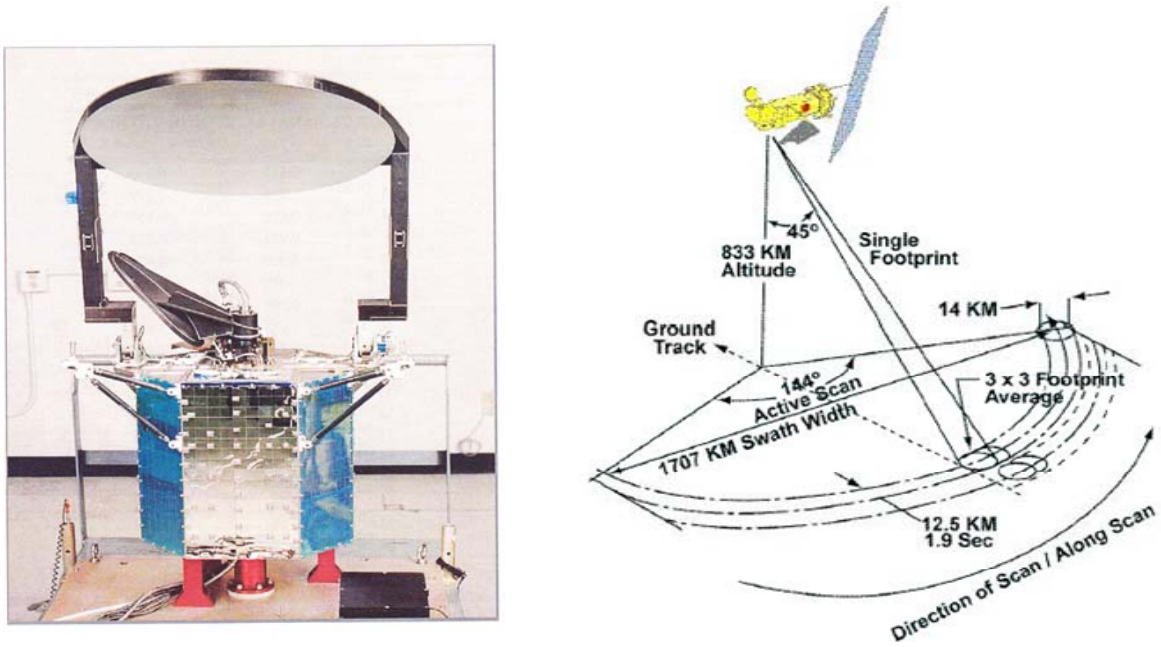

Fig. 1.4 The Special Sensor Microwave Imager/Sounder (SSMIS)

1.3.3 The Advanced Microwave Sounding Unit (AMSU)
The AMSU system is implemented in two separate modules: the AMSU-A and AMSU-B (or MHS – Microwave Humidity Sounder). The AMSU is a multi-channel microwave radiometer that is used for measuring global atmospheric temperature profiles and provides information on atmospheric water in all of its forms (with the exception of small ice particles, which are transparent at microwave frequencies)
AMSU is derived from the Microwave Sounding Unit (MSU) which began service in 1978 on TIROS-N and continued on the NOAA 6 through 14 satellites. AMSU flies on the NOAA KLM satellites: NOAA 15, launched 13 May 1998; NOAA 16, launched 21 September 2000; and NOAA 17, launched 24 June 2002.
AMSU-A is primarily a temperature sounder that provides atmospheric information in the presence of clouds, which can be used to correct the infrared measurements for the effects of clouds. This is possible because microwave radiation passes, as already mentioned, to a varying degree, through clouds - in contrast with visible and infrared radiation, which are

stopped by all but the most tenuous clouds. Table 1. shows the channel characteristics of AMSU-A.

Tab. 1.2 Radiometric characteristics of SSMIS

SSMIS	Special Sensor Microwave - Imager/Sounder
Satellites	DMSP F 16 and DMSP S 17 to 20
Status (June 2009)	Operational - Utilisation period: 2003 to ~ 2016
Mission	Multi-purpose MW imager with temperature/humidity sounding channels for improved precipitation
Instrument type	21-frequency, 24-channel MW radiometer
Scanning technique	Conical: 53.1° zenith angle, swath 1700 km – Scan rate: 31.9 scan/min = 12.5 km/scan
Coverage/cycle	Global coverage once/day
Resolution (constant)	Changing with frequency, consistent with an antenna diameter of 61 x 66 cm
Resources	Mass: 96 kg - Power: 135 W - Data rate: 14.2 kbps

Central frequency (GHz)	Bandwidth (MHz)	Polarisations	Accuracy (NEΔT)	IFOV	Pixel
19.35	400	V, H	0.7 K	45 x 68 km	25.0 x 12.5 km
22.235	400	V	0.7 K	40 x 60 km	25.0 x 12.5 km
37.0	1500	V, H	0.5 K	24 x 36 km	25.0 x 12.5 km
50.3	400	H	0.4 K	18 x 27 km	37.5 x 12.5 km
52.8	400	H	0.4 K	18 x 27 km	37.5 x 12.5 km
53.596	400	H	0.4 K	18 x 27 km	37.5 x 12.5 km
54.4	400	H	0.4 K	18 x 27 km	37.5 x 12.5 km
55.5	400	H	0.4 K	18 x 27 km	37.5 x 12.5 km
57.29	350	-	0.5 K	18 x 27 km	37.5 x 12.5 km
59.4	250	-	0.6 K	18 x 27 km	37.5 x 12.5 km
60.792668 $\pm$ 0.357892 $\pm$ 0.050	120	V + H	0.7 K	18 x 27 km	37.5 x 12.5 km
60.792668 $\pm$ 0.357892 $\pm$ 0.016	32	V + H	0.6 K	18 x 27 km	75.0 x 12.5 km
60.792668 $\pm$ 0.357892 $\pm$ 0.006	12	V + H	1.0 K	18 x 27 km	75.0 x 12.5 km
60.792668 $\pm$ 0.357892 $\pm$ 0.002	6	V + H	1.8 K	18 x 27 km	75.0 x 12.5 km
60.792668 $\pm$ 0.357892	3	V + H	2.4 K	18 x 27 km	75.0 x 12.5 km
63.283248 $\pm$ 0.285271	3	V + H	2.4 K	18 x 27 km	75.0 x 12.5 km
91.655	3000	V, H	0.9 K	10 x 15 km	12.5 x 12.5 km
150	1500	H	0.9 K	10 x 15 km	37.5 x 12.5 km
183.31 $\pm$ 6.6	1500	H	1.2 K	10 x 15 km	37.5 x 12.5 km
183.31 $\pm$ 3.0	1000	H	1.0 K	10 x 15 km	37.5 x 12.5 km
183.31 $\pm$ 1.0	500	H	1.2 K	10 x 15 km	37.5 x 12.5 km

The AMSU-A instrument consists of two independent modules (AMSU-A1 and AMSU-A2), with each module having separate spacecraft interfaces. AMSU-A is a crosstrack scanner.
AMSU-A1 has two antenna/receiver systems and AMSU-A2 has one for processing the microwave channels. The three receiving antennas are parabolic focusing reflectors that rotate continuously, completing one revolution in 8 seconds. The 8-second scan cycle is divided into three segments. In the first segment the Earth is viewed at 30 different angles, symmetric around the nadir direction, in a step-and-stare sequence.
Each of the 30 Earth views (scene stations) takes about 0.2 seconds, for a total of approximately 6 seconds.

Table 1.3 Radiometric characteristics of AMSU-A

AMSU-A	Advanced Microwave Sounder Unit - A
Satellites	NOAA 15 to 19 - MetOp 1 to 3 - EOS-Aqua
Status (May 2008)	Operational – Utilisation period: 1998 to ~ 2014 on NOAA, 2006 to ~ 2020 on MetOp, 2002 to ~ 2009 on EOS-Aqua
Mission	Temperature sounding in nearly-all-weather conditions
Instrument type	15-channel MW radiometer
Scanning technique	Cross-track: 30 steps of 48 km s.s.p., swath 2250 km - Along-track: one 48-km line each 8 s
Coverage/cycle	Near-global coverage twice/day
Resolution (s.s.p.)	48 km IFOV
Resources	Mass: 104 kg - Power: 99 W - Data rate: 3.2 kbps

Central frequency (GHz)	Bandwidth (MHz)	Polarisation	Radiometric accuracy (NEΔT)
23.800	270	V	0.30 K
31.400	180	V	0.30 K
50.300	180	V	0.40 K
52.800	400	V	0.25 K
53.596 ± 0.115	170	H	0.25 K
54.400	400	H	0.25 K
54.940	400	V	0.25 K
55.500	330	H	0.25 K
$f_0 = 57.290344$	330	H	0.25 K
$f_0 \pm 0.217$	78	H	0.40 K
$f_0 \pm 0.3222 \pm 0.048$	36	H	0.40 K
$f_0 \pm 0.3222 \pm 0.022$	16	H	0.60 K
$f_0 \pm 0.3222 \pm 0.010$	8	H	0.80 K
$f_0 \pm 0.3222 \pm 0.0045$	3	H	1.20 K
89.000	6000	V	0.50 K

The second segment is a rapid scan covering a cold space view and an internal (warm) blackbody calibration target. Finally, each antenna returns to the starting position to start a new scan cycle.

Since the incidence angle changes moving cross-track, the effect of polarisation also changes, thus the information stemming from dual polarisation would be very difficult to be used, and in effect the various frequencies are observed under a single polarisation, V or H.

The AMSU-B (and MHS) is a crosstrack, continuous line scanning, total power radiometer and provides measurements of scene radiance in five channels.

The instrument has an IFOV of 1.1° (at the halfpower points). Spatial resolution at nadir is nominally 16 km (9.94 mi).The antenna provides a crosstrack scan, scanning ±48.95° from nadir with a total of 90 Earth fields-of-view per scan line. The instrument completes one scan every 2.66 seconds.

Table 1.4 shows the channel characteristics of AMSU-B and MHS. Most AMSU-B MHS frequencies lie in the 183 GHz band of H_2O, for humidity profiling.

Table 1.4 Radiometric characteristics of AMSU-B and MHS

AMSU-B	Advanced Microwave Sounder Unit - B
Satellites	NOAA 15 to 17
Status (May 2008)	Operational – Utilisation period: 1998 to ~ 2009
Mission	Humidity sounding in nearly-all-weather conditions. Also precipitation
Instrument type	5-channel MW radiometer
Scanning technique	Cross-track: 90 steps of 16 km s.s.p., swath 2250 km - Along-track: one 16-km line each 8/3 s
Coverage/cycle	Near-global coverage twice/day
Resolution (s.s.p.)	16 km IFOV
Resources	Mass: 50 kg - Power: 90 W - Data rate: 60 kbps

Central frequency (GHz)	Bandwidth (MHz)	Polarisation	Radiometric accuracy (NEΔT)
89.0	1000	V	0.37 K
150.0	1000	V	0.84 K
183.31 $\pm$ 7.0	2000	V	0.60 K
183.31 $\pm$ 3.0	1000	V	0.70 K
183.31 $\pm$ 1.0	500	V	1.06 K

MHS	Microwave Humidity Sounder Unit
Satellites	NOAA 18 to 19 - MetOp 1 to 3
Status (May 2008)	Operational - Utilisation period: 2005 to ~ 2014 on NOAA, 2006 to ~ 2020 on MetOp
Mission	Humidity sounding in almost all-weather conditions. Also precipitation rate
Instrument type	5-channel MW radiometer
Scanning technique	Cross-track: 90 steps of 16 km s.s.p., swath 2180 km - Along-track: one 16-km line each 8/3 s
Coverage/cycle	Near-global coverage twice/day
Resolution (s.s.p.)	16 km IFOV
Resources	Mass: 63 kg - Power: 93 W - Data rate: 3.9 kbps

Central frequency (GHz)	Bandwidth (MHz)	Polarisation	Radiometric accuracy (NEΔT)
89.0	2800	V	0.22 K
157.0	2800	V	0.38 K
183.31 $\pm$ 3.0	2000	H	0.42 K
183.31 $\pm$ 1.0	1000	H	0.57 K
190.311	2000	V	0.45 K

Figure 1.5 shows the geometry of cross track scanning of AMSU. These cross-track scanners provide images with constant angular sampling across track, implying that the IFOV elongates as the beam moves from nadir toward the edge of the scan (see figure 1.5). The elongation is such that:
- for AMSU-A the IFOV at nadir is: 48 x 48 km^2, at the edge of the 2250 km swath: 80 x 150 km^2;
- for AMSU-B and MHS the IFOV at nadir is: 16 x 16 km^2; at the edge: 27 x 50 km^2.

Fig. 1.6 shows the composite coverage of SSM/I-SSMIS and AMSU-MHS. It is important to note that precipitation retrieval from AMSU-MHS is essential for complementing SSM/I-SSMIS coverage, which would otherwise lead to observational gaps lasting ~ 10 h.

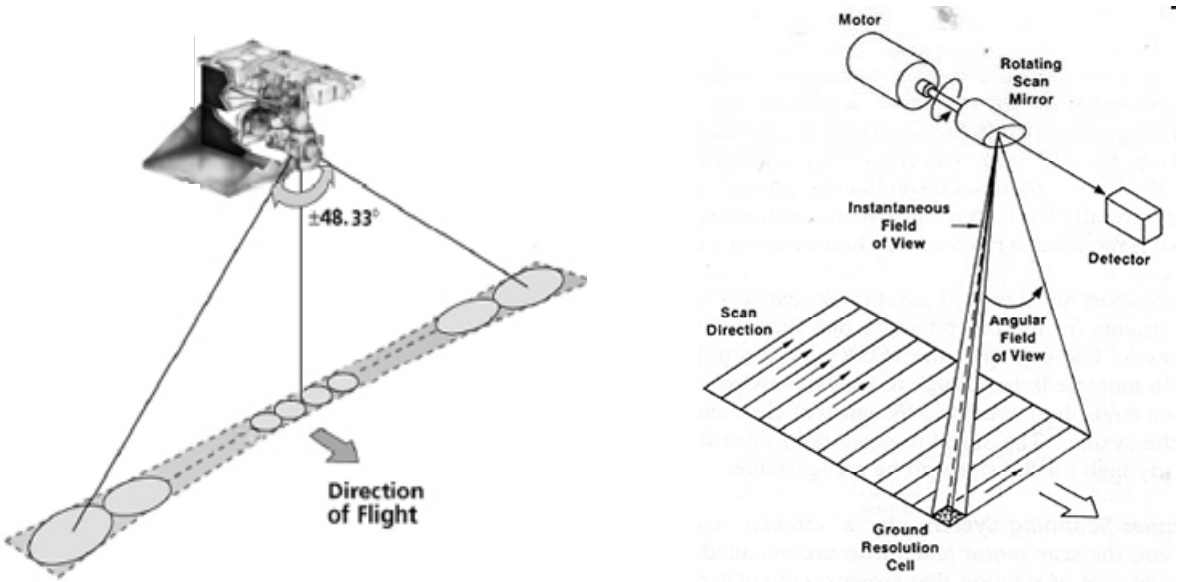

Fig. 1.5 AMSU–A and MHS of cross-track scanning (left), and schematic representation of cross track scanning geometry (right).

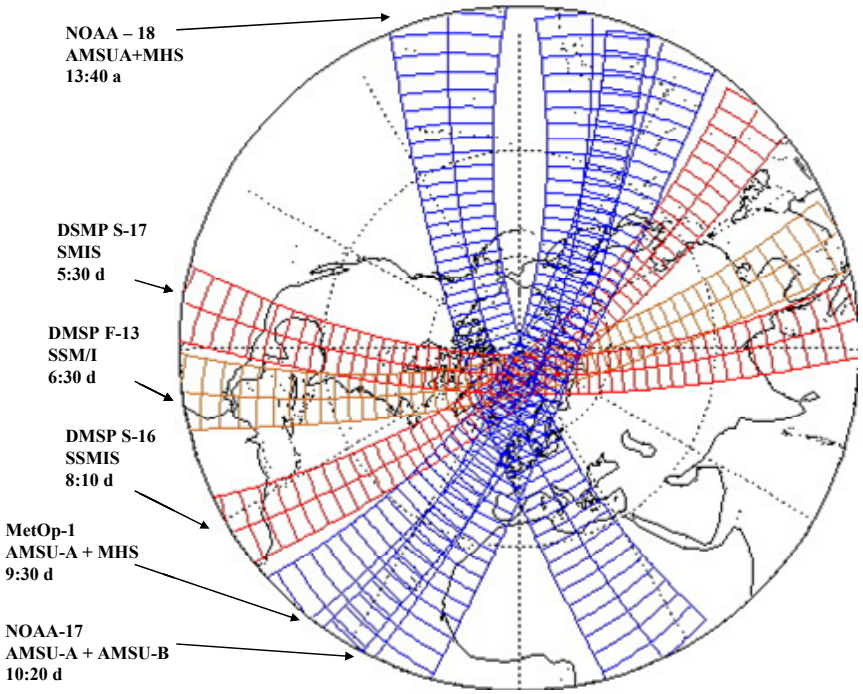

Fig. 1.6 Composite coverage of SSM/I – SSMIS and AMSU – MHS.

1.3.4 The Advanced Microwave Scanning Radiometer (AMSR-E)

The AMSR-E is a conically scanning total power passive microwave radiometer sensing microwave radiation (brightness temperatures) at 12 channels and 6 frequencies ranging from 6.9 to 89.0 GHz. Horizontally and vertically polarized radiation is measured separately at each frequency. There are 2 separate horns at 89 GHz, one being slightly offset from the centerline of the feedhorn array.

The AMSR-E instrument has an offset parabolic reflector 1.6 meters in diameter. Figure 1.7 shows the AMSR-E instrument (left), and the Aqua satellite with AMSR-E mounted in front (right). The atmospheric radiation is focused by the main reflector into an array of six feedhorns which then feed the radiation to the detectors.

A cold load reflector and a warm load are mounted on the transfer assembly shaft and do not rotate with the drum assembly. They are positioned off axis so that they pass between the feedhorn array and the parabolic reflector, occulting it once each scan. The cold load reflector reflects cold sky radiation into the feedhorn array thus serving, along with the warm load, as calibration references for the AMSR-E. Calibration of the radiometers is essential for the collection of useful data. Corrections for spillover and antenna pattern effects are incorporated in the data processing algorithms.

The AMSR-E rotates continuously about an axis parallel to the local spacecraft vertical at 40 revolutions per minute (rpm). At an altitude of 705 km, it measures the upwelling scene brightness temperatures over an angular sector of ±61 degrees around the sub-satellite track, resulting in a swath width of 1445 km.

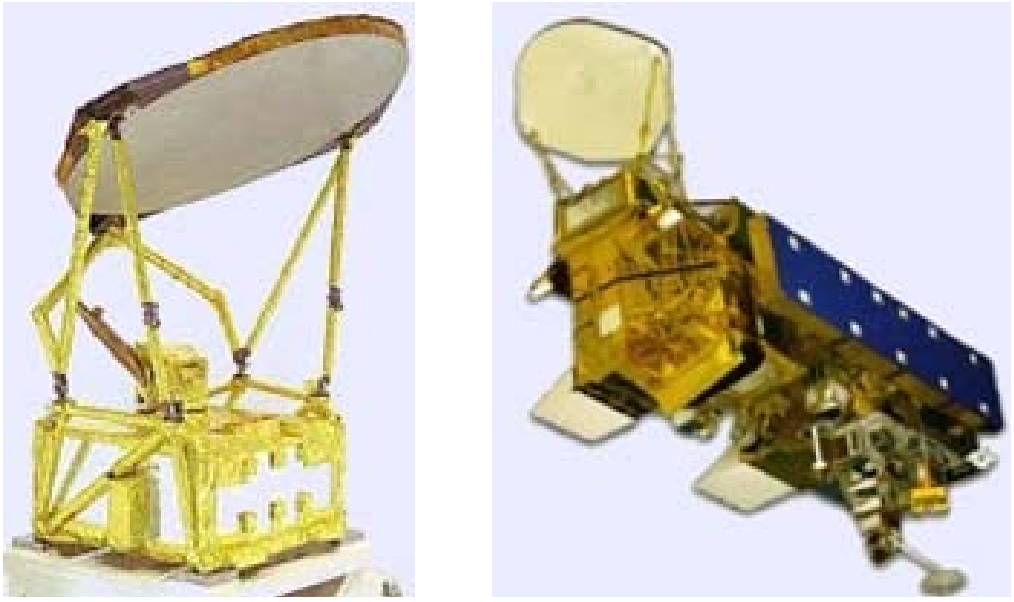

Fig. 1.7 The AMSR-E instrument (left), and the Aqua satellite with AMSR-E mounted in front (right).

Table 1.5 Radiometric characteristics of AMSR-E

AMSR-E	Advanced Microwave Scanning Radiometer for EOS
Satellites	EOS-Aqua
Status (May 2008)	Operational - Utilisation period: 2002 to ~ 2009
Mission	Multi-purpose MW imager
Instrument type	MW radiometer with 6 frequencies / 12 channels
Scanning technique	Conical: 55° zenith angle; swath: 1450 km - Scan rate: 40 scan/min = 10 km/scan
Coverage/cycle	Global coverage once/day
Resolution	Changing with frequency, consistent with an antenna diameter of 1.6 m
Resources	Mass: 314 kg - Power: 350 W - Data rate: 87.4 kbps

Central frequency (GHz)	Bandwidth (MHz)	Polarisations	Accuracy (NEΔT)	IFOV	Pixel
6.925	350	V, H	0.3 K	43 x 75 km	10 x 10 km
10.65	100	V, H	0.6 K	29 x 51 km	10 x 10 km
18.7	200	V, H	0.6 K	16 x 27 km	10 x 10 km
23.8	400	V, H	0.6 K	14 x 21 km	10 x 10 km
36.5	1000	V, H	0.6 K	9 x 14 km	10 x 10 km
89.0	3000	V, H	1.1 K	4 x 6 km	5 x 5 km

During a period of 1.5 seconds the spacecraft sub-satellite point travels 10 km. Even though the instantaneous field-of-view for each channel is different, active scene measurements are recorded at equal intervals of 10 km (5 km for the 89 GHz channels) along the scan. The half cone angle at which the reflector is fixed is 47.4° which results in an Earth incidence angle of 55.0°. Table 1.5 shows the channel characteristics of AMSR-E.

1.4 The HSAF, RISKMED, and FLASH projects

The research activity on the Bayesian estimation of precipitating cloud parameters, which is carried out at CNR ISAC, is part of international research projects that are aimed at producing weather forecasts, particularly for severe precipitation events. The results of the projects consist of the organization of early warning systems, addressed to regional authorities and civil protection agencies. In this way they contribute to the protection of lands and people from adverse weather conditions.

The projects are based on international cooperation, which also includes research centers carrying out research projects on the remote sensing of atmosphere. The results of scientific investigations are then directly transferred to the users through the project's products. The research activities developed within the projects concern different approaches to the analysis of atmospheric phenomena, including precipitation estimates on the ground using satellite-based passive microwave measurements, or using combined microwave (LEO) and infrared (GEO) measurements, or using combined microwave and lighting measurement, as lighting activity can be an effective indicator of heavy convective precipitation events. Other research concerns the estimate of other meteorological events, as the accumulated precipitation at the ground by blended MW and IR data, the global surface soil moisture by radar scatterometer, the snow detection -snow mask- by VIS/IR radiometry.

The contribution of CNR-ISAC is mainly focused on the precipitation retrieval from satellite-based passive microwave measurements. Particularly, the results of the current research activity on surface rain rate retrieval (as described in the following ch. 3 and ch. 4) are steadily

examined and validated with the contribution of other partners, and then inserted in the project's products. The results and the new research lines are also analyzed and evaluated with the collaboration of the Department of Atmospheric and Oceanic Sciences at the University of Wisconsin, USA.
In the following paragraphs a short description of the basic elements of the projects will be presented.

1.4.1 The H-SAF project

The "EUMETSAT (European Organisation for the Exploitation of Meteorological Satellites) Satellite Application Facility on Support to Operational Hydrology and Water Management (H-SAF)" was established by the EUMETSAT Council on 3 July 2005, and kicked-off on 16 September 2005. The Development Phase will last 5 years, until late 2010. The work programme makes distinction between two phases. The first phase regards product development, prototype generation, and preliminary validation. The second phase deals with regular production, extended validation, and hydrological validation.
The H-SAF objectives are, in particular:
- to provide new satellite-derived products from existing and future satellites with sufficient time and space resolution to satisfy the needs of operational hydrology;
- to perform independent validation of the usefulness of new products for fighting against floods, landslides, avalanches, and evaluating water resources.
The project is based on international cooperation among Italy (CNR and CNMCA (Centro Nazionale di Meteorologia e Climatologia Aeronautica)) responsible for precipitation products, Austria (ZAMG (Zentralanstalt für Meteorologie und Geodynamik) and ECMWF (European Centre for Medium-range Weather Forecasts)) responsible for soil moisture products, Finland and Turkey (FMI (Finnish Meteorological Institute) and TSMS (Turkish State Meteorological Service)) responsible for snow products.

1.4.2 The RISKMED project

The RISKMED project originates from the awareness that extreme weather events have an adverse impact on humans as well as on a large number of social and economic activities. The main objective of the project is to tackle this problem by building an early warning system that provides accurate and detailed weather forecasts and disseminates the appropriate warnings. The project is conducted by scientific groups involved in the production of detailed weather forecasts, based on observations (mainly from satellites since a majority of participating countries are covered by the sea) as well as from high-resolution weather and wave models.
The scientific partners are the University of Ioannina (Greece), the CNR-ISAC, the University of Malta, the Cyprus Meteorological Service, the National Observatory of Athens.
The main activities of the project comprise:
- Use of satellite and lightning data and meteo-marine sensors for the monitoring of severe weather events over the area
- Operational use of high resolution modelling for the provision of weather forecasts in all major meteorological parameters (winds, rain, snow, temperature, etc).
- Use of a wave model in case of strong winds and adverse marine conditions near selected coasts

- Presentation of the results in a user-friendly way, according to the requirements of the end-users, and dissemination of warnings (through a dedicated web page, e-mails, text messages to mobile phones etc).

The main deliverable will be the early warning system over four areas (Southern Italy, Malta, Northwestern Greece and Cyprus), in an operational mode.

1.4.3 The FLASH project

The FLASH project is focused on observations, analysis and modeling of lightning activity in thunderstorms, for use in short term forecasting of flash floods.

Floods result from large weather systems with embedded severe thunderstorms that deposit large amounts of rainfall in short periods of time. Since lightning activity can be detected and monitored continuously from thousands of kilometers away, the project considers the use of lightning data to better nowcast (3-hour prediction) and forecast (24-48 hour prediction) the location, intensity and timing of heavy convective precipitation events.

For this, the aim of the research is to analyse rainfall-lightning relationships using lightning and precipitation data sets in the Mediterranean region. It will also use lightning information in conjunction with infrared / microwave observations from geostationary / low Earth orbiting satellites to improve cloud characterization, convection detection and precipitation retrieval from space.

The participants are: The Aviv University and the Open University of Israel, the CNR-ISAC, the National Observatory of Athens, the University of Barcelona, the Ministry of Agriculture, Natural Resources and Environment – Cyprus Meteorological Service of Cyprus.

The contribution of CNR-ISAC is included in the research on precipitation retrieval using lightning data in combination with passive-microwave (MW) measurements from Low Earth Orbit (LEO) satellites and visible-infrared (VIS-IR) measurements from geosynchronous (GEO) Meteosat Second generation (MSG) satellites.

CHAPTER 2 – Microwaves radiative transfer

The observed microwave radiances at the top of the atmosphere originate partly at the earth's surface and partly from atmospheric constituents. The contribution from the earth's surface depends primarily upon the nature of the surface (i.e., water or land) and on the temperature of that surface. Atmospheric constituents such as oxygen, water vapour and cloud water act to absorb and emit upwelling radiation. Large precipitation drops further act to scatter upwelling radiation. Because of the varied, and often complex nature of each of these components, it is necessary to first describe the basic process of radiative transfer in the atmosphere and then consider the effects of these components on the propagation of radiation through the atmosphere.

In this chapter, the radiative transfer in the atmosphere and the radiative transfer equation are described first (section 2.1). Then, the passive microwave sensing of atmosphere, under clear-sky conditions, both from upward looking and downward looking radiometers, is presented (section 2.2). In section 2.3 the different microwave frequencies of satellite-borne radiometers are considered with reference to the oxygen and water vapour absorption spectra. In section 2.4 the effects of emission and scattering processes of hydrometeors on precipitation measurements are analyzed. Finally, section 2.5 presents an example of methods used in empirical algorithms for measuring rain rate.

2.1 The radiative transfer equation

Before starting with the radiative transfer equation, it is appropriate to recall some basic quantities that are necessary for obtaining the equation (Wallace and Hobbs 1977, Ulaby et al. 1986, Galati and Gilardini 2000).

Radiant flux is the rate of energy transfer by electromagnetic radiation, and it is measured in joules per second or watts. The irradiance (E) is the flux divided by the area (orthogonal to the direction of the radiation) through which it passes, and it is expressed in units of watts per square meter. The irradiance per unit wavelength interval at wavelength λ is called the monochromatic irradiance E_λ; it has the units of watts per square meters per micrometer. The irradiance is therefore equal to

$$E = \int_0^\infty E_\lambda d\lambda \,. \qquad (\mathrm{W/m^2}) \qquad (2.1)$$

Radiance (or intensity) is defined as the irradiance per unit solid angle and it is expressed in watts per square meter per steradian.

The spectral radiance I (or specific intensity) is defined as the radiance per unit frequency interval (W m^{-2} sr^{-1} Hz^{-1}) or per unit wavelength (W m^{-2} sr^{-1} μm^{-1}).

Figure 2.1 shows the passage of a radiation of spectral radiance I(ν,r) through a cylindrical elementary volume having its axis in the direction **r** (r is the abscissa along **r**). In the figure dS is the surface of the base of the cylinder. It is supposed that the spectral radiance enters the cylinder in the direction **r,** that is normally to the surface dS, and that the material of the cylinder is homogeneous. I(ν,r+dr) is the spectral radiance coming out from the other base of the cylinder, in the direction **r**. The difference between I(ν,r) and I(ν,r+dr) is due to the interaction of the radiation with the material. The interaction can produce a reduction in the spectral radiance due to the absorption and scattering processes, and it can also produce an

increase due to the emission of the material and the scattering from all other directions in the direction **r**.

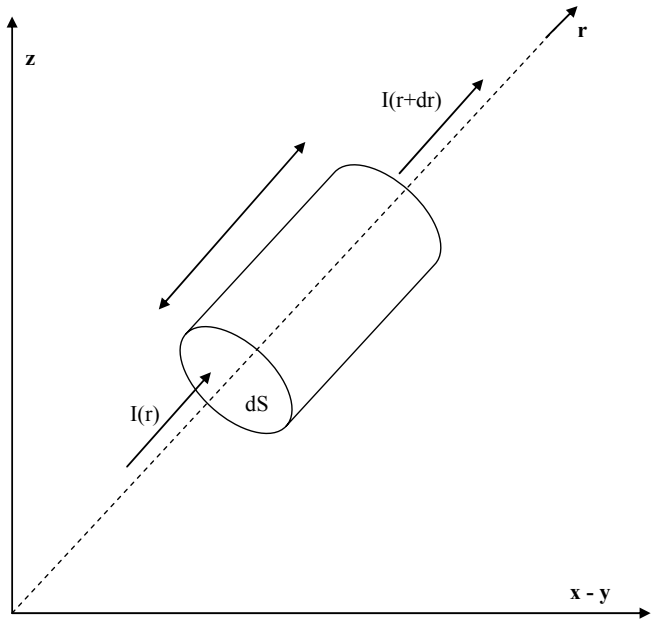

Fig. 2.1 Radiation transfer through a cylindrical elementary volume.

The effect of the absorption can be described using the volume absorption coefficient $k_a(\nu,r)$

$$k_a(\nu,r) = \frac{dI_a(\nu,r)\cdot dS\cdot d\Omega\cdot d\nu}{dS\cdot dr\cdot I(\nu,r)\cdot d\Omega\cdot d\nu} = \frac{dI_a(\nu,r)}{dr\cdot I(\nu,r)} \qquad (\mathrm{m}^{-1}) \qquad (2.2)$$

where the term $dI_a(\nu,r)\cdot dS\cdot d\Omega\cdot d\nu$ represents the power absorbed by the cylinder, $I(\nu,r)\cdot d\Omega\cdot d\nu$ represents the incident irradiance and $dS\cdot dr$ the volume of the cylinder (Galati and Gilardini 2000).

The variation (reduction) of the spectral radiance due to the absorption is then

$$dI_a(\nu,r) = -\,k_a(\nu,r)\, I(\nu,r)\, dr. \qquad (2.3)$$

The effect of the scattering can be similarly expressed using the volume scattering coefficient $k_s(\nu,r)$ defined as

$$k_s(\nu,r) = \frac{dI_s(\nu,r)\cdot dS\cdot d\Omega\cdot d\nu}{dS\cdot dr\cdot I(\nu,r)\cdot d\Omega\cdot d\nu} = \frac{dI_s(\nu,r)}{dr\cdot I(\nu,r)} \qquad (\mathrm{m}^{-1}) \qquad (2.4)$$

where $dI_s(\nu,r)\cdot dS\cdot d\Omega\cdot d\nu$ is the power scattered by the cylinder. The reduction of the spectral radiance due to the scattering process is then

$$dI_s(\nu,r) = -\,k_s(\nu,r)\, I(\nu,r)\, dr. \qquad (2.5)$$

It is possible to consider the overall extinction of the spectral radiance, as both the processes are linear, introducing the volume attenuation coefficient $k_e(\nu,r)$

$$k_e(\nu,r) = k_a(\nu,r) + k_s(\nu,r) \qquad (\mathrm{m}^{-1}). \qquad (2.6)$$

The coefficients k_e, k_a, and k_s are also measured in units neper m-1, when the $\log_e$ is used for the ratio dI/I.

The overall extinction can be expressed as

$$dI_e(\nu,r) = - (k_a(\nu,r)\, I(\nu,r)\, dr + k_s(\nu,r)\, I(\nu,r)\, dr) = - k_e(\nu,r)\, I(\nu,r)\, dr. \quad (2.7)$$

The process of thermal emission, that increases the value of the spectral radiance I(ν,r+dr) coming out from the cylinder, is related to the increase in temperature T of the cylinder consequent to the absorption of the energy of the incident radiation. Taking Kirchhoff's law into account, with reference to the equilibrium between thermal emission and absorption, the increase in the spectral radiance due to the thermal emission can be expressed as

$$dI_{te}(\nu,r) = k_a(\nu,r)\, B(\nu,T(r))\, dr \quad (2.8)$$

where B(ν,T(r)) is the spectral radiance of the blackbody at temperature T, that is (Plank's law)

$$B(\nu,T(r)) = \frac{2h\nu^3}{c^2(e^{h\nu/kT}-1)} \quad (2.9)$$

where h is the Plank's constant, K the Boltzmann's constant, and c the light speed in the vacuum.

Another process that can also increase the value of the spectral radiance concerns the scattering of the radiation, travelling along directions different from **r,** which enters the cylinder and is diffused along **r**. The corresponding variation of the spectral radiance is

$$dI_{sc}(\nu,r) = k_s(\nu,r)\, J_s(\nu,r)\, dr \quad (2.10)$$

where $J_s(\nu,r)$ is a 'source function' that takes into account the contributions of the radiation coming from all directions and that is diffused along **r**. Denoting with $I(\mathbf{r_i})$ the spectral radiance entering the cylinder along the direction $\mathbf{r_i}$, and with $\Psi(\mathbf{r},\mathbf{r_i})$ a function that takes into account the coupling between the incident and the diffused intensities, the 'source function' can be expressed as

$$J_s(\nu,r) = \frac{1}{4\pi}\int_{4\pi} \Psi(\mathbf{r},\mathbf{r_i})\; I(\mathbf{r_i})\, d\Omega. \quad (2.11)$$

The equation of transfer is then

$$\frac{dI(\nu,r)}{dr} = dI_e(\nu,r) + d_{te}(\nu,r) + dI_{sc}(\nu,r) = -k_e(\nu,r)I(\nu,r) + k_a(\nu,r)B(\nu,T(r)) + k_s(\nu,r)J_s(\nu,r). \quad (2.12)$$

Introducing the 'total source function' J(ν,r)

$$J(\nu,r) = \frac{k_a}{k_e}B(\nu,T(r)) + \frac{k_s}{k_e}J_s(\nu,r) = (1-w)B(\nu,T(r)) + wJ_s(\nu,r) \quad (2.13)$$

where $w = k_s/k_e$ is called the single scattering albedo, the radiative transfer equation can be written as

$$\frac{dI(\nu,r)}{dr} = -k_e(\nu,r)I(\nu,r) + k_eJ(\nu,r) = \left[J(\nu,r) - I(\nu,r)\right]\cdot k_e. \quad (2.14)$$

Introducing the optical thickness increment, $d\tau = k_e dr$ (dimensionless), the (2.14) can be expressed in the form

$$\frac{dI(\nu,r)}{d\tau} + I(\nu,r) = J(\nu,r), \quad (2.15)$$

and the optical thickness between $r = r_1$ and $r = r_2$ in the form

$$\tau(r_1, r_2) = \int_{r_1}^{r_2} k_e dr \,. \tag{2.16}$$

The solution of the radiative transfer equation (2.15), for a semi-infinite medium with an attenuation coefficient k_e and a total source function J, has the expression (Galati and Gilardini 2000)

$$I(r) = I(0) \cdot e^{-\tau(0,r)} + \int_0^r k_e(r') \cdot J(r') \cdot e^{-\tau(r',r)} \cdot dr' \tag{2.17}$$

where I(r) is the spectral radiance at the abscissa r, in the direction **r**, I(0) is the 'boundary' spectral radiance for r = 0. The first term on the right side of (2.17) represents the contribution, to the spectral radiance observed at the abscissa r, in the direction **r**, of the radiance I(0) at r = 0. I(0) is reduced by the term ($e^{-\tau(0,r)}$) that represents the extinction effect of the medium. The second term on the right side of (2.17) represents the contributions (thermal emission and scattering in the direction **r**) of all the elements dr' of the medium, situated between 0 and r, reduced by the attenuation between r' and r.

The complete solution of (2.17) is difficult, but some simplifications can be obtained if the spectral radiance is in the range of the microwaves. In this case $h\nu/kT << 1$ and the spectral radiance of the blackbody can be written in the approximated form (Rayleight-Jeans)

$$B(\nu, T(r)) \approx \frac{2h\nu^3}{c^2(1 + \frac{h\nu}{kT(r)} - 1)} = 2kT(r)\frac{\nu^2}{c^2} = \frac{2kT(r)}{\lambda^2} \,. \tag{2.18}$$

The (2.18) shows that in the microwave region the spectral radiance B(ν,r) is proportional to the physical temperature T(r).

The spectral radiance at the abscissa r, I(ν,r), can be expressed in terms of the 'apparent temperature' $T_{AP}(\nu,r)$, that is representative of the spectral radiance at the abscissa r,

$$T_{AP}(\nu, r) = \frac{I(\nu, r)c^2}{2k\nu^2} = \frac{I(\nu, r)\lambda^2}{2k} \,. \tag{2.19}$$

Considering the (2.18), the $T_{AP}(\nu,r)$ can also be seen as the temperature of a hypothetical blackbody emitting an identical amount of radiation at the same wavelength. For this reason the $T_{AP}(\nu,r)$ is sometimes also referred as the 'brightness temperature' Tb.

Introducing the temperature T_{SC}, defined as

$$T_{SC} = \frac{1}{4\pi} \int_{4\pi} \Psi(r, r_i) \cdot T_{AP}(r_i) \cdot d\Omega \tag{2.20}$$

the solution (2.17) can be expressed in the form

$$T_{AP}(r) = T_{AP}(0) \cdot e^{-\tau(0,r)} + \int_0^r k_e(r') \cdot \left[(1-w) \cdot T(r') + w \cdot T_{SC}(r')\right] \cdot e^{-\tau(r',r)} dr' \tag{2.21}$$

For a non-scattering atmosphere ($k_s = 0$) in local thermodynamic equilibrium, the (2.21) can be simplified in

$$T_{AP}(r) = T_{AP}(0) \cdot e^{-\tau(0,r)} + \int_0^r k_a(r') \cdot T(r') \cdot e^{-\tau(r',r)} dr' \tag{2.22}$$

and the optical thickness (2.16) results equal

$$\tau(r',r) = \int_{r'}^{r} k_a(r'') \cdot dr''. \qquad (2.23)$$

The units of $\tau(r',r)$ are neper (Np) or dB, depending on whether the absorption coefficient $k_a(r)$ is expressed in neper per unit length or dB per unit length, respectively.

2.2 Passive microwave sensing of the atmosphere

With reference to a ground-based radiometer (figure 2.2), the radiation incident upon the radiometer antenna, in the microwave region and for a non-scattering atmosphere in local thermodynamical equilibrium, can be represented by the apparent temperature T_{AP} (Ulaby et al. 1986)

$$T_{AP}(\nu,\vartheta) = T_{DN}(\nu,\vartheta) + T_{EXTRA}(\nu) \cdot e^{-\tau_\nu(0,\infty)\sec\vartheta} \qquad (2.24)$$

where $T_{DN}(\nu,\theta)$ represents atmospheric radiation at frequency ν downwelling at angle θ from the zenith,

$$T_{DN}(\nu,\theta) = \sec\theta \cdot \int_0^{\infty} k_\nu(z) \cdot T(z) \cdot e^{-\tau_\nu(0,z)\cdot\sec\vartheta} dz\,. \qquad (2.25)$$

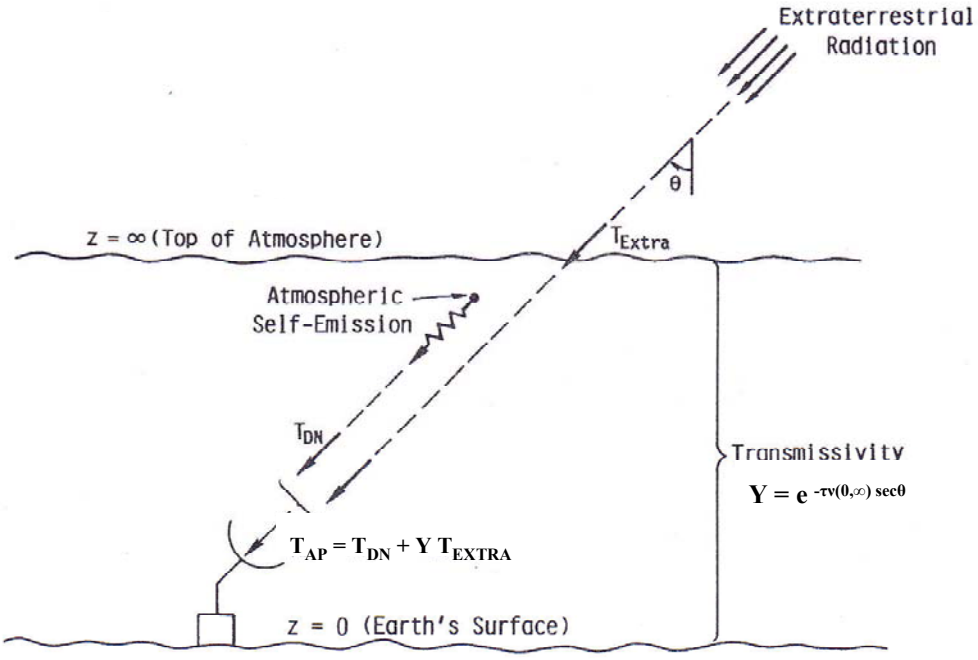

Fig. 2.2 Upward-looking radiometer observing the atmosphere at zenith angle θ (Ulaby et. al 1986).

$T_{EXTRA}(\nu)$ represents radiation of extraterrestrial origin (prior to entering the earth's atmosphere), and $\tau_\nu(0,\infty)$ is the zenith opacity of the atmosphere

$$\tau_\nu(0,\infty) = \int_0^\infty k_\nu(z')dz'. \tag{2.26}$$

where $k_\nu(z')$ is the total absorption coefficient at frequency ν and height z (km). In the (2.24) it is supposed the atmosphere horizontally stratified (plane parallel) so that both the temperature and the absorption coefficient depend only on the height z.
The transmissivity $Y_{\nu\theta}(0,\infty)$ of the atmosphere is related to the opacity by

$$Y_{\nu\theta}(0,\infty) = e^{-\tau_\nu(0,\infty)\cdot\sec\vartheta} = [Y_\nu(0,\infty)]^{\sec\theta} \tag{2.27}$$

where

$$Y_\nu(0,\infty) = e^{-\tau_\nu(0,\infty)} \tag{2.28}$$

is the zenith transmissivity.
Under clear sky conditions, $k_\nu(z)$ is equal to the absorption coefficient due to atmospheric gases ($k_{g\nu}(z)$). In general cases, however, it can also depend on the effect of hydrometeors included in the layer at height z and it can be expressed in the form

$$k_\nu(z) = k_{g\nu}(z) + k_{c\nu}(z) + k_{p\nu}(z) \tag{2.29}$$

where g, c, and p refer to gases, clouds, and precipitation, respectively.
Figure 2.3 shows the microwave absorption spectra of oxygen and water vapour, which, in clear air conditions, make a prevalent contribution to the absorption with respect to ozone and other gases.

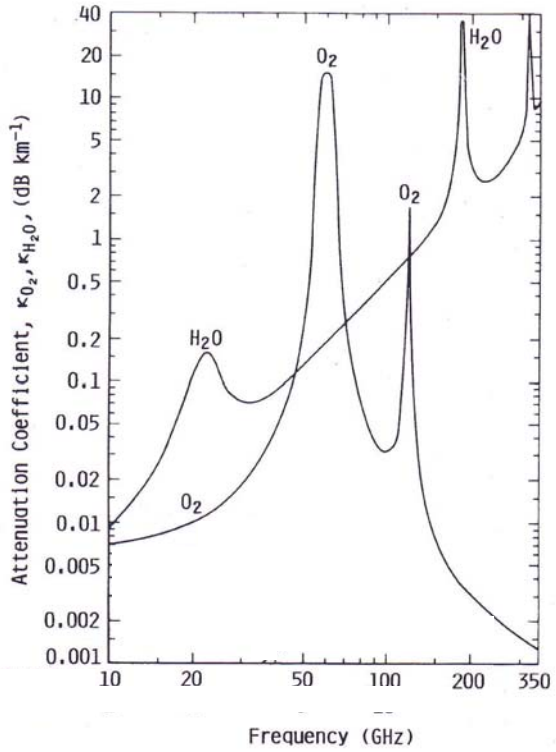

Fig. 2.3 Computed microwave absorption spectra of oxygen and water vapour at sea level, in clear air conditions (Ulaby el al. 1986).

Figure 2.4 shows the microwave spectra of the zenith opacity of a clear atmosphere, for surface water vapour densities of 0, 3, and 10 gm^{-3} and assuming a 2-km scale height for water vapour (Ulaby el al. 1986). The zenith opacity has a strong sensitivity to the surface water vapour density, except within the bands surrounding the oxygen absorption resonances centred at 60 GHz and 118.75 GHz.

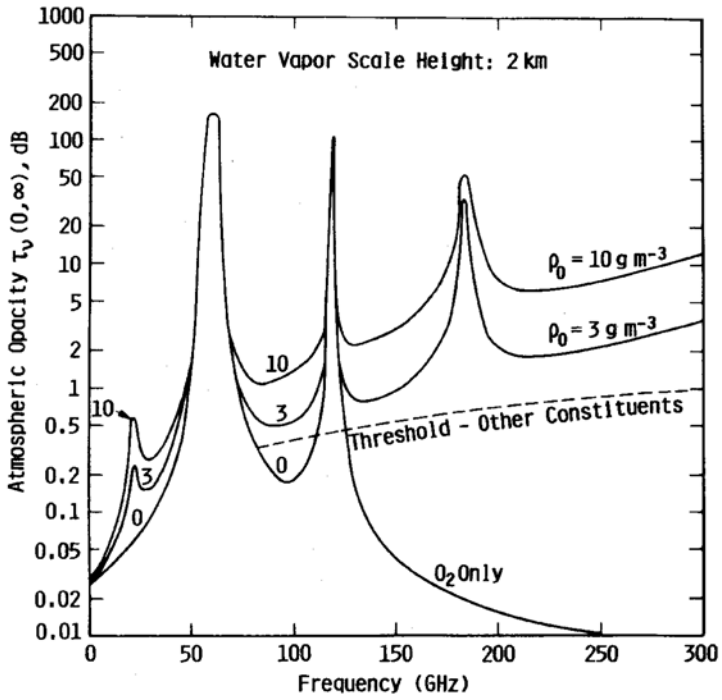

Fig. 2.4 Zenith opacity of the US Standard Atmosphere for surface temperature T_0=288 K, surface pressure P_0=1020.5 mbar, moist atmosphere (ρ_0=3 and 10 g m^{-3}) and 1013 mbar for the O_2 atmosphere (Ulaby et al.1986).

Figure 2.5 displays the microwave spectra of the zenith transmissivity $Y_\nu(0,\infty)$ for three different atmospheres, characterized by different surface temperatures T_0 and total integrated water vapour content M_v. In the figure four window bands can be seen from 25 to 50 GHZ (B1), from 70 to 115 GHz (B2), from 125 to 160 GHz (B3), and from 200 to 250 GHz (B4).

Using the expression (2.24), and defining an 'effective (or mean) radiating temperature $T_m(\nu)$' as

$$T_m(\nu) = \frac{\int_0^\infty T(z)\cdot k_\nu(z)\cdot e^{-\tau_\nu(0,z)}dz}{\int_0^\infty k_\nu(z)\cdot e^{-\tau_\nu(0,z)}dz} \qquad (2.30)$$

the measure of the zenith opacity $\tau_v(0,\infty)$ of the atmosphere is possible, using a ground based radiometer directed along the zenith direction (θ=0).

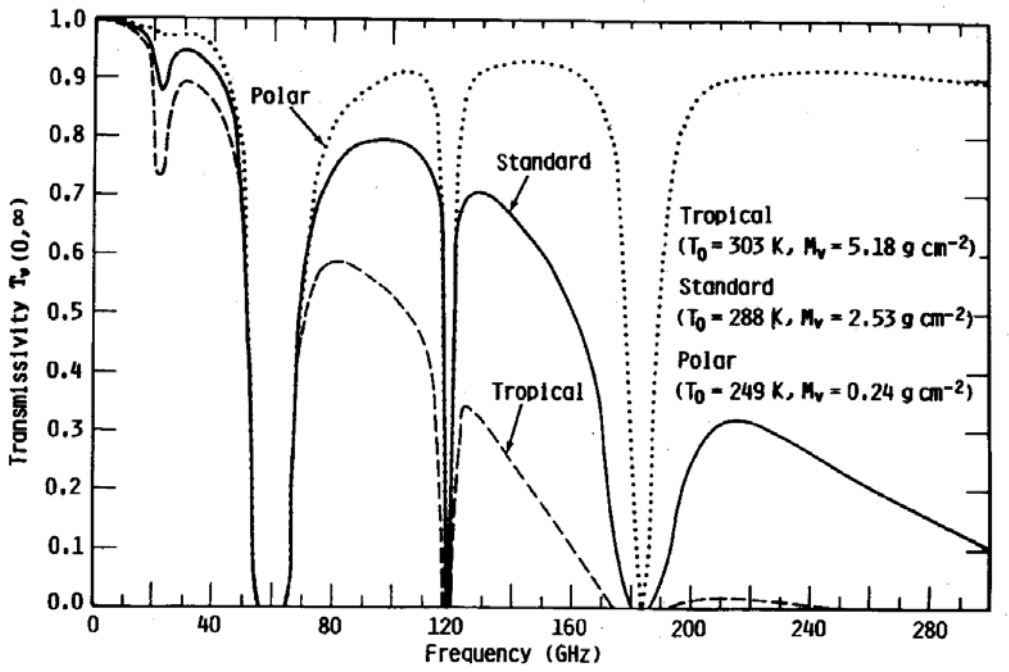

Fig. 2.5 Atmospheric transmittivity as characterized by different surface temperatures T_0 and integrated water vapour content M_v (Ulaby et al. 1986).

The denominator of (2.30) can be reduced as follows:

$$\int_0^{\infty} k_v(z)\cdot e^{-\tau_v(0,z)}dz = \int_0^{\tau_v(0,\infty)} e^{-\tau_v(0,z)}d\tau_v(0,\infty) = \left[1-e^{-\tau_v(0,\infty}\right] \qquad (2.31)$$

Then, combining (2.30) and (2.31) with (2.24), $T_{AP}(\nu)$ can be expressed as

$$T_{AP}(\nu) = T_{COS}\cdot e^{-\tau_v(0,\infty)} + T_m(\nu)\left[1-e^{-\tau_v(0,\infty)}\right] \qquad (2.32)$$

where the extraterrestrial radiation has been considered equal to the cosmic radiation, $T_{EXTRA} \approx T_{COS} = 2.7$ K.
From the (2.32) the expression of $\tau_v(0,\infty)$ can be obtained

$$\tau_v(0,\infty) = \ln\left(\frac{T_m(\nu)-T_{COS}}{T_m(\nu)-T_{AP}(\nu)}\right) \qquad (2.33)$$

The temperature $T_m(\nu)$ can be estimated through statistical analysis of the radiosonde measurements, and then $\tau_v(0,\infty)$ can be estimated from a measurement of $T_{AP}(\nu)$.
From the values of $T_{AP}(\nu)$, many other measurements of atmospheric variables (such as profiles and integrated values) can be performed.

Figure 2.6 presents the schema of the atmospheric sounding by satellite radiometers.

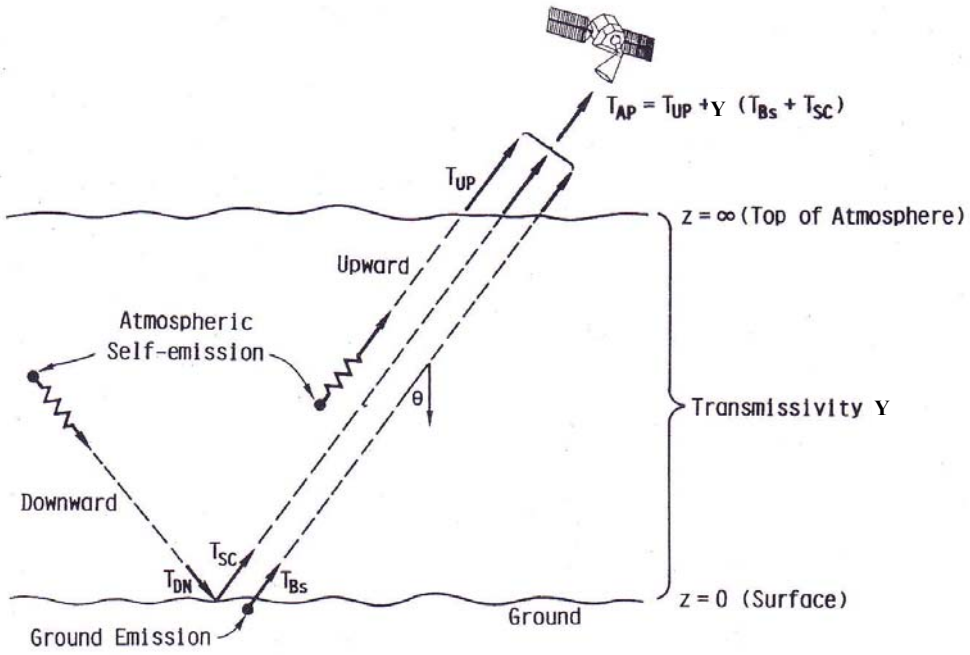

Fig. 2.6 Satellite-borne radiometer observing the earth at a nadir angle θ (Ulaby et al.1986).

The apparent temperature observed by a satellite borne radiometer observing the earth at an angle θ relative to the nadir direction is given by

$$T_{AP}(\nu,\theta) = T_{UP}(\nu,\theta) + Y_{\nu\theta}(0,\infty)[T_{Bs}(\nu,\theta) + T_{SC}(\nu,\theta)] \quad (2.34)$$

where $Y_{\nu\theta}(0,\infty)$ is the transmissivity of the entire atmosphere, defined as (see 2.28)

$$Y_{\nu\theta}(0,\infty) = e^{-\tau_\nu(0,\infty)\sec\theta}. \quad (2.35)$$

The term $T_{UP}(\nu,\theta)$ represents the upward emission by the atmosphere and is given by

$$T_{UP}(\nu,\vartheta) = \sec\theta \cdot \int_0^\infty k_\nu(z) \cdot T(z) \cdot e^{-\tau_\nu(z,\infty)\cdot\sec\theta} dz \quad (2.36)$$

and is an important term for atmospheric sensing. The term $Y_{\nu\theta}(0,\infty)T_{Bs}(\nu,\theta)$ represents the emission by the earth surface (T_{Bs}) as attenuated by the intervening atmosphere. The surface brightness temperature $T_{Bs}(\nu,\theta)$ is given by

$$T_{Bs}(\nu,\theta) = e_s(\nu,\theta)T_s \quad (2.37)$$

where $e_s(\nu,\theta)$ is the emissivity of the surface and T_s is its physical temperature. For non-nadir ($\theta \neq 0$) observations, $e_s(\nu,\theta)$ is a function of the roughness and the dielectric properties of the surface and is polarization dependent. The last term in (2.34), $T_{SC}(\nu,\theta)$, is the surface scattered contribution and represents the part of the downward-emitted radiation that is reflected (scattered) toward the radiometer antenna by the surface. An approximate expression for $T_{SC}(\nu,\theta)$ is

$$T_{SC}(\nu,\theta) \approx [1- e_s(\nu,\theta)]\ T_{DN}(\nu,\theta) \quad (2.38)$$

where $[1- e_s(\nu,\theta)]$ is the surface reflectivity and $T_{DN}(\nu,\theta)$ is the downward brightness temperature of the atmosphere (2.25).

The (2.34) can then be expressed in the form

$$T_{AP}(\nu,\theta) = \sec\theta \cdot \int_0^{\infty} k_\nu(z) \cdot T(z) \cdot e^{-\tau_\nu(z,\infty)\cdot\sec\theta} dz + \\ + Y_{\nu\theta}(0,\infty) \cdot \left\{ e_s(\nu,\theta) \cdot T_s + \left[1 - e_s(\nu,\theta)\right] \cdot T_{DN}(\nu,\theta) \right\} \qquad (2.39)$$

The contribution of the two terms on the right side of (2.39) to the apparent temperature observed by the radiometer, depends on the frequency. If a frequency is chosen corresponding to a low transmissivity of the atmosphere ($Y_{\nu\theta}(0,\infty) \approx 0$), the second term becomes negligible and $T_{AP}(\nu,\theta) \approx T_{UP}(\nu,\theta)$. On the other hand, if the satellite-borne radiometer is intended to provide information about the surface, the frequency should be chosen so that $Y_{\nu\theta}(0,\infty) \approx 1$, in which case $T_{AP}(\nu,\theta)$ approaches the surface brightness temperature.

From (2.39) it is also possible to evaluate the surface emissivity using the brightness temperature observed by a satellite antenna (Schiavon et al. 1989). An approximate expression for $e_s(\nu,\theta)$ as a function of $T_{AP}(\nu,\theta)$, in absence of scattering phenomena, is (Pierdicca et al. 2008)

$$e_s(\nu,\theta) = \frac{T_{AP}(\nu,\theta) - \left[T_{mDN}(\nu,\theta) \cdot e^{-\tau_\nu(0,\infty)\sec\theta} + T_{mUP}(\nu,\theta)\right] \cdot (1 - e^{-\tau_\nu(0,\infty)\sec\theta})}{\left[T_s - T_{mDN}(\nu,\theta) \cdot (1 - e^{-\tau_\nu(0,\infty)\sec\theta})\right] \cdot e^{-\tau_\nu(0,\infty)\sec\theta}} \qquad (2.40)$$

that is obtained from (2.39) using the expressions

$$T_{mDN} = \frac{T_{DN}(\nu,\theta)}{1 - e^{-\tau_\nu(0,\infty)}} \qquad \text{and} \qquad T_{mUP} = \frac{T_{UP}(\nu,\theta)}{1 - e^{-\tau_\nu(0,\infty)}} \qquad (2.41)$$

where T_{mDN} and T_{mUP} represent the mean radiative temperatures associated with the downwelling and upwelling radiation respectively. These temperature can be defined as the temperatures that an isothermal atmosphere should have to be equivalent to the actual one and are determined applying the radiative transfer scheme to the atmospheric vertical profiles of pressure, temperature and relative humidity.

2.3 The microwave frequencies of satellite-borne radiometers

Looking at the evolution of atmospheric sounding by satellite radiometers, starting from the early observations in 1968 (see table 2.1), an increase emerges in the number and range of frequencies utilized, and a consequent improved precipitation retrieval capability from space.
Figures 2.7-2.10 show the frequencies utilized by SSM/I, SSMIS, AMSU, and AMSR-E.
Many frequencies are placed near the absorbing lines of water vapour, at 22 and 183 GHz, and near the absorbing lines of oxygen, at 60 and 118 GHz. Other channels (<22, 85-91 and 150 GHz) are in the window regions between the absorbing lines.

The channels near 60 GHz - the frequency corresponding to an oxygen absorption band - are the "temperature sounding channels". By operating at these frequencies, where the absorption coefficient $k_\nu(z)$ is dominated by the oxygen-absorption coefficient $k_{O_2}(z)$, the apparent temperature (2.39) can be expressed in the form

$$T_{AP}(\nu,\theta) \approx \sec\theta \cdot \int_0^{\infty} k_\nu(z) \cdot T(z) \cdot e^{-\tau_\nu(z,\infty)\cdot\sec\theta} dz \qquad (2.42)$$

because the atmospheric transmissivity is quite small ($Y_{\nu\theta}(0,\infty) \approx 0$) at these frequencies (see fig. 2.5) and the last term on the right of the expression (2.39) is reduced to a negligible value.

Table 2.1 Examples of radiometer frequencies in the history of satellite-based radiometer systems.

Launch date	Spacecraft and instrument acronym	Frequencies (GHz)
Sept. 1968	Cosmos 243	3.5, 8.8, 22.2, 37
11 Dec. 1972	Nimbus 5 ESMR	19.3
	NEMS	22.2, 31.4, 53.6, 54.9, 58.8
Mar. 1978	DMSP 5D-1 SSM/T	50.5, 53.2, 54.3, 54.9, 58.4, 58.8, 59.4
24 Oct. 1978	Nimbus 7 SMMR	6.6, 10.7, 18.21, 37
	DMSP	
1987	SSM/I	19.3, 22.2, 37, 85.5
2003	SSMIS	19.3, 22.2, 37, 50.3, 52.8, 53.6, 54.4, 55.5, 57.3, 59.4, 63.3, 63.8(5), 91.6, 150, 183.3(3)

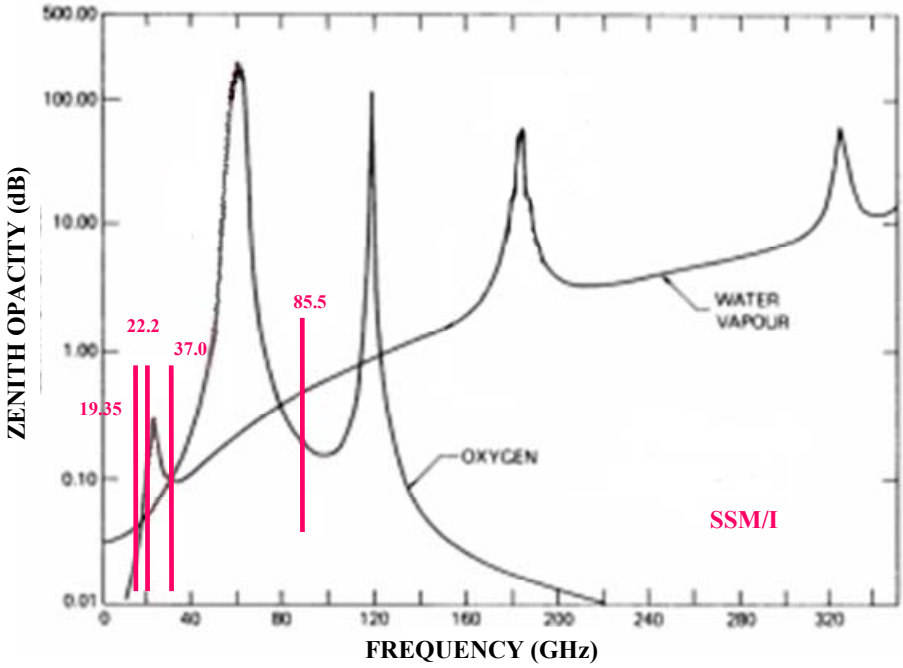

Fig. 2.7 Channels of SSM/I sensor. The channels are marked on the water vapour and oxygen opacity behaviour as a function of frequency.

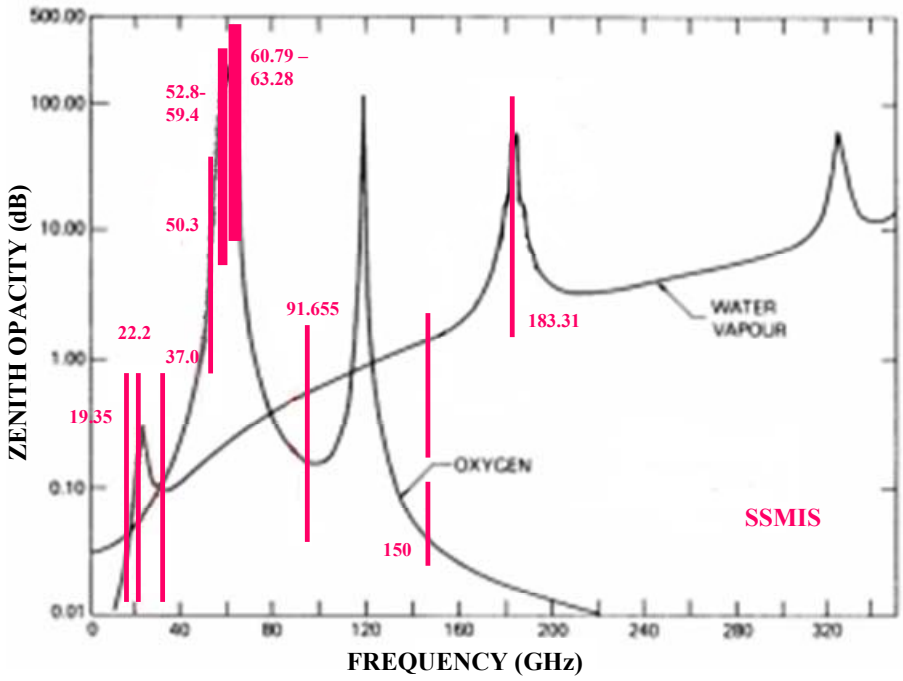

Fig. 2.8 Channels of SSMIS sensor. The channels are marked on the water vapour and oxygen opacity behaviour as a function of frequency.

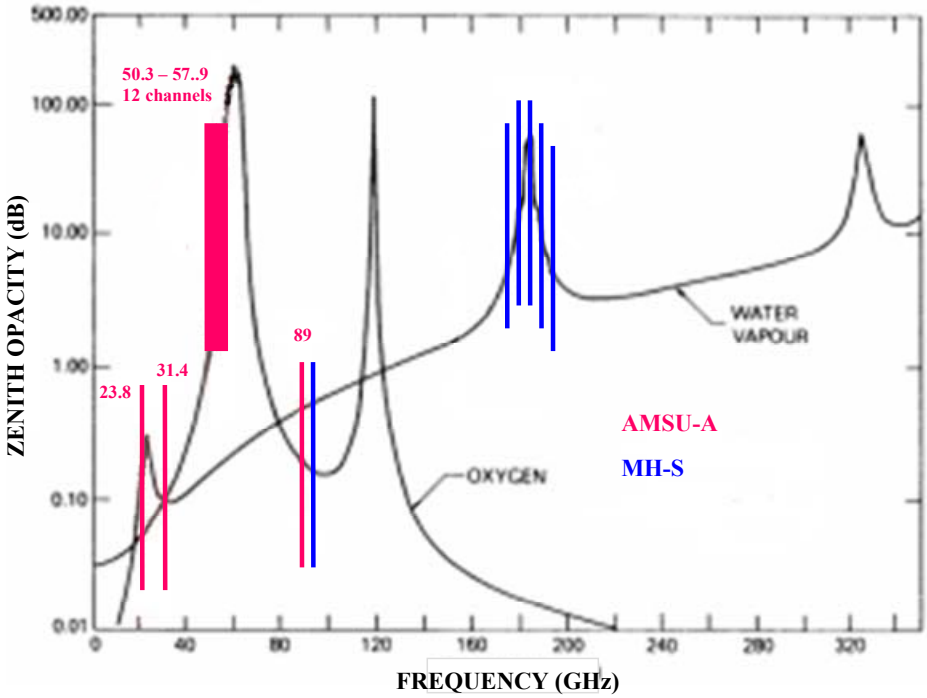

Fig. 2.9 Channels of AMSU-A and MH-S sensors. The channels are marked on the water vapour and oxygen opacity behaviour as a function of frequency.

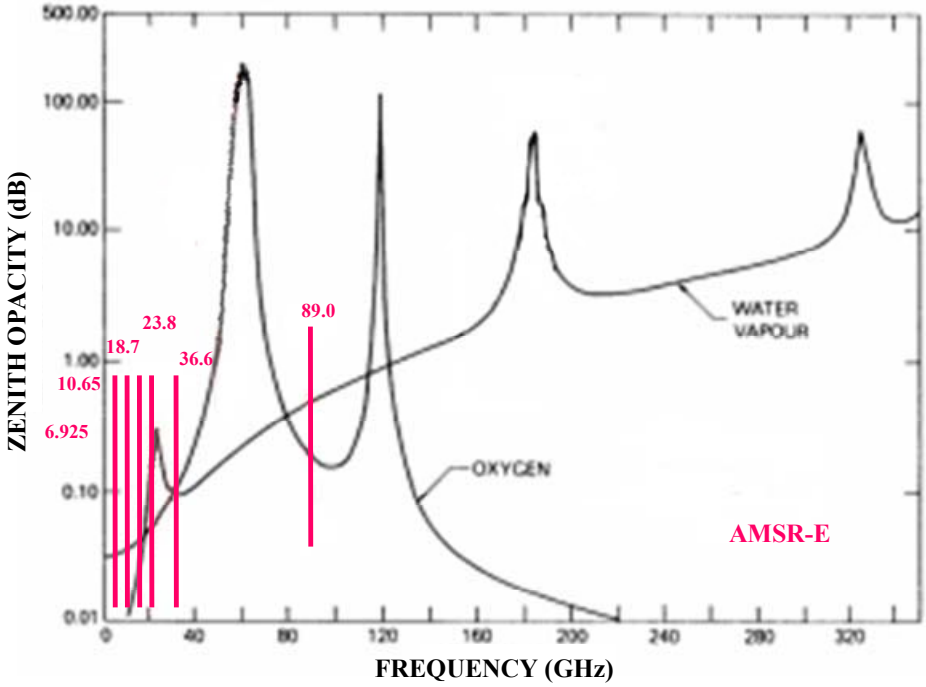

Fig. 2.10 Channels of AMSR-E sensor. The channels are marked on the water vapour and oxygen opacity behaviour as a function of frequency.

The (2.42) can be rewritten in the form

$$T_{AP}(\nu,\theta) \approx \int_0^{\infty} W_T(\nu,\theta,z)\cdot T(z)\cdot dz \qquad (2.43)$$

where $W_T(\nu,\theta,z)$ is the temperature weighting function

$$W_T(\nu,\theta,z) = k_\nu(z)\cdot e^{-\tau_\nu(z,\infty)\cdot\sec\theta}\sec\theta\,. \qquad (2.44)$$

The reason for selecting frequencies in the oxygen-absorption band for the temperature retrieval problem is that $k_{O_2}(z)$ is strongly dependent on the partial pressure of oxygen in the atmosphere $P_{O_2}(z)$. Moreover, oxygen has a uniform and time-invariant mixing ratio in the atmosphere ($P_{O_2}(z)$ = 0,21 P(z)) and it follows that $W_T(\nu,\theta,z) = W_T(\nu,\theta,P(z))$. That is, W_T depends on the height z through the pressure P(z). Moreover, the height variation of atmospheric pressure is generally known. These reasons, in addition to the fact that the oxygen absorption coefficient is only weakly dependent on temperature, underlie the choice of the oxygen bands as a means of retrieving T(z). Figure 2.11 shows plots of the temperature weighting functions for three channels in the oxygen band 50-60 GHz. Similar plots can be obtained using the other absorbing line of oxygen near 118 GHz.

The channels near the absorption bands of water vapor, at 22 and 183 GHz, are the "humidity sounding channels". They are used to estimate, often in association with other channels, some quantities related to water vapour in the atmosphere, as are for example the integrated precipitable water vapour or the integrated cloud liquid.

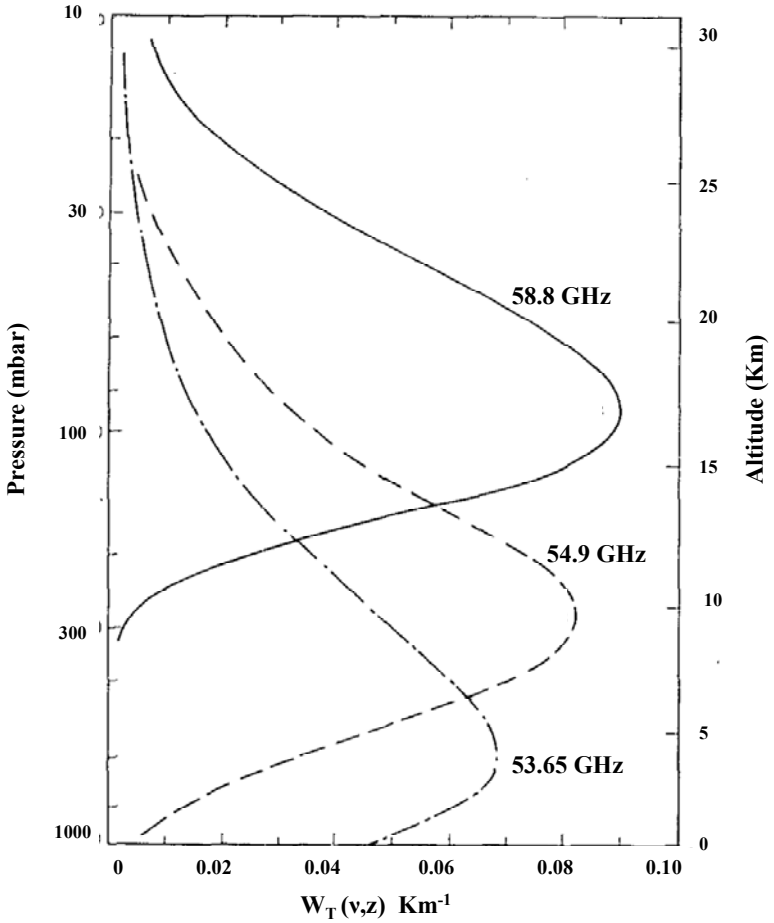

Fig. 2.11 Temperature weighting functions for downward-looking observations, assuming zero surface reflectivity (Waters et al. 1975).

Other channels are located in the window bands B1, B2, and B3 and are largely utilized in studies of meteorological events. In particular, the application of SSM/I channels, most of them lie in window bands, to the passive microwave estimation of precipitation is presented in the next section.
Figure 2.12 shows an overall view of microwave channels of SSM/I, SSMIS, AMSU and AMSR-E in the plane of the atmospheric transmissivity versus frequency.

2.4 Emission-based and scattering-based measurements of precipitation

"Precipitation" usually refers to hydrometeors reaching the surface of the earth. The measurement of precipitation using satellite-borne passive radiometers is generally based on one of two different physical processes (Wilheit 1986, Wilheit et al. 1991, Berg and Chase 1992, Spencer et al. 1989, Kummerow et al. 1996, Petty 2001, Kummerow et al. 2001, Stephens and Kummerow, 2007). The first is emission-based, where liquid precipitation causes

brightness temperature increases over a radiometrically cold background. The second is scattering-based, where precipitation, especially that above freezing level, causes brightness temperature decreases over a radiometrically warm background.

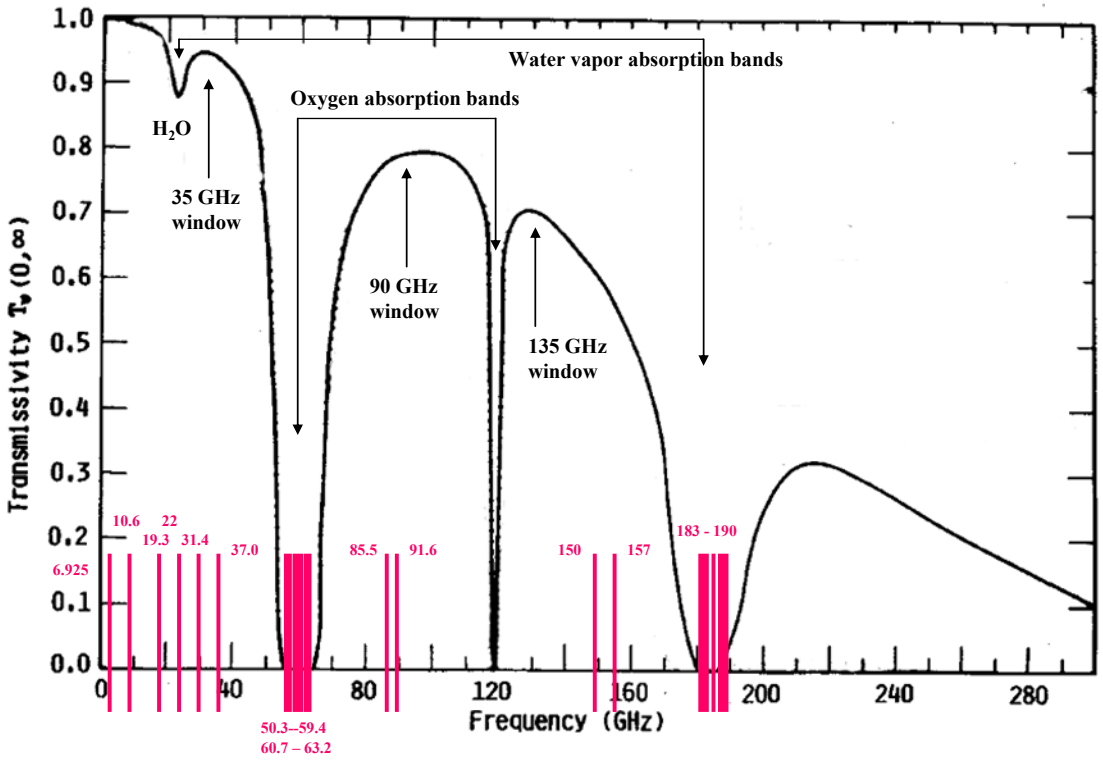

Fig. 2.12 Channels of SSM/I, SSMIS, AMSU, and AMSR-E sensors.

The first process relates rainfall to the emission of thermal energy associated with absorption by liquid raindrops (Kirchoff's law); the second associates the scattering by frozen hydrometeors in upper cloud regions with rainfall. In the last process, the scattering (Mie) reflects upwelling radiation back to the surface, lowering the observed brightness temperatures. While emission-based measurements represent observations of the liquid hydrometeors (raindrops) themselves and thereby can be considered direct measurements of rainfall, scattering-based measurements are observations of the ice phase, which is involved in the raindrop formation process, and are an intermediate case between the very direct microwave attenuation and very indirect visible/infrared technique. Moreover, the brightness temperatures that are observed in the scattering regime depend on the many details of the frozen hydrometeors such as particle sizes, shapes and density which do not appear to be uniquely related to rainfall intensity.

In the emission-based process, a cold background is required in order to clearly observe the increase of the brightness temperature due to rainfall. Therefore, this process works well over ocean that appears uniformly cold due to its low emissivity at microwave frequencies. On the

other hand, it cannot work over land where high surface emissivity obscures the emission signal.

The emission-based measurements of precipitation generally use the lower frequencies of microwave passive sensors, below 22 GHz, where rain is highly absorptive. The scattering-based measurements use frequencies above the 60 GHz oxygen complex, where scattering dominates. At the intermediate frequencies, roughly from 25 to 50 GHz, both approaches are considered.

Using the Mie theory, and a Marshall-Palmer size distribution the radiation absorption and scattering properties of hydrometeors can be analyzed (Wilheit et al. 1994, Spencer et al. 1989). With reference to SSM/I channels, passing from the lowest frequency (19.35 GHz) to the highest (85.5 GHz), dramatic increases in the volume scattering (k_s) and absorption (k_a) coefficients, and single scattering albedo ($k_s/(k_s+k_a)$) are observed. Figures 2.13 and 2.14 (Spencer et al. 1989) show the variations of these coefficients as a function of SSM/I frequencies and rain rate (water and ice spheres). Ice has much smaller absorption coefficients than water, leading to high albedo. A single scattering albedo approaching unity indicates that any thermal radiation upwelling from below an ice layer will be scattered out of the radiation field of view. If the scattering coefficient is large enough (such as at 85.5 GHz), very low brightness temperatures can result. On the contrary, if the value of single scattering albedo is low (as it is for water at 19.35 GHz) absorption is prevalent on scattering.

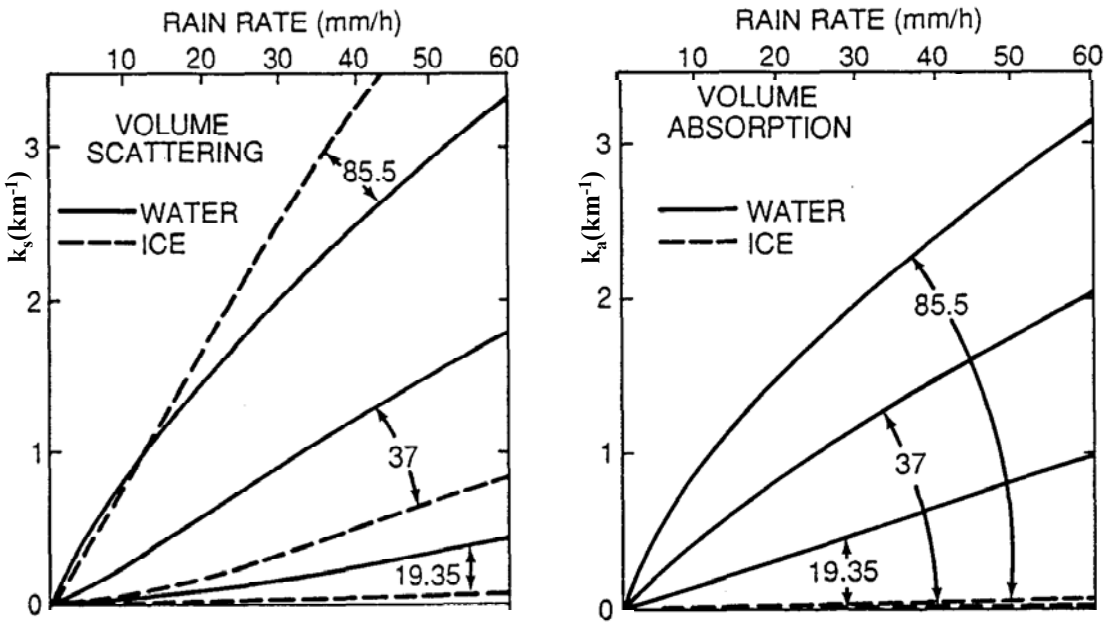

Fig. 2.13 Mie volume scattering coefficients (left), and volume absorption coefficients (right) for a Marshall-Palmer precipitation size distribution of water and ice spheres. The behavior for SSM/I frequencies is shown (Spencer et al. 1989).

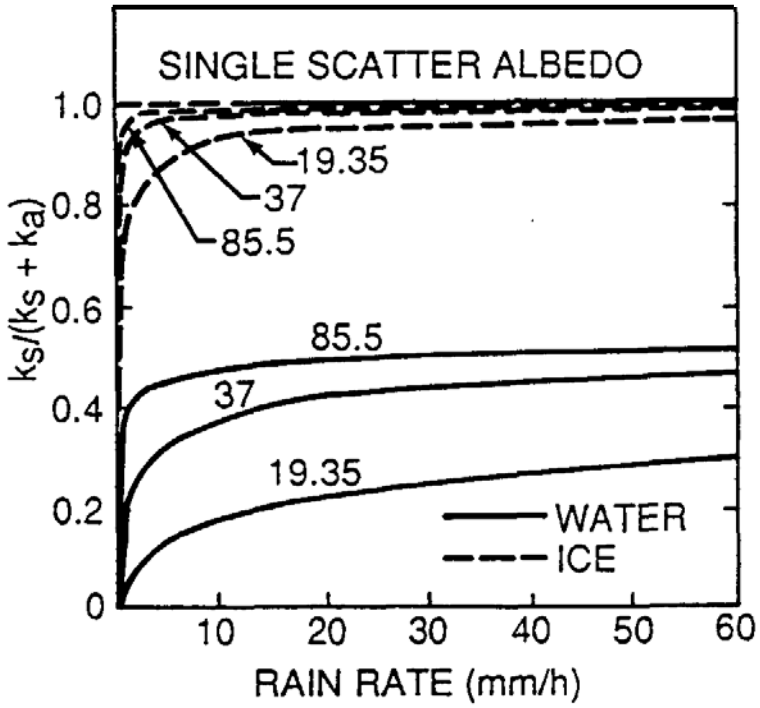

Fig. 2.14 Single scattering albedo for a Marshall-Palmer precipitation size distribution of water and ice spheres. The behaviour for SSM/I frequencies is shown (Spencer et al. 1989).

Most SSM/I frequencies lie in window channels, therefore are mostly suitable for observation over the ocean, where surface emissivity is minimal. The lower frequencies are mostly sensitive to liquid water. The 85-GHz frequency is sensitive to cloud ice scattering, thus it is also applicable over land. SSMIS adds temperature and humidity sounding channels that transmit information on the atmospheric thermal-hygrometric structure.

2.5 Empirical algorithms for measuring rain rate

A number of algorithms for measuring rain rate from satellite-borne microwave sensor data have been proposed since 1977, when the data from the Electrically Scanned Microwave Radiometers (Nimbus satellites) became available. Many of these algorithms are described by Wilheit et al. (1994) and are broadly classified as either empirical or physical. Empirical algorithms (e.g. Adler and Rodgers 1977, Grody 1984, Spencer 1986, Petty and Katsaros 1990, Todd and Bailey 1995) are based on regression relations between satellite-observed brightness temperatures and surface- (e.g. radar-) measured rainfall rates. Physical algorithms (e.g. Wilheit et al, 1977, Mugnai et al. 1993, Kummerow and Giglio 1994b, Smith et al. 1994b, Mugnai et al. 2001, Tassa et al. 2003, Di Michele et al. 2003) use a radiative transfer model of varying sophistication to predict the radiation emerging at the top of the atmosphere.
It must be specified that algorithms classified as empirical are not actually entirely empirical. All the algorithms use insights derived from radiative transfer models to select which brightness temperatures, or functions of the brightness temperatures, are used as independent variables in a regression against ground-based measurements.

While the physical algorithms, and particularly the algorithm we have developed at CNR ISAC, are described in chapter 3, some aspects of empirical algorithms are outlined in this section.

The development of empirical algorithms has been supported by the fact that they avoid the need to determine the cloud microphysical structure that has proved difficult for physical algorithms. On the other hand, empirical algorithms depend on factors such as surface temperature and emissivity, that vary both spatially and temporally. Consequently, an algorithm optimized for a given location at a given time can be not optimal for different locations and/or times. For example, the relation proposed by Spencer (1986) has been developed for convective oceanic rain systems, based on the decrease of the polarization of the satellite-observed 37 GHz brightness temperature (Tb) due to scattering caused by rain:

$$R = a(b \cdot Tb_{37H} - Tb_{37V} + c) \qquad (2.45)$$

In (2.45) R is the rain rate (mm/h), Tb_{37H} and Tb_{37V} are the 37 GHz Tb's (horizontal and vertical polarization, respectively), a,b and c are three constants that are obtained experimentally. The method is quite sensitive to the ice content of rain systems, so variations in storm-ice contents from different climate regimes do not allow the global application of (2.45).

Grody (1991) proposed a method for the global classification of precipitation and snow cover that has been utilized in many algorithms for measuring rain rate. It is based on the consideration that the microwave radiation emitted from most natural materials depends primarily on the absorption properties of water.

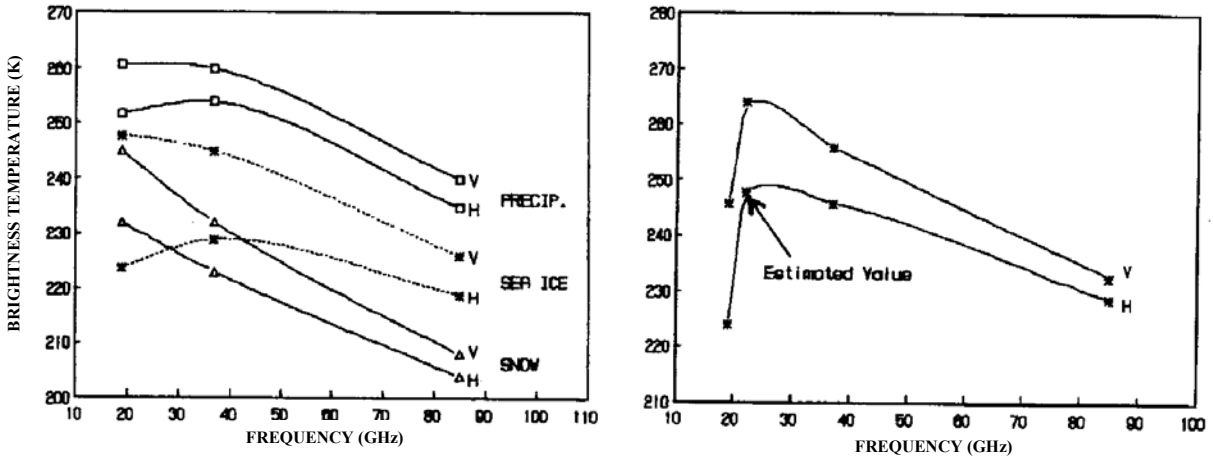

Fig. 2.15 Examples of SSM/I measurements for snow cover, aged sea ice, precipitation over land (left panel) and for precipitation over ocean (right panel). Brightness temperatures at vertical (V) and horizontal (H) polarization are plotted as a function of frequency. In the right panel the value of the horizontal polarization channel at 22 GHz is estimated using the vertical polarization measurement (Grody 1991).

Since the absorption due to water increases with frequency, the emitted radiation also increases with frequency. This is the case of soil, vegetation and melting snow that are classified as "absorbers" for this reason. On the contrary, materials such as snow cover and precipitation

clouds, composed of ice particles which scatter microwave radiation, are classified as "scattering materials". Since the scattering cross section of these materials generally increases with frequency, the radiation emerging from them drops as frequency increases.
Using the brightness temperatures at 22 and 85 GHz, the two classes of materials can be classified in the following way

Scattering materials ($Tb_{22} > Tb_{85}$) Absorbing materials ($Tb_{22} < Tb_{85}$).

Figure 2.15 shows two examples of SSM/I measurements over land (left panel) and over ocean (right panel).
In the panel on the left the brightness temperatures for snow cover, aged sea ice and precipitation (scattering materials) are plotted as a function of frequency for the horizontal (H) and vertical (V) polarization measurements. In the panel on the right an example of precipitation measurements over ocean is shown. Since the low frequencies are least affected by scattering and absorption, they respond most strongly to the surface emission. This fact explains the different results at 19 GHz in the two panels. Moreover, since both the 22 and 85 GHz channels respond to water vapour (fig. 2.7), the relatively lower measurement at 85 GHz is due to scattering effects. It follows that a "positive" difference between the 22 and 85 GHz vertical polarization channels can be used to indicate precipitation (and scattering surfaces) over ocean as well as land. In essence, this procedure uses the 22 GHz channel measurements to estimate the non-scattering contribution of the 85 GHz measurements. In order to obtain a better estimate of the 85 GHz measurements in the absence of scatterers, Grody (1991) has considered additional channels and a large training dataset containing a wide variety of surface and atmospheric conditions. Moreover, to eliminate any possibility of scattering surfaces or precipitation, the data set contains only measurements where the 22 GHz channel exceeds the 85 GHz channel measurements by more than 10 K. The resulting most accurate two-channel relationship estimating the non-scattering contribution of the 85 GHz measurement has the form

$$F = A + B \cdot Tb_{19V} + C \cdot Tb_{22V} + D \cdot (Tb_{22V})^2 \qquad (2.46)$$

Then, the difference between the 22 and 85 GHz channels is replaced by the "scattering index"

$$SI_{85V} = F - Tb_{85V} . \qquad (2.47)$$

Index values greater than 10 K are used to identify scattering materials. In order to distinguish the different scattering materials, geographic location can be utilized in some cases (desert sand and snow cover). Moreover, using SSM/I measurements of precipitation and snow cover, Grody (1991) has found a procedure for classifying snow cover and precipitation over land. Figure 2.16 shows the results based on snow (left) and precipitation (right) measurements. Both graphs contain three reference lines

$Tb_{22V} = Tb_{85V}$ $Tb_{22V} = 257$ $Tb_{22V} = 158 + 0.49\ Tb_{85V}$

As seen when comparing the two panels, the measurements bound by these empirical relationships are predominantly due to precipitation or snow cover conditions. The procedure for classification is composed of the following sequential steps:
Condition 1 : check for scatterers

$$SI_{85V} > 10$$

Condition 2 : identify snow cover

$$Tb_{22V} < 257 \quad \text{and}$$
$$Tb_{22V} < 158 + 0.49\ Tb_{85V}$$

Condition 3 : identify precipitation

$$Tb_{22V} > 257 \quad \text{or}$$

$$Tb_{22V} > 158 + 0.49\ Tb_{85V}$$

For classification over oceans, a fourth condition is obtained using a similar procedure:
Condition 4 : identify precipitation (oceans only)

$$Tb_{22V} > 38 + 0.88\ Tb_{19V.}$$

Finally, to provide an adequate separation between precipitation and desert sand the polarization difference of the 19 GHz channel is utilized.
Condition 5 : identify desert sand

$$Tb_{19V} - Tb_{19H} > 20.$$

The scattering index has also been applied to directly estimate the value of the rain rate (Ferraro and Marks, 1995, Kummerow et al. 2001, Wilheit et al 2003). The form of the rainfall rate estimation equation for land is

$$R = 0.00513\ SI_{85V}^{1.9468} \qquad (2.48)$$

where R is the rain rate in mm/h.

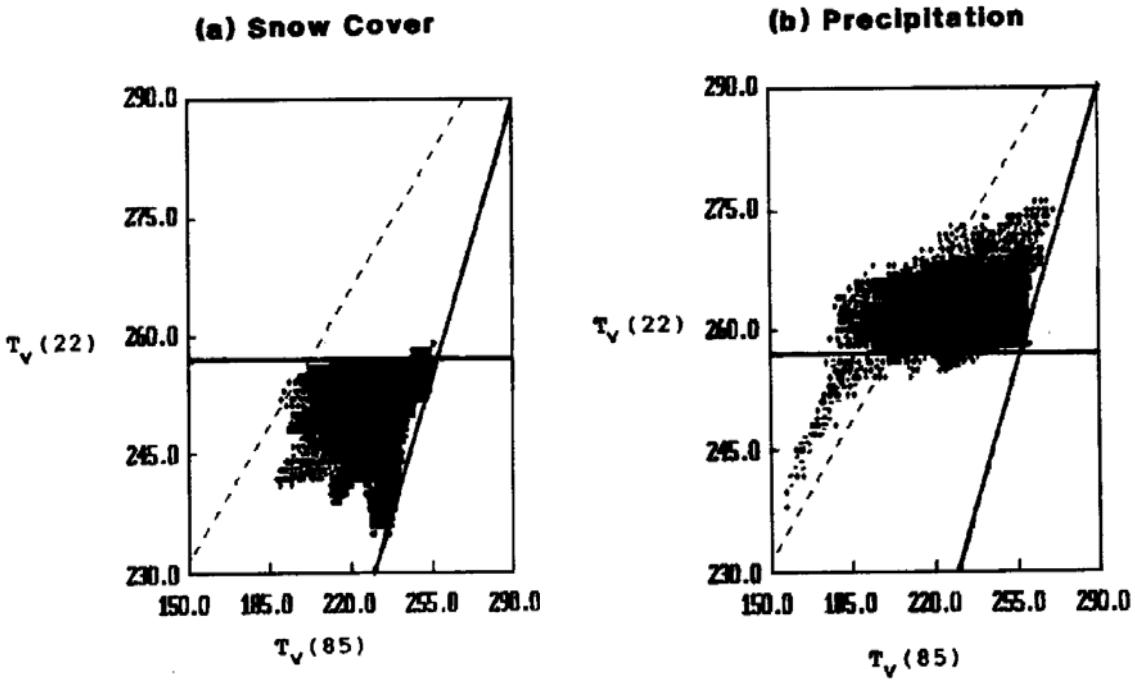

Fig. 2.16 SSM/I measurements at 22 GHz plotted against the 85 GHz vertically polarized measurements for (left) snow cover and (right) precipitation over land. For the expressions of the three lines see the text (Grody 1991).

CHAPTER 3 – The Bayesian algorithm for precipitation retrieval

Atmospheric sounding using satellite radiometers started in 1968 (Ulaby et al. 1986) with the launch of the first satellite carrying microwave radiometers, designed to make measurements of the earth surface and atmosphere. But, the first experimental spacecrafts suitable for rainfall measurements were launched from 1972 to 1978: Nimbus 5 (1972), Nimbus 6 (1975) with the Electrically Scanned Microwave Radiometers (EMSRs) and Nimbus 7 (1978) with the Scanning Multichannel Microwave Radiometers (SMMRs) (Spencer 1984, Spencer 1986, Prabhakara et al. 1982, Petty and Katsaros 1990). The first instruments used relatively simple sensors with few channels and limited spatial resolution, so, the first results were unsatisfactory for the meteorological and hydrological communities (Wilheit et al 1994).
The launch of the Special Sensor Microwave/Imager (SSM/I) on the operational Defense Meteorological Satellite Program (DMSP) satellite (F-8) in 1987 introduced a new era of data continuity and quality. But it was in 1997, after the launch of the TRMM platform, that the retrieval of precipitation profiles received a new significant development (Simpson et al. 1988; Kummerow et al. 2000).
Several techniques (empirical or physical) have been proposed and applied in the last two decades for estimating cloud and precipitation parameters from measurements taken by space-borne microwave radiometers, especially the SSM/I (Wilheit et al. 1994, D.M. Smith et al. 1998). Important approaches have been based on multiple regression and Maximum Likelihood methods. Recently, Bayesian (physical) techniques have proven to have a large potential and flexibility for precipitation profiling (e.g., Evans et al. 1995; Kummerow et al. 1996; Pierdicca et al. 1996; Marzano et al. 1999; Kummerow et al. 2001, Mugnai et al. 2001).
Briefly, Bayesian techniques (Kummerow et al.1996, Tassa et al. 2003, Di Michele et al. 2003, Di Michele et al. 2005) consist of two parts. The first (forward problem) is the generation of a database (the Cloud Radiation Database (CRD)) in which the simulated brightness temperatures (Tbs), that would be measured by a space-born radiometer, are associated with the various structures generated by a cloud-resolving numerical model, to create "profiles" (the components of the database). The second (inverse problem) is the retrieval of atmospheric parameters, like surface rain rate, using the experimental data (brightness temperatures) of a microwave radiometer, and the probabilistic (Bayesian) analysis of the CRD. In this second part, the profiles used for retrieval are chosen and given weights based on the proximity of the observed microwave radiances to those of the database. The unique feature of these techniques is that they constitute a rigorous statistical framework for developing cloud model-based inversion methods. As opposed to empirical methods, where measurements of both Tbs and precipitation parameters are collected to train a retrieval algorithm, the model-based approaches are based on refined physical models to simulate the measurements (e.g., Mugnai and Wiscombe 1980, Smith and Mugnai 1988, Smith et al. 1992; Mugnai et al. 1993; Smith et al. 1994a, Smith et al. 1994b). This point of view offers the possibility to avoid *in situ* measurements and to deepen the understanding of the problem. On the other hand, model-based approaches have to tackle the critical issues of tuning simulations to the measurement manifolds in order to be representative of real observations (Panegrossi et al. 1998; Tassa et al. 2003, Tassa et al. 2006), as well as the difficulties of an accurate representation of the microphysical properties of the atmosphere (Stephens and Kummerow 2007).

In this chapter, several aspects of precipitation retrieval based on a physical approach are presented. In particular the algorithm we have developed at the CNR ISAC, named Bayesian Algorithm for Microwave-based Precipitation Retrieval (BAMPR), and the microwave measurements from DMSP satellite are described.
The chapter is organized as follows. Section 3.1 presents the "forward problem", that is the procedure followed to calculate the simulated Tbs and the implementation of CRD database. Then, section 3.2 gives a general description of the inversion methodology, that is of the "inverse problem". Section 3.2.1 delineates the main elements of the BAMPR algorithm implemented at CNR. Section 3.2.2 is focused on the "screening problem" - the problem of rejecting areas (pixels) without rain or with a very low probability of rain, and therefore not suitable for retrieval. Finally, section 3.3 describes an application of the screening procedure to atmospheric disturbances over Italy.

3.1 The forward problem

BAMPR is a cloud model-based statistical retrieval technique for estimating surface precipitation and cloud profiles. The retrieval is based on the Bayesian estimation theory. A schematic block diagram of BAMPR is shown in fig. 3.1.

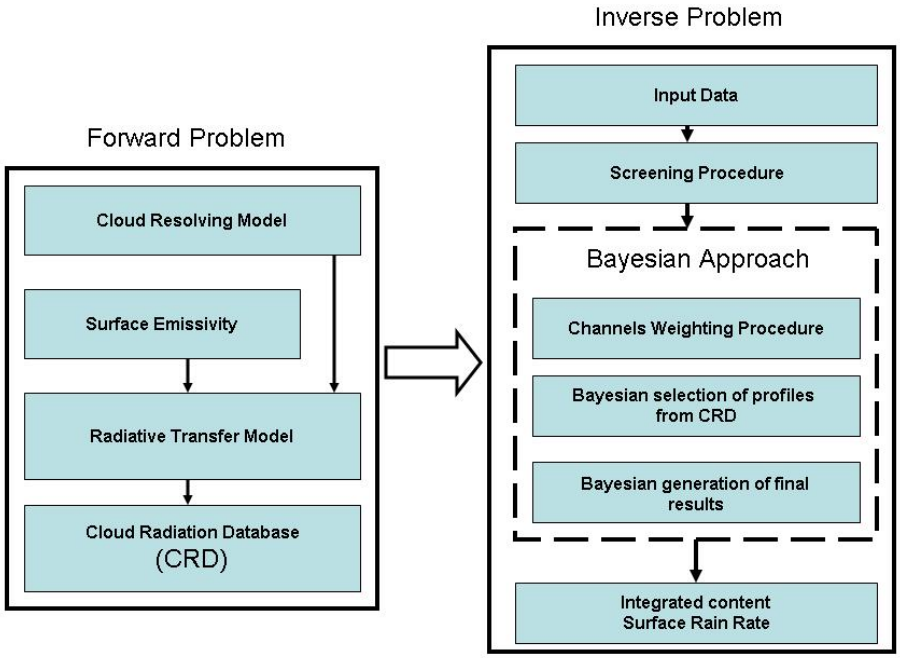

Fig. 3.1 – Block diagram of the Bayesian Algorithm for Microwave-Based Precipitation Retrieval (BAMPR).

The two boxes refer to the two main blocks common to all physically based retrieval approaches. They are generally referred as the "forward problem" and the "inverse problem".
The forward problem consists in the generation of a database (the Cloud Radiation

Database (CRD)), using a Cloud Resolving Model (CRM) and a Radiative Transfer Model.
At the base of the forward problem there is the fact that precipitation on the ground can not be directly observed from space. However, in principle it can be derived from knowledge of cloud microphysical structure along the direction of sight. Consequently, information relating cloud microphysics to observations from satellite-borne microwave radiometers needs to be contributed from external sources. Such microphysical information can be derived from a Cloud Resolving Model. A shortcoming of this approach is that it is currently not possible to run these models in-line with the flow of satellite data. It is therefore necessary to run the CRM off-line for a number of well-documented events (generally, results of re-analysis exercises) and collect the results in a database. Then, in a post-analysis phase, a detailed Radiative Transfer Model (RTM), which is particularly necessary when ice is involved in the precipitation event, is applied to the CRM output to compute the upwelling brightness temperatures (Tbs) that would be measured by a satellite-borne MW radiometer. The collection of cloud and precipitation microphysical profiles for a series of different CRM simulations and of the associated Tbs at the instrument (for instance SSM/I or SSMIS) channel frequencies constitutes the Cloud-Radiation Database.
It is important to use several cloud model simulations for different types of precipitation systems, and to generate the corresponding cloud-radiation databases in order to specialize the algorithm to different storm structures. In essence, the algorithm's performance can be improved by generating a statistically significant CRD by means of a large number of different CRM simulations representing all precipitation regimes that occur in the zone and season under investigation. Figure 3.2 shows the scheme of the forward problem.
The inverse problem consists in the retrieval of meteorological parameters, the hydrometeor columnar content and the surface rain rates, using the experimental data (the brightness temperatures) of a microwave radiometer, and a probabilistic analysis (Bayesian) of the CRD. Particularly, precipitation retrieval is performed by means of a physical-statistical profile-based Bayesian algorithm that has been developed and is continuously being improved at CNR-ISAC. The algorithm makes use of the CRD to search for the most probable profile(s) according to the proximity of measured and modelled Tbs and on *a priori* probabilities of occurrence of the various profile structures. Surface rain rates are computed by means of the model rain rates for the solution hydrometeor profiles.

3.1.1 Cloud Resolving Model

The model used is the CRM "University of Wisconsin – Non-hydrostatic Modeling System" (UW-NMS) (Tripoli and Cotton, 1981, Tripoli 1992).
The UW-NMS is a three-dimensional (3-D), time-dependent cloud/mesoscale numerical model capable of simulating atmospheric phenomena with horizontal scales ranging from the microscale (turbulence) to the synoptic scale (extratropical cyclones, fronts, etc.). It is based on the non-Boussinesq quasi-compressible dynamical equations. Model thermodynamics are based on the prediction of a moist ice-liquid entropy variable, designed to be conservative over all ice and liquid adiabatic processes. Dynamic properties of flow such as vorticity, kinetic energy and potential enstrophy are conserved by the advection scheme in the UW-NMS. The model uses variable step topography capable of capturing steep topographical slopes, while at the same time accurately representing subtle topography variations.

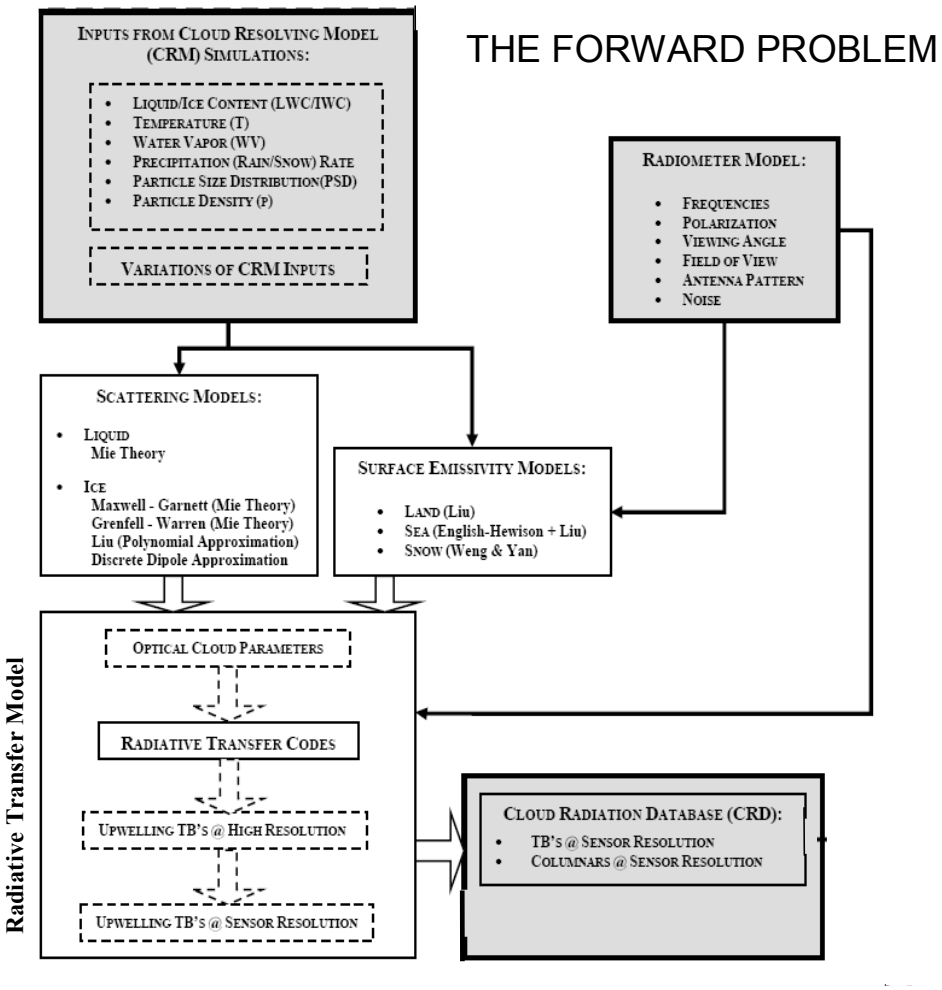

Fig. 3.2 – Scheme of the Cloud Radiation Database (CRD) generation (forward problem).

Conservation equations for the specific humidity of total water and several ice and liquid water hydrometeor categories are also included.
The model is formulated on a two-way multiply nested grid system. The microphysical module used in the UW-NMS version, is based on the scheme described by Flatau et al. (1989) and Cotton et al. (1986). The microphysics is a bulk microphysics parameterization, which includes six hydrometeor categories labelled as: 1) suspended cloud droplets, 2) precipitating rain drops, 3) suspended pristine ice crystals, and precipitating 4) ice aggregates, 5) low-density graupel particles (or snow) and 6) high density graupel particles. Depending on the application, all or some of these categories may be selected. Any combination of frozen and liquid hydrometeors can coexist within the same grid volume at any given time to allow hydrometeor category interaction to take place.

3.1.2 The Radiative Transfer Model
In order to simulate the upwelling brightness temperatures (Tbs) to be included in the database, the radiative transfer (RT) code has been applied to the microphysical outputs of the simulated

precipitation events in order to compute the upwelling radiances over the simulated satellite footprints. To this end, fully 3-D RT schemes should be used. However, these schemes are computationally heavy, and rely completely on the macrophysical structure of the cloud model simulation. Thus, it is customary to resort to simpler one-dimensional (1-D) plane-parallel schemes, which are much faster – though less accurate.

A 3-D adjusted plane parallel RT scheme, which has been developed by Roberti et al. (1994) (see also Liu et al. 1996, Bauer et al. 1998, Tassa et al. 2003) has been used. In this approach, the plane-parallel cloud structures are generated from the cloud model paths along the radiometer direction of sight, rather than from the vertical cloud model columns. The RT is therefore performed along a slanted profile in the direction of observation of the radiometer. Remarkably, the downward flux is computed through the cloud structure along the specular line reflected at the surface, a fact that may have a significant effect at cloud edges at low frequencies. This method is computationally efficient, and accounts for the geometrical errors that a complete 1-D RT scheme is prone to, partially reducing errors in radiative transfer modelling. However, pure 3-D radiative effects are neglected, since the radiation is still trapped inside the slanted (and reflected) column, and in case of enhanced horizontal inhomogeneities, the scheme may produce significant discrepancies with the results obtained from a fully 3D model.

The performance of the slanted-path plane-parallel RT approximation has been deeply investigated by several authors (Roberti et al. 1994, Bauer et al. 1998, Kummerow 1993) who generally agree on the errors being limited to a few K on average scenes, even though local values may be important in case of large horizontal gradients (e.g., at the cloud edges) (see Liu et al. 1996, Czekala et al. 2000, Olson et al. 2001).

Once the monochromatic upwelling radiances have been computed at high resolution (i.e., at the resolution of the CRM model – 2 km) for the full cloud model domain, the upwelling Tbs at sensor resolution (i.e., which would be observed by a real radiometer) are computed for each channel using the instrument transfer function: i.e., by first integrating the monochromatic upwelling radiances over the channel-width, taking into account the channel spectral responsivity, and then integrating the channel upwelling radiances over the field of view (i.e., over all cloud-model pixels that are contained in the field of view), taking into account the radiometer antenna pattern and radiometric noise.

Then, the corresponding high-resolution hydrometeor liquid/ice water content profiles, as well as the corresponding precipitation rate profiles for both rain and ice, are extracted from the cloud model simulation and averaged over the field of view to produce the same quantities at sensor resolution. A key point of this process concerns the definition of the cloud structures which have to be associated to the simulated Tbs. In principle, for each channel a different cloud structure – (basically) filling up the slanted elliptical cylinder with sizes corresponding to the cross-track and along-track resolutions of the considered channel – should be associated with each Tb point of the database. This strategy, however, would make the multi-frequency retrieval rather complex and not univocal. The simplest choice is therefore to choose a common single resolution for the microphysical parameters belonging to the cloud-radiation database. Slanted cloud structures corresponding to the resolution of the 89 GHz frequency has been associated, as a reasonable compromise.

Some of the outputs of the CRM simulations are inputs for the radiative transfer model in order to generate the upwelling Tbs. In detail, these quantities are the vertical profiles of the

liquid/ice water contents (LWC and IWC, respectively) of the various hydrometeors, together with the surface temperature and the temperature / moisture profiles.
Other inputs to the RTM are: the radiometer model, the surface emissivity model, and the single-scattering model (fig. 3.2).

Radiometer Model
The radiometer model is a secondary input to the RTM and specifies all characteristics of the radiometer that have to be simulated – i.e. frequency, polarization and width of the candidate channels; viewing angle of the radiometer; field of view and antenna pattern of the various channels. In principle, an Instrument Transfer Function has to be defined for each channel in order to compute the upwelling Tbs from the upwelling monochromatic radiances. For this study, the channel characteristics of the following radiometers have been used:
Special Sensor Microwave Imager (SSM/I)
Special Sensor Microwave Imager/Sounder (SSMIS)
Advanced Microwave Sounding Unit – A (AMSU-A)
Advanced Microwave Sounding Unit – B (AMSU-B)
Microwave Humidity Sounder (MHS)
TRMM Microwave Imager (TMI)
Advanced Microwave Scanning Radiometer-EOS (AMSR-E)

Surface Emissivity Models
Surface emissivity impacts the upwelling Tbs especially at the lower window frequencies. It depends on frequency and polarization, observation geometry, and surface characteristics (land/ocean, surface roughness, type of soil and soil cover, soil humidity, etc.). Thus, three different surface emissivity models were selected to best represent the different surface backgrounds of the selected CRM simulations.
The three surface emissivity models that have been implemented are:
For land surfaces, the forest and agricultural land surface emissivity by Hewison (2001) ;
For a sea surface, the fast and accurate ocean emissivity model of English and Hewison (1998) (see also Hewison and English 2000, and Schluessel et al. 1998), which provides accurate estimates of surface emissivity between 10 and 200 GHz for view angles up to 60° and wind speeds from 0 to 20 m s^{-1}.
For snow covered surfaces, the snow emissivity model that has been empirically derived by Hewison and English (1999) from satellite retrievals and ground-based measurements; in particular, five different snow cover types have been considered that cover the full range of snow emissivity presented by the previous authors – i.e., forest +snow, deep dry snow, fresh wet snow, frozen soil, first year ice, compact snow.

Single-Scattering Models
Computation of the single-scattering properties of the various hydrometeor species is straightforward if only pure water and ice spheres are considered (i.e., for Mie scattering), but can be a major challenge for natural ice hydrometeors (especially for snowflakes and ice aggregates) due to their wide variety of sizes, densities, and shapes. Since information on shape is not available from the UW-NMS microphysical parameterization scheme, some assumptions have been taken; i.e.:

Liquid (cloud and rain) particles are assumed to be spherical and homogeneous, and therefore their scattering properties are computed by means of Mie theory (Bohren and Huffman, 1983) using an efficient code developed by Wiscombe (1980).
Graupel particles are assumed to be spherical with densities near to that of pure ice (0.9 g cm^{-3}). They are assumed to be "equivalent homogeneous spheres" having an effective dielectric function obtained by combining the dielectric functions of ice and air (or water, in case of melting) according to the effective medium Maxwell-Garnett mixing theory for a two-component mixture of inclusions of air (water) in an ice matrix (see Bohren and Huffman 1983). As a consequence, Mie theory is used even in this case.
Pristine ice particles are highly non-spherical, and the use the Grenfell and Warren Approximation (1999) (see also Neshyba et al. 2003) was chosen. The single-scattering properties of each nonspherical ice particle were computed by means of a collection of n_s equal-size solid-ice spheres having a diameter determined by the volume to cross-sectional area ratio (V/A) of the original nonspherical ice particle. The volume (V) is provided by the UW-NMS simulation. For calculating the cross-sectional area (A), the observational relationship

$$A/(\pi D^2/4) = C_0 D^C \qquad (3.2.3)$$

has been used. The relation 3.2.3 was published by Heymsfield and Miloshevich (2003) for several different individual particle habits [here, D (in cm) is the maximum diameter of the particle, while the coefficients C_0 and C depend on ice particle habit]. For pristine ice crystals and aggregates, we used the values $C_0 = 0.18$ and $C = 0.2707$, that are indicated by the same authors as appropriate averages for midlatitude, continental mixed-habit cirrus clouds. As a result, the diameter (D_s) and the number (n_s) of the equivalent solid-ice spheres are given by:

$$D_s = \frac{\rho}{\rho_{ice}} \cdot \frac{D}{C_0 \cdot D^C} \qquad n_s = \frac{C_0}{1-C} \cdot \frac{D^{3+C}}{D_s^3}$$

Where $\rho_{ice} = 0.916$ g cm^{-3} while the density ρ of the pristine ice crystals is usually equal to 0.1 g cm-^{3}.
Snowflakes and *ice aggregates* are low-density, fluffy ice particles (as long as they are completely frozen) that can not be modeled according to Maxwell-Garnett mixing theory – the resulting "equivalent homogeneous soft-ice spheres" would, according to Mie theory, have very large asymmetry factors (> 0.9) at the higher microwave frequencies and would not adequately "cool" the upwelling radiation. To overcome this problem, the Chinnawat and Staelin (2005) model was used, in which non-spherical results were fitted using Mie calculations for spheres having a density that is a function of the wavelength.

3.1.3 The Cloud Radiation Database
To generate the CRD database for the European region sixty simulations of different precipitation events over the European area for the March 2006 – February 2007 one-year period were performed by means of the cloud resolving model UW-NMS, in such a way as to take into account the various climatic regions, types of precipitation and seasonal variations. Table 3.1 provides the details of all simulations.
Figure 3.3 shows the geographic location (inner domain) of the simulation. The season and the duration of the simulations are also specified.

Table 3.1 – Details of the 60 UW-NMS simulations, divided by season.

	code	Initialization Date	Initialization Time	Duration in hours	Lat	Lon (E > 0)
SPRING	100	2-mar-06	12.00	36	48,0	4,0
	101	6-mar-06	0.00	36	38,0	28,0
	102	9-mar-06	12.00	36	48,0	22,0
	103	19-mar-06	12.00	36	42,0	-9,0
	104	25-mar-06	12.00	24	40,0	-15,0
	105	26-mar-06	12.00	24	50,0	10,0
	106	4-apr-06	6.00	24	62,0	-18,0
	107	9-apr-06	6.00	36	59,0	28,0
	108	13-apr-06	12.00	36	65,0	-25,0
	109	22-apr-06	6.00	30	36,0	-6,0
	110	3-mag-06	18.00	30	54,0	-7,0
	111	8-mag-06	0.00	24	30,5	17,0
	112	12-mag-06	0.00	36	63,0	0,0
	113	16-mag-06	12.00	24	50,0	-15,0
	114	25-mag-06	0.00	24	55,0	15,0
SUMMER	115	5-giu-06	12.00	36	62,0	33,0
	116	10-giu-06	12.00	30	35,0	9,0
	117	14-giu-06	0.00	24	41,0	-6,0
	118	16-giu-06	18.00	30	46,0	2,0
	119	23-giu-06	18.00	30	57,0	-5,0
	120	2-lug-06	0.00	24	42,0	27,0
	121	5-lug-06	18.00	30	47,0	1,0
	122	13-lug-06	6.00	24	35,0	-2,0
	123	22-lug-06	12.00	36	50,0	28,0
	124	28-lug-06	0.00	24	63,0	14,0
	125	2-ago-06	12.00	30	60,5	-22,0
	126	6-ago-06	12.00	30	47,0	12,0
	127	12-ago-06	18.00	36	41,0	17,0
	128	20-ago-06	6.00	24	54,0	25,0
	129	28-ago-06	0.00	24	52,0	-20,0
FALL	130	2-set-06	12.00	24	57,0	5,0
	131	5-set-06	12.00	30	53,0	35,0
	132	7-set-06	18.00	24	57,0	30,0
	133	16-set-06	12.00	36	68,0	17,0
	134	2-ott-06	12.00	30	48,0	5,0
	135	6-ott-06	18.00	24	47,0	7,0
	136	9-ott-06	18.00	36	36,0	23,0
	137	17-ott-06	18.00	24	55,0	5,0
	138	22-ott-06	12.00	30	57,0	13,0
	139	31-ott-06	6.00	24	36,5	31,0
	140	5-nov-06	18.00	24	60,0	25,0
	141	6-nov-06	12.00	24	57,0	-5,0
	142	10-nov-06	12.00	24	53,0	5,0
	143	11-nov-06	18.00	24	64,0	-20,0
	144	19-nov-06	0.00	24	53,0	-10,0
WINTER	145	2-dic-06	18.00	24	53,0	-2,0
	146	9-dic-06	18.00	24	45,0	24,0
	147	12-dic-06	0.00	24	34,0	-3,0
	148	20-dic-06	12.00	36	40,0	14,5
	149	23-dic-06	12.00	36	37,0	12,0
	150	1-gen-07	12.00	36	63,0	7,0
	151	3-gen-07	6.00	36	60,0	5,0
	152	5-gen-07	18.00	24	51,0	-3,0
	153	10-gen-07	6.00	24	58,0	23,0
	154	12-gen-07	18.00	30	35,0	30,0
	155	2-feb-07	0.00	36	65,0	-20,0
	156	5-feb-07	12.00	36	33,0	35,0
	157	12-feb-07	12.00	30	45,0	17,0
	158	16-feb-07	12.00	36	43,5	-17,0
	159	23-feb-07	12.00	30	67,0	5,0

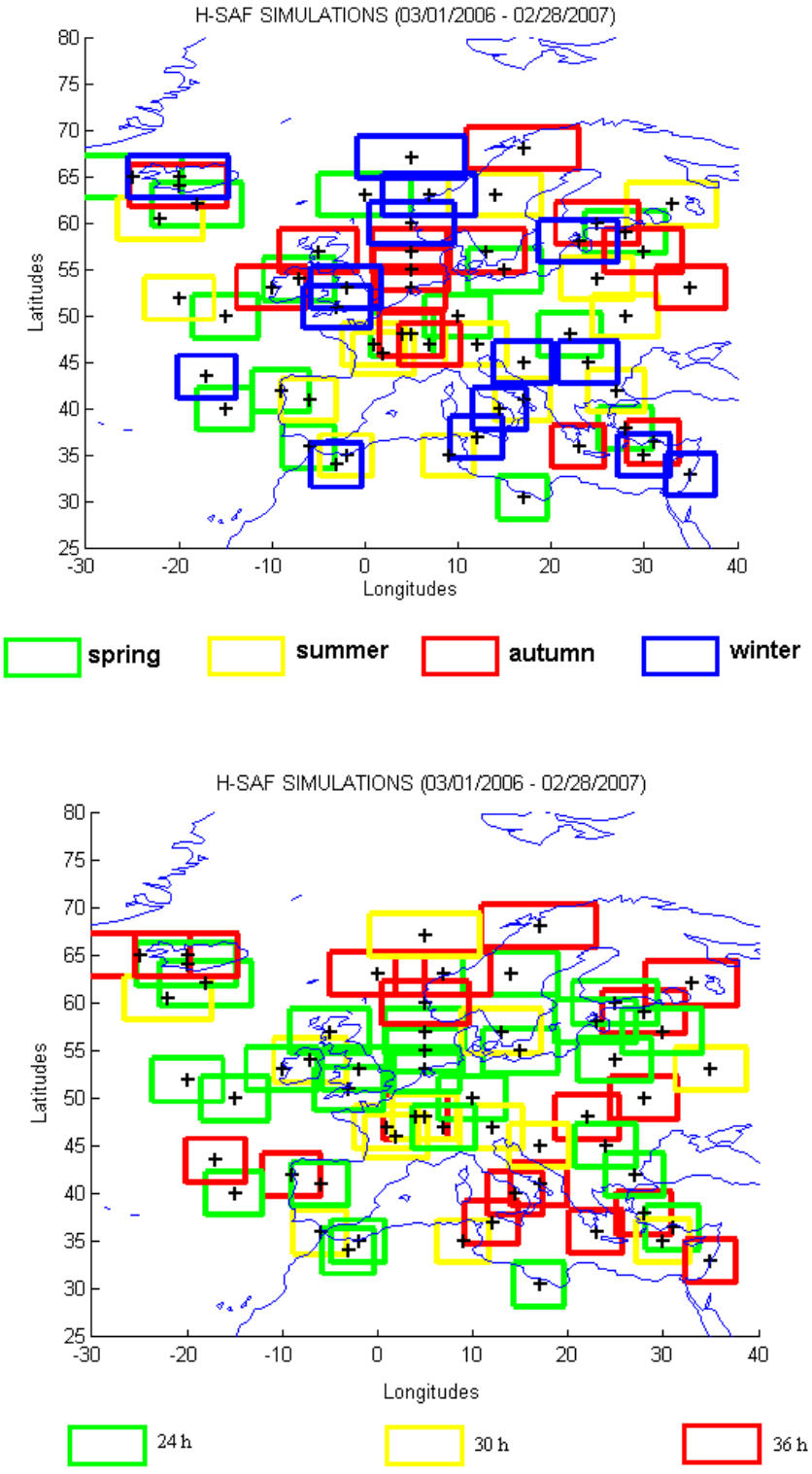

Fig. 3.3 – Geographical location of the NMS simulations. In the two panels, the season (top) and the duration (down) of the simulations are also shown.

For all UW-NMS simulations, all particles are assumed to be spherical. While cloud droplets and pristine ice crystals are assumed to be monodispersed (with characteristic diameters of 0.002 and 0.024 cm, respectively), the other hydrometeors are supposed to be distributed with size (diameter *DR* of the circumscribed sphere) according to inverse-exponential constant-slope / constant-intercept distributions (Panegrossi et al. 1998)

$$n(DR) = A \exp(-B\,DR) \ \text{cm}^{-3}\,\text{cm}^{-1} \qquad (3.2.1)$$

where the intercept (A) or the slope (B) are derived by the model at each grid point. Specifically, constant intercepts of 0.08 cm^{-4}, 0.071 cm^{-4}, and 0.014 cm^{-4} are assumed for rain, graupel, and snow, respectively; for aggregates, a constant slope of 10 cm^{-1}. Finally, while ice crystals and graupel particles have constant density ρ equal to 0.1 g cm^{-3}, and 0.9 g cm^{-3} respectively, ice aggregates have size-dependent densities

$$\rho(DR) = 0.015 / DR^{0.6} \ \text{g m}^{-3}\,, \qquad (3.2.2)$$

as in Panegrossi et al. (1998). Finally snowflakes have a density related with snowflake history that is directly predicted by the CRM.

For each simulation, three nested, concentric and steady grids were used – as schematically shown in Figure 3.4. The first and outer grid was set at 50 km resolution, covering a large region of 4550 km x 4550 km (Domain A). The second and intermediate grid was set at 10 km resolution, covering a 910 km x 910 km region (Domain B). The third and inner grid was set at 2 km resolution, covering a 502 km x 502 km region (Domain C). For all grids, 35 vertical levels were used up to about 18 km.

Each simulation was run for 24 or 36 hours with a 12-hour spin-up time. This initial period is necessary to better initialize the model by adapting the initial data to the maximum resolution of the model. The NOAA National Centers for Environmental Prediction (NCEP) Global Forecasting System (GFS) gridded analysis fields at about 100 km resolution were used as initial conditions and to nudge the boundaries of the outer grid every six hours throughout the simulation period. After the first 12 hours, the model extracts hydrometeor profiles over the inner domain C – this is done every hour of the remaining simulation time.

As an example, Figure 3.5 shows some details of the simulation of an oceanic storm that occurred near the Azores islands on March 25, 2006 (simulation number 104 – see table 3.1). It is evident that in the synoptical wind pattern of the outer domain (Domain A); a large scale wind convergence triggers strong convection that is aligned along the convergence line itself. Once convection has developed, it exalts convergence with a positive feedback and produces intense convective clouds in the inner grid (Domain C). Then, the simulated upwelling brightness temperatures were computed, following the procedures explained in Section 3.1.1, on the basis of all high-resolution (Domain C) atmospheric and hydrometeor profiles at all one-hour time steps of all 60 simulations.

Database contents and statistics

The CDR database generated at CNR ISAC, contains about 1,000,000 rainy profiles (selected from about 70,000,000 simulated profiles), obtained from the aforementioned 60 simulations. These profiles and the associated Tbs have been averaged to produce the sensor-resolution (15 km) profiles and the associated Tbs that simulate the SSM/I – SSMIS observations. There are about 300.000 of these profiles that contain at least one high-resolution rainy profile. These are the profiles that enter in the database, together with the associated Tbs. As an example, table 3.2 shows the components of each profile in the database, for SSM/I.

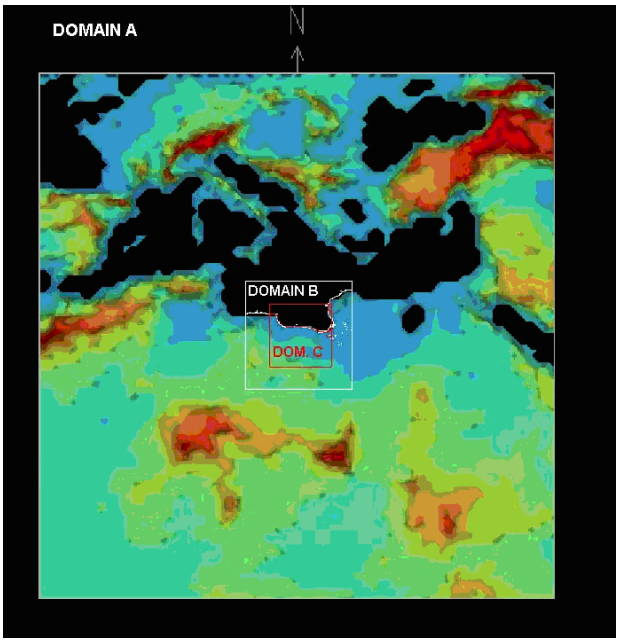

Fig. 3.4 – Example of grid nesting design (3 grids for each UW-NMS simulation).

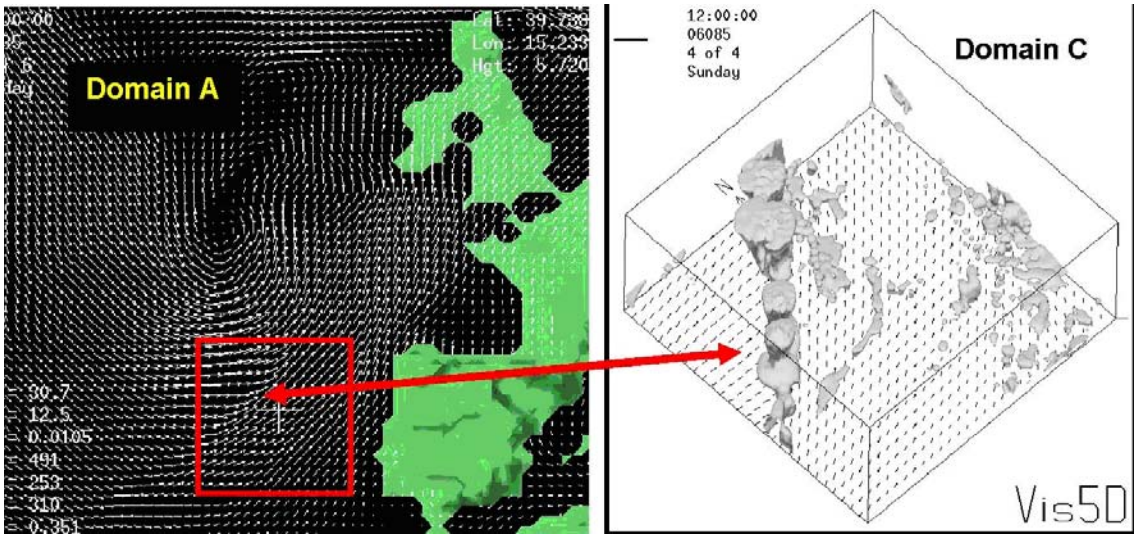

Fig. 3.5 – UW-NMS simulation of a storm over the Atlantic Ocean (case 104). Left panel: sea-level wind field in a portion of outer Domain A. Right panel: sea-level wind field and cloud field within inner Domain C.

Table 3.2 Components of a profile in CRD.

$Tb_{19.35V}$ (K)	$Tb_{85.00V}$ (K)	$Tb_{150.00H}$(K)	$Tb_{52.80H}$(K)
$Tb_{19.35H}$ (K)	$Tb_{85.00H}$(K)	$Tb_{183.31\pm7H}$(K)	$Tb_{53.59H}$(K)
$Tb_{22.24V}$ (K)	$Tb_{91.66V}$(K)	$Tb_{183.31\pm3H}$(K)	
$Tb_{37.00V}$ (K)	$Tb_{91.66H}$(K)	$Tb_{183.31\pm1H}$(K)	
$Tb_{37.00H}$ (K)	$Tb_{150.00V}$(K)	$Tb_{50.30H}$(K)	

Vert-integrated cloud water path (kg/m**2)
Vert-integrated rain water path (kg/m**2)
Vert-integrated graupel water path (kg/m**2)
Vert-integrated pristine water path (kg/m**2)
Vert-integrated snow water path (kg/m**2)
Vert-integrated aggregates water path (kg/m**2)
Surface rainrate (mm/hr)
Surface pristine (mm/hr)
Surface aggregate (mm/hr)
Surface graupel (mm/hr)
Surface snow (mm/hr)

Profile number	Latitude	Longitude
Percent land	Percent snow	Percent ice
Height of surface (km)		

Microphysical quantities
Table 3.3 and figures 3.6 and 3.7 provide some simple statistics of the microphysical properties of the cloud structures in the CRD database. It is quite evident that even though the cases of low water/ice contents and low precipitation are the majority, there is a large variability in the cloud microphysical properties which is related to the fact that our simulations attempt to cover the different climatic regions, types of precipitation and seasonal variations that can occur in the European area. Additional brief comments are inserted at the end of table and figure captions.

Upwelling brightness temperatures
Tables 3.4 and 3.5 and figures 3.8 to 3.10 provide the same statistics for the simulated upwelling Tbs for all relevant SSM/I-SSMIS channels within the CRD database. Large variations may be observed, which are due to the wide range of different meteorological and environmental conditions of the simulated events. Additional brief comments are inserted at the end of table and figure captions.

Comparison of observed and simulated brightness temperatures

As underlined in next chapter, the database plays an essential role in the Bayesian technique. Two properties of the database are relevant in this sense: the "completeness" (number of simulated profiles) and the "consistency" with the experimental data.

Table 3.3 - Statistical indexes of simulated Tbs over land

	mean	variance	spread
Cloud Columnar Content (Kg m^{-2})	0,26	0,12	0 - 5,66
Rain Columnar Content (Kg m^{-2})	0,34	0,53	0 - 32,95
Graupel Columnar Content (Kg m^{-2})	0,06	0,18	0 - 18,57
Pristine Ice Columnar Content (Kg m^{-2})	0,74	2,51	0 - 22,38
Snow Columnar Content (Kg m^{-2})	0,54	0,56	0 - 5,31
Aggregate Columnar Content (Kg m^{-2})	0,07	0,04	0 - 10,02
Surface Rain Rate (mm hr^{-1})	1,11	7,00	0 - 130,69

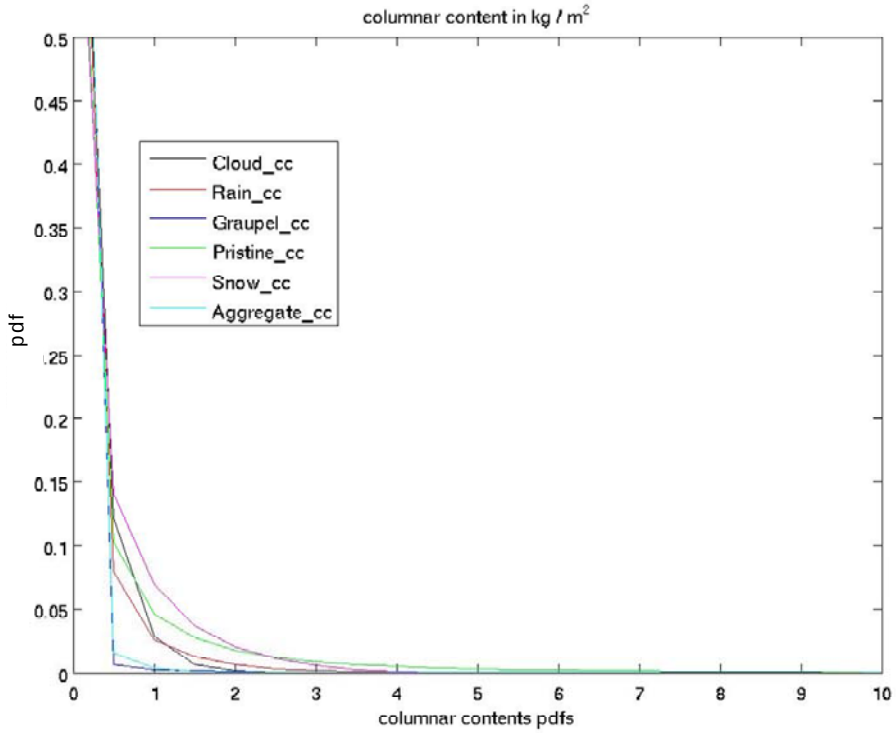

Fig. 3.6 – Probability Distribution Functions (PDFs) of the columnar contents (CC) of liquid and frozen hydrometeors within the CRD European database. Note that all quantities are strongly peaked at 0 kg/m^2.

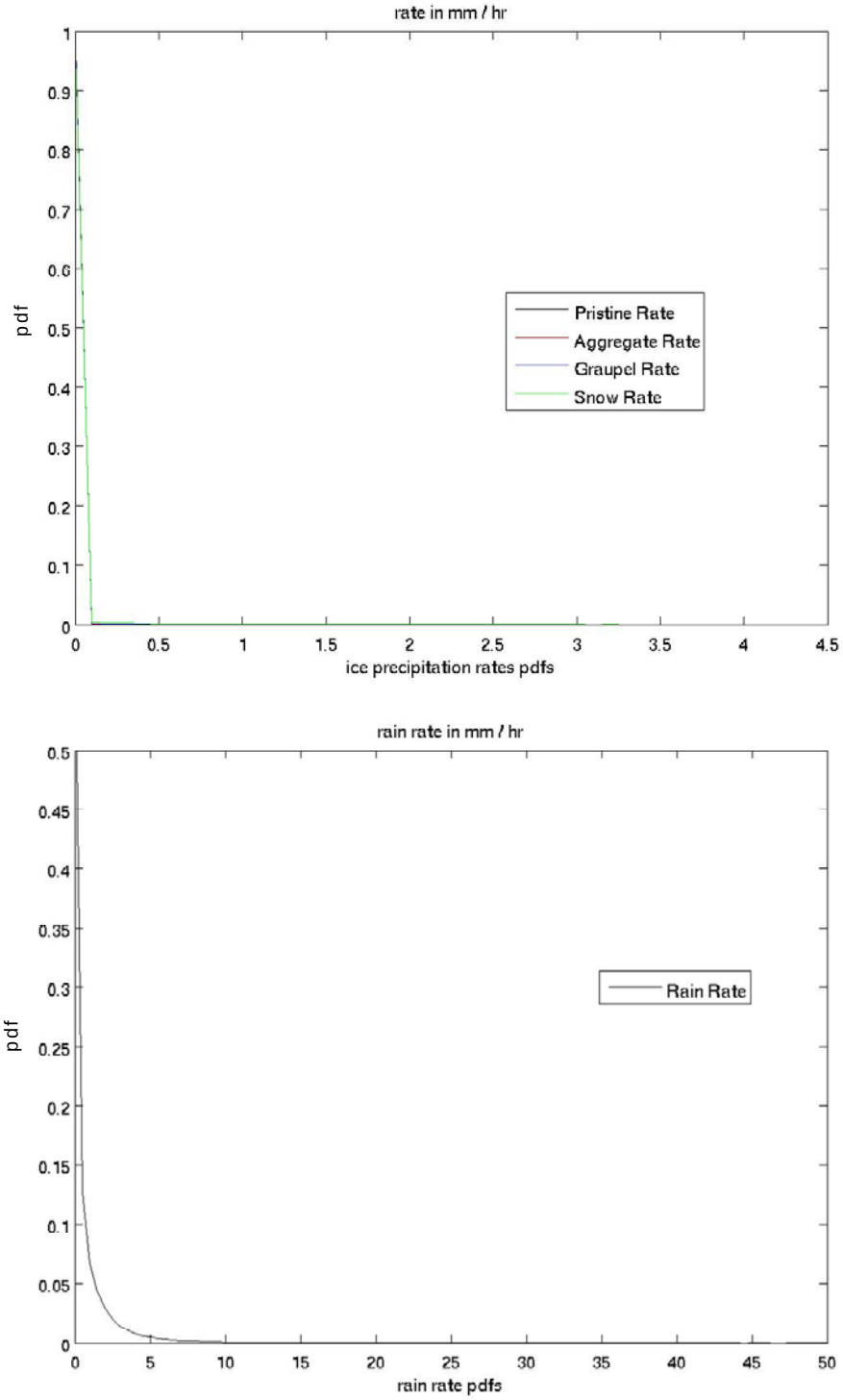

Fig. 3.7 - PDFs of liquid (bottom) and solid (top) precipitation rates at the surface within the CRD European database. As observed also in Table 3.3, liquid precipitation may have very high rates, while solid precipitation is always low.

Table 3.4 - Statistical indexes of simulated Tbs over land.

Over land	polarization	mean	variance	spread	mode
tb 19.35GHz	V	275	41	220 - 294	279
tb 19.35GHz	H	271	207	164 - 294	279
tb 22.235GHz	V	275	24	232 - 293	277
tb 37 GHz	V	274	25	224 - 293	276
tb 37 GHz	H	271	104	193 - 293	276
tb 85 GHz	V	269	85	110 - 294	271
tb 85 GHz	H	268	106	110 - 294	272
tb 91.66 GHz	V	269	93	105 - 294	273
tb 91.66 GHz	H	268	112	105 - 294	273
tb 150 GHz	V	266	158	92 - 290	273
tb 150 GHz	H	266	161	92 - 290	273
tb 183.31±7	H	242	19	133 - 261	240
tb 183.31±3	H	253	31	107 - 272	252
tb 183.31±1	H	261	80	96 - 281	263
tb 50.3 GHz	H	268	39	188 - 285	271
tb 52.8 GHz	H	258	15	198 - 268	260
tb 53.596 GHz	H	245	9	210 - 251	246

Table 3.5 - Statistical indexes of simulated Tbs over ocean.

Over Ocean	polarization	mean	variance	spread	mode
tb 19.35GHz	V	196	122	178 - 266	185
tb 19.35GHz	H	136	348	98 - 251	118
tb 22.235GHz	V	219	249	189 - 273	203
tb 37 GHz	V	222	121	165 - 263	210
tb 37 GHz	H	170	536	127 - 260	149
tb 85 GHz	V	256	69	60 - 279	260
tb 85 GHz	H	232	470	60 - 273	256
tb 91.66 GHz	V	258	68	59 - 282	259
tb 91.66 GHz	H	235	453	59 - 274	247
tb 150 GHz	V	267	80	66 - 290	266
tb 150 GHz	H	259	144	66 - 289	270
tb 183.31±7	H	242	21	81 - 261	239
tb 183.31±3	H	253	24	73 - 271	250
tb 183.31±1	H	262	45	70 - 282	260
tb 50.3 GHz	H	235	131	121 - 266	225
tb 52.8 GHz	H	253	31	135 - 266	247
tb 53.596 GHz	H	242	23	159 - 252	239

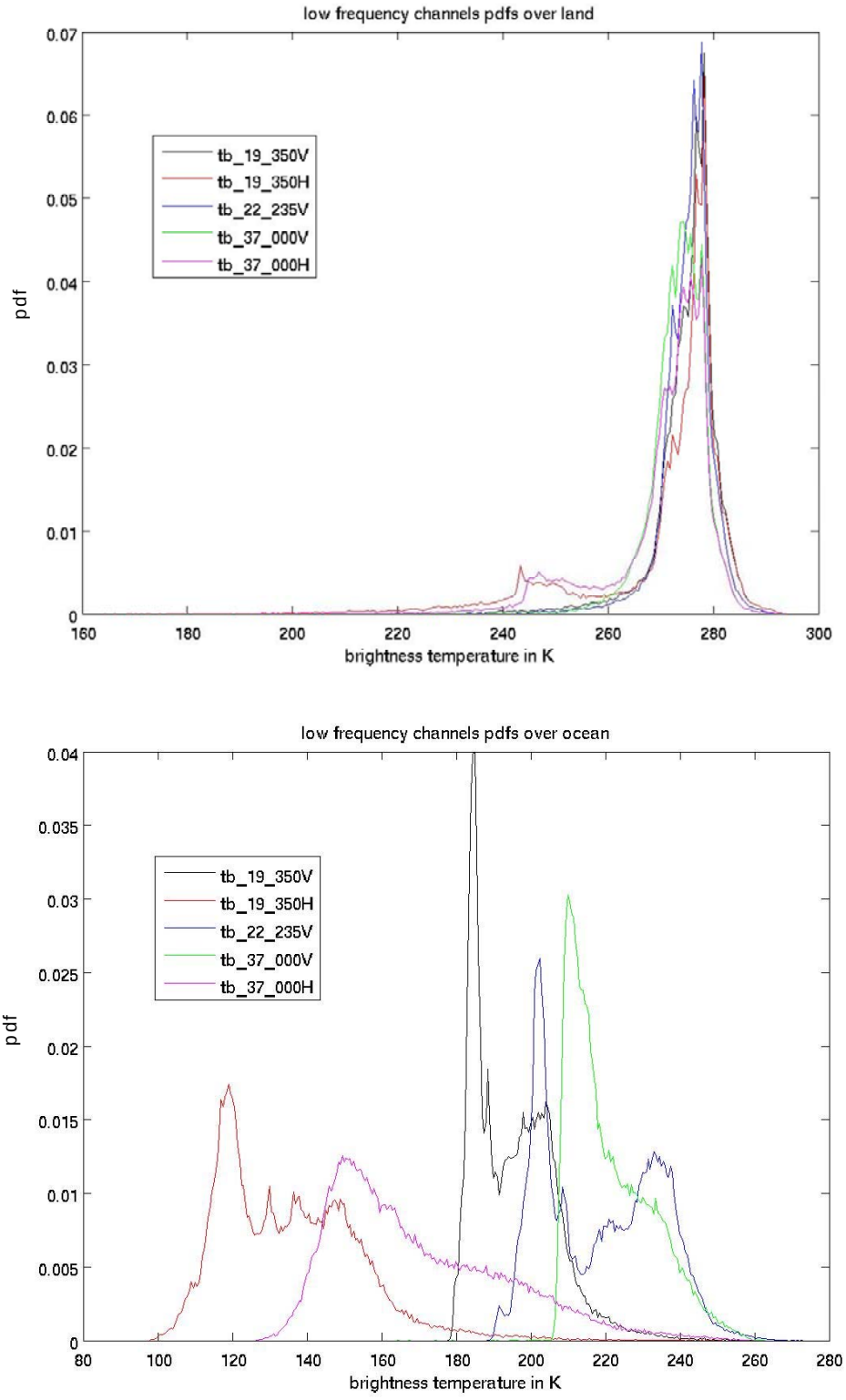

Fig. 3.8 - PDFs of the simulated upwelling Tbs in the CRD European database for the five low-frequency SSM/I – SSMIS window channels over land (top) and ocean (bottom). As expected, we find: a) a large difference between the PDF peaks for land and ocean, which is due to the "cold" emission from the sea surface as compared to land surfaces; and b) a large difference over ocean between the two polarizations for each frequency, which is due to the higher ocean emissivity at vertical polarization.

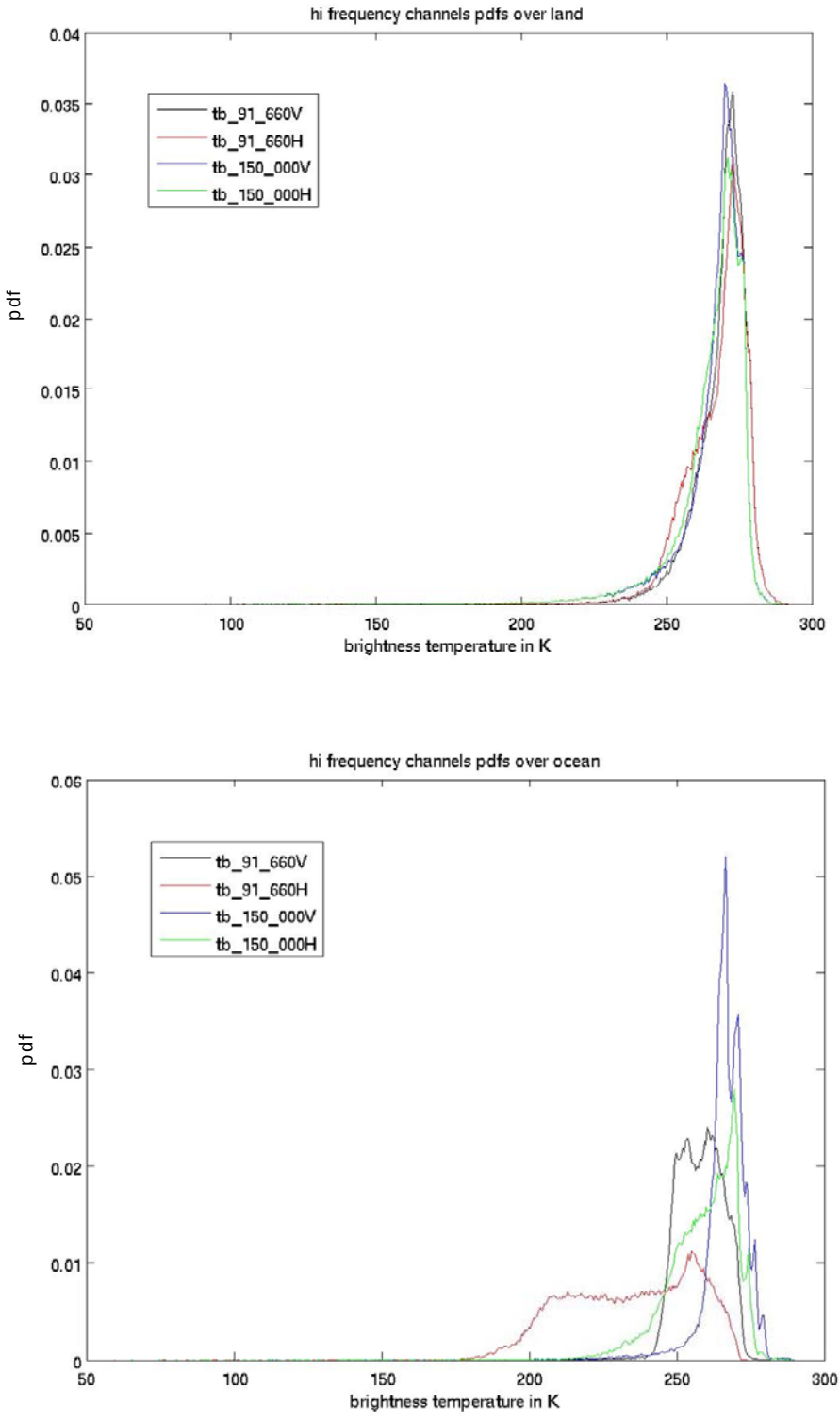

Fig. 3.9 - Same as figure 3.8, but for the high-frequency window channels. As expected, the differences between land and ocean and between the two polarizations are considerably lower than for the low-frequency channels because of the much larger atmospheric contribution to the upwelling Tbs.

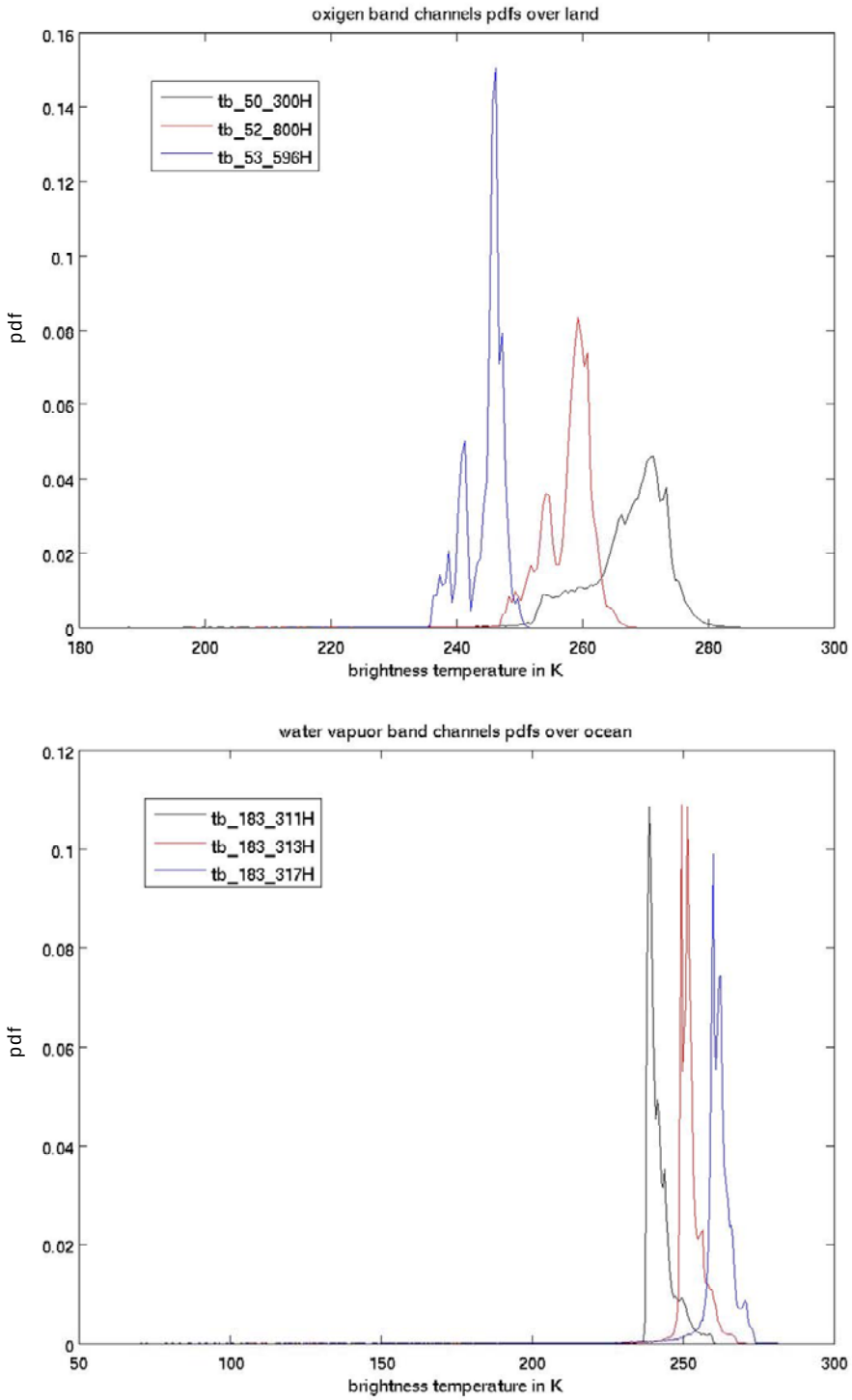

Fig. 3.10 - PDFs of the simulated Tbs for the three lower SSMIS channels in the 50-60 GHz oxygen band over land (top) and for the three SSMIS channels in the 183 GHz water vapor line over ocean (bottom). In both cases, the corresponding results for the other background are not shown because at these absorption frequencies the atmosphere has a much larger effect than the background. As expected, in each panel the PDF peak position is colder for channels that have a weighting function peaked at higher atmospheric levels. In the lower panel, a cold tail is found for the 183.31±7 channel since it is more external to the absorption band and therefore more influenced from ice scattering.

A good completeness is obtained if the N-dimensional space of the simulated Tbs contains the space of the experimental Tbs. More precisely, the minimum distance among each experimental point and the simulated points in this space must be less than the uncertainty of the experimental measure. A good consistency is obtained if the relation between the Tbs are equal in the simulated and experimental Tbs.
To analyze the database in terms of consistency and completeness a sample of experimental Tbs was built collecting data from 9976 SSM/I and 1011 SSMIS overpasses.

With reference to the "consistency" analysis, figures 3.11- 3.15 show the results of a study on the relations between couples of Tbs existing in both the simulated and observed data.
In each image the two Tbs are reported on the axes, and for each point the log of the occurrences is shown. A preliminary analysis was performed using two different scattering models for ice particles: Maxwell-Garnett and Grenfell-Warren. The best agreement between observed and simulated data was found with the Grenfell-Warren model. A good overlapping is evident in some cases (i.e. fig. 3.14), but some problems are pointed out in others (i.e. fig. 3.15) highlighting the limits of the CRD and of the forward model. For this reason in the retrieval procedure a low weight (Wj) was assigned to these channels.

Figure 3.16 shows the result of a study on the completeness of the database. To obtain the figure the following procedure was followed:

1 - In the Tb's space of the database, a neighbourhood with a radius of 1K was fixed.
2 - For each experimental point in this space, the number of simulated points included in its neighborhood was considered; N_0 is the number of experimental points with no simulated points in its neighbourhood, and N_1 is the number of experimental points with at least 1 simulated point in its neighbourhood.
3 – The value of $N_{01} = N_0/(N_0+N_1)$ was then calculated.
4 – Steps 2 and 3 were then repeated using radii ranging from 1 to 10K.

The complete procedure was repeated for different groups of channels.

Figure 3.16 shows the result of this study for three different groups of Tbs. On the vertical axis N_{01} (the % of missed points), and on the x axis the radius of the neighbourhood, are shown. For the 'all frequencies' (black line) analysis, the dataset shows a good completeness for a radius of about 10K, considering only the highest frequencies (red line), or the window frequencies (without 19GHz) (green line) a good completeness is obtained with a radius of about 7K.
This result gives an important reference in the determination of the minimum distance in the selection of profiles of the database in the Bayesian retrieval algorithm.

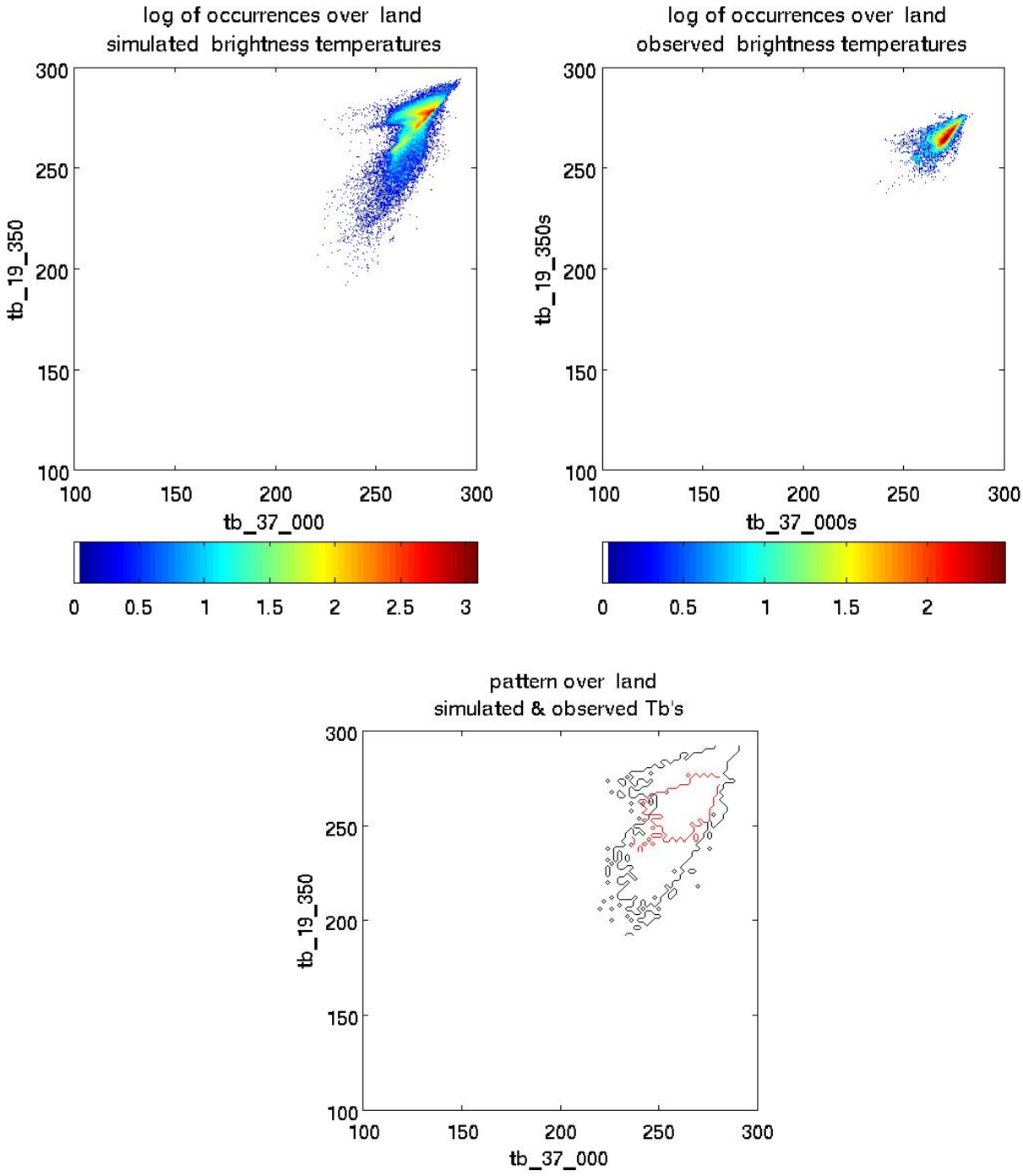

Fig. 3.11 – Relation between the Tbs at 19.350 and 37.000 GHz for the simulated (top-left), and observed data (top-right) over land. The log of occurrences is shown for each point. The overlapping of simulated and observed points is also shown (down).

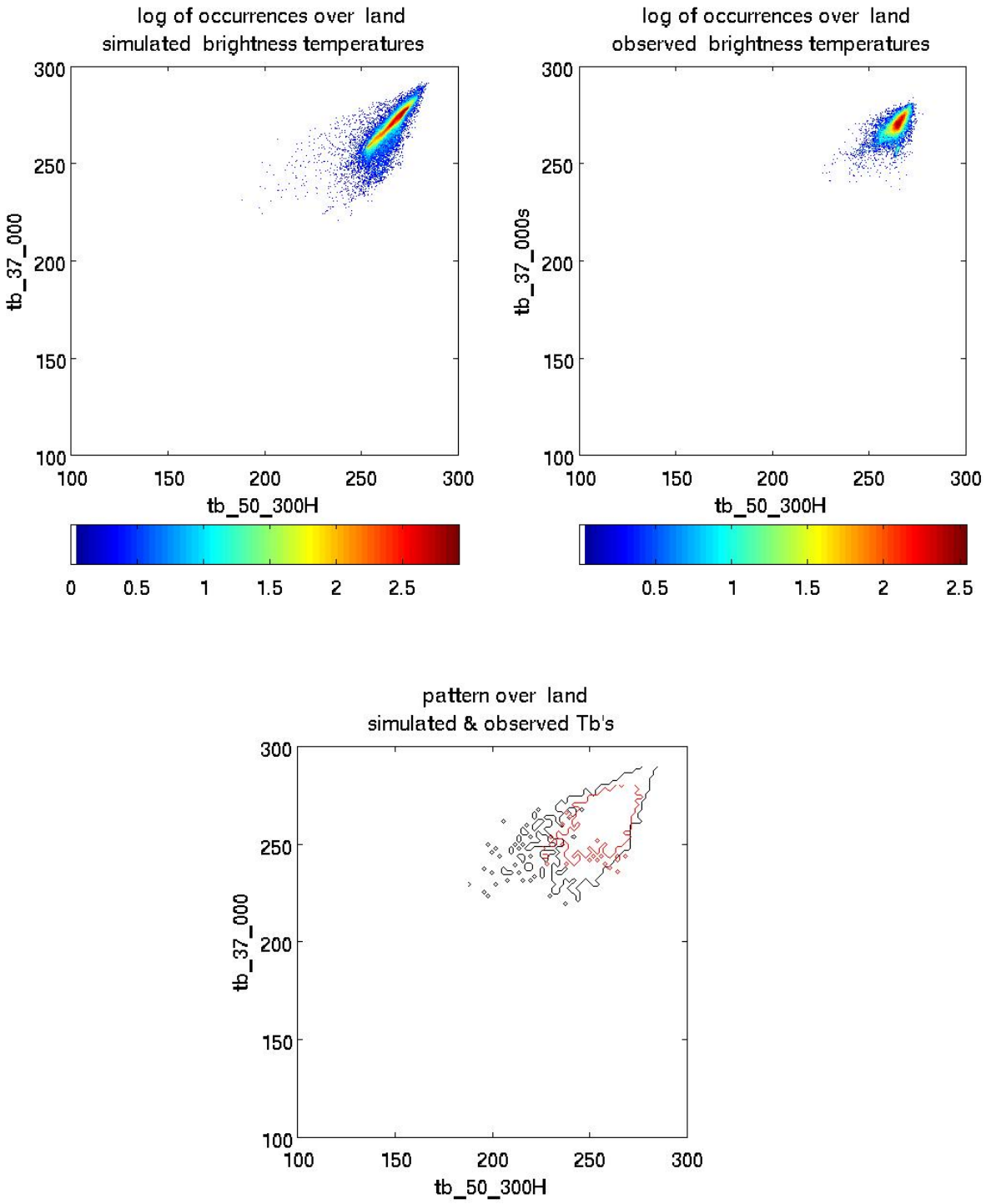

Fig. 3.12 - Relation between the Tbs at 37.000 and 50.300 GHz for the simulated (top-left), and observed data (top-right) over land. The log of occurrences is shown for each point. The overlapping of simulated and observed points is also shown (down).

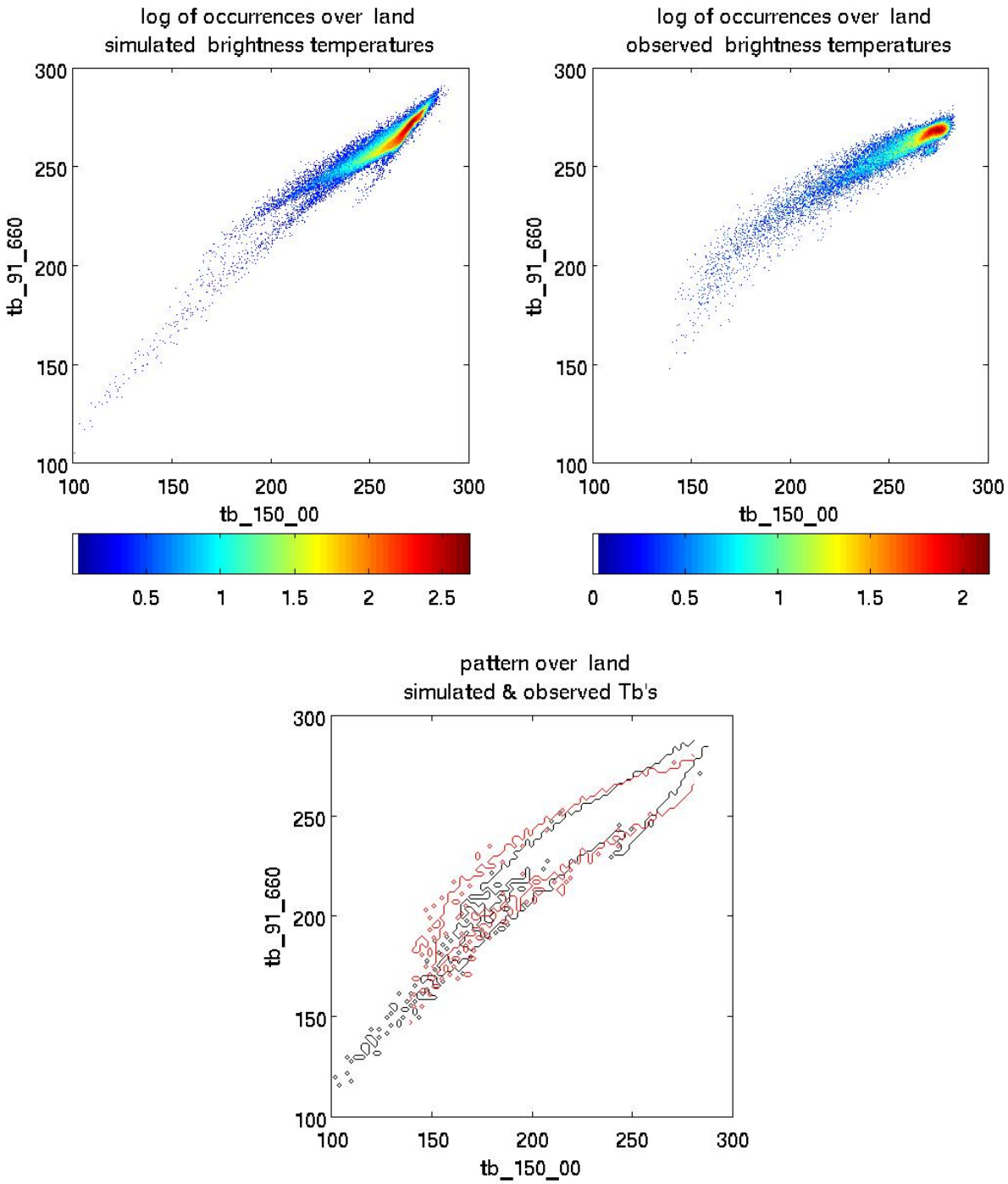

Fig. 3.13 - Relation between the Tbs at 91.660 and 150.000 GHz for the simulated (top-left), and observed data (top-right) over land. The log of occurrences is shown for each point. The overlapping of simulated and observed points is also shown (down). The two distributions are very similar.

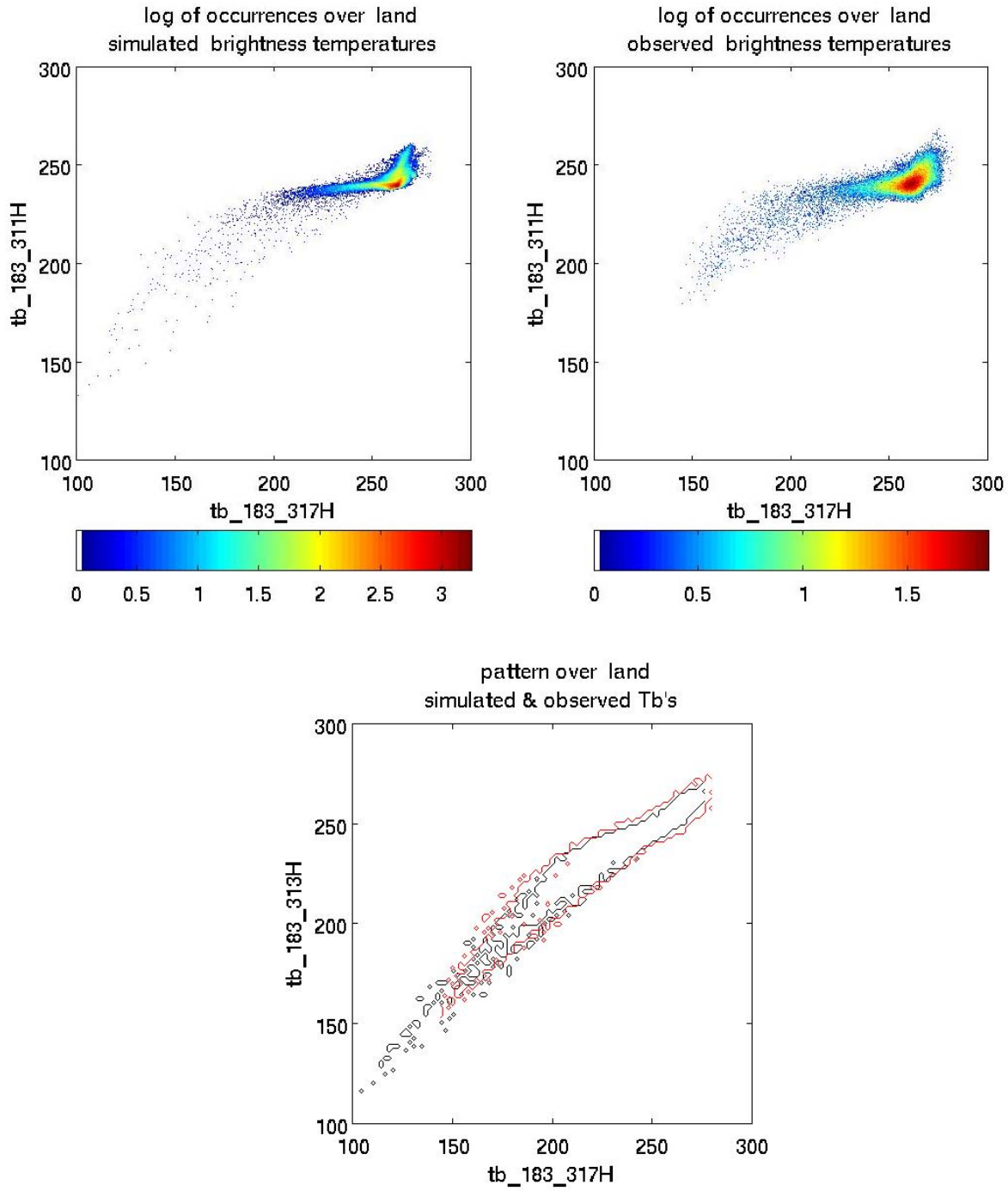

Fig. 3.14 - Relation between the Tbs at 183.313 and 183.317 GHz for the simulated (top-left), and observed data (top-right) over land. The log of occurrences is shown for each point. The overlapping of simulated and observed points is also shown (down). The two distributions, of the sounding channels in the water vapor band, are very similar.

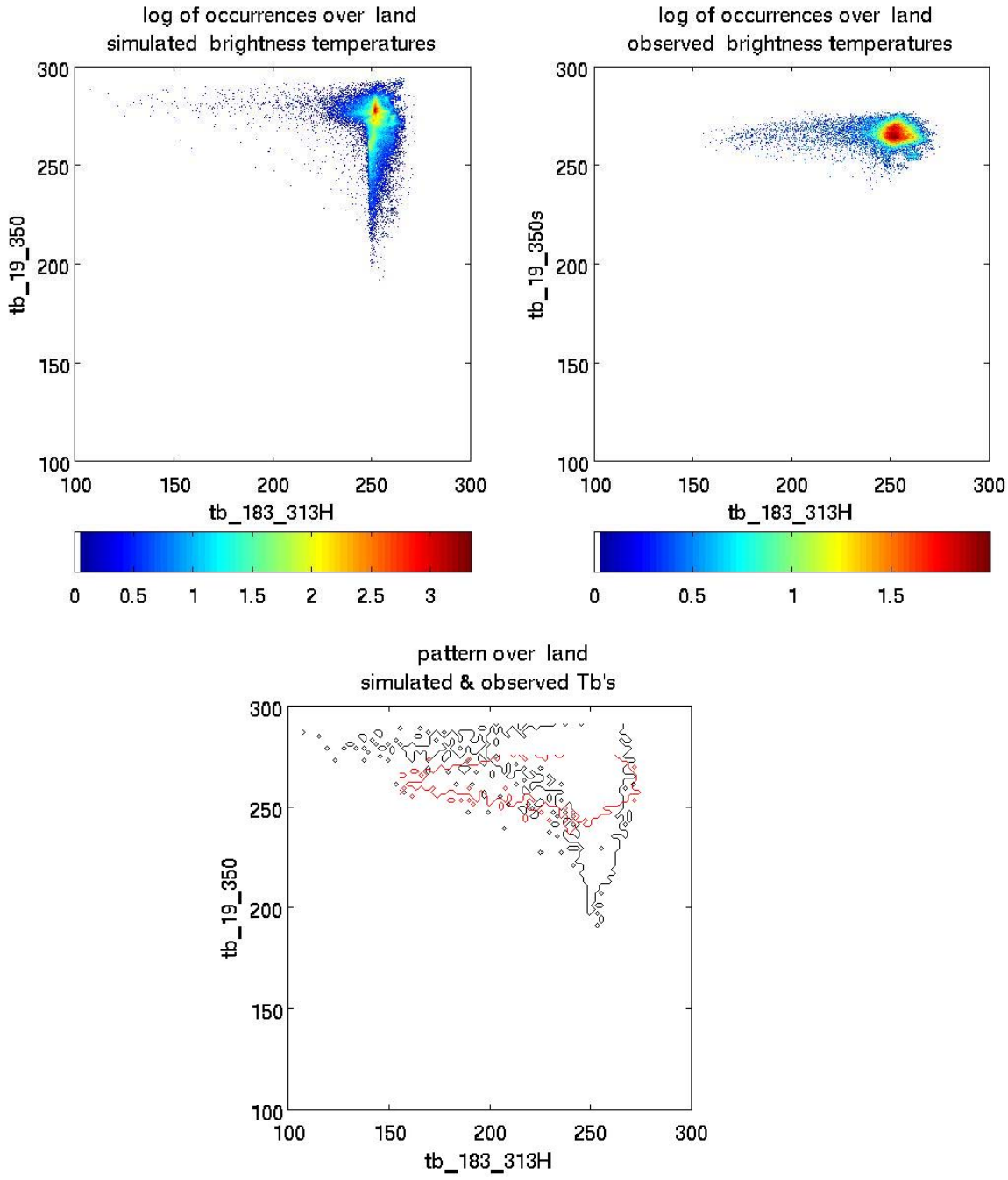

Fig. 3.15 - Relation between the Tbs at 19.350 and 183.313 GHz for the simulated (top-left), and observed data (top-right) over land. The log of occurrences is shown for each point. The overlapping of simulated and observed points is also shown (down). The two distributions are very different. The vertical tail of the simulated Tbs is missing in the observed Tbs. This tail, corresponding to variations of the 19 GHz Tbs not observed experimentally, points out a mismatch probably due to errors in the surface parameterization.

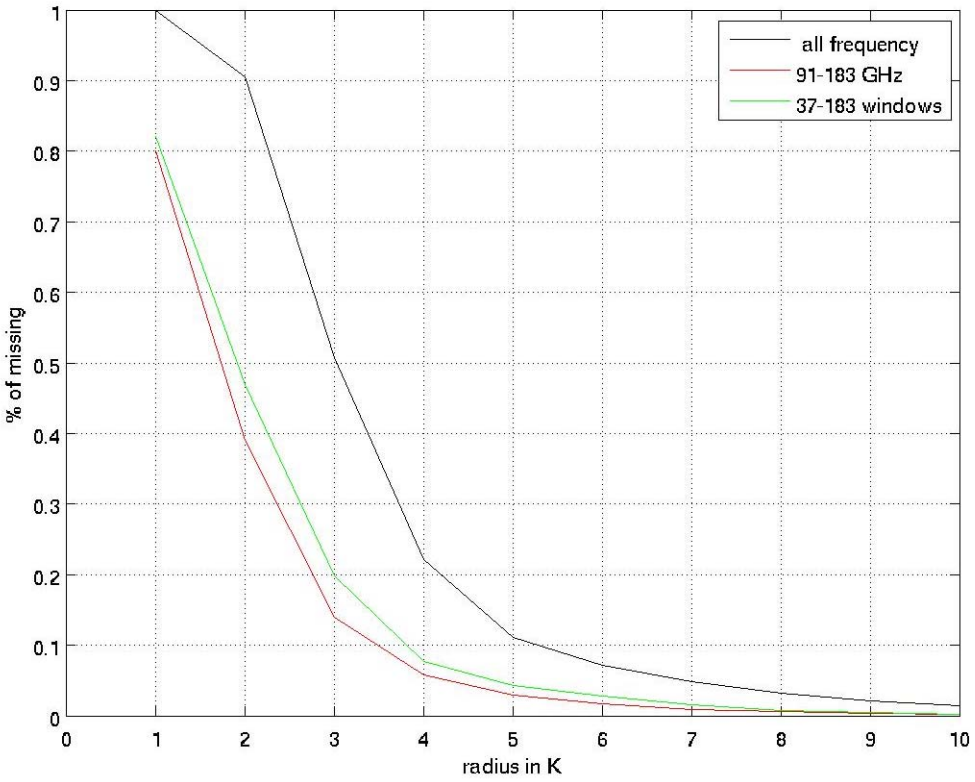

Fig. 3.16 – Analysis of the completeness of the database (see the text).

3.2 The inverse problem

The inverse problem consists in the retrieval of meteorological parameters, like the hydrometeor columnar content and surface rain rates, using the experimental data (the brightness temperatures) of a microwave radiometer, and a probabilistic analysis (Bayesian) of the CRD data. The scheme of the inversion technique is shown on the right side of fig. 3.1.
The Bayesian approach to precipitation retrieval has become fairly common in the remote sensing community (Kummerow et al. 1996). Indeed, the adjective "Bayesian" is very often synonymous of a statistical inversion algorithm, resembling a Maximum Likelihood estimation trained by a CRD (Marzano et al. 1994). Strictly speaking, a Bayesian algorithm simply uses the Bayes theorem to obtain an optimal estimation of a set of random parameters from a given set of measurements (observables). Although the inversion techniques have been widely described (see for instance Evans et al. (1995), Pierdicca et al. (1996)), the theoretical concepts representing the basic underlying principles used in implementing the algorithm are expounded in this section.

3.2.1 The BAMPR algorithm

The BAMPR technique is based on a probabilistic approach, due to the statistical nature of precipitating cloud parameters.

Let us consider the vector $\mathbf{g}$ of cloud parameters as a random variable: it is fully described by the probability density function (pdf) $p(\mathbf{g})$. Making the measurement $\mathbf{t}_m$, the conditional pdf of $\mathbf{g}$ given $\mathbf{t}_m$, indicated as $p(\mathbf{g}|\mathbf{t}_m)$, is called the a posteriori probability. In principle, the result of estimating $\hat{\mathbf{g}}$ through the observation $\mathbf{t}_m$ is given by the complete pdf $p(\mathbf{g}|\mathbf{t}_m)$, although it is often convenient to represent it with only one value $\hat{\mathbf{g}}$. Criteria to define such a value are identified in the framework of the decision theory, where a "weight" $\mathbf{w}(\mathbf{g},\hat{\mathbf{g}})$ is assigned to the couples $(\mathbf{g},\hat{\mathbf{g}})$ of all possible va1ues of the cloud parameters $\mathbf{g}$ and their estimates $\hat{\mathbf{g}}$. The weight represents a measure of the quality of the estimation and is expressed as a non negative real function $\mathbf{W}$ of the two random variables $\mathbf{g}$ and $\hat{\mathbf{g}}$. The ensemble average of the weight function is called "risk function" R (Barkat, 1991):

$$\mathbf{R} = \langle \mathbf{W}(\mathbf{g}, \hat{\mathbf{g}}) \rangle \tag{3.3.1}$$

The risk function $\mathbf{R}$ can be interpreted as the confidence interval of the estimate. The value of $\mathbf{g}$ that minimizes $\mathbf{R}$ is intended as an optimal Bayesian estimation. Different forms of the weight function give different kinds of estimation, but two are the forms leading to the most frequently used estimation criteria. The first one is the uniform weight function:

$$\mathbf{W}(\mathbf{g}, \hat{\mathbf{g}}) = \begin{cases} 0 \text{ if } \mathbf{g} = \hat{\mathbf{g}} \\ 1 \text{ elsewhere} \end{cases} \tag{3.3.2}$$

When $\mathbf{W}$ has the expression in (3.3.2), minimizing $\mathbf{R}$ we obtain as optimal estimation the value of $\mathbf{g}$ corresponding to the maximum of $p(\mathbf{g}|\mathbf{t}_m)$, i.e. its modal va1ue:

$$\hat{\mathbf{g}}_{MAP} = \text{Mode}\{\mathbf{g}|\mathbf{t}_m\} \tag{3.3.3}$$

This represents the estimation criterion of the Maximum A posteriori Probability (MAP).
A second common form for $\mathbf{W}$ is the quadratic one:

$$\mathbf{W}(\mathbf{g}, \hat{\mathbf{g}}) = (\mathbf{g} - \hat{\mathbf{g}})^2 \tag{3.3.4}$$

In this case, it can be demonstrated that the optimal estimation is the expected value of $\mathbf{g}$, given a set of measurements $\mathbf{t}_m$:

$$\hat{\mathbf{g}}_{MMS} = E\{\mathbf{g}|\mathbf{t}_m\} = \int \mathbf{g}\, p(\mathbf{g}|\mathbf{t}_m)\, dg \tag{3.3.5}$$

This choice for the weight function leads to the estimation criterion of the Minimum Mean Square (MMS).
From a numerical point of view, the implementation of (3.3.3) imposes the search of a histogram maximum. This algorithmic aspect can be very sensitive to the sampling and the density of cloud structure parameters (and corresponding Tbs) within the CRD (Marzano et al. 2001). To overcome these difficu1ties intrinsic to the MAP solution, in the retrieval scheme we have developed at CNR ISAC the MMS criterion expressed by (3.3.5) was utilized. Introducing the vector $\mathbf{t}$ of simulated Tb and the function $\mathbf{t}(\mathbf{g})$ that represents the adopted radiative transfer model, $\mathbf{t}_m$ (the measurement of a real radiometer when observing $\mathbf{g}$) can be written as (Pierdicca et al. , 1996) :

$$\mathbf{t}_m = \mathbf{t}(\mathbf{g}) + \boldsymbol{\varepsilon}_t(\mathbf{g}) \tag{3.3.6}$$

where $\boldsymbol{\varepsilon}_t(\mathbf{g})$ takes into account both the radiometric absolute accuracy ($\boldsymbol{\varepsilon}_{t,rad}(\mathbf{g})$) and all other possible sources of error due to the forward modelling ($\boldsymbol{\varepsilon}_{t,mod}(\mathbf{g})$):

$$\boldsymbol{\varepsilon}_t(\mathbf{g}) = \boldsymbol{\varepsilon}_{t,rad}(\mathbf{g}) + \boldsymbol{\varepsilon}_{t,mod}(\mathbf{g}) \tag{3.3.7}$$

Under the previous assumptions, we have (Di Michele et al. 2005):

$$p(\mathbf{t}_m|\mathbf{g}) = p[(\mathbf{t}(\mathbf{g})+ \boldsymbol{\varepsilon}_t(\mathbf{g}))|\mathbf{g}] = p[\boldsymbol{\varepsilon}_t(\mathbf{g})] \quad (3.3.8)$$

Thus, according to Bayes theorem, $p(\mathbf{t}_m|\mathbf{g})$ can be transformed in the following way:

$$p(\mathbf{g}|\mathbf{t}_m) = \frac{p(\mathbf{t}_m \mid \mathbf{g})p(\mathbf{g})}{p(\mathbf{t}_m)} = \frac{p[\boldsymbol{\varepsilon}_t(\mathbf{g})]p(\mathbf{g})}{p(\mathbf{t}_m)} \quad (3.3.9)$$

where $p(\mathbf{t}_m)$ is the pdf of $\mathbf{t}_m$.

A common approach is to take as $p(\mathbf{g})$ the occurrence of $\mathbf{g}$ into the CRD. This is reasonable when the consistency and the completeness of the database are good enough to avoid considering any additional virtual measurements (for example, climatological statistics).

Substituting (3.3.9) in (3.3.5) $\hat{\mathbf{g}}_{MMS}$ can be expressed in the form:

$$\hat{\mathbf{g}}_{MMS} = \int \mathbf{g} \frac{p[\boldsymbol{\varepsilon}_t(\mathbf{g})]p(\mathbf{g})}{p(\mathbf{t}_m)} d\mathbf{g} \quad (3.3.10)$$

Making the further hypothesis that the error sources are independent (Lorenc, 1986), the central limit theorem let us assume that $\boldsymbol{\varepsilon}_t(\mathbf{g})$ is a random variable with Gaussian distribution:

$$p[\boldsymbol{\varepsilon}_t(\mathbf{g})] = \frac{1}{(2\pi)^{1/2}\sqrt{\det(\mathbf{C}_{\varepsilon t})}} \exp[-0.5\,(\boldsymbol{\varepsilon}_t(\mathbf{g}) - \bar{\boldsymbol{\varepsilon}}_t(\mathbf{g}))^T \mathbf{C}_{\varepsilon_t}^{-1}(\mathbf{g})(\boldsymbol{\varepsilon}_t(\mathbf{g}) - \bar{\boldsymbol{\varepsilon}}_t(\mathbf{g}))] \quad (3.3.11)$$

where $\bar{\boldsymbol{\varepsilon}}_t(\mathbf{g})$ and $\mathbf{C}_{\varepsilon t}(\mathbf{g})$ are the mean value and the covariance matrix of $\boldsymbol{\varepsilon}_t$, respectively, whi1e T stands for matrix transposition. Alternative forms for the measurement error model are also possible, i.e. a uniform distribution function could be more suitable in case we want profiles of the CRD that have Tbs "close enough" to the measured ones to equally contribute to the estimation.

Since the two components in (3.3.7) are supposed to be independent (thus uncorrelated), the error covariance matrix can be written as:

$$\mathbf{C}_{\varepsilon}(\mathbf{g}) = \mathbf{C}_{\varepsilon t,rad}(\mathbf{g}) + \mathbf{C}_{\varepsilon t,mod}(\mathbf{g}) \quad (3.3.12)$$

If the radiometric noise has zero mean value, we also have:

$$\bar{\boldsymbol{\varepsilon}}_t(\mathbf{g}) = \bar{\boldsymbol{\varepsilon}}_{t,mod}(\mathbf{g}) \quad (3.3.13)$$

When the dependence of $\boldsymbol{\varepsilon}_t$ from $\mathbf{g}$ is not considered, (3.3.11) allows to express (3.3.10) as:

$$\hat{\mathbf{g}}_{MMS} = \frac{1}{p(\mathbf{t}_m)(2\pi)^{1/2}\sqrt{\det(\mathbf{C}_{\varepsilon t})}} \int \mathbf{g} \exp\left[-0.5(\boldsymbol{\varepsilon}_t - \bar{\boldsymbol{\varepsilon}}_t)^T C_{\varepsilon t}^{-1}(\boldsymbol{\varepsilon}_t - \bar{\boldsymbol{\varepsilon}}_t)\right] \cdot p(\mathbf{g}) d\mathbf{g} \quad (3.3.14)$$

This equation represents a common expression for the solution of the inversion problem. Quantification of retrieval accuracy can become almost as important a demand as the estimate itself. For example, satellite rainfall estimates can be assimilated into numerical weather prediction models only when the corresponding accuracies are also provided (Marecal and Mahfouf, 2002). Difficulties in modelling the various parameters of the forward model lead to Tb ambiguities that propagate into the final estimate. The Bayesian approach allows us to take them into account in a rigorous way. When $\mathbf{W}$ has the form in (3.3.4), it can be proved (Di Michele et al. 2005) that $\mathbf{R}$ is equa1 to the conditional covariance matrix of $\mathbf{g}$ given $\mathbf{t}_m$:

$$\mathbf{R}_{MMS} = \mathbf{C}_{\hat{g}_{MMS}} = \int (\mathbf{g} - \hat{\mathbf{g}}_{MMS})(\mathbf{g} - \hat{\mathbf{g}}_{MMS})^T p(\mathbf{g} \mid \mathbf{t}_m) d\mathbf{g} \quad (3.3.15)$$

Thus, the MMS estimate has, as a confidence interval, the conditional variance $\mathbf{C}\,\hat{g}_{MMS}$ of the estimate. For this reason the MMS solution can be also referred to as the Minimum Variance (MV) algorithm. Applying (3.3.9), the previous expression can be rewritten as:

$$\mathbf{C}\,\hat{g}_{MMS} = \int (\mathbf{g}-\hat{\mathbf{g}}_{MMS})(\mathbf{g}-\hat{\mathbf{g}}_{MMS})^T \frac{p[\boldsymbol{\varepsilon}_t(\mathbf{g})]p(\mathbf{g})}{p(\mathbf{t_m})}\,d\mathbf{g} \tag{3.3.16}$$

The previous establishes the desired relationship between the retrieval error ($\mathbf{g}$ - $\hat{\mathbf{g}}_{MMS}$) and the modeling one $\boldsymbol{\varepsilon}_t$. In case the components of $\mathbf{g}$ are uncorrelated, $\mathbf{C}\,\hat{g}_{MMS}$ becomes diagonal, with the following vector of variances:

$$\boldsymbol{\sigma}^2\,\hat{g}_{MMS} = \int \mathbf{g}^2 \frac{p[\boldsymbol{\varepsilon}_t(\mathbf{g})]p(\mathbf{g})}{p(\mathbf{t_m})}\,d\mathbf{g} \;-\; \hat{\mathbf{g}}^2_{MMS} \tag{3.3.17}$$

If the modeling error can be expressed as a sum of the contributions from different sources, i.e. :

$$\boldsymbol{\varepsilon}_t(\mathbf{g}) = \boldsymbol{\varepsilon}_{t,1}(\mathbf{g}) + \ldots + \boldsymbol{\varepsilon}_{t,n}(\mathbf{g}) \tag{3.3.18}$$

then it is possible to quantify the partial contribution to the uncertainty given only by a particular source introducing in (3.3.16) only the corresponding term.

The implementation of (3.3.14) can be easily carried out when an analytical expression for $p(\mathbf{g})$ is chosen. Typically, for the sake of simplicity, uniform, normal or log-normal distributions are chosen, but each of these choices can often be unrealistic. In general, available $p(\mathbf{g}_i)$ are not continuous functions, and any assumption for $p(\mathbf{g}_i)$ can often be unrealistic. $p(\mathbf{g}_i)$ can be approximated by

$$\mathbf{p}(\mathbf{g}_i) \cong \frac{h(\mathbf{g}_i, \Delta\mathbf{g}_i)}{k'} \tag{3.3.19}$$

where $h(\mathbf{g}_i,\Delta\mathbf{g}_i)$ is the histogram relative the sample $\mathbf{g}_i$ within a variable bin $\Delta\mathbf{g}_i$ and k' a constant such that

$$\sum_i p(\mathbf{g}_i)\Delta\mathbf{g}_i = 1 \tag{3.3.20}$$

Noting that the database CRD consists of a discrete number of profiles (NP), the relation (3.3.14) can be approximated by (Tassa et al. 2003)

$$\hat{\mathbf{g}}_{MMS}(i) = \frac{1}{k}\sum_{j=1}^{NP} \mathrm{g}_j(i)\cdot\exp(-0{,}5\cdot(\mathbf{t}(g_j)-\mathbf{t_m}-\bar{\boldsymbol{\varepsilon}}_t)^T\cdot\mathbf{C}_{\varepsilon t}^{-1}\cdot(\mathbf{t}(\mathrm{g}_j)-\mathbf{t_m}-\bar{\boldsymbol{\varepsilon}}_t))\cdot h(\mathrm{g}_j(i),\Delta\mathbf{g}_j) \tag{3.3.21}$$

where $\mathbf{g}_j$ is the j-th profile sample of the CRD with $\mathbf{g}_j(i)$ the i-th element, $\mathbf{t}(\mathbf{g}_j)$ is the corresponding Tb, and $\mathbf{C}_{\varepsilon t}$ is the error covariance matrix. The normalizing constant k is given by the expression

$$k = \sum_{j=1}^{NP} \exp(-0{,}5\cdot(\mathbf{t}(\mathrm{g}_j)-\mathbf{t_m}-\bar{\boldsymbol{\varepsilon}}_t)^T\cdot\mathbf{C}_{\varepsilon t}^{-1}\cdot(\mathbf{t}(\mathrm{g}_j)-\mathbf{t_m}-\bar{\boldsymbol{\varepsilon}}_t))\cdot h(\mathrm{g}_j(i),\Delta\mathbf{g}_j)\,. \tag{3.3.22}$$

The variance of the estimated $\hat{g}_{MMS}(i)$ is (Di Michele et al. 2005)

$$\boldsymbol{\sigma}^2 = \frac{1}{k'}\sum_{j=1}^{NP} \mathrm{g}_j^2(i)\cdot\exp(-0{,}5\cdot(\mathbf{t}(\mathrm{g}_j)-\mathbf{t_m}-\bar{\boldsymbol{\varepsilon}}_t)^T\cdot\mathbf{C}_{\varepsilon t}^{-1}\cdot(\mathbf{t}(\mathrm{g}_j)-\mathbf{t_m}-\bar{\boldsymbol{\varepsilon}}_t))\cdot h(\mathrm{g}_j(i),\Delta\mathbf{g}_j)\cdot\hat{\mathbf{g}}_{MMS}^2(i) \tag{3.3.23}$$

In all the following applications of (3.3.21), (3.3.22) and (3.3.23), the total error $\boldsymbol{\varepsilon}_t(\mathbf{g})$ has been assumed additive, Gaussian, and with zero mean value.
Fig. 3.17 presents the scheme of the inversion procedure in greater detail.
The Tbs measured by SSM/I or SSMIS (Tab. 3.6) are processed first (data processing block) in order to estimate the Tb measurements by all different channels at the same geographical position (latitude and longitude). This is necessary because the low frequency channels (19, 22, and 37 GHz) have larger footprints than the higher-frequency channels, and therefore a lower number of Tbs is measured for them during each swath (fig. 3.18). Thus, an interpolation procedure is used for the low resolution channels.
Subsequently, all the data are analyzed with a "screening procedure" in order to reject areas (pixels) having incorrect Tb values due to sensor errors, or recognized as areas without rain or with a very low probability of rain.
The Tbs of selected pixels are then used for the inversion algorithm, using the MMS Bayesian criterion and the Tbs of the CRD. For each pixel the "Bayesian distance" between the multi-frequency experimental Tb vector and all simulated multi-frequency Tb vectors of the CRD database are computed

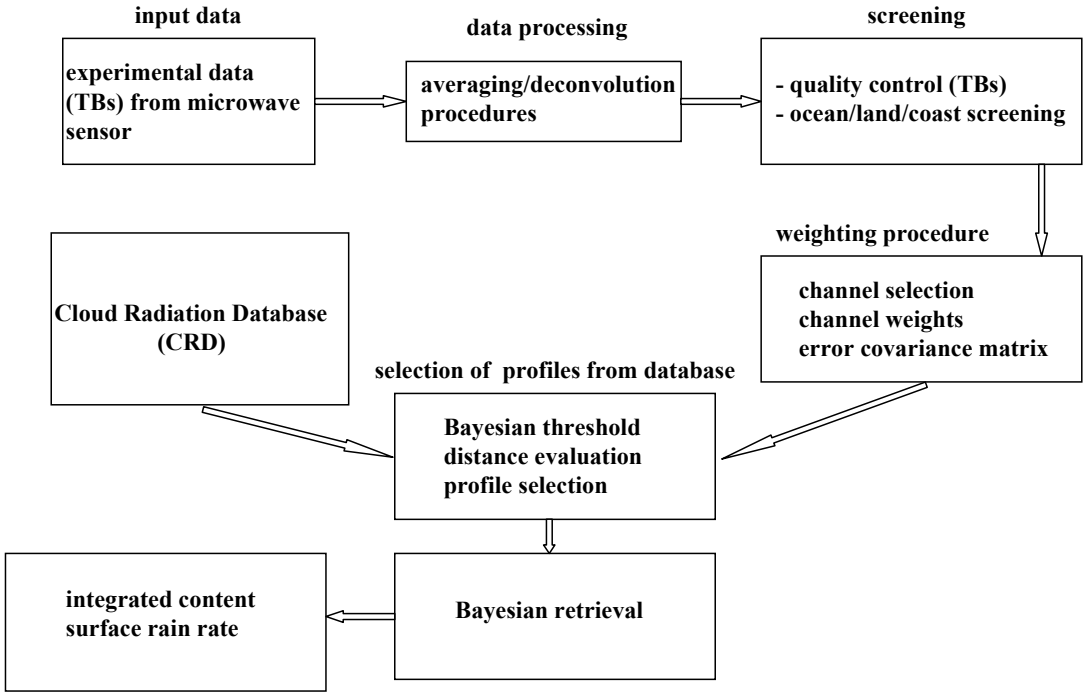

Fig. 3.17 - Block diagram of the Bayesian retrieval algorithm (inverse problem).

The distance is based on the expression 3.3.21 and is given by

$$d2tb(\mathbf{g}_i) = ((\mathbf{t}(\mathbf{g}_i) - \mathbf{t}_\mathbf{m})^T \cdot \mathbf{C}_{zt}^{-1} \cdot (\mathbf{t}(\mathbf{g}_i) - \mathbf{t}_\mathbf{m})) \cdot \mathbf{W} \qquad (3.3.24)$$

where $\mathbf{t}(\mathbf{g}_i)$ and $\mathbf{t}_\mathbf{m}$ are respectively the Tb vectors of the profile $\mathbf{g}_i$ selected in the database and the experimental Tbs; **W** is the weight vector of the microwave channels. Profiles with a distance d2tb>dthre (dthre is an a-priori fixed threshold) are rejected.

Finally, all selected CRD profiles are used, with their different Bayesian weights, to compute the average value of the retrieved surface rain rate (3.3.21 and 3.3.22) and the associated rain rate Bayesian variance (3.3.23). Table 3.7 shows the components of a typical output of BAMPR (for each pixel).
In the following paragraph the screening procedure is presented in detail.

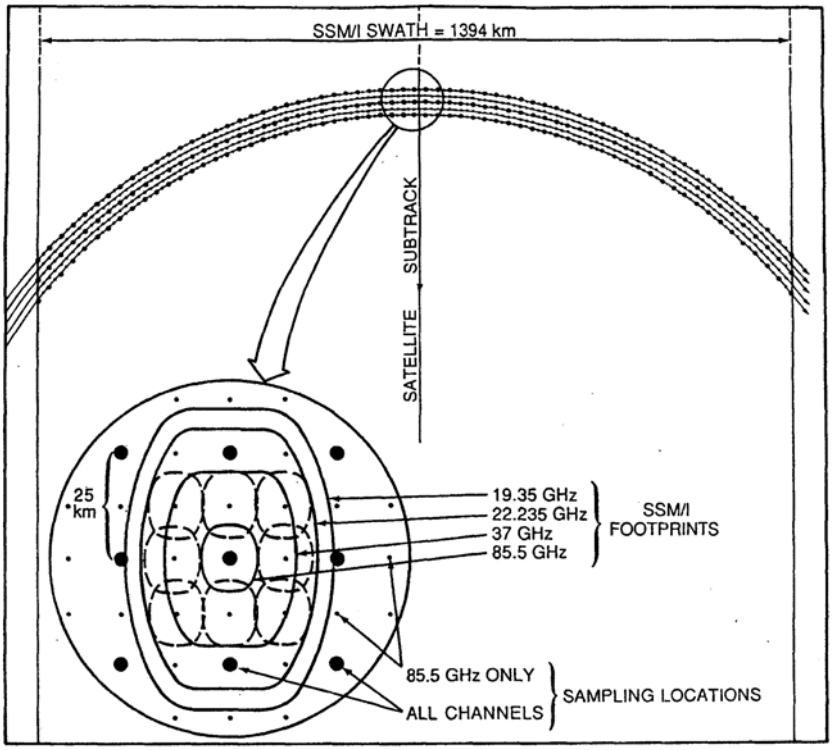

Fig. 3.18 - Scheme of the SSM/I scan geometry, including swath extent, and footprint sampling location and integrated fields of view (Spencer 1989).

Tab. 3.6 - Microwave channels of SSMIS and SSM/I radiometers

channels	SSM/I	SSMIS
1	19V	91V
2	19H	91H
3	22V	150H
4	37V	183
5	37H	183
6	85V	183
7	85H	19V
8		19H
9		22V
10		37H
11		37V
12		50
13		52
14		53
15		54
16		55
17		57
18		59
19		59
20		63
21		64
22		64
23		64
24		64

3.2.2 The "screening" problem

There are two kinds of screening procedures that are normally included in the retrieval algorithm.

The first is a "quality control" screening aimed at rejecting telemetry errors that result in non physical antenna temperatures. For this, in the retrieval algorithm, a check is carried out on the brightness temperatures. If they are out of reasonable physical limits (50 – 350 K) the pixels are rejected. These limit values represent ranges in Tb that are thought to be the approximate physical limitations of measurements in the SSM/I and SSMIS FOV and are based on both empirical and radiative transfer calculations.

The second is a "geographic" screening and it is linked to the type of surface (land or ocean or coast). In fact, rainfall retrieval presents different levels of difficulty depending on the surface examined.

It must be mentioned that many screening methodologies are based on the experimental results mentioned in sections 2.4 and 2.5, concerning the emission- and scattering-based measurements. As pointed out in section 2.4, while over the sea surface, with a relatively low and constant emissivity, the retrieval do not appears to be complex, over land it is more difficult due to the large and variable emissivity of the land surface. Specifically, the high emissivity masks the emission signature that is related directly to the water content in the atmosphere. Instead, only the brightness temperature depression due to scattering in the upper

portion of clouds is observed. As scattering increases with increasing frequencies (section 2.5), brightness temperature depressions at the 85-GHz channel will contain the least ambiguous signal of scattering by ice and/or large raindrops.

Table 3.7 - Components of a typical output of BAMPR (for each pixel)

Pixel enumeration
Surface type (ocean/land/coast)
Rain status (rain/no rain)
Latitude, Longitude
Number or profiles of the CRD that contributed to the retrieval
Vertical-integrated vapor water path (kg/m^2)
Vertical-integrated cloud water path (kg/m^2)
Vertical-integrated rain water path (kg/m^2)
Vertical-integrated graupel water path (kg/m^2)
Vertical-integrated pristine water path (kg/m^2)
Vertical-integrated snow water path (kg/m^2)
Vertical-integrated aggregates water path (kg/m^2)
Surface rainrate (mm/hr)
Surface pristine (mm/hr)
Surface aggregate (mm/hr)
Surface graupel (mm/hr)
Surface snow (mm/hr)
Experimental Tbs mean values (land/ocean) of the pixel (Tb_{19V}, Tb_{19H}, Tb_{22V}, Tb_{37V}, Tb_{37H}, Tb_{85V}, Tb_{85H})
Surface rain rate variance $(mm/hr)^2$

A further complication that arises over land is the lack of consistent backgrounds against which to compare the Tb depression. To solve this problem caused by the varying emissivity associated with changes in surface characteristics (e.g., surface wetness, snow cover, vegetation, etc.), a rain/no-rain temperature depression threshold is required. Additionally, snow and desert surfaces cause depressed Tbs at high frequencies (due to the high volume scattering coefficient k_s) and can be confused with the rain signature. If these surface types are not properly screened, they can be misinterpreted as ice scattering in clouds.
Over coasts, the microwave footprint is a mixture of the radiometrically cold ocean and radiometrically warm land surface. This fact increases the difficulties in the rainfall retrieval and makes the screening procedure an essential part of the retrieval algorithm.
Thus, a preliminary step in a retrieval is the selection of pixels for which some rain is likely, before attempting to quantify the rainfall, in order to minimize the contribution due to false alarms; this is the so called “screening” problem.
Many of the screens developed are empirical in the sense that the equations are based upon comparisons between observed precipitation and actual SSM/I (or SSMIS) measurements.
Although many of the screening methodologies appear simple in formulation and originate from empirical analysis, they play an important role in the retrieval procedure. Failure to properly identify surface types can ultimately lead to the discrediting of the retrieval algorithm;

even the most brilliantly conceived retrieval scheme can be rendered impotent if the screening portion of the algorithm cannot distinguish between raining and non-raining pixels.
Moreover, an important advantage of the statistical-empirical algorithm is the simplicity of their calculation.
The complicated interaction of earth-emitted microwave radiation with various surface types and atmospheric variables makes it very difficult to develop surface screens that work everywhere. Therefore three different "geographic" screening procedure are currently used for land, ocean, and coast, to take into account the different criteria suitable for these surfaces.

3.2.2.1 – Screening over ocean
A sea surface has a low and relatively constant emissivity (approximately 0.4 - 0.5), so that the radiation emitted by the surface is small. Any precipitation over this surface (emissivity 0.8) will augment the radiation stream by emission, increasing the amount of radiation received by the satellite. The rain area will thus appear as warm area against a cold background.
With reference to the SSMI/S channels, in the case of clouds over oceans, each channel responds differently to cloud liquid water depending on the cloud droplet size. The 19 GHz channel provides the most direct measurement of liquid water for rain-bearing clouds; that is, its linear response does not saturate for large drop size (Grody 1993). However, the 37 GHz channel is more sensitive to non-precipitating clouds with a smaller size. For low-lying thin stratus clouds with the smallest amount of liquid water, the 85 GHz channel offers the highest sensitivity; it is, however, strongly affected by the scattering from precipitation sized ice particles (Weng et al. 1977).
Rain identification over ocean is accomplished through both scattering and emission-based methods. Many of these are detailed in Smith et al. (1998). Obviously, the validation of such techniques becomes difficult over open ocean where little or no validation data exist. Recent use of ship reports to evaluate the occurrence of rainfall retrieved by the SSM/I provides some insight as to which techniques perform best in certain rainfall regimes (Petty 1995).
Some of the simpler methods that can be used as a first guess of the rain–no rain boundary include the scattering index approach (e.g., Ferraro et al. 1994b), and the emission approach (e.g., Weng and Grody 1994). As described in section 2.6, the scattering index (SI), worked out by Grody (Grody 1991), and used also for rainfall retrieval over land, is based on the values of the brightness temperatures at the frequencies of 19, 22 and 85 GHz. (Wilheit 2003) The rationale is first to develop a relationship using the 19 and 22GHz channels which could best predict the 85GHZ Tb under non-raining conditions for the water surface in question. Then, by subtracting the actual 85GHz Tb, a measure of the depression due to scattering by precipitating ice/rain drops can be determined.
Specifically, the scattering index is defined as

$$SI_S = F_S - Tb_{85V}$$

$$F_S = A + B \cdot Tb_{19V} + C \cdot Tb_{22V} + D \cdot Tb_{22V}^2$$

Where S indicates the surface type (land or water), and the coefficients A,B,C and D, are derived empirically by assembling a global dataset of SSM/I observations under rain-free conditions.
The form of the SI for ocean is:

$$SI_o = 0.7152(Tb_{19V}) + 2.4387(Tb_{22V}) - 0.00504(Tb_{22V}^2) - 174.38 - Tb_{85V} \qquad (3.3.25)$$

Through an exhaustive evaluation, Grody (1991) found that a SI value of 10K or greater was a good global indicator of rain (see section 2.6).

In addition to the scattering signatures, an emission component of rain is used over the ocean: the liquid water path (LWP). To measure the large dynamic range of cloud liquid water, Weng and Grody (1994) proposed a composite algorithm based on the values of LWP obtained using different SSMI/ channels:

$$LWP_{19V} = -3.20[\ln(290 - Tb_{19V}) - 2.80 - 0.42\ln(290 - Tb_{22V})] \quad (3.3.26)$$

$$LWP_{37V} = -1.66[\ln(290 - Tb_{37V}) - 2.90 - 0.35\ln(290 - Tb_{22V})]. \quad (3.3.27)$$

The first algorithm (LWP_{19V}) concerns a test for moderate to heavy rain in which a Tb_{37V} would be saturated; the second (LWP_{37V}) concerns light rain in which a Tb_{19V} would exhibit too little dynamic range. For the 19-GHz test, if LWP_{19V} exceeds a threshold, nominally 0.6 kg m^{-2}, then rain is assumed present; at 37 GHz, if LWP_{37V} exceeds a corresponding threshold, nominally 0.2 kg m^{-2}, then rain is assumed present.

Some other tests are necessary to complete rain identification over the sea. In fact, sea ice and surface winds increase the emission and can cause misclassification in the retrieval procedure. To separate and remove sea ice from rain, the following condition is utilized (Ferraro et al.1998)

$$Tb_{22V} < 44 + 0.85Tb_{19V}.$$

This relationship accounts for all types of sea ice (e.g., new and multiyear), including the 19-GHz footprint partially filled by ice. A second check is used to separate sea ice from heavy precipitation and is given by (Ferraro et al.1998)

$$Tb_{22V} > 264 \quad \text{and} \quad Tb_{22V} - Tb_{19V} < 2.$$

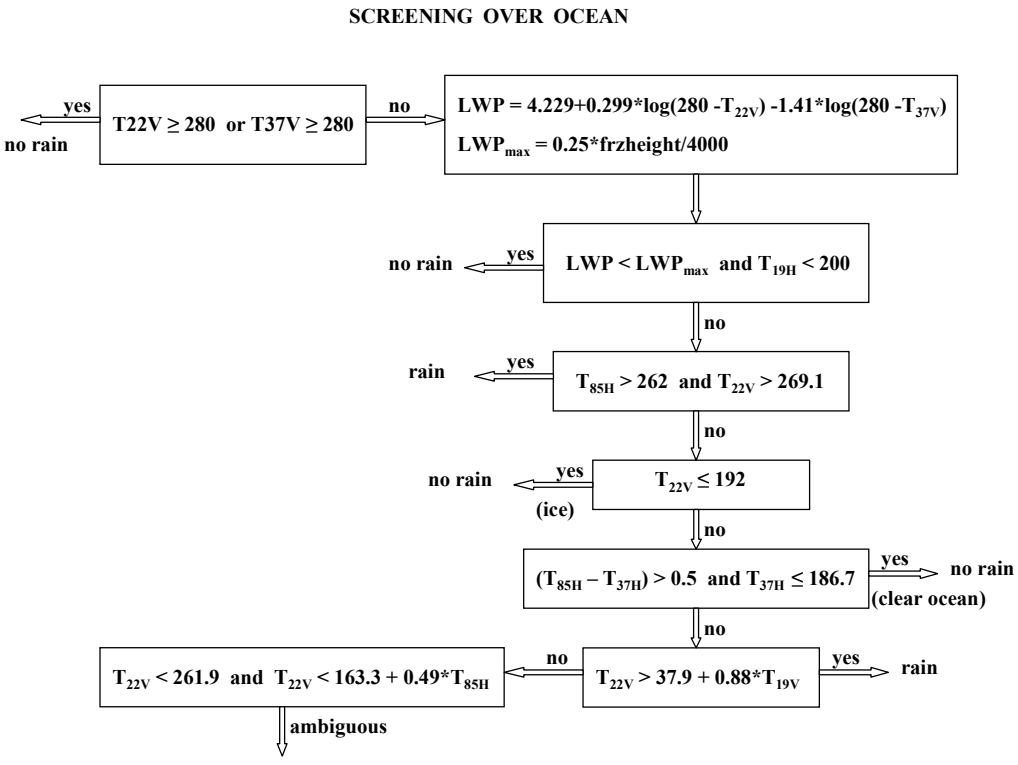

Fig. 3.19 – Screening procedure over ocean used in the BAMPR algorithm.

To identify the effect of surface winds, some retrieval algorithms have been proposed, based on the use of the lower frequencies of SSM/I and polarization differences. In fact, strong winds near the ocean surface impacts the emitting temperature and dramatically reduce the polarization, especially at lower frequencies.
Finally, some other tests are suggested to eliminate misclassifications due to a "cold" ocean. Under clear, calm conditions, the ocean surface emissivity is at its lowest. If the atmosphere is dry, extremely low Tbs are found. These can pose a serious problem to some retrieval algorithms, especially those 85-GHz scattering-based techniques that use single polarization temperature thresholds to delineate rain areas and retrieve rain rate. An empirically derived test developed by Adler et al. (1993) identifies these regions by means of the following two conditions

$$Tb_{85H} - Tb_{37H} > 3K \quad \text{and} \quad Tb_{37H} < 190K.$$

Some tests on ocean rain detection using both the scattering (SI) and the emission approach (LWC), have pointed out that the emission-method can produce a better identification of rain. This fact depends on the use of the 37 GHz channel, which is more sensitive to light rain. For this reason and also on the base of the results of tests, in the application of the screening procedure in BAMPR algorithm, the check on the liquid water path was preferred (fig. 3.19). If the estimated liquid water path is above a threshold, which depends on the estimated freezing level height, that area (pixel) is accepted for rainfall retrieval. However, additional screens are necessary to ensure that cold (either clear ocean or possibly ice) surfaces are either screened or flagged if there is ambiguity in the signal.
After all, the complete definition of the screening procedure of the BAMPR algorithm has required many experimental tests, in order to verify their efficiency in the environmental conditions of the present (Europe) BAMPR applications.
Only a few of the checks mentioned above have been utilized for the screening, on the base of their experimental effectiveness in the identification of raining surface. Moreover, both the coefficients used in these checks and the thresholds have been modified in order to optimize the screening. The values obtained resulted slightly different from those used in the literature.

3.2.2.2 – Screening over land
As mentioned before, the difficulties in retrieving the rain over land are due to the large and variable emissivity of the surface (depending on the type of surface: vegetation, snow cover, deserts, semiarid land, etc). The rather high emissivity, ranging from 0.6 to 0.95 (Grody 1988), in fact masks the emission signature of the liquid water content in the atmosphere. Consequently, detection of the emission signals of clouds and rain over land is not always possible, and essentially all land-based rain-retrieval algorithms utilize the scattering properties of rain. Fig. 3.20 shows "typical" Tb and polarization variations with frequency for a variety of surface types (see also section 2.5). These were obtained from actual SSM/I measurements where additional data were available to classify the different surface types. As the figure demonstrates, there are several surface types (i.e., snow and desert, semiarid land) that exhibit a scattering typical behaviour (signature) that is similar to precipitation, especially light rain. All of these surfaces must be screened properly in order to identify rain in the satellite FOV.
Polarization differences [e.g., Tb(V) − Tb(H)] are also a function of surface type and frequency, and these are depicted in Fig. 3.20(b). For most surfaces, the polarization is greater at 19 GHz than at 85 GHz, whereas precipitation exhibits a rather flat polarization signature with frequency. Finally, desert surfaces generally have the highest polarizations of all land

surfaces although some snow surfaces also exhibit similar characteristics. It is evident from fig. 3.20 that the use of a single channel or a single polarization difference cannot identify the rain signature, given the variety of surface types. Two steps are necessary; the detection of the scattering signature of rain and the surface type identification.

The scattering signatures of rain can generally be detected by using the decrease in Tb with frequency as illustrated in fig.3.20. This signature is most easily obtained by comparing a low-frequency measurement (e.g., 19 or 22 GHz) with a high-frequency measurement (e.g., 85 GHz). Ferraro et al. (1994) present this basic identification of scatterers as any occurrence of the $Tb_{22V} > Tb_{85V}$.

A more precise measurement of scattering can be obtained using the "scattering index" (Grody 1991), which combines the 19, 22, and 85 GHz channels. The form of the "index" is the same used for ocean (see previous chapter), but with different values for the coefficients

$$SI_L = -0.4400(Tb_{19V}) - 1.7750(Tb_{22V}) + 0.00574(Tb_{22V}^2) + 451.88 - Tb_{85V} \qquad (3.3.28)$$

The departure of this estimate from the actual measurement at 85 GHz is a measure of the scattering signal, with the potential rain areas being identified by an index value exceeding 5–10 K.

Other methods include simple thresholds of the 85-GHz temperatures (i.e., the GSCAT2 algorithm in PIP-2), or utilize climatological Tb information based upon data for a period prior to the

retrievals or a similar time period from previous years (i.e., Kniveton et al. 1994; Conner and Petty 1996).

Finally, the polarization corrected temperature (PCT) method, that will be described in next paragraph (screening over coasts), has been widely used in screening over land.

As mentioned before, the methods described can present problems in the retrieval of rain over surfaces such as desertified regions, cold semiarid regions, or snow cover, all of which exhibit significant scattering signatures. Further tests are then required to distinguish the contribution of these surfaces to measured Tb.

Deserts are much more highly polarized than precipitation and other surfaces, so they can be removed from the rain signature using the condition (Grody 1991)(section 2.5)

$$Tb_{19V} - Tb_{19H} > 20.$$

Other more complicated methods have also been proposed by some investigators (Neale et al. 1990, Hollinger 1991) for desert identification.

Arid regions can also produce a scattering signature. These surfaces are generally non vegetated and consist of dry soil for a portion of the year. They exhibit strong polarization characteristics but not as strong as desert regions. A check, developed by Ferraro et al. (1994), used to identify and remove these features, is

$$Tb_{85V} > 253 \quad \text{and} \quad Tb_{19V} - Tb_{19H} > 7$$

Another check, developed for use by the GSCAT2 algorithm, that may perform better globally is given as

$$Tb_{19V} - Tb_{19H} > 10.5 \quad \text{and} \quad Tb_{19V} - Tb_{19H} > 0.25\,(301 - Tb_{85H}) \qquad (3.3.29)$$

There are several classes of snow cover (dry snow, wet/melting snow, and refrozen snow) that need to be identified for proper rainfall classification.

The algorithms proposed (i.e. Grody and Basist 1996) utilize the scattering (SCAT= max(Tb_{22V}-Tb_{85V}; Tb_{19V}-Tb_{37V}) and polarization signatures to identify snow and separate snow cover from other surface types, and involve several steps and checks. Fig. 3.21 shows the proposed procedure in detail.

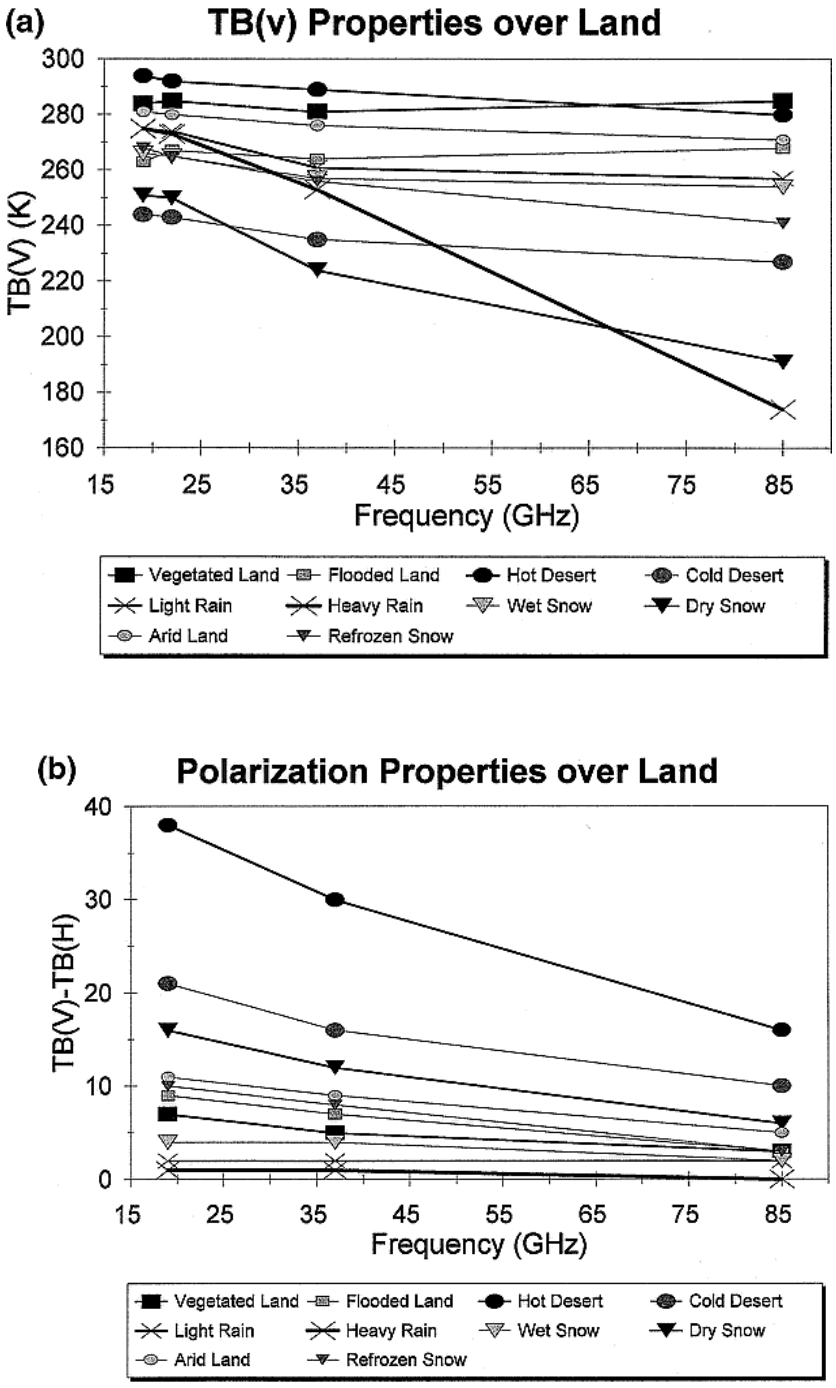

Fig. 3.20 - Brightness temperature variations as a function of frequency for various land surfaces, and for rain. (a) Vertical polarization variations and (b) polarization differences (Ferraro et al. 1998).

Another approach is to use local climatological information to screen for snow cover. This climatology concerns the mean snow cover (obtained from many years of measurements), probability of occurrence, and snow cover variance.

Once the snow cover is identified, the rain contribution to the Tb can be separated using simple threshold conditions on the Tb (Grody 1991). Whenever the

$$Tb_{22V} > 264 \text{ K},$$

rain is present, provided that a scattering signal exists. This condition assumes that the surface is colder for snow conditions than in the case of rain. The threshold condition also works because the large ice crystals within the snow pack scatter at low frequencies, while the smaller-sized ice particles associated with light to moderate rain produce little scattering. The 264K threshold represents average conditions and the local value can deviate by approximately ±3 K depending on the surface and atmospheric conditions. For example, cold rain can reduce the Tb_{22V} to 261 K while melting snow increases Tb_{22V} to 267 K. The problem is difficult for winter storm systems, where snow and rain generally fall adjacent to one another.

The GSCAT2 approach to this problem is to label observations near this threshold as ambiguous and introduce another check that examines the standard deviation of the Tb_{85H} in a 5 × 5 set of pixels centred around the pixel in question. Low values of this parameter indicate likely snow, while high values indicate convective rain.

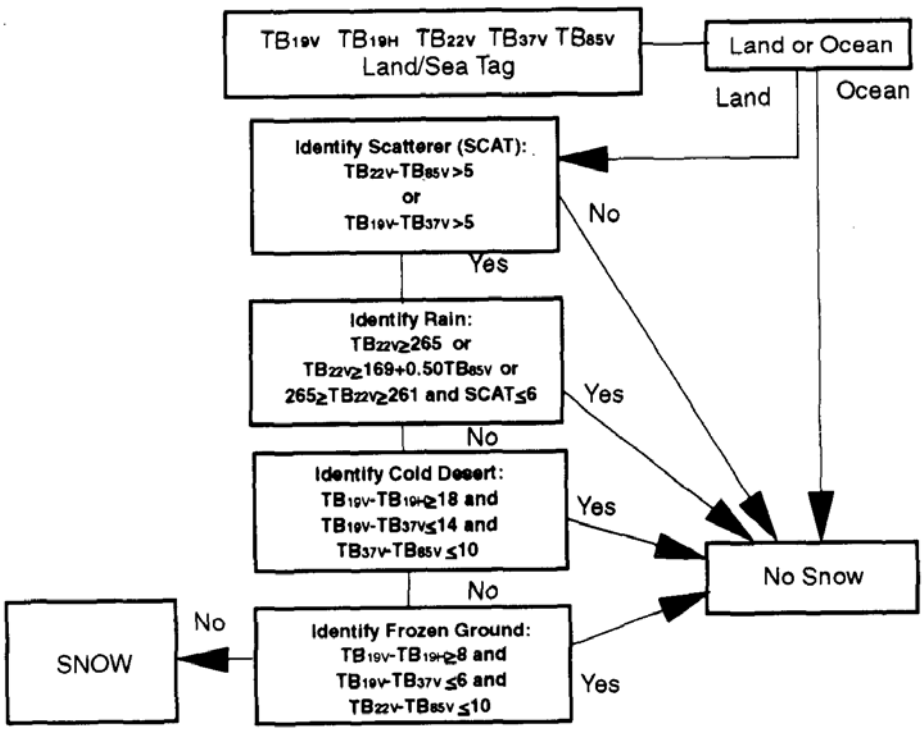

Fig 3.21 - Decision tree structure of the snow cover retrieval algorithm (Grody and Basist 1996, Ferraro et al. 1996).

For intense convective rain, which contains large ice particles, scattering occurs at low frequencies for both rain and snow. This can cause the Tb_{22V} to fall below 264 K. However, this confusion can easily be eliminated by applying the threshold under cold seasons and over certain latitude zones (i.e., the use of climatological limits of snow). However, a second condition is necessary to separate intense rain from snow cover (Grody 1991) and is given by

$$Tb_{22V} > 175 + 0.49Tb_{85V}.$$

As mentioned, the use of this check depends on the latitude and the season. An incorrect use could eliminate some pixels in intense convective systems. As previously described, the GSCAT2 method would classify these situations as rain if the standard deviation of the Tb_{85H} measurements of adjacent pixels is large.

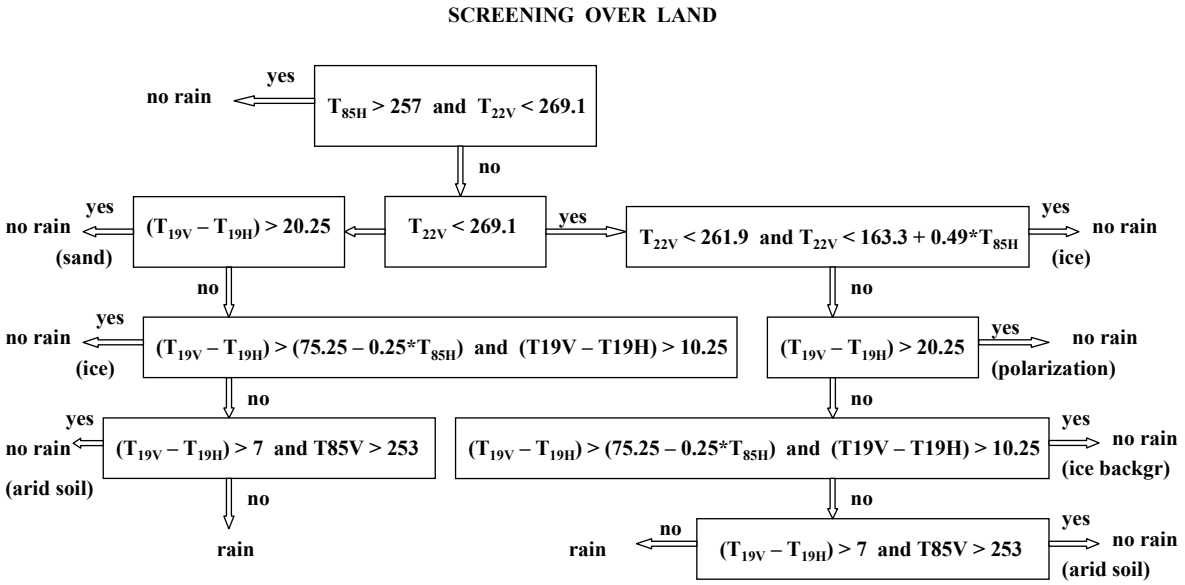

Fig. 3.22 – Screening procedure over land used in the BAMPR algorithm.

Fig. 3.22 shows the screening procedure over land used in the BAMPR algorithm. Only a few simple checks have been selected, among those proposed in the literature, on the basis of tests carried out during the case studies. Moreover, the coefficients used in these checks have been modified in order to optimize screening efficiency.

3.2.2.3 – Screening over coasts

Rainfall retrieval over coasts is crucial for regions like Italy where a high portion of the region is considered to be 'coastal'. Nevertheless, the retrieval presents real difficulties for the presence of sea and land areas in the same footprint, with different emission signatures. In fact, over coasts the microwave footprint is a mixture of radiometrically cold ocean and radiometrically warm land surfaces.

The main problem originates from the fact that land or water, adding the opposite surface into the footprint, has the same effect as rain. Over land, adding surface water to the footprint will

reduce the Tbs, as scattering caused by rain does; adding land to a water footprint will increase Tbs, with a similar effect of the rain over water (emission). This is illustrated in Fig. 3.23 using the GPROF (Goddard Profiling Algorithm) surface-type classification map.
The black lines are for TMI water footprints, and these Tbs increase with increasing rain rate, except for Tb_{85V}, which decreases above 1 mm h^{-1} due to scattering. The coloured lines are for footprints that are classified as coast, but starting with those footprints bordering the water classification and thus, not containing much land (coast < 10 km from ocean). As the distance from the footprints classified as water increases, the fraction of land within the footprints and the Tbs at all frequencies increase.
One method to account for the complexity of the land-water mixture is to develop an algorithm to use the effective antenna pattern function and scan geometry of the microwave instrument, along with a very high resolution land water mask to estimate the fraction of land versus water in each footprint. A study (Bennartz 1999) of this methodology pointed out the difficulties in its application related to satellite navigation uncertainties and to the highly variable land surface emissivity.

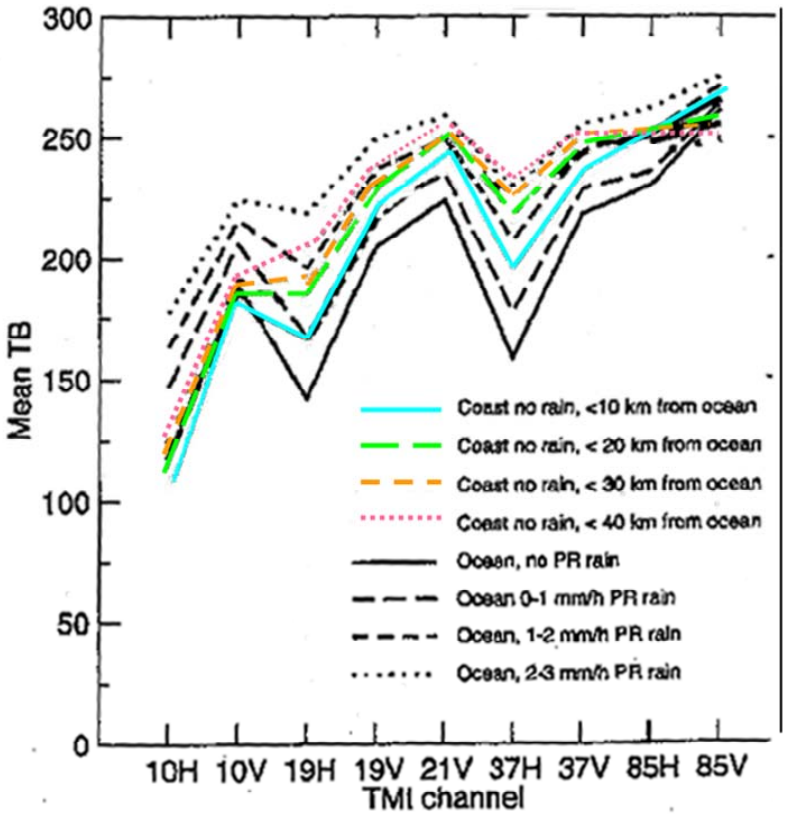

Fig. 3.23 - Brightness temperatures spectrum over water for increasing rain rate, and over non-raining coasts with increasing land fractions (McCollum 2005).

The easiest method for coastline identification is to simply discard any observation tagged as coast and perform no retrievals there. However, this will eliminate raining coastal pixels. Since the SSM/I FOVs are relatively large, they contain a mixture of land and water that extends farther than one pixel from the coast and can cause false rain signatures.

Another scheme used to minimize the coastline effects, and employed by the National Environmental Satellite, Data and Information Systems (NESDIS) (Smith et al. 1998, Ferraro 1997), was to use a 5 × 5 grid of A-scan observations surrounding the pixel for which the retrieval is performed. Any coastline or land identified in this grid was classified as land.

They simply used their land algorithm over these coast and "near coast" FOVs. This approach seems to reduce many of the false signatures along the coastline. The trade-off for this approach is that the sensitivity to emission-type rain is lost along the coast; however, this is better than no retrieval at all. In addition, there is not much difference noted in convective rain.

One of the first global rainfall algorithms, developed specifically for coasts, was proposed by Adler et al. (1993). It is a sophisticated algorithm, with a decision-tree method for coasts to isolate possible rain from the similar brightness temperature signatures resulting from the different relative fractions of land and ocean in the footprint. The identification of non-precipitating coastline pixels is performed with the following procedure.

Clear-sky coast is identified as (Adler et al.1993)

$$\sigma\,[Tb_{85H}] > 10K \quad \text{and} \quad \rho\,[Tb_{37H}, Tb_{85H}] > 0.5 \quad \text{and} \quad \text{slope} < 1.2 \qquad (3.3.30)$$

where σ is the standard deviation, ρ is the cross correlation, and slope is defined as

$$\text{slope} = \rho\,[Tb_{37H}, Tb_{85H}] \times \sigma\,[Tb_{85H}] \times \sigma\,[Tb_{37H}] \qquad (3.3.31)$$

all of which are computed on a 5 × 5 pixel array centered on the pixel of interest. Adler et al. (1993) also recommend another test, run before (3.3.30) and (3.3.31), to identify cases that satisfy the coast check but proved to have precipitation in verification studies. This "not-coast" test diagnoses the presence of precipitation when

$$Tb_{85H} - Tb_{37H} \leq -10 \text{ K}. \qquad (3.3.32)$$

Finally, the use of the polarization-corrected temperature (PCT) approach (Spencer et al. 1989) and similar procedures (Conner and Petty 1996) has been diffusely used to minimize coastline effects. These procedures involve a linear transformation between Tb_V and Tb_H that effectively removes the land–ocean emissivity contrast.

In fact, the PCT corrects the passive microwave measurements to unify surface emissivity by combining the vertical and horizontal brightness temperatures Tbv and Tb_H, respectively, at a single microwave frequency. The theoretical basis is outlined by Grody (1984) . The radiative transfer equation (Ulaby et al.1986), describing the emission contributions received by a spaceborne PM sensor, is (see fig. 2.6, and expression 2.34)

$$Tb(p) = \tau\ \varepsilon(p)\, T + T_{UP} + \tau\,[1 - \varepsilon(p)]\ T_{DOWN} + \tau^2\,[1 - \varepsilon(p)]\ T_{SP} \qquad (3.3.33)$$

where Tb(p) is the satellite-measured brightness temperature at polarization p, ε(p) is the surface emissivity at polarization p, τ is the atmospheric transmittance, $T_{UP} = T_{DOWN}$ is the total atmospheric emission, T_{SP} = 2.7 K is the cosmic residual radiation, and T is the surface temperature.

Grody (1984) introduced a parameter β, function of emissivities at the vertical ε_v and horizontal ε_h polarizations, as

$$\beta = \frac{1-\varepsilon_v}{1-\varepsilon_h} \tag{3.3.34}$$

This relation between ε_v and ε_h for a given microwave frequency enables surface emissivity to be removed from (3.3.33). Substitution of (3.3.34) into (3.3.33) for both vertical and horizontal polarization yields

$$Tb_V = \tau\ \varepsilon_v T\ +\ T_{UP}\ +\ \tau\,[1 - \varepsilon_v]\ T_{DOWN}\ +\ \tau^2\,[1 - \varepsilon_v]\ T_{SP}$$
$$Tb_H = \tau\ \varepsilon_h T\ +\ T_{UP}\ +\ \tau\,[1 - \varepsilon_h]\ T_{DOWN}\ +\ \tau^2\,[1 - \varepsilon_h]\ T_{SP}$$

Using 3.3.34

$$\varepsilon_v = 1 - \beta + \beta\ \varepsilon_h$$

and substituting in previous expressions

$$Tb_V = \tau\ (1 - \beta + \beta\ \varepsilon_h)\ T\ +\ T_{UP}\ +\ \tau\,\beta[1- \varepsilon_h]\ T_{DOWN}\ +\ \tau^2\,\beta[1- \varepsilon_h]\ T_{SP} =$$
$$\tau\ (1 - \beta)\ T + T_{UP}(1 - \beta) + \beta\ \tau\ \varepsilon_h\ T + \beta T_{UP+}\ \tau\,\beta[1- \varepsilon_h]\ T_{DOWN}\ +\ \tau^2\,\beta[1- \varepsilon_h]\ T_{SP} =$$
$$\tau\ (1 - \beta)\ T + T_{UP}(1 - \beta) + \beta\ Tb_H$$

Therefore,

$$\frac{Tb_V - \beta Tb_H}{1-\beta} = T_{UP} + \tau T \tag{3.3.35}$$

Thus, with β defined, the PCT can be established from the left side of (3.3.35). To simplify the use of the PCT, Barrett and Kidd (1990) further defined a Θ parameter as

$$\Theta\ =\ \frac{\beta}{1-\beta} \tag{3.3.36}$$

such that by insertion of (3.3.36) into (3.3.35) the PCT can be defined as

$$PCT = (1 + \Theta)Tb_V - \Theta\ Tb_H\ =\ Tb_V\ +\ \Theta\ (Tb_V\ -\ Tb_H) \tag{3.3.37}$$

According to (3.3.35) the PCT is equivalent to the Tb for a unity emissivity surface and in principle is sensitive only to surface temperature and atmospheric emission.

The value of Θ needs to be set in relation to the meteorological conditions prevailing at the time, and a threshold needs to be chosen to discriminate rain from no-rain. The values of theta are dependent on the rain/no-rain threshold: as theta increases the rain/no-rain threshold also increases.

Any dual polarized frequency can be used, but high frequencies are preferred where sensitivity to rainfall is greatest and the spatial resolution is the best available. Although the 85 GHz channels, and hence the PCT at 85 GHz, will be strongly affected by thick cirrus, the sensitivity to light precipitation makes it ideal for rain/no-rain discrimination.

In the expression (3.3.37), the value of PCT is equal to Tb_V for Θ=0. As the value of Θ increases, the amount of polarization added to the vertical channel increase so that when Θ=1, the PCT is the polarization (Tb_V - Tb_H) added to the vertical brightness temperature.

Areas with low vertical brightness temperatures, but high polarization, like sea surfaces, will increase their PCT faster then those with high vertical brightness temperatures but low polarization, like land surfaces. Therefore, a point is reached where the low vertical brightness temperature/high polarization pixels exceed the PCT of the high vertical brightness temperature/low polarization pixels. The intercept of the two straight lines corresponds to the value of Θ that normalize the different background emissivities. Fig. 3.24 shows the PCT

behaviour as a function of Θ, for ocean and land, obtained in a case study (see section 3.4) over Calabria.
The intercept also gives, on the vertical axis, the value of PCT corresponding to the condition

$$Tb_{VS} + \Theta\,(Tb_{VS} - Tb_{HS}) = Tb_{VL} + \Theta\,(Tb_{VL} - Tb_{HL})$$

of normalization of the different background emissivities.
Then, any rain will appear as lower PCT values due to the scattering of the upwelling radiation stream.

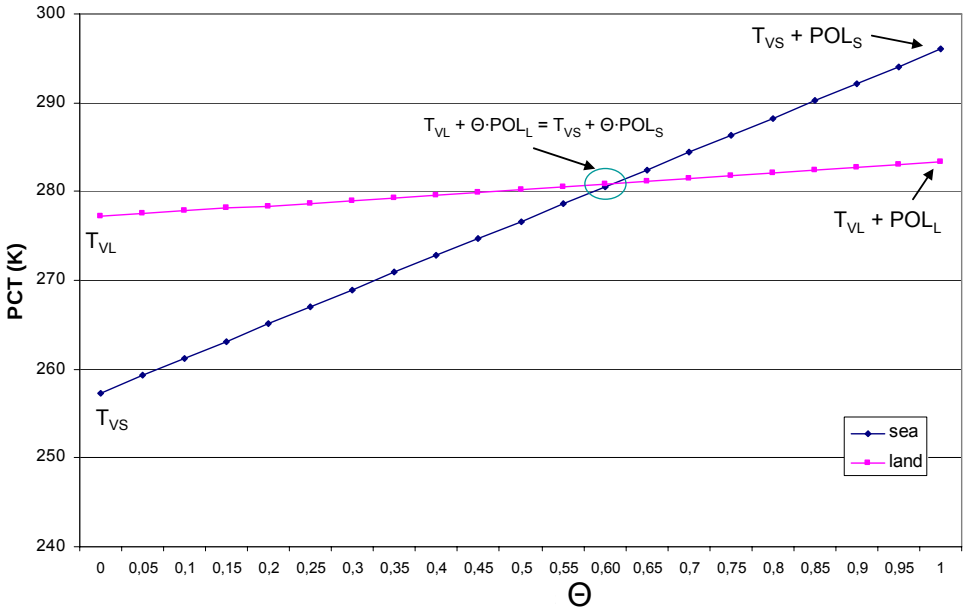

Fig. 3.24 - Polarization-corrected temperature as a function of Θ for two different surface types, sea and land. T_{VS} is the vertical brightness temperature of sea, T_{VL} the brightness temperature of land, POL_S the polarization difference of sea (T_{VS} -T_{HS}), POL_L the polarization difference of land (T_{VL} -T_{HL}).

The screening on coasts can be based on this value of PCT. The area used in determining a valid value of Θ and the threshold is, however, crucial. In fact, this technique relies upon the premise that values of PCT are based on non-raining observations. Therefore a careful balance needs to be met between an area small enough to have a homogeneous meteorological regime, but large enough to provide a representative number of non-raining samples.
Moreover, a study (Kidd 1998) throughout a year over the UK region has pointed out that there are seasonal variations in Θ and threshold values. Calibration studies have shown that the rain/no rain boundary can be set at about 4 ÷ 10K below this value.

Figure 3.25 shows the complete screening procedure over coasts used in the BAMPR algorithm.
The check on the PCT is the first step in the procedure. Further steps concern the discrimination of clear ocean and ice emissivities, and a few tests for light precipitation

identification. As pointed out for previous screenings over ocean and land, also the procedure over coast has been defined after testing the effectiveness of the different checks in the environmental conditions of the present (Europe) BAMPR applications.

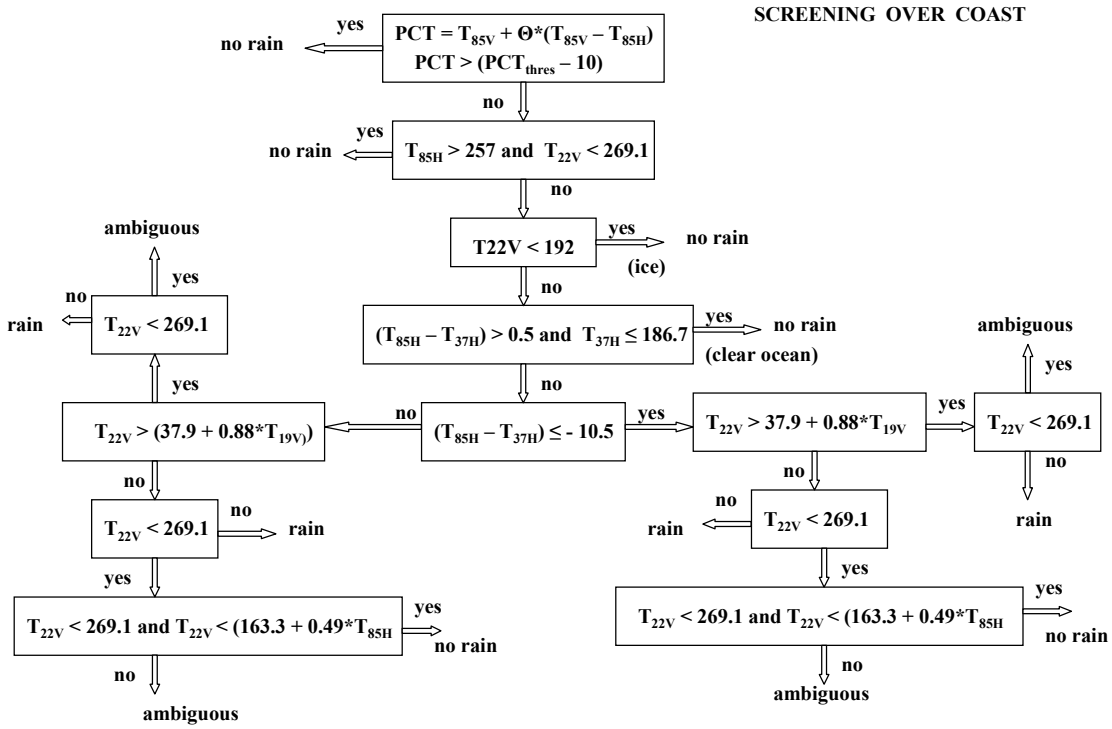

Fig. 3.25 - Screening procedure over coast used in BAMPR algorithm.

3.3 Tests on the screening procedures

An application of the PCT algorithm is presented in this section. A study concerning a disturbance, located on the Balkans, that affected the Calabria region and the Ionian Sea (13 August 2006) has been carried out. A strong thermal gradient was present that triggered a strong mesoscale convection over the South of Italy (fig 3.26). Figures 3.27-3.29 show the experimental Tbs measured at 16:06 UTC by the SSM/I radiometer on board satellite DMSP F-14 of the U.. Defense Meteorological Satellite Program (DMSP). The figures clearly show the thermal variations due to the presence of the disturbance.

The screening problem has been experimentally analyzed in this study, to test the different possible screening criteria (sect. 3.2.2), and find the most suitable procedures for Europe and the Mediterranean Sea (figg.3.19, 3.22, 3.25).

The values of PCT and Θ were obtained using the technique of fig 3.24 (at 85GHz).

The following figures 3.30 and 3.32 show the results obtained.

Figure 3.30 shows the effects of the screening procedure, and the resulting rain/no-rain/ambiguous classification (rain status) of pixels (see figg. 3.19, 3.22, 3.25). The red area corresponds to pixels rejected as corresponding to no-rain situations (their rain status, that is represented in the figure, is labelled with a negative value). The orange pixels correspond to clear rain situations (labelled with 0), and yellow areas correspond to "ambiguous" pixels where the rain is considered probable (labelled with a positive number).

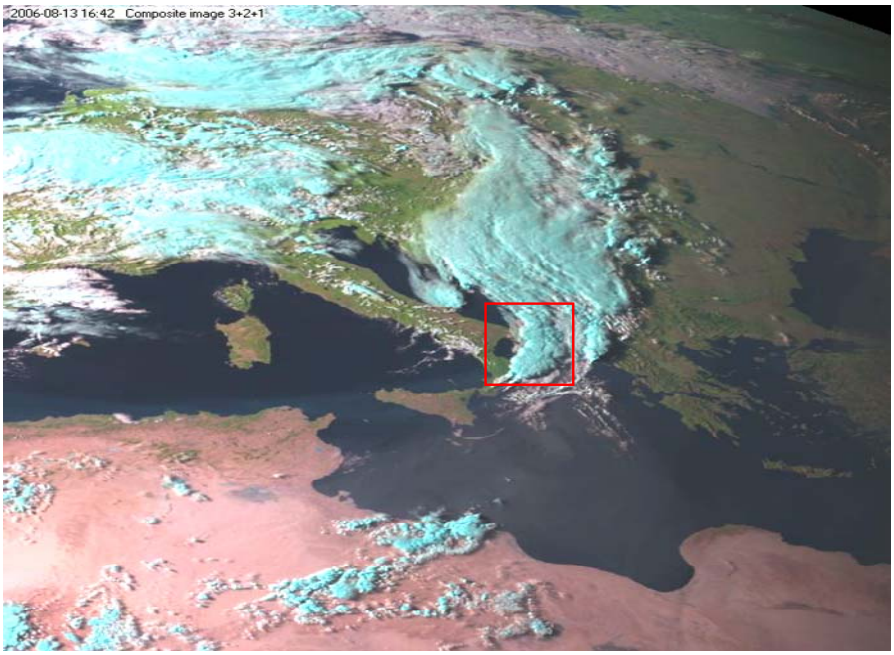

Fig. 3.26 – Case study Calabria, 13 August 2006 h 16:06

The orange and yellow pixels are then accepted and passed to the Bayesian procedure for the comparison with the profiles of CRD, and the retrieval of meteorological variables.
Figure 3.31 shows the direct effect of the application of the PCT. The figure compares the Tb at 85Ghz and the PCT ($\Theta = 0.65819$). It is evident in the figure how the use of PCT reduces the effect of background surface emissivities, unifying the surface brightness temperatures and then making it possible to delineate areas of rainfall over varying surface types.

The result of the screening procedure is shown, in a different way in fig. 3.32. This figure distinguishes the area with no/rain (black area) from the area considered for the retrieval procedure: Moreover, the figure shows the values of Tb at 85 GHz that contribute (with the others channels) to the Bayesian estimation of rain rate.

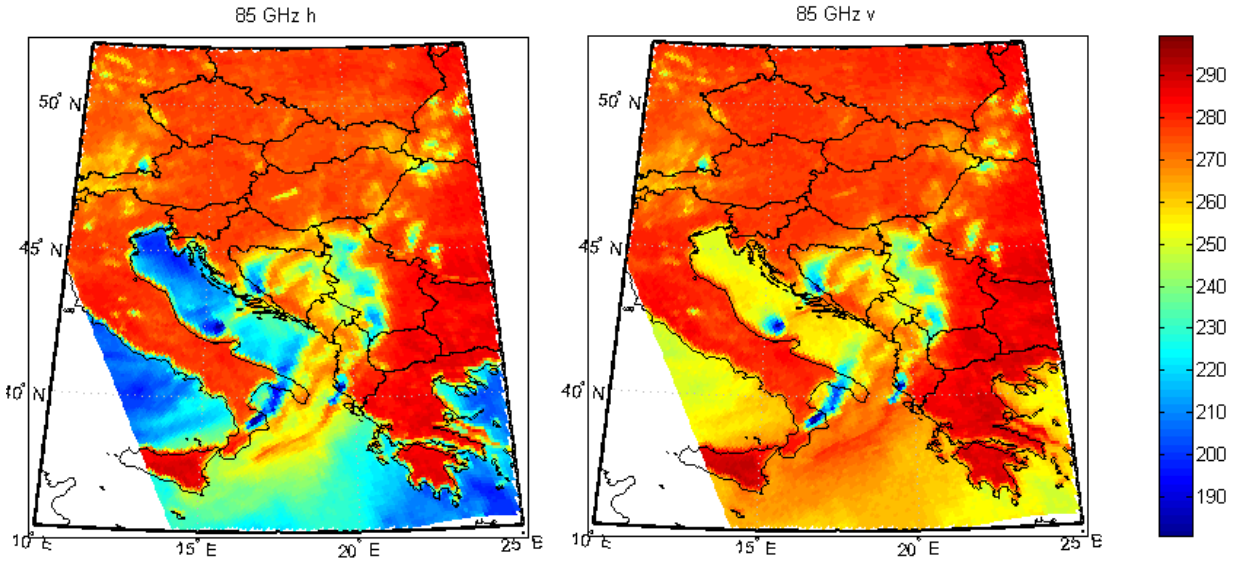

Fig. 3.27 - Case study Calabria, 13 August 2006 h 16:06 (DMSP F-14): SSM/I brightness temperatures (K) at 85 Ghz (H and V).

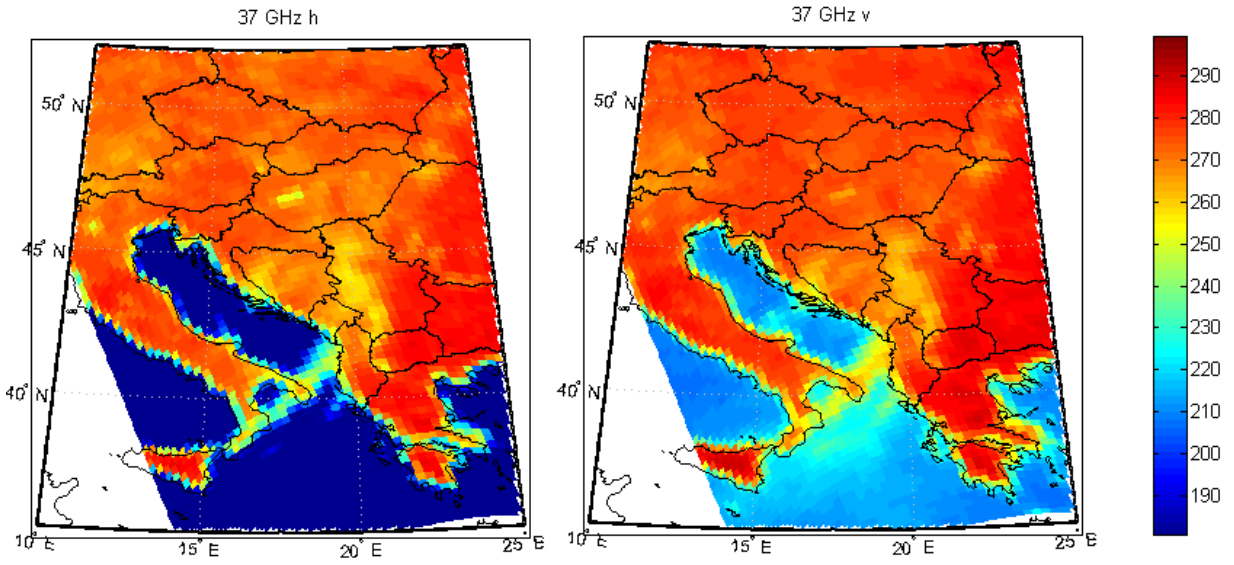

Fig. 3.28 - Case study Calabria, 13 August 2006 h 16:06 (DMSP F-14): SSM/I brightness temperatures (K) at 37 Ghz (H and V).

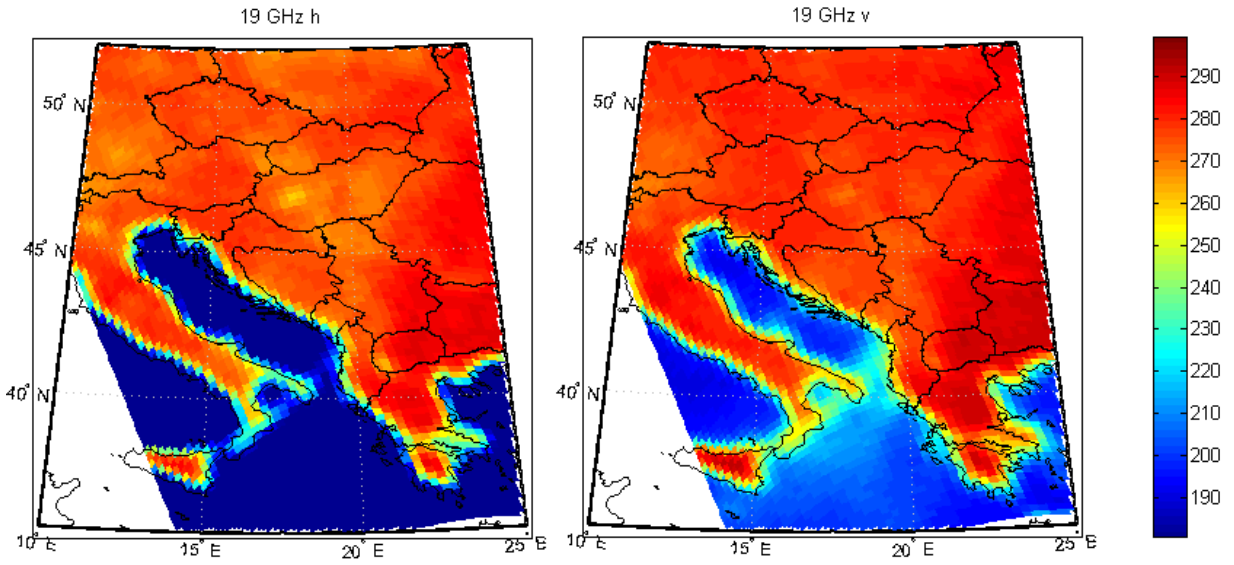

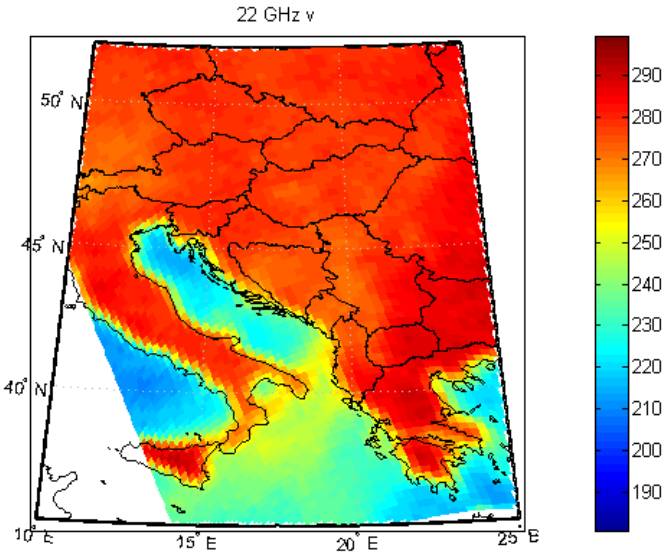

Fig. 3.29 - Case study Calabria, 13 August 2006 h 16:06 (DMSP F-14): SSM/I brightness temperatures (K) at 19 Ghz (H and V) and 22V GHz

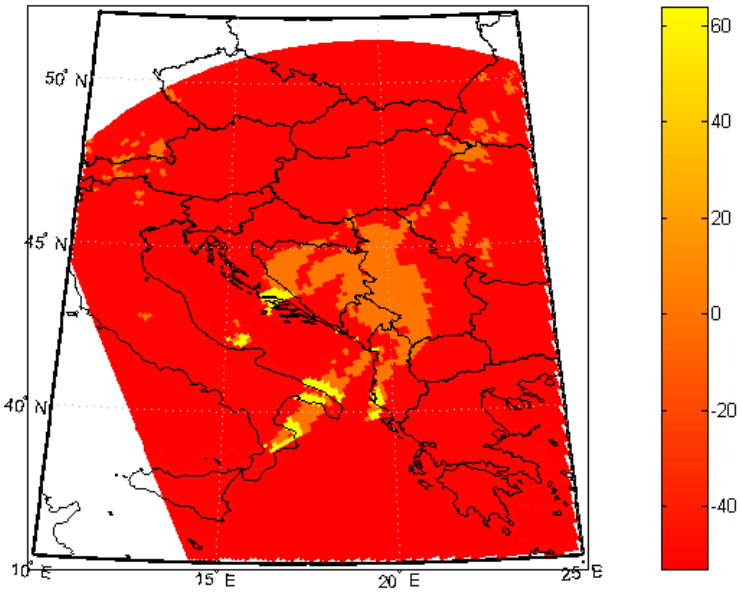

Fig. 3.30 – Case study Calabria, 13 August 2006 h 16:06 (DMSP F-14). Effect of screening procedure, showing the rain/no rain selection of pixel. The red areas correspond to pixels rejected as corresponding to no rain situations (their rain status is labelled with a negative value). The orange pixels correspond to rain situations (labelled with 0), and yellow areas correspond to pixels with probable rain (labelled with a positive number).

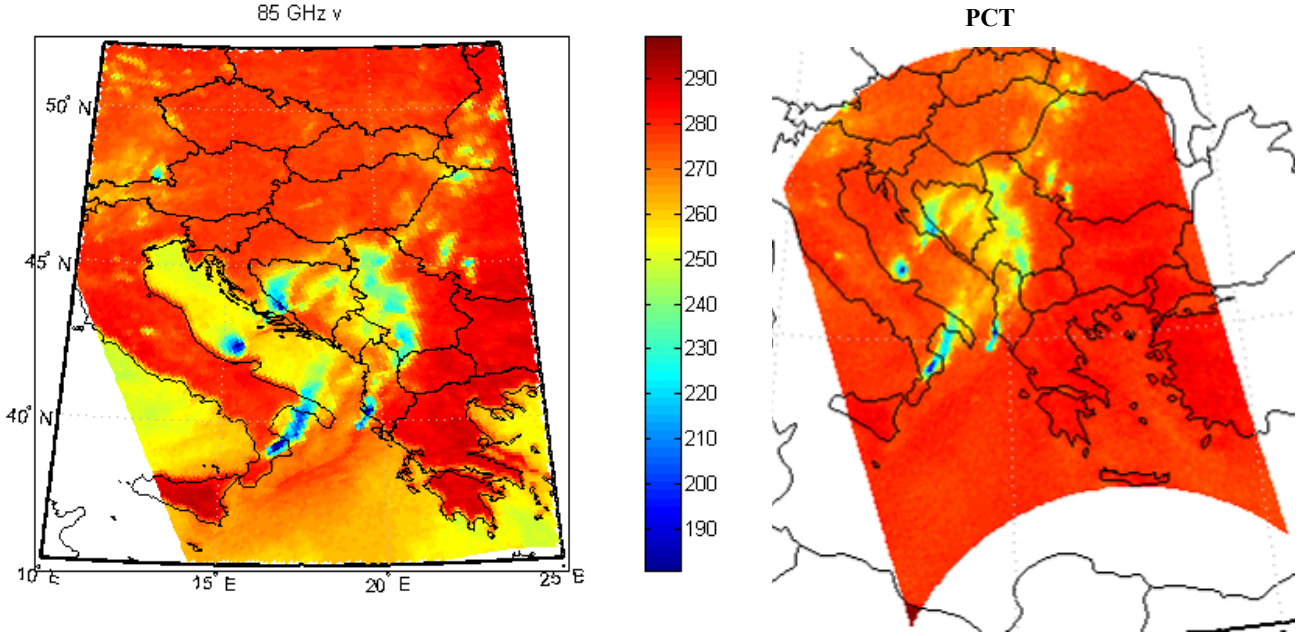

Fig. 3.31 - Case study Calabria, 13 August 2006 h 16:06 (DMSP F-14). Effect of the use of the PCT (right panel) that makes the surface brightness temperatures in no/rain areas uniform.

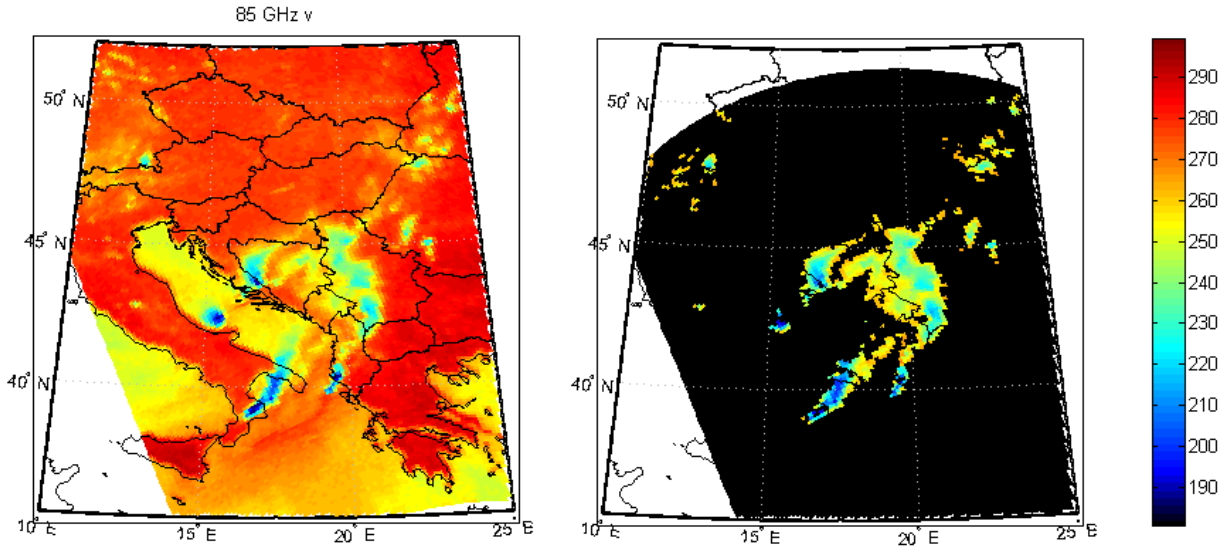

Fig. - 3.32 Case study Calabria, 13 August 2006 h 16:06 (DMSP F-14). Effect of screening procedure, showing the rain/no rain selection of pixel. The left panel shows the Tb (K) at 85 GHz, the right panel points out the pixels rejected (black area). In the right panel the values of Tb at 85 GHz are shown for pixels accepted for the retrieval procedure.

CHAPTER 4 – The use of information on dynamical and thermodynamical structure of the atmosphere

Passive microwave techniques for the estimation of rainfall have advanced considerably over the past years, due largely to an increased understanding of the transfer of microwave radiation through precipitating clouds. Moreover, especially in the last two decades, the large number of satellite missions with an ever-increasing number of sensors have improved the amount of measurements available, and have increased their ground resolution and reliability. Then, a large number of algorithms have been proposed in the literature (Wilheit et al. 1994, E.A. Smith et al. 1998, Kummerow et al. 2000) for retrieving rainfall from passive microwave brightness temperature, based on different approaches and often classified in different classes, as emission-based or scattering-based (Todd and Bailey 1995) or multichannel-inversion-based (Kummerow et al 1996, Shin and Kummerow 2003), as empirical or physical (D.M. Smith et al. 1998). In comparison with this large number of methods, little has been written about the quantitative assessment of the expected uncertainties in these rainfall products. This is certainly related to two factors: sparse validation sites over most of the world's oceans, and algorithm sensitivities to rainfall regimes that cause inconsistencies against validation data collected at different locations. Precipitation, unfortunately, is one of the most difficult atmospheric parameters to measure because of the large variations in space and time. But, there is on the basis the fact that understanding and quantifying the real capability of satellite-based cloud and precipitation observing systems is a complex task. As a consequence, errors are very often only superficially derived, overlooking main error sources, and in some instances no error estimates are given. Validation of these errors too is a complex task, and one that has generally remained elusive. For this reason, various precipitation algorithm intercomparison projects have been conducted in order to assess the state of the art and the degree of accuracy possible with satellite-based methods (E.A. Smith et al. 1998, Conner and Petty 1998, Kummerow et al. 2000, Masunaga et al. 2002). Various analyses have also been carried out on the various possible errors that affect rainfall retrieval (Bauer et al. 2002, Kummerow et al. 2006, Stephens and Kummerow 2007).

In the evaluation of the complete process of retrieval, the sources of possible errors are manifold and distributed along all the steps of the algorithms. The experimental data of the microwave sensor, for example, may be affected by different kinds of errors: large blocks of scans can occasionally be located incorrectly by up to several thousand kilometers (incorrect geolocation); an incorrect antenna temperature for a single pixel can result from telemetry errors. Another error can be present in the data if the rainfall is not homogeneous across the satellite field of view. This is called the "beamfilling" error, and can lead to underestimates in the retrieved precipitation (Kummerow 1998, Kummerow et al. 2004). Fortunately, many experimental errors can be detected and corrected, or it can be proven that their effect on the retrieval is not relevant. On the contrary, the approximations in the forward model can be important sources of error in the retrieval procedure. They can be responsible for the non-uniqueness of the CRD. This means that even if the database includes a full spectrum of possible cloud/precipitation profiles, the radiometer observations may be compatible with several different profiles, and so the actual profile may not be uniquely identified. For this reason, current research activities on the algorithm consider that the utilization of further information on the state of the atmosphere, in addition to brightness temperatures, can

represent a suitable constraint in the selection of profiles of CRD, and can consequently reduce retrieval uncertainties (Hoch 2006, Hoch et al. 2006).
In this chapter, the problem of uncertainties in retrieval is analyzed, and some preliminary results are presented from a new Bayesian approach, which uses new dynamical and thermodynamical variables in order to reduce the ambiguity in the retrieval procedure.
The chapter is organized as follows. Section 4.1 describes a mathematical tool for the evaluation of uncertainties in retrieval. In particular, it allows the estimation of the contribution of the CRD to the overall uncertainty. Section 4.2 presents new possible dynamical and thermodynamical variables that can be combined with the brightness temperatures in retrieval. Section 4.3 delineates the main elements of the new BAMPR algorithm, that include the use of the dynamical and thermodynamical variables, and that we are at present developing. Section 4.4 presents the application of the new BAMPR to some disturbances over Italy, and gives some evaluations of the effects of the new variables on retrieval. Section 4.5 presents the results of a comparison of the new BAMPR with the "NESDIS" algorithm of NOAA.

4.1 The uncertainties in the forward-inverse problems

The retrieval uncertainties associated with the forward-inverse systems presented in chapter 3, depend on various sources of error, They can derive from the experimental measurements and the approximations in the forward model (cloud and radiative transfer) and in the model parameters, in the inversion parameters and in the "a priori knowledge" used in the systems.
An "error model", proposed by L'Ecuyer and Stephens (2002), provides a mathematical tool for the evaluation of the contribution to retrieval uncertainties of the database (CRD) structure, and the measurements and model approximations. Starting from the equations 3.3.21 and 3.3.22, the following simplified expression can be written

$$\hat{g}_{MMS} = \frac{\sum_j g_j W_j^{'}}{\sum_j W_j^{'}} \tag{4.1}$$

where the index i is omitted and the "weight" $W_j^{'}$ has the expression

$$W_j^{'} = \exp(-0.5(t(g_j) - t_m)^T C_{\varepsilon t}^{-1}(t(g_j) - t_m)\,. \tag{4.2}$$

$\hat{g}_{MMS}$ is then composed of two distinct quantities, the profile sample g_j of the CRD and the weight $W_j^{'}$. If we can estimate the uncertainties associated with these quantities, the uncertainty in the product $g_j W_j^{'}$ can be evaluated using the standard error combination theory

$$\delta(g_j W_j^{'}) = \left[(W_j^{'}\delta g_j)^2 + (g_j \delta W_j^{'})^2 + g_j W_j^{'} \delta_{g_j W_j^{'}}\right]^{1/2}$$

where $\delta_{g_j W_j^{'}}$ is the estimated error covariance of g_j and $W_j^{'}$. Similarly, the uncertainty associated with the summation of j such products is

$$\delta\left(\sum_j g_j W_j^{'}\right) = \left(\sum_j ((W_j^{'}\delta g_j)^2 + (g_j \delta W_j^{'})^2 + g_j W_j^{'} \delta_{g_j W_j^{'}}) + \sum_{j=1}^{j_M - 1} \sum_{k=j+1}^{j_M} \delta_{jk}\right)^{1/2}$$

where δ_{jk} represents the error covariance of $(g_j W_j^{'})$ and $(g_k W_k^{'})$, and j_M is the total number of profiles (NP) in summation (4.1). Finally, the uncertainty associated with the denominator of equation (4.1) is

$$\delta\left(\sum_j W_j^{'}\right) = \left(\sum_j (\delta W_j^{'})^2 + \sum_{j=1}^{j_M-1}\sum_{k=j+1}^{j_M} \delta_{W_j^{'}W_k^{'}}\right)^{1/2}$$

where $\delta_{W_j^{'}W_k^{'}}$ is the error covariance of weights $W_j^{'}$ and $W_k^{'}$.

The overall uncertainty in $\hat{g}_{MMS}$ is, therefore

$$\frac{\delta\hat{g}_{MMS}}{\hat{g}_{MMS}} = \left(\frac{\sum_j \left[(W_j^{'}\delta g_j)^2 + (g_j \delta W_j^{'})^2 + g_j W_j^{'} \delta_{g_j W_j}\right] + \sum_{j=1}^{j_M-1}\sum_{k=j+1}^{j_M}\delta_{jk}}{\left(\sum_j g_j W_j^{'}\right)^2} + \right.$$

$$\left. + \frac{\sum_j (\delta W_j^{'})^2 + \sum_{j=1}^{j_M-1}\sum_{k=j+1}^{j_M}\delta_{W_j^{'}W_k^{'}}}{\left(\sum_j W_j^{'}\right)^2} - \frac{\delta_{nd}}{\left(\sum_j g_j W_j^{'}\right)\left(\sum_j W_j^{'}\right)} \right)^{1/2}$$

where δ_{nd} is the correlation in errors between the numerator and the denominator. Due to the complexity of this formula, it is convenient to use a simpler expression, assuming that all the uncertainties are uncorrelated (that is $\delta_{nd} = \delta_{W_j W_k} = \delta_{g_j W_j} = \delta_{jk} = 0$). The result is

$$\frac{\delta\hat{g}_{MMS}}{\hat{g}_{MMS}} = \left(\frac{\sum_j \left[(W_j^{'}\delta g_j)^2 + (g_j \delta W_j^{'})^2\right]}{\left(\sum_j g_j W_j^{'}\right)^2} + \frac{\sum_j (\delta W_j^{'})^2}{\left(\sum_j W_j^{'}\right)^2} \right)^{1/2} \qquad (4.3)$$

which represents a first-order approximation to the overall uncertainty in $\hat{g}_{MMS}$.

The last equation demonstrates that the overall uncertainty in the retrieval consists of two factors. The first component,

$$\frac{\sum_j (g_j \delta W_j^{'})^2}{\left(\sum_j g_j W_j^{'}\right)^2} + \frac{\sum_j (\delta W_j^{'})^2}{\left(\sum_j W_j^{'}\right)^2} \qquad (4.4)$$

derives from uncertainty in computing the weights assigned to each profile, while the second

$$\frac{\sum_j (W_j' \delta g_j)^2}{\left(\sum_j g_j W_j'\right)^2} \tag{4.5}$$

accounts for the impact of the finite cloud database. Equation (4.3) allows the determination of the dominant source of uncertainty in the retrieval.

Considering the expression (4.2) of W_j, the fractional uncertainty in W_j results as

$$\frac{\delta W_j'}{W_j'} = \sqrt{\left[t(g_j) - t_m\right]^T C^{-1} \left[t(g_j) - t_m\right]}$$

This takes into account the errors of both the measurements and the models used for the simulated profiles (forward problem).

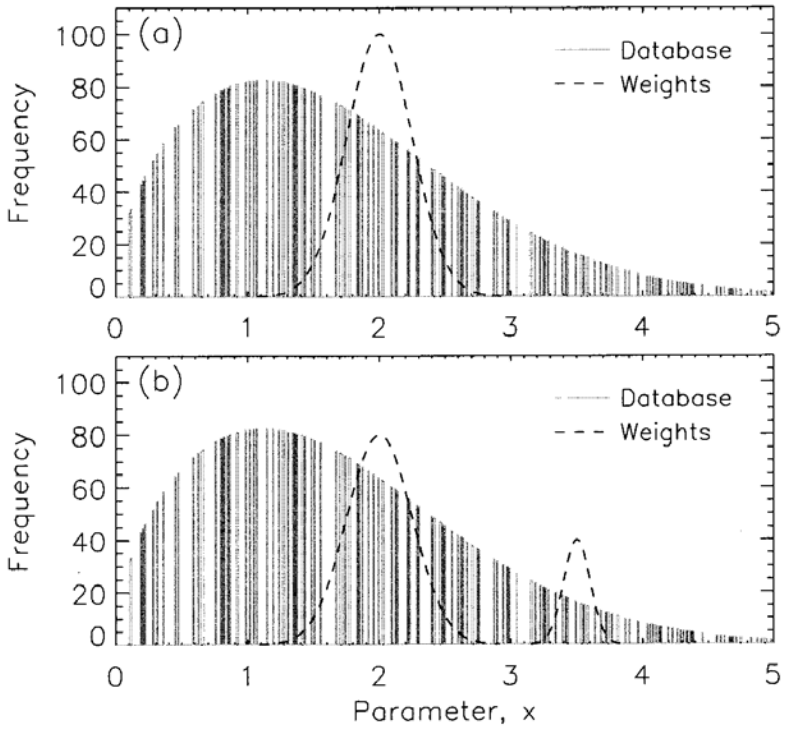

Fig. 4.1 - Graphical representation of two different situations in the retrieval process. Panel (a) illustrates a case where all profiles are uniquely identified by their measurement (Tbs) signatures; panel (b) illustrates the problem of non-uniqueness. On the x axis a hypothetical parameter (for example surface rain rate) is represented (L'Ecuyer and Stephens 2002).

In order to analyze the database uncertainty, resulting from formula (4.5), let us consider that each profile in the database is a point in the multidimensional space defined by the Tbs. The retrieval algorithm proceeds by finding the point in this multi-dimensional space which most closely corresponds to the observations and assigns the largest weight to that parameter

(hydrometeor or rain rate). All parameters are utilized with the appropriate weights to produce the retrieved value. Figure 4.1 graphically represents this process, from a theoretical point of view, for a hypothetical parameter x (for example rain rate). The histogram represents the distribution of profile frequencies, in a hypothetical database, as a function of the value of the parameter x. In the figure there are also dashed curves, which represent the weights (in case of Gaussian distribution of weights) assigned to parameters based on a particular set of measurements. Two distinct cases emerge. Figure 4.1(a) corresponds to the case where the profiles in the database contribute to the retrieval with a unique set of measurements. In this case, x varies only moderately over the range of simulated measurements for which the weights are significant. As a result, the measurements drive the retrieval towards the correct result. Figure 4.1 (b) displays a scenario where significantly different values of x yield similar simulated measurements. Under these circumstances, the shape of the database is critical in determining the total weight assigned to each parameter. The main issue regarding the 'completeness' (sect. 3.1.3) of the database is, therefore, one of non-uniqueness. Formula (4.5) gives an evaluation of the non-uniqueness contribution to the uncertainty.
A relevant point of this mathematical procedure is the possibility of separating the database contribution, indicating its weight on the overall uncertainty.
In spite of the theoretical approach of the method, an application to the Goddard Profilig Algorithm (GPROF) (Kummerow and Giglio 1994b) was carried out by L'Ecuyer and Stephens (2002).
An important result of this application is that, in rain rate retrieval, database uncertainty contributed for more than 50% of the total, for rain rate below 4 mm/h. A large number of profiles were indistinguishable from one another through the brightness temperatures alone, particularly in conditions characterized by light rainfall.

Indeed, the non-uniqueness of the database, also referred to as "ambiguity" (Tassa et al. 2006, Bauer 2001), is a severe limit for retrieval methodology. The problem is that a non unique relationship exists between Tbs and precipitation parameters. Different profiles can generate similar Tb vectors that cannot be distinguished as long as they remain within the resolution distance from the experimental Tb.
Fig 4.2 shows an example of this problem in the CRD implemented at CNR ISAC, which was described in chapter 3.
Starting from the plot of the relation between the Tb at 91 GHz and the Tb at 150GHz (top left in the figure), a detail is enlarged showing the corresponding values of rain rate. It is evident from the figure that many different values of rain rate are concentrated in small areas in the Tb space. Another example concerning this problem is shown in fig. 4.3, where four panels present the distribution of rain rate, ice rate, columnar liquid water content and columnar ice water content values in the CRD, for the Tb at 150 GHz. Also in this example, many values of the four variables correspond to the same value (i.e. 250K in the figure) of Tb.

A detailed analysis of this problem, and in general of the main sources of uncertainties present in many retrieval methodologies, has been performed by Stephens and Kummerow (2007) using the schematic diagram of the "satellite observing system" shown in fig. 4.4.
The figure identifies the main component of the observing system transfer function that determines the relationship between a given input of the system and the desired output of the system. In the figure, x(r,t) is the input signal (cloud or precipitation parameters) to the system

(r is the spatial coordinate and t the time), y(r,t) is the measured quantity (brightness temperatures for example), and $\hat{x}(r,t)$ is the output/retrieved signal (that is cloud and precipitation parameters of the observed atmosphere). In an ideal situation when the system is operated correctly, $\hat{x}(r,t)$ reproduces exactly x(r,t).

In the real situation the uncertainties associated with the forward-inverse system cause the differences between the two signals.

In the figure, F(x,b) represents the real (correct) forward model, and b are the parameters that defines this model; $f(\hat{x},\hat{b})$ is the approximate model used in the retrieval process, and $\hat{b}$ represents the approximate values of b; x_a (with the error ε_a) and c represent other inputs to the system (a priori information about the "state" of the system, for example).

The output signal of the system (physical parameters retrieved, as cloud and precipitation parameters) is obtained from the inversion process utilizing the approximate forward function $f(\hat{x},\hat{b})$

$$\hat{x} = I(f(\hat{x},\hat{b}), x_a, c, \ldots)$$

and is therefore affected by all the approximations and errors mentioned. In fact, it is in this part of the system that several sources of uncertainty get into the process, producing the total error of the system.

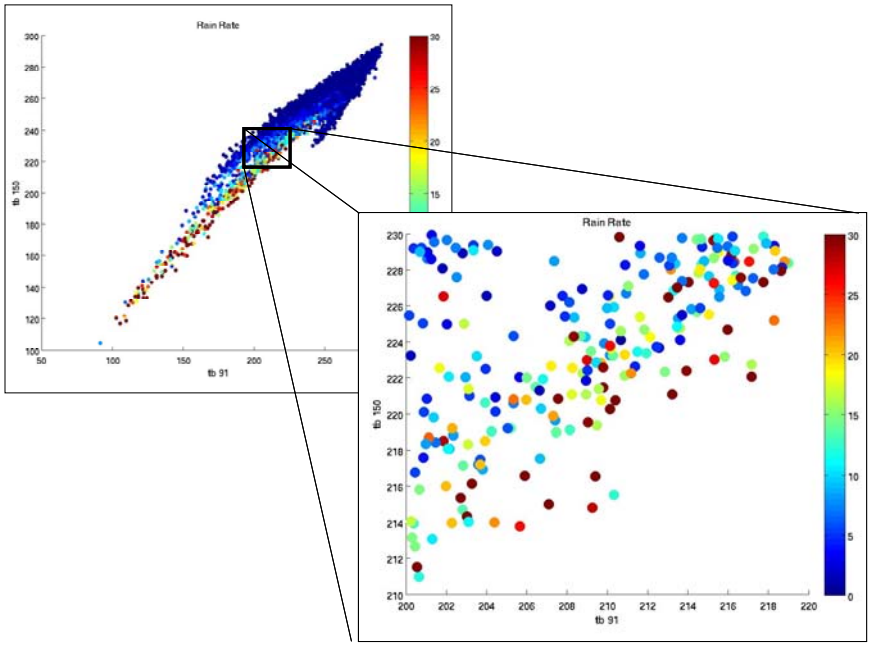

Fig. 4.2 - Relation between Tbs at 91 and 150 GHz (top left) in the CRD, and detail of the plot showing rain rate values (mm/h).

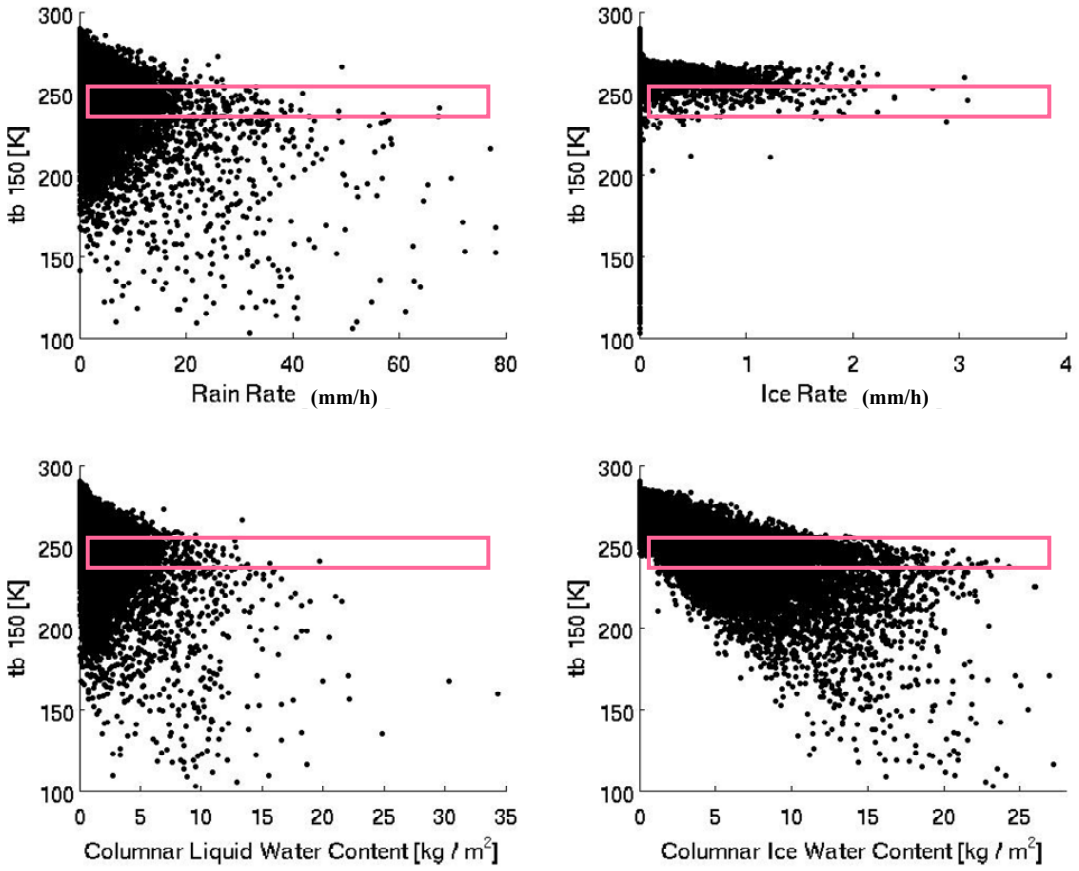

Fig. 4.3 - Plot of the values of rain rate, ice rate, columnar liquid water content and columnar ice water content as a function of TB 150 GHz in the database (CRD). Different values corresponding to 250K are highlighted.

An evaluation of the contribution of the different uncertainties to the output signal, carried out by Stephens and Kummerow (2007), has pointed out the important role of the atmosphere model. In fact, while the measurement error ε_y associated with y due to instrument factors, including calibration uncertainties, is usually minor compared to all others, the approximations in the function $f(\hat{x}, \hat{b})$ (due to simplified atmosphere models) and in the approximate parameters $\hat{b}$ (due to the uncertainties associated, for example, with microphysical properties of particles, such as shape, size, concentrations, etc.), represent one of the most significant source of errors of the entire inversion process. This fact affects the quality of the CRD and is the cause of its ambiguity.

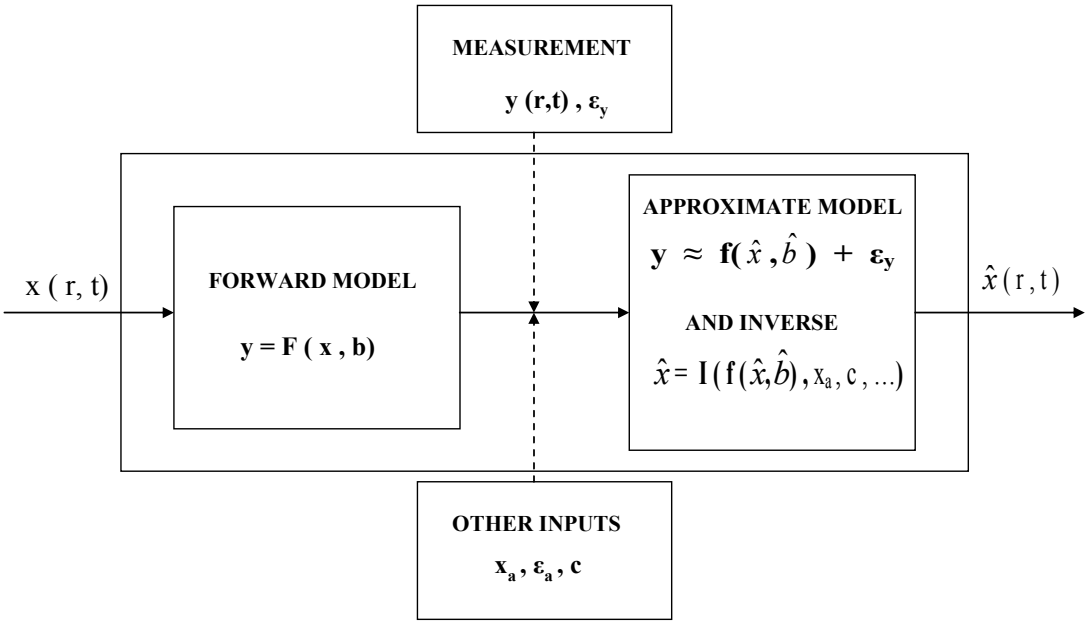

Fig. 4.4 – Schematic representation of the transfer function of a satellite observing system. x(r,t) and $\hat{x}$ (r,t) represent respectively the input and the output of the system; F(x,b) is the (physical) forward model of the system and f($\hat{x}$, $\hat{b}$) the approximate forward model; y(r,t) is the measured quantity (radiance) and x_a and c are other inputs (Stephens 2007).

4.2 From CRD to CDRD

As mentioned in previous section, a problem with CRD based retrieval systems is that hydrometeor profiles obtained as result of the retrieval algorithm are, in some cases, unrepresentative of the dynamical and thermodynamical state of the atmosphere under observation. This is a consequence of the fact that often various configurations of hydrometeors can produce similar brightness temperatures. And this is, after all, a result of the approximations contained in the model used to describe the atmosphere, the cloud and precipitation structure embedded in that atmosphere, and the radiative transfer (forward problem).

Clearly, a better definition of the atmospheric state, and the vertical structure of clouds and precipitation, will improve the information extracted from satellite observations.

Therefore, despite some reasonable success with the CRD and the Bayesian approach, there is a considerable reservoir of potential information available that is not usually tapped. This ancillary information exists in the knowledge of the "synoptic situation" of the considered event and the geographical and temporal location of the event. This knowledge renders some entries into the CRD more relevant than others by virtue of how similar the circumstances of the simulated event are to those of the event for which the database is applied. This

information can be captured in the form of "dynamical tags" which can be used to link a satellite-observed event to a subset of the entire CRD using an independent estimate of these tags always available from short-term model forecast products, such as the Global Forecasting System (GFS) model of the National Oceanic and Atmospheric Administration (NOAA). Here the term "dynamical tags" actually refers not only to ancillary dynamics information such as geostrophic forcing or frontal lifting, but also thermodynamic and geographical information. To accomplish this, the CRD must be expanded to include these "dynamical tags". The expanded CRD is called the Cloud Dynamics and Radiation Database (CDRD) (Mugnai et al. 2006c, Mugnai et al. 2007c, Hoch 2006, Hoch et al 2006, Sanò et al. 2007, Casella et al. 2009). Presently we are testing a new passive microwave precipitation retrieval algorithm which employs these tags, and that we denote as the "new BAMPR" algorithm.

4.2.1 The dynamical tags

As previously mentioned, the utilization of further knowledge of the state of the atmosphere, in addition to brightness temperatures, can represent further constraints in the selection of profiles of CRD, and can consequently reduce the retrieval uncertainties.

Different dynamical and thermodynamical parameters (dynamical tags) can contribute to this purpose and are currently under test at CNR ISAC.

A first group of tags, we have selected to be included in the CDRD, is composed by:

Surface Height (m)
Freezing Level (m)
Vertical Moisture Flux at 50 mb AGL (Above the Ground Level) ($g*m^{-2}*s^{-1}$)
Vertical Wind velocity at 700 mb (Omega) (Pa/s)
Convective Available Potential Energy (CAPE) (J/kg)
Wind Shear at 300 mb (s^{-1})

Surface height (m) is certainly an important parameter when the orography has a relevant influence on cloud dynamics and leads to the formation of orographic precipitation. The topography has an important role in convection triggering. When a flow advances toward a mountain it is forced to rise over the mountain and the air parcels can reach the free convection level. During the warm season, solar warming concurs to the destabilization of the atmosphere and the topography enhances this effect, so the greater portion of summer convection occurs over mountainous regions.

Freezing level (m), or *0°C (zero-degree) isotherm*, represents the altitude in which the temperature is at 0°C in a free atmosphere. The profile of this level, and its variations, are important parameters in meteorological evaluations. In fact, it is an important element in determining the part of a water column consisting of liquid water and the part consisting of ice. It is also a climatologic parameter that, together with the surface temperature, can guide a preliminary rough selection of profiles in the database in terms of season and latitude of the event. This role of the freezing level is, in fact, already utilized in retrieval algorithms (Kummerow and Giglio 1994b, Kummerow et al. 2001).

Vertical Moisture Flux at 50 mb AGL (Above the Ground Level) ($g*m^{-2}*s^{-1}$) is the vertical flux of surface moisture due to atmospheric turbulent transport. It is very often connected with

precipitation. Moisture is a necessary ingredient for the production of clouds and precipitation. In fact, no amount of rising air will produce precipitation unless moisture is present. The more moisture that is present, the higher the potential is for precipitation if uplift mechanisms are in place. In order for thunderstorms to occur, there must be moisture in the low levels of the troposphere (between the surface and 700 millibars).

Vertical Wind velocity at 700 mb (Omega) (ω=dp/dt (Pa/s)). The combined utilization of this parameter with the vertical moisture flux near the surface can characterize areas of precipitation. At mid-latitudes, there is a high probability of rain in the areas with a strong vertical flux at 700 mb and enough moisture at low level. High values of moisture flux will increase this probability.

The *Convective Available Potential Energy (CAPE, J/kg*) at the surface is closely connected to the intensity of vertical motions. It is a measure of the amount of energy available for convection, and in fact, it is directly related to the maximum potential vertical speed within an updraft.
The potential energy is given by the buoyancy of a parcel warmer than the environment.
The expression of CAPE can be obtained starting from the vertical momentum equation (Holton 1979) in the simplified form

$$w\frac{\partial w}{\partial z} = \frac{-\rho'}{\rho_0} g \qquad (4.6)$$

where w is the vertical velocity of an isolated parcel of atmosphere dV

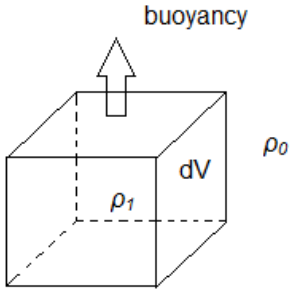

ρ_0 is the density of the environment, ρ_1 is the density of the parcel and $\rho' = \rho_1 - \rho_0$.
Integrating the (4.6), an equation for the profile of the vertical component of the specific kinetic energy is obtained

$$\frac{w^2}{2} = \int_0^z \frac{-\rho'}{\rho} \cdot g \cdot dz \qquad (4.7)$$

It can be thought of as an upper bound (because it neglects potentially dissipative forces (viscosity), adverse pressure gradients and the entrainment of less vigorous air) on the energy a parcel achieves when displaced from rest to some height z.
Using the moist equation of state ($p = \rho \cdot R_d \cdot T_v$), small perturbations in the density can be related to perturbations in the virtual temperature T_v (T_v of a moist air parcel is the temperature at which a theoretical dry air parcel would have a total pressure and density equal to the moist parcel of air):

$$\frac{p'}{p} = \frac{\rho'}{\rho} + \frac{T_v'}{T_v}$$

and assuming that pressure perturbations are negligible ($p' \approx 0$)

$$\frac{\rho'}{\rho} = -\frac{T_v'}{T_v}$$

Then
$$CAPE = \int_{zf}^{zn} g \cdot \left(\frac{T_{v-parcel} - T_{v-envir}}{T_{v-envir}} \right) \cdot dz \qquad (4.8)$$

where zf and zn are, respectively, the heights of the level of free convection and equilibrium (neutral buoyancy). $T_{v\text{-}parcel}$ is the virtual temperature of the specific parcel, $T_{v\text{-}envir}$ is the virtual temperature of the environment, and g is acceleration due to gravity.
If convection starts, this potential energy will be converted to kinetic one as vertical wind.
Using the CAPE the maximum theoretical vertical velocity and the intensity of the storm can be estimated. The upper bond on the maximum vertical velocity of a buoyant parcel is

$$w_{\max} = 2 \cdot \sqrt{CAPE}$$

In particular, high values of vertical velocities are correlated to hailstorm because of mechanical sustentation of heavy hailstones in the cloud by the strong updraft.
Higher values of CAPE indicate greater potential for instabilities and severe weather:

CAPE value	Convective potential
0	Stable
0-1000	Marginally unstable
1000-2500	Moderately unstable
2500-3500	Very unstable
> 3500	Extremely unstable

Wind shear (s^{-1}) is a difference in wind speed and direction over a relatively short distance in the atmosphere. Wind shear can be broken down into vertical and horizontal components. It is an important parameter in the presence of fronts and tornadoes and it is a key factor in the creation of severe thunderstorms and in the development of big convective structures such as multicell systems and supercells (Houze 1993). The mechanism of self sustainment of a complex storm is shown in figure 4.5. The heavy rainfall generates a cold core in the cloud that falls down violently and when the downdraft impacts with the ground, the cold air expands horizontally in a sort of small cold front (gust front). If the wind shear is in a favourable configuration, strong forced updrafts occur in some points of the gust front. In these points new cumulus clouds develop generating new storm cells and the process starts again.

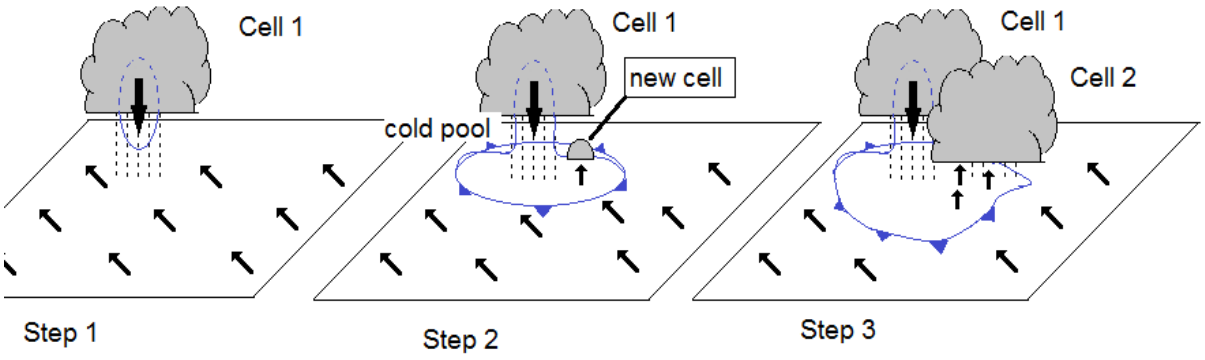

Fig. 4.5 - Schematics of a multicell storm. The small arrows represent low level winds. The cold air falling down is depicted in blue. The convergence of ambient wind with a gust front generated by the cold pool generates new cells.

4.2.2 The dynamical tags in the CDRD

The inclusion of the dynamical tags in the CDRD has required a preliminary test on the consistency of the methodologies for the production of tags used by the UW-NMS and the GFS models. To perform this test, the tags corresponding to all the events simulated in the CRD (section 3.1.3), produced from both models, were compared. Figures 4.6 - 4.10 show some results of this analysis. Figures 4.6 and 4.7 present the scatterplots of *freezing level* and *vertical moisture flux at 50 mb AGL* values, obtained from UW-NMS (vertical axis) and GFS (horizontal axis) models. Figure 4.8 shows the similar scatterplot for *vertical wind velocity at 700 hPa (Omega).* Apart from some minor statistical differences, the figures point out a good consistency between the two models. Figures 4.9 and 4.10 present the resulting pdf's for *vertical moisture flux at 50 mb AGL* and *vertical wind velocity at 700 mb*, corresponding to the UW-NMS (black line) and GFS (red line) results. These figures also point out a quite good agreement between the two models.

4.3 The new BAMPR

4.3.1 The new Bayesian distance

Some changes to the algorithm are necessary in order to follow the new structure of the database.

A new vector $\mathbf{t}_g$, having the tag values as components, is inserted in the Bayesian retrieval procedure. Since the tags and brightness temperatures errors can be considered statistically independent, the conditional a posteriori pdf (3.3.9) can be expressed as follows (Marzano et al. 1999)

$$p(\mathbf{g}|\mathbf{t}_m,\mathbf{t}_g) = \frac{p(\mathbf{t}_m \mid \mathbf{g})\,p(\mathbf{t}_g \mid \mathbf{g})\,p(\mathbf{g})}{p(\mathbf{t}_m,\mathbf{t}_g)}$$

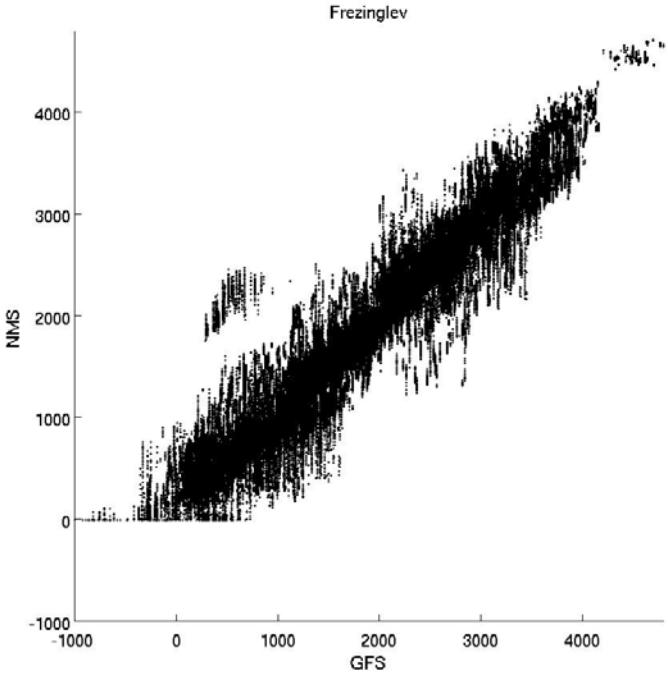

Fig. 4.6 - Scatterplot of *freezing level* values (m), for the CDRD simulated events (sect. 3.1.3), obtained from UW-NMS (vertical axis) and GFS (horizontal axis) models.

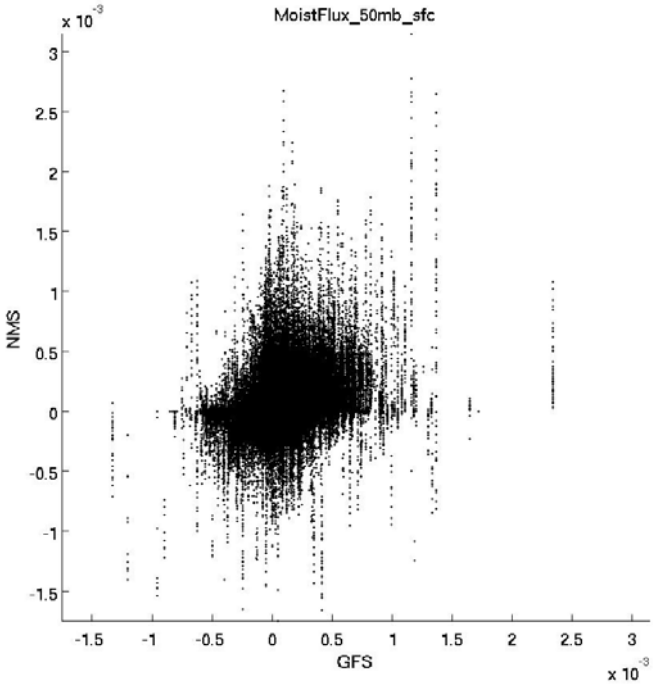

Fig. 4.7 - Scatterplot of *vertical moisture flux at 50 mb AGL* values ($g*m^{-2}*s^{-1}$), for the CDRD simulated events (sect. 3.1.3), obtained from UW-NMS (vertical axis) and GFS (horizontal axis) models.

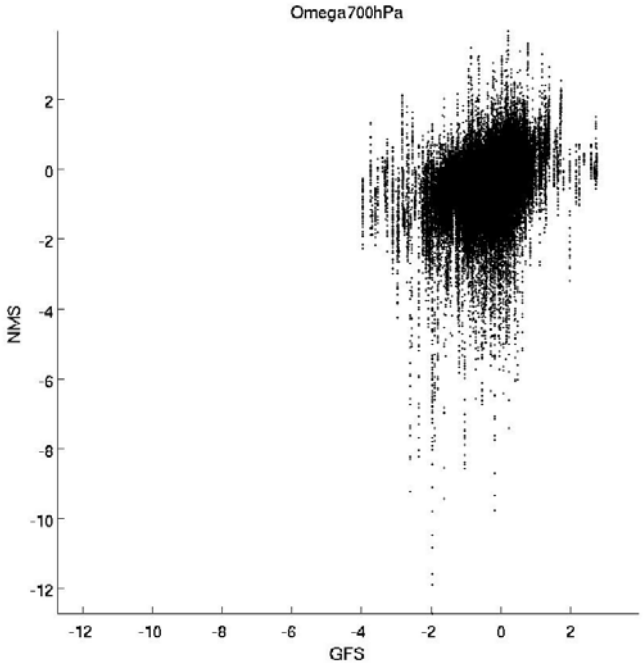

Fig. 4.8 - Scatterplot of *vertical wind velocity at 700 hPa (Omega)* values (Pa/s), for the CDRD simulated events (sect. 3.1.3), obtained from UW-NMS (vertical axis) and GFS (horizontal axis) models.

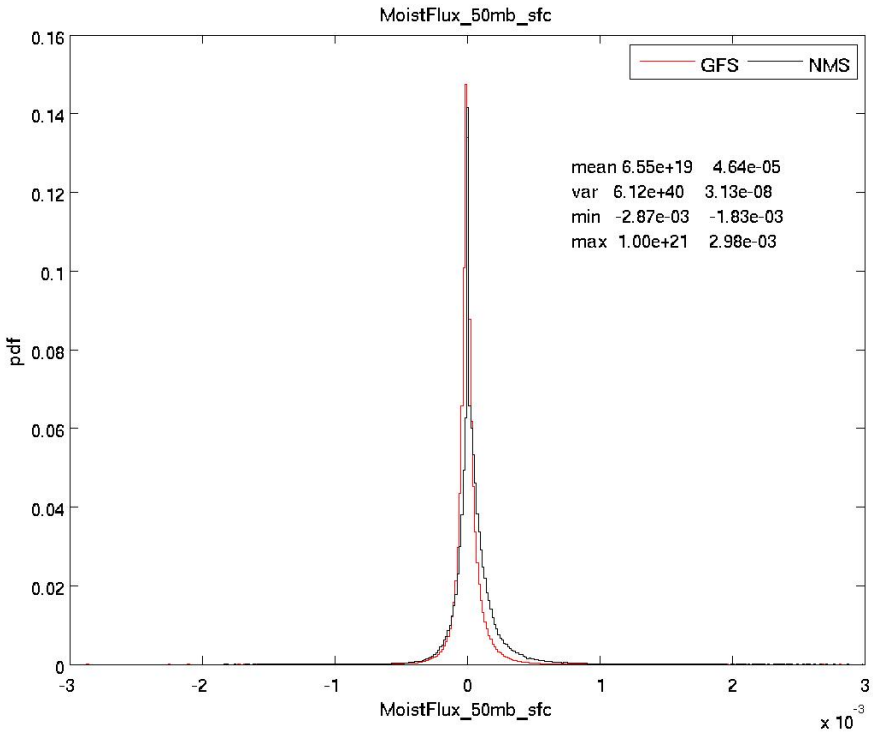

Fig. 4.9 - Pdf of *vertical moisture flux at 50 mb AGL* ($g*m^{-2}*s^{-1}$) for the CDRD simulated events (sect. 3.1.3), obtained from UW-NMS (black line) and GFS (red line) models.

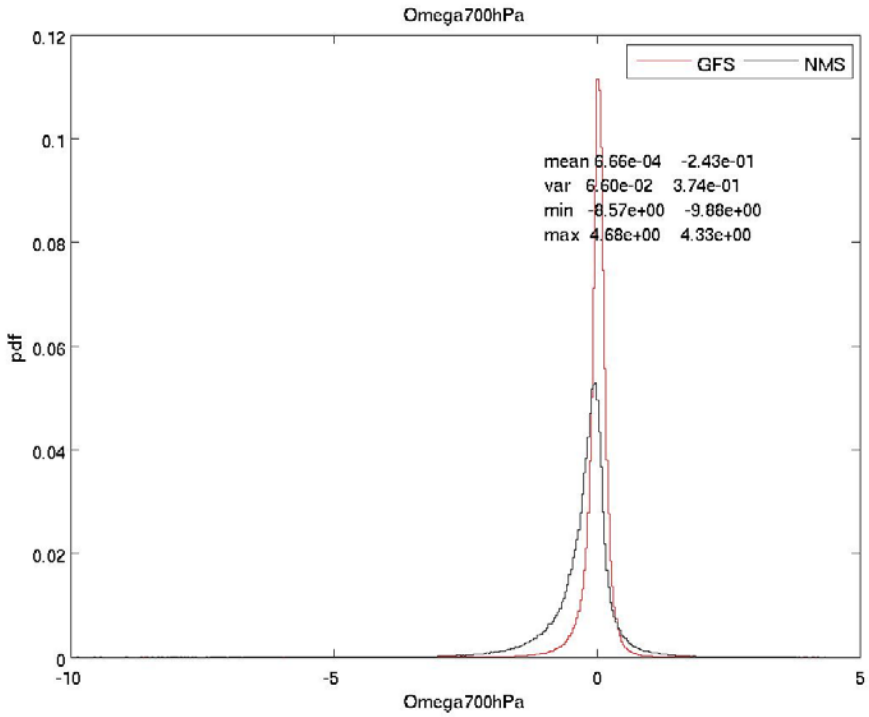

Fig. 4.10 - Pdf of *vertical wind velocity at 700 mb (Omega)* (Pa/s), for the CDRD simulated events (sect. 3.1.3), obtained from UW-NMS (black line) and GFS (red line) models.

Therefore a new distance, among tags (measured and simulated), must be evaluated. In fact, the selection of profiles from the new database (CDRD) needs, in addition to the check on the distance among the brightness temperatures, also a check on the distance among the dynamical tags.
The Bayesian distance among the tags is given by

$$dtag(\mathbf{g}_i) = \left[\left(\frac{\mathbf{t}_g(\mathbf{g}_i)}{\boldsymbol{\sigma}_{td}} - \frac{\mathbf{t}_{gm}}{\boldsymbol{\sigma}_{tm}} \right)^T \cdot \mathbf{C}_{etag}^{-1} \cdot \left(\frac{\mathbf{t}_g(\mathbf{g}_i)}{\boldsymbol{\sigma}_{td}} - \frac{\mathbf{t}_{gm}}{\boldsymbol{\sigma}_{tm}} \right) \right] \cdot \mathbf{p}$$

where $\mathbf{t_g}(\mathbf{g}_i)$ and $\mathbf{t_{gm}}$ represent the tag vectors of the profile $\mathbf{g}_i$ selected in the database and of the experimental tags, respectively; $\boldsymbol{\sigma}_{td}$ and $\boldsymbol{\sigma}_{tm}$ represent the standard deviation vectors of $\mathbf{t_g}(\mathbf{g}_i)$ and $\mathbf{t_{gm}}$, respectively; $\mathbf{p}$ is the weight vector of the tags. Due to the different physical dimensions of tags, the dimensionless variable tag/σ is used.
Taking into account the Bayesian distance (d2tb) defined for the Tbs (3.3.24), the resulting distance between the experimental data and the data of the selected profile ($\mathbf{g}_i$) in the database is

$$\text{dist}(\mathbf{g}_i) = \text{d2tb}(\mathbf{g}_i) + \text{dtag}(\mathbf{g}_i).$$

Only the profiles of the database with dist<dthre (dthre is an a-priori fixed threshold) are considered for the Bayesian retrieval of surface rain rate and the other cloud parameters.

4.3.2 The new retrieval system

The retrieval methodology described in chapter 3 has been modified in order to respond to the introduction of tags. The first change concerns the new Bayesian distance, as mentioned in the previous section. The second concerns the interpolation of tags. In fact the values obtained from NOAA need to be interpolated to match those of CDRD, in terms of time and geographical location (latitude, longitude). Figure 4.11 schematically represents the block diagram of the processing procedure of tags. The two preliminary checks concern the time of acquisition and the location of the data. Regarding the time, two files of the Global Forecast System of NOAA are selected, approximately corresponding to the time of Tbs measurements. The values of tags at this time are then computed by an interpolation.

In order to increase the flexibility of the algorithm, the selection of the channels (NC) to be utilized in the retrieval, up to a maximum of 19 (SSMIS), has been allowed. This means also an automatic change of the dimensions of vectors and matrices in the algorithm (i.e the error covariance matrix $C_{\varepsilon t}$), in accordance with the Tbs selected.

Moreover, three different weights for the channels (W_j) and three different thresholds (dthre) are used, for measurements over ocean, land and coast, in order to allow different selection criteria.

Fig. 4.12 shows the block diagram of the algorithm.

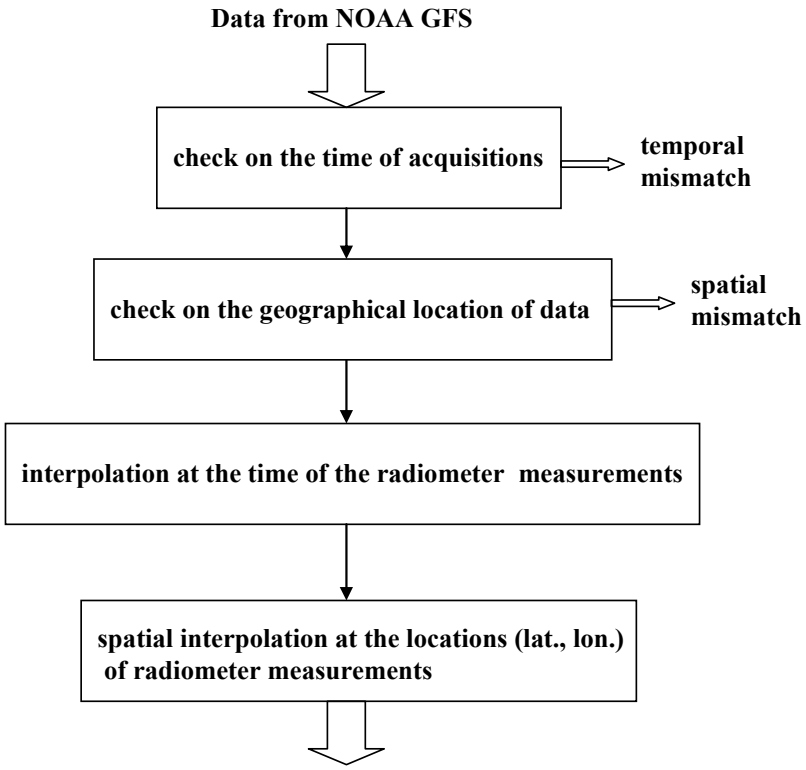

Fig. 4.11 - Schematic diagram of the checks and the interpolation procedure of tags.

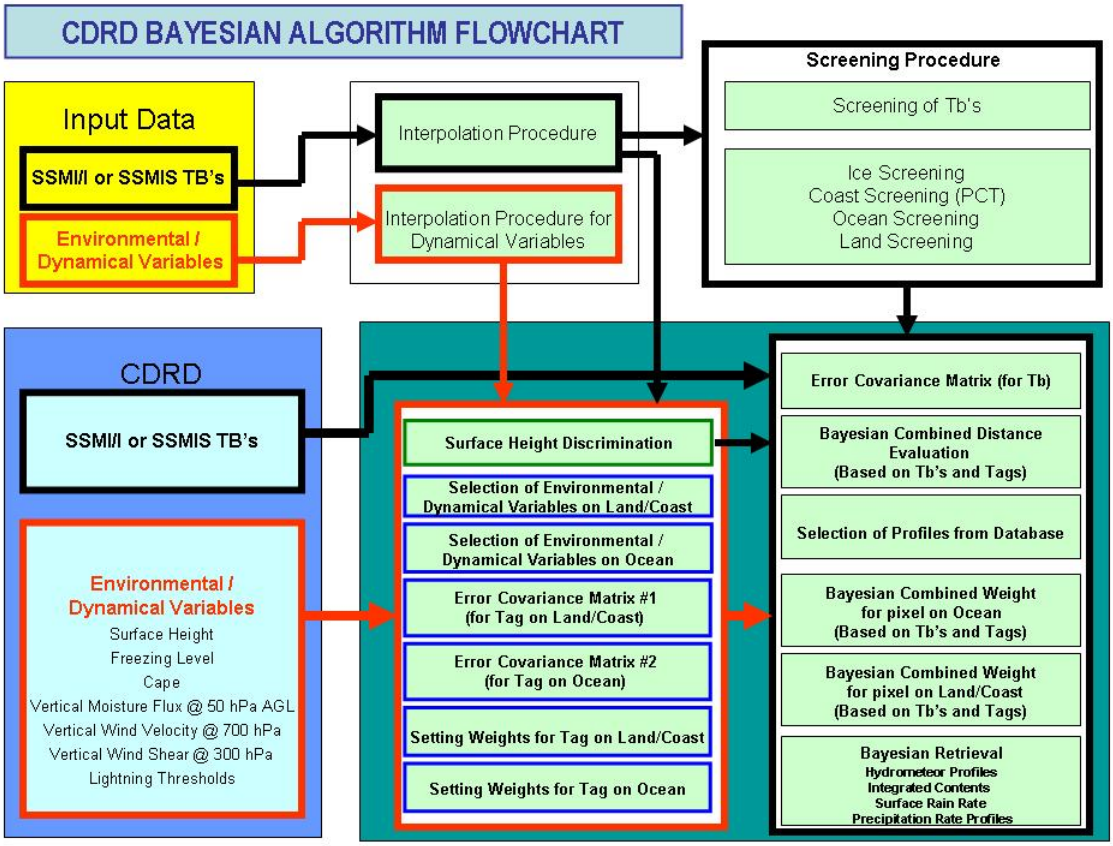

Fig. 4.12 - Block diagram of the new Bayesian retrieval algorithm (CDRD database).

4.4 Case studies

In the following section, some case studies of meteorological events over Italy are presented. The studies are aimed at testing the new Bayesian algorithm, and at analyzing the effects of tags on retrieval.

The check of the real effectiveness of the dynamical tags in the selection of profiles, in order to reduce the "ambiguity" of the CDRD is, in fact, a fundamental aim of this research. To this end, the effects (on rain rate estimate and variance) of each tag are first analyzed separately. Then the combined use of the tags is studied.

Regarding tags, we started with the use of *vertical wind velocity at 700 mb (Omega)*, *vertical moisture flux at 50 mb AGL*, *CAPE* and *freezing level*, as certainly related to the structure of the events considered in the studies.

As the case studies concern the Rome and the Lazio area, and the evaluation of the results are based on a comparison with simultaneous measurements of the CNR-ISAC Polar55 radar, a short description of this radar is first presented.

4.4.1 The ISAC-CNR Polar55 radar

The CNR-ISAC radar meteorology group employs the coherent C-band Doppler dual polarization Polar 55C radar for research in the field of meteorological and hydrological application of radar polarimetry.

Table 4.1 – Characteristics of the CNR-ISAC Polar55 radar

Polar 55C characteristics	
Antenna	
Type	Offset fed Paraboloid
Feed	Corrugated horn
Aperture diameter	4.57 m
Polarization	Horizontal and Vertical
Azimuth beamwidth	0.92 deg
Elevation beamwidth	1.02 deg
Gain	45.5 dB
Sidelobe level	-32 dB
Cross Polarization	-27 dB
Transmitter	
Power Amplifier	Klystron VCK 7762
Frequency	Fixed, selectable in the band 5600-5650 MHz
Peak Power	500 kW
Pulse width (maximum)	0.5 – 1.5 - 3.0 μs
PRF	1200 – 600 – 300 Hz
Average Power	300 – 450 – 450 W
Available polarizations	H and V
Receiver	
Number of channels	2: (RX and TX sample down conversion to IF)
Noise figure	2.0 dB from the input of the first down
Image Rejection	> 50dB
Dynamic range	> 100dB at 1dB compression
IF	60 MHz
IF bandwidth	2.0 – 0.7 – 0.5 MHz

The most common algorithms using polarimetric measurements are

$$R\left(K_{dp}\right) = a_2 K_{dp} \qquad R\left(Z_h, Z_{dr}\right) = a_3 Z_h^{b_3} Z_{dr}^{c_3}$$

where R is the rainfall rate (mm h^{-1}), Z_h is the horizontal reflectivity ($mm^6 m^{-3}$), Z_{dr} (dimensionless) is the differential reflectivity and K_{dp} (deg km^{-1}) is the specific differential phase. Coefficients of these algorithms are determined through simulations assuming theoretical or experimentally derived distribution of the DSD parameters, a drop shape model, and a fixed temperature.

R(K_{dp}) is a robust estimator, especially in the presence of heavy rain, where it can benefit from the property that, being based on a phase measurement, it is affected by neither attenuation, nor by calibration bias
R(*Zh*, Zdr) represents a good compromise, providing accurate measurement over a wide range of rainfall rate, from moderate to heavy. For this reason it is used to develop the procedure at C-band.

The exact position of the Polar 55C corresponds to North Latitude 41° 50' 24", East Longitude 12° 38' 50" and a height of 102 m. The figure below shows reflectivity observed at an elevation angle of 1.04° on 6 June 2002.

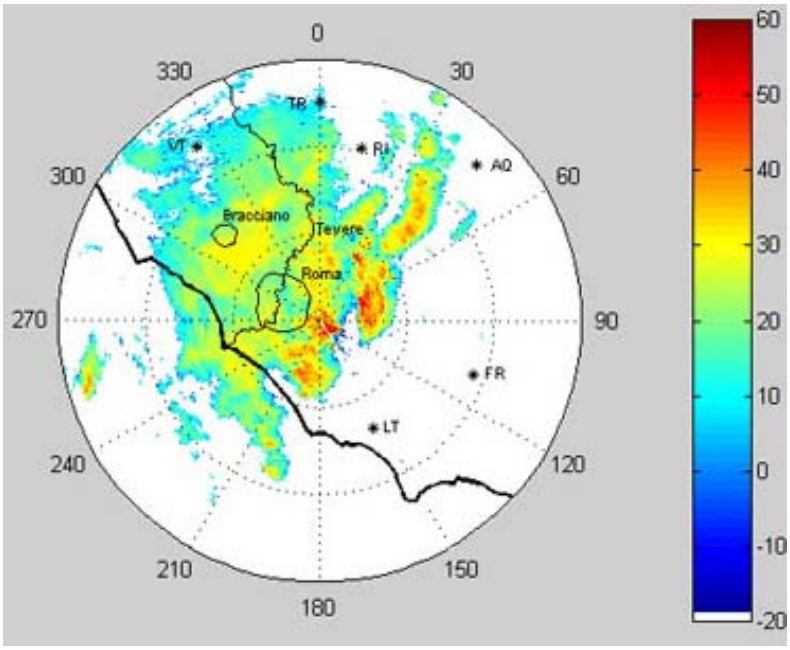

Fig. 4.13 – CNR-ISAC polar55c radar. Reflectivity observed at an elevation angle of 1.04° on 6 June 2002 (http://polar55c.artov.isac.cnr.it/).

Main limitations to visibility are created by Monte Cavo, located a few kilometers south of the radar site, by the two minor hills of Monti Prenestini and Monti Sabini located 20 km in the E-NE direction, and finally by the tall Mount Terminillo, located 70 km from the radar site along the N-NE direction. The occultation constituted by Monte Cavo is total and determines the presence of an occulted sector, from 120° to 150°, recognizable in the map. Good visibility in the North West sector allows the monitoring of precipitation over the Tyrrhenian Sea.

4.4.2 Case study over Lazio area (November 4, 2008 16:18 UTC)

On November 4, 2008, a deep low pressure area centred near the Balearic Islands was carrying a strong southern flux over the Tyrrhenian Sea. Pictures in figure 4.14 show the analyses (pressure and geopotential) produced by the Global Forecasting System (GFS) global model of the U.S. National Oceanic and Atmospheric Administration (NOAA). The strong southern winds collected a lot of moisture from the sea that was still relatively warm because of the energy accumulated during the summer. The air became unstable and the complex pattern of the coasts and orography produced many low level wind convergence lines. Strong multicell storms developed along these lines.

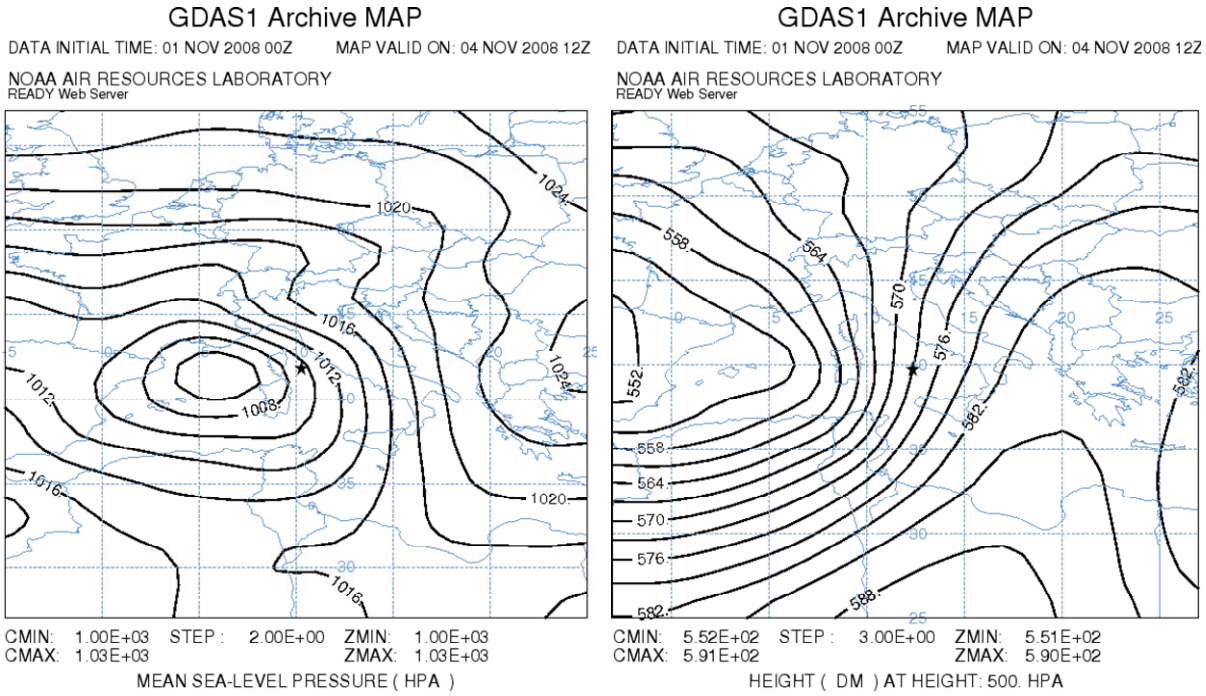

Fig. 4.14 – Case study over Lazio, November 4, 2008. Left panel: sea level pressure map. Right panel: 500 mb geopotential pattern.

In addition, a cold flux entering from the western Mediterranean Sea increased air instability as shown in figure 4.15.

Figure 4.16 shows the Meteosat Second Generation (MSG) images of the event. The left panel shows the IR (10.8 m) image with superimposed ZEUS (Lagouvardos et al. 2009) lightning; the right panel shows the MSG image at the HRV visible channel; there are many overshooting tops rising over the cumulonimbi.

Using the UW-NMS model, we have carried out at CNR ISAC a simulation of the event. Figure 4.17 shows a three dimensional visualization of the NMS results; the white surfaces are the cloud field with surface winds (arrows) and precipitation patterns (blue shading). The storm is structured as a "line" because the storm cell developed along a low level wind convergence.

This case study points out a variety of precipitation regimes; in fact although it is a convective system with well defined heavy rain clusters, it evolves into a long lasting cloud system with extensive stratiform rain. This characteristic is shown in figure 4.18 that presents the radar rainfall measurements, taken at two different instants of the event. The top panel in the figure shows the young phase of the convective system with clusters of heavy rain without a large stratiform area (red circle).
The bottom panel clearly shows a vast area with weak uniform rain, typical of the dissipating stage of storms, with long lasting clouds (anvils) (green circle). In this situation, large snow fields develop from high level clouds that melt in light rain fields extended for many kilometres.

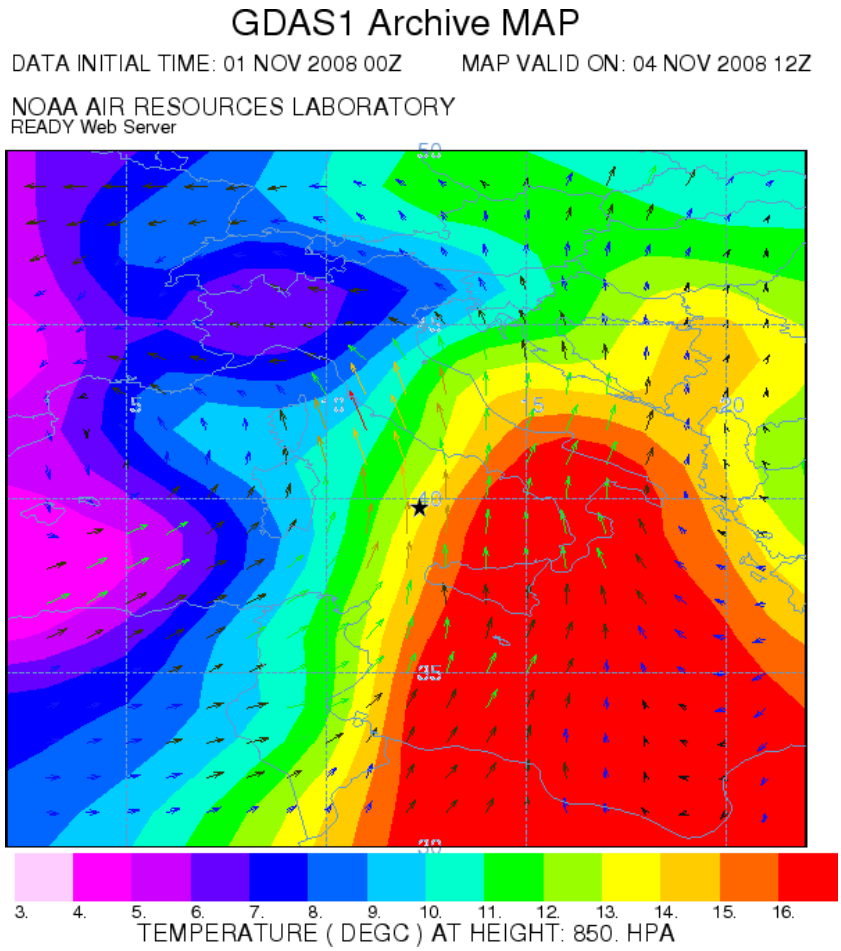

Fig. 4.15 - Case study over Lazio, November 4, 2008. Thermal field superimposed to the wind at 850 mb.

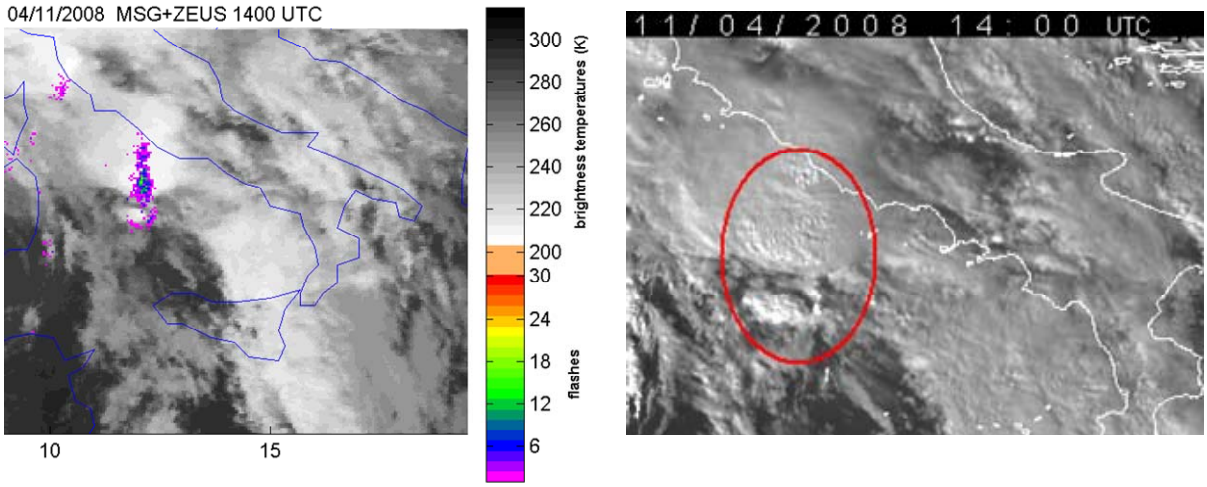

Fig. 4.16 - Case study over Lazio, November 4, 2008. MSG image at the IR band (10.8 m) with ZEUS lighting superimposed (left panel), and MSG image at the HRV visible channel (right panel).

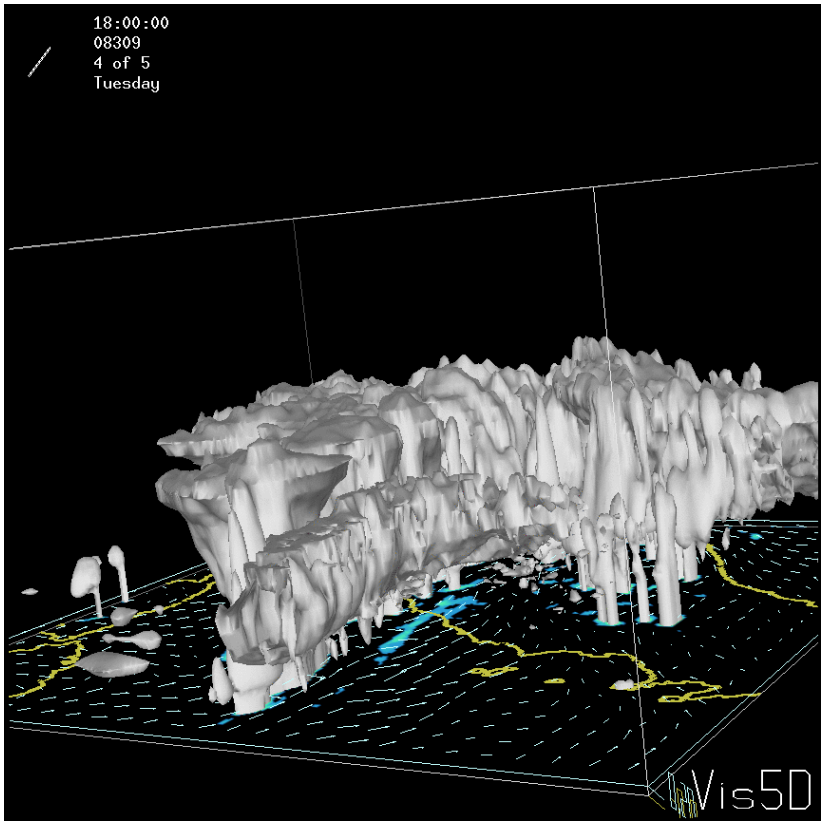

Fig. 4.17 – Case study over Lazio, November 4, 2008. UV-NMS simulation. The storm line is approaching the coast of central Italy.

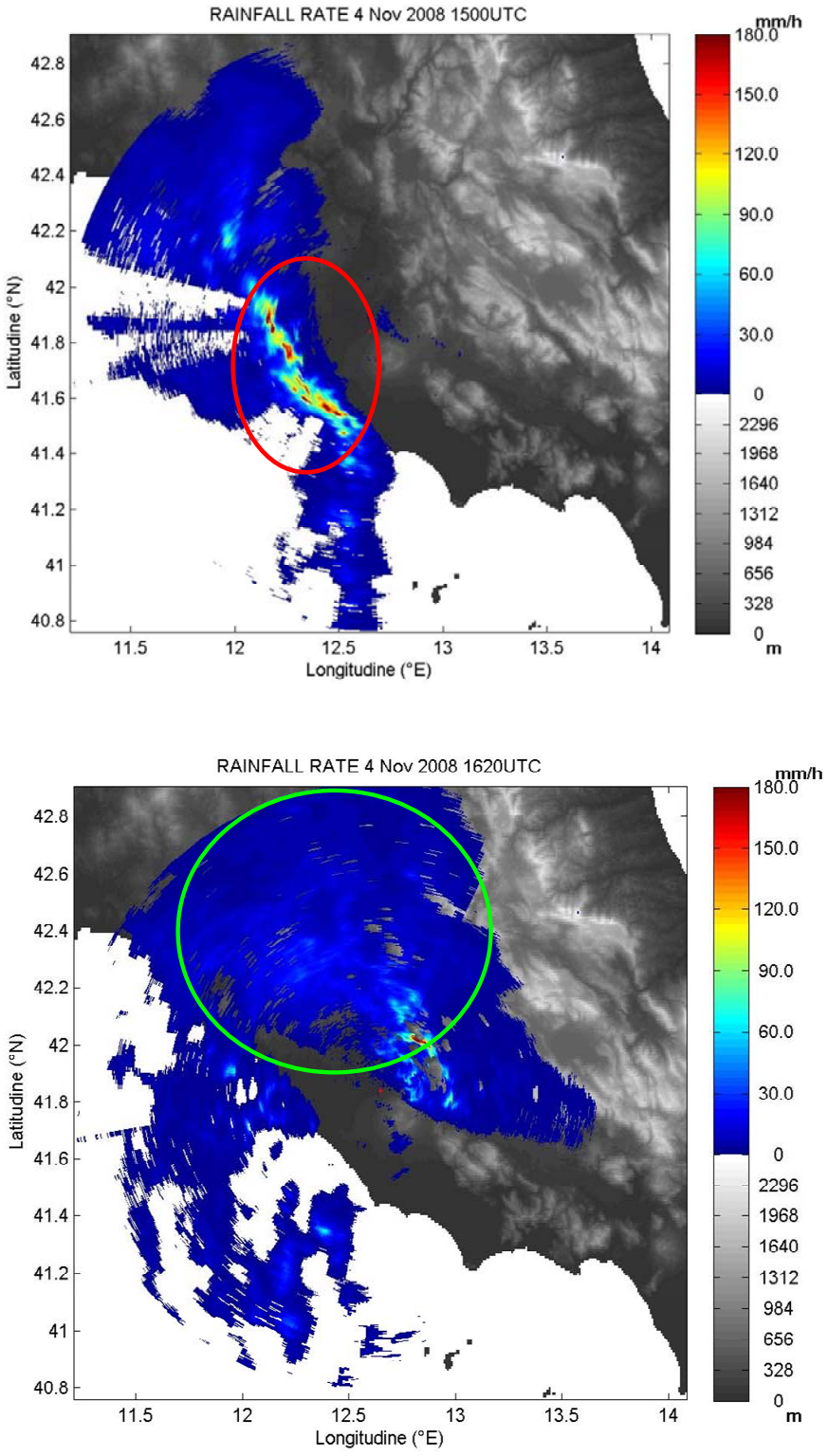

Fig. 4.18 – Rainfall rates on November 4, 2008 at UTC 15:00 (top) and 16:20 (bottom) as result from radar measurements (CNR-ISAC C-band polarimetric Doppler radar Polar 55C).

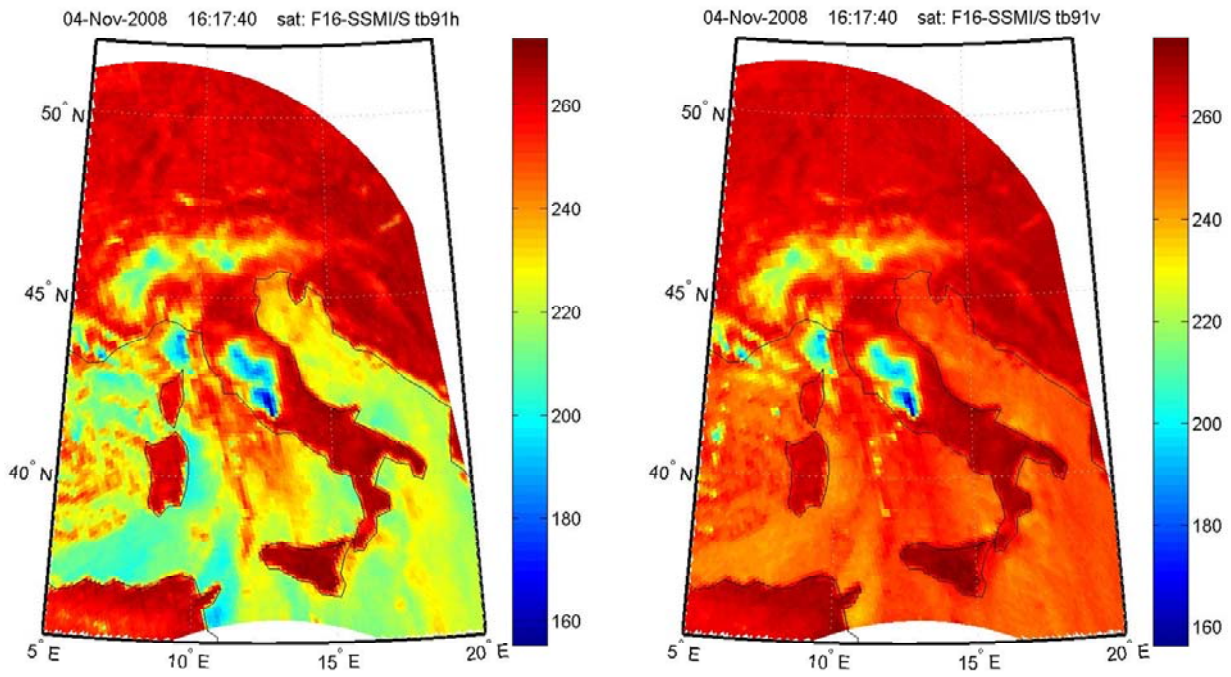

Fig. 4.19 - Case study over Lazio, November 4, 2008, 16.18 UTC. Microwave brightness temperatures (K) at 91 (H,V) GHz, as measured by the SSMIS radiometer onboard the DMSP F-16 satellite.

Figure 4.19 shows the brightness temperatures at 91 (H,V) GHz, obtained from SSMIS radiometer onboard satellite DMSP F-16, on November, 4 2008.
Figure 4.20 shows the corresponding microwave brightness temperatures at 150 (H), and 183 (H) GHz (see Tab. 1.2 of chapter 1). In both figures, and especially in the last one, the atmospheric disturbance over the Rome area is quite evident. The corresponding retrieval results of the new BAMPR algorithm are shown in figures 4.21 and 4.22.

The CRD version of the database is used, i.e. the one without dynamical tags. Figure 4.21 shows the surface rain rate and points out some rain rate peaks of about 20-25 mm/h.
Figure 4.22 shows, in the left panel, the number of profiles of CRD for each pixel contributing to the retrieval (common logarithm); in the right panel the variance to rain rate ratio (mm/h). For each pixel a large number of profiles from the CRD database are selected for the Bayesian retrieval. A greater number of profiles are selected for low rain rates, depending on the structure of CRD that has a profile majority corresponding to low rain rate values.
Figure 4.23 shows the result of Polar 55C radar measurements over Lazio at 16:21 UTC, and figure 4.24 compares the BAMPR retrievals (top right panel) over Lazio with the corresponding radar (top left panel) measurements. To carry out this comparison, radar measurements and satellite retrievals have been reduced to the same resolution. A smoothing procedure (3x3 filter) has then been applied to the data. In the figure some statistical indexes are shown: the direction coefficient of the fit (m fit), the sum of residuals about the bisector

(sum B res), the summed square of residuals (sqr B res), sum of squares due to error (sse - this index measures the total deviation of the response values from the fit to the response values), the square of the correlation between the response values and the predicted response values (rsquare - this index measures how successful the fit is in explaining the variation of the data). The results of figure 4.24 show that there is quite a good agreement both in terms of precipitation path and rain rate values, even though the scatterplot points out that the BAMPR algorithm slightly overestimates the rain rate with respect to the radar measurements

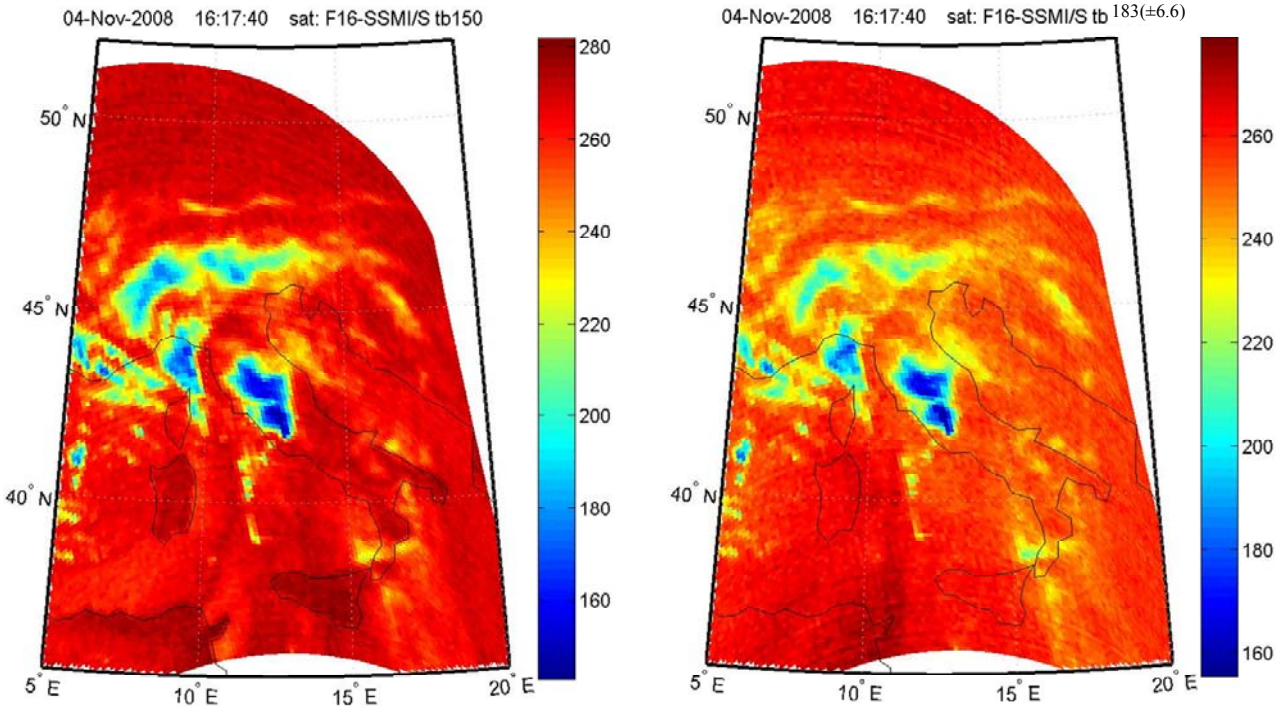

Fig. 4.20 – Case study over Lazio, November 4, 2008, 16.18 UTC. Microwave brightness temperatures (K) at 150 (H), and 183 (H) GHz (see Tab. 1.2 of chapter 1), as measured by the SSMIS radiometer onboard the DMSP F-16 satellite.

In order to check the effect of the dynamical tags on the retrieval, we analyzed the changes in new BAMPR output (rain rate and relative Bayesian variance) introducing, in a preliminary test, the tags *freezing level*, *vertical moisture flux at 50 mb AGL* and *vertical wind velocity at 700 mb (Omega)* in the Bayesian procedure.

Figures 4.25 and 4.26 show the values of these tags during the event. The circles in the figures delimitate the area selected for the comparison with radar. Figure 4.25 shows the tags *vertical moisture flux at 50 mb AGL* (left panel) and *vertical wind velocity at 700 mb (Omega)* (right panel).

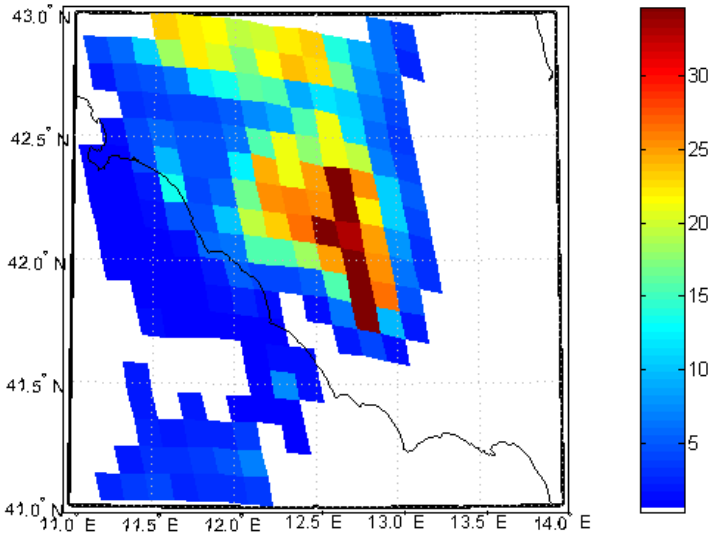

Fig. 4.21 - Case study over Lazio, November 4, 2008, 16.18 UTC (DMSP F-16). Surface rain rate (mm/h) obtained by BAMPR algorithm (CRD version).

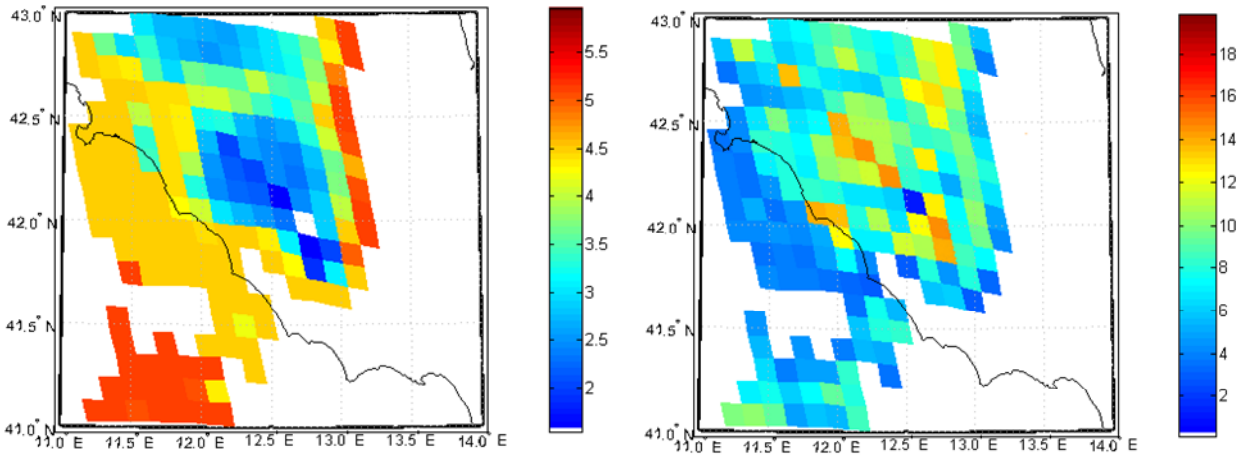

Fig. 4.22 - Case study over Lazio, November 4, 2008, 16.18 UTC (DMSP F-16). Outputs of BAMPR algorithm: the panel on the left shows the number of profiles of CRD that contributed to the retrieval (common logarithm); the panel on the right shows the variance to rain rate ratio (mm/h).

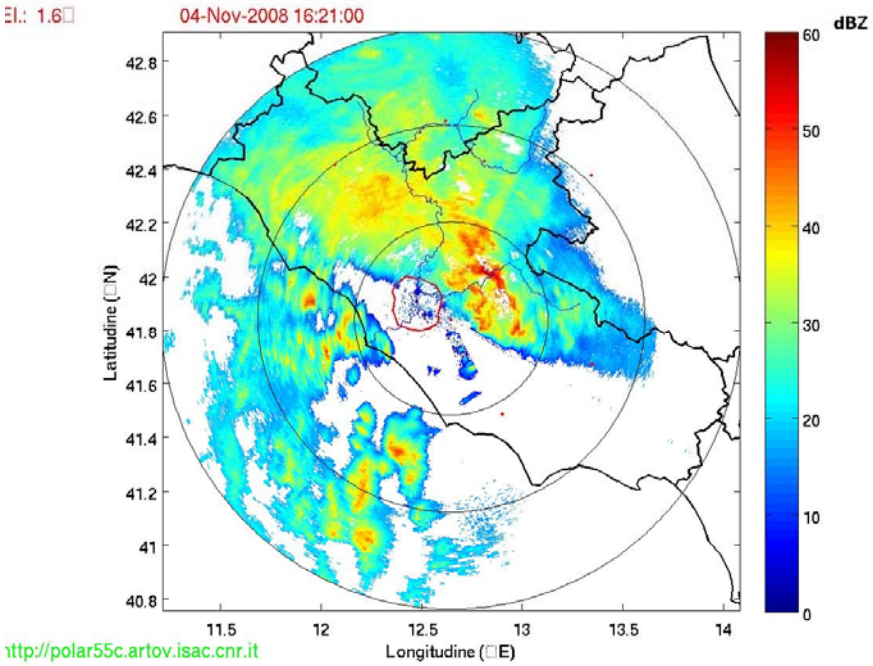

Fig. 4.23 – Reflectivity measured on 4 November 2008 at 16:21 UTC by the CNR-ISAC C-band polarimetric Doppler radar Polar 55C – note that the Rome area is delimited by the red line.

The *vertical moisture flux at 50 mb AGL* presents a slight decrease from the coast toward the area of the event, while the *wind velocity at 700 mb (Omega)* presents a more evident variation, with an increase in the values from the coast to the area of the event.

Fig. 4.26 shows the tags *CAPE* (left panel) and *freezing level* (right panel). The *CAPE* presents, in the circled area, an evident variation, with a decrease in proximity to the coast. The values in the area of the event are in the range 200-1100 J/kg, denoting that by this time the potential energy is converted into kinetic energy. Therefore, this tag cannot be useful in the retrieval procedure.
The *freezing level* presents a slight variation in the circled area, with an increase moving from the coast to the area of the event.

These variations of tag values are presented in a more detailed way in figure 4.27, which concerns only the circled areas of previous figures 4.25 and 4.26. In the figure the values of the *vertical moisture flux at 50 mb AGL* (top left panel), of the *vertical wind velocity at 700 mb (Omega)* (top right panel) and *freezing level* (bottom panel) are shown. The *CAPE* is not presented in the figure.
The details suggest that, in this convective system evolving into a long lasting cloud system with extensive stratiform rain, the *vertical wind velocity at 700 mb (Omega)* should play an

important role in the retrieval procedure, allowing a more correct selection of profiles in the CDRD. This fact is confirmed by figures 4.28 and 4.29 that present three scatterplots concerning the distribution of the profiles of CDRD with respect to the *vertical moisture flux at 50 mb AGL*, the *vertical wind velocity at 700 mb (Omega)*, and the rain rate. Particularly, fig. 4.28 shows, in the panel on the left, the scatterplot of the *vertical wind velocity at 700 mb (Omega)* and the rain rate (the log of occurrences of profiles in CDRD is shown).
In the panel, the range of this tag in the detailed area of figure 4.27 (top right panel) is also specified. In the panel on the right of figure 4.28, a similar scatterplot for the *vertical moisture flux at 50 mb AGL* is shown.

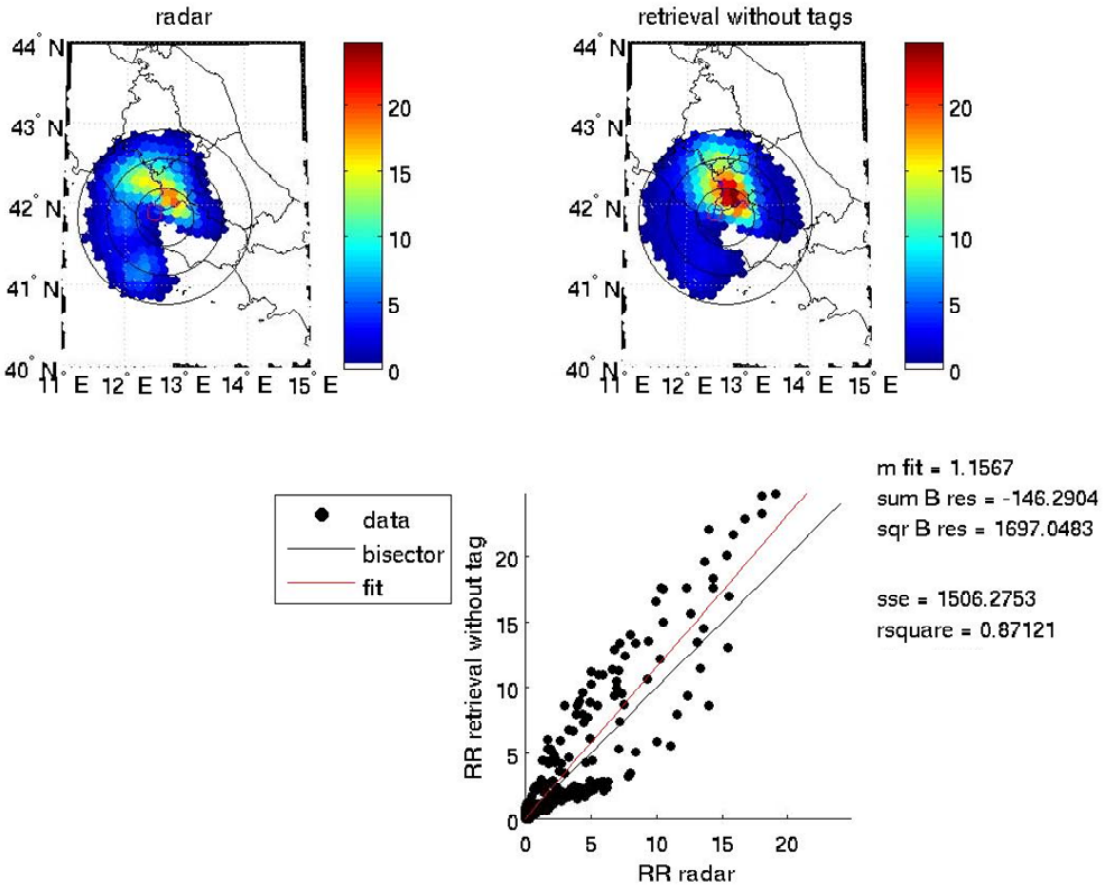

Fig 4.24 – Case study over Lazio, November 4, 2008, 16.18 UTC. Average (see the text for more details) surface rain rates (mm/h) measured by the Polar 55C radar (top left) and estimated by the Bayesian algorithm (CRD version) (top right). Bottom panel: scatterplot of satellite rainfall retrievals of top-right panel vs. corresponding radar measurements of top-left panel.

It is evident in the figure that both the ranges include the area with highest occurrences (red area) in the database. It follows that the examined event is well represented in the CDRD.

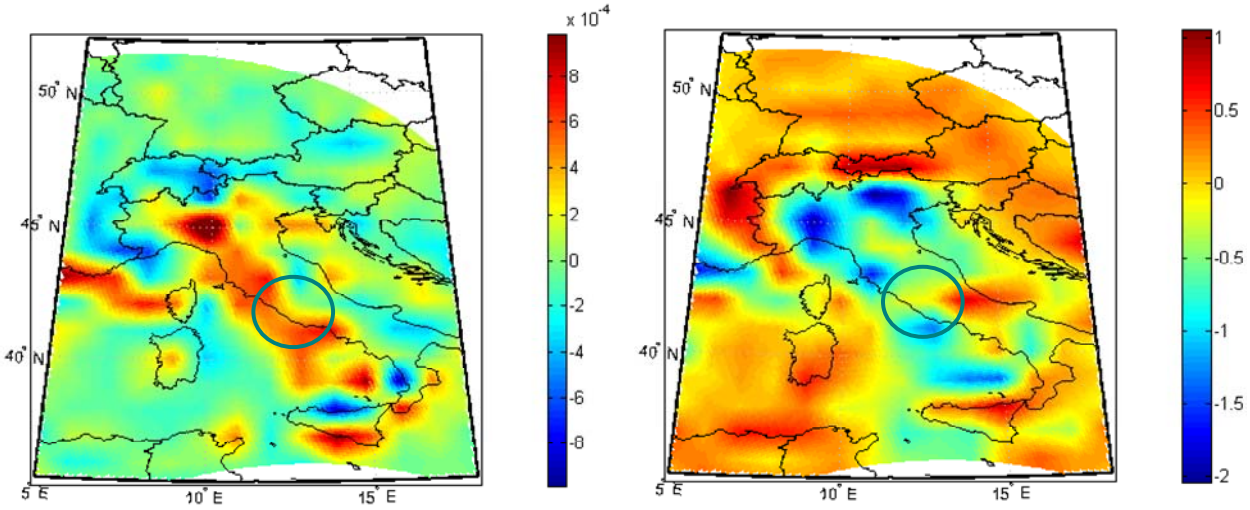

Fig. 4.25 – Case study over Lazio, November 4, 2008, 16.18 UTC. Values of the *vertical moisture flux at 50 mb AGL* ($g*m^{-2}*s^{-1}$) (left panel), and *vertical wind velocity at 700 mb (Omega)* (Pa/s) (right panel). The circles show the area analyzed in the comparison with radar measurements.

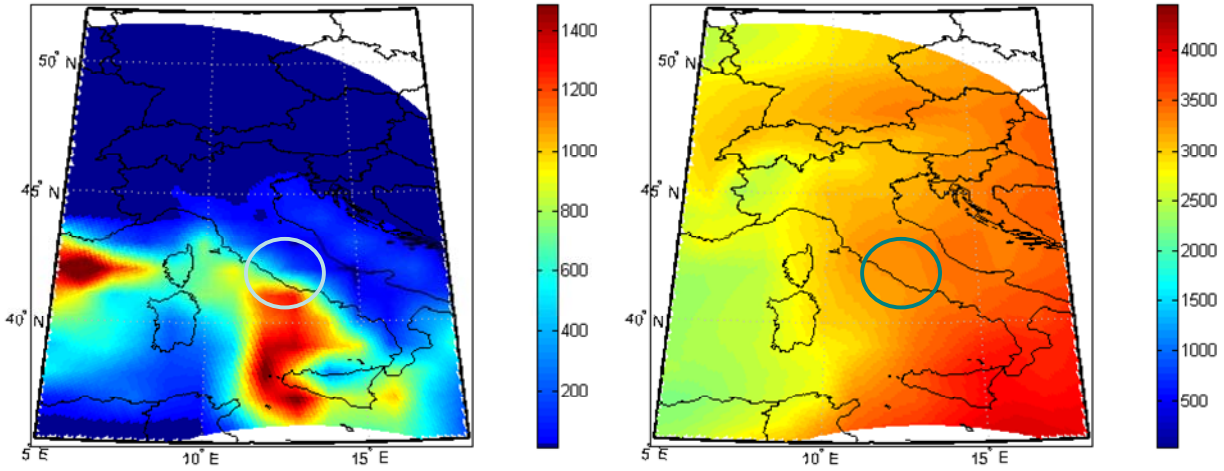

Fig. 4.26 - Case study over Lazio, November 4, 2008, 16.18 UTC. Values of the *convective available potential energy (CAPE)* (J/kg) (left panel), and *freezing level* (m) (right panel). The circles show the area analyzed in the comparison with radar measurements.

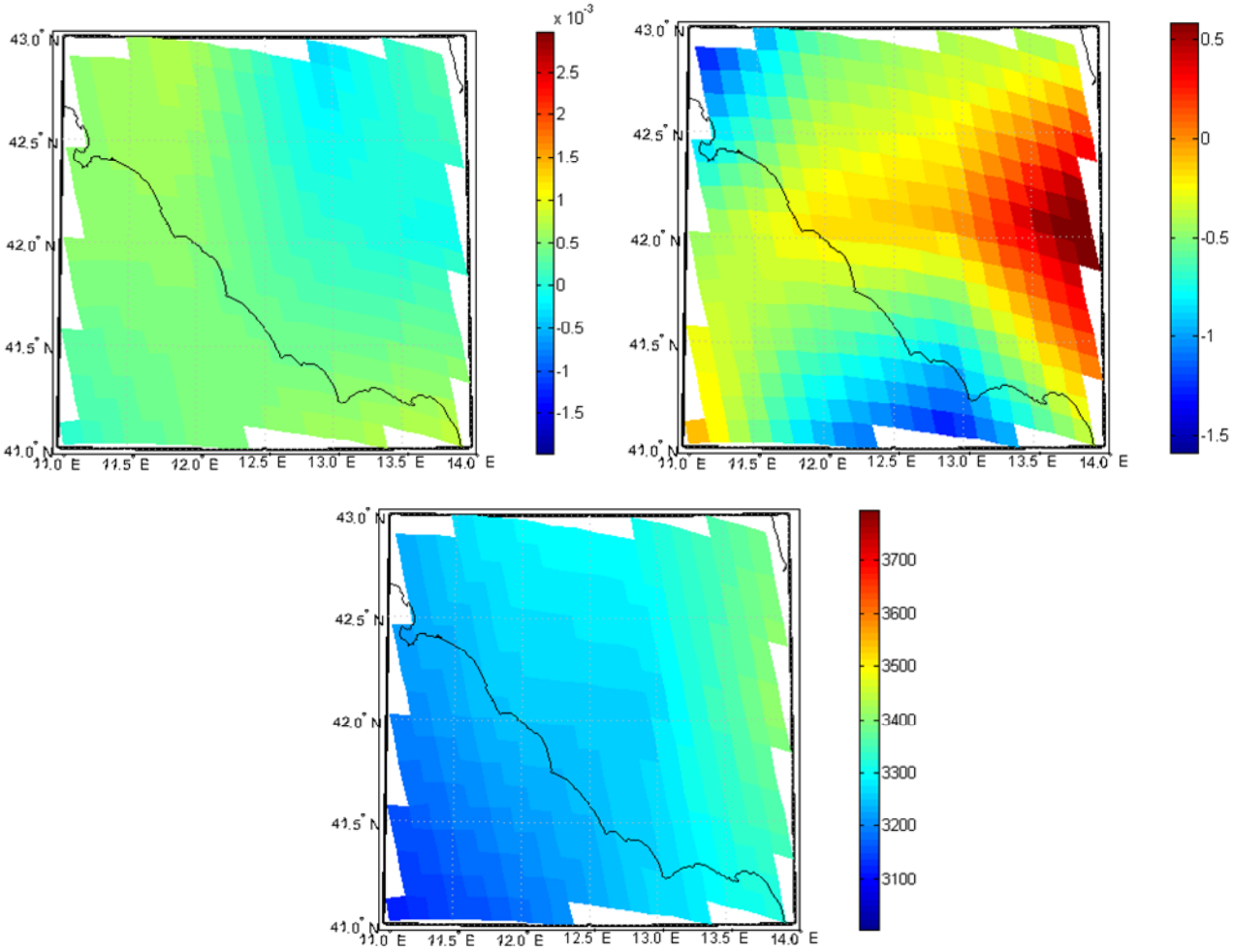

Figure 4.27 – Details of the values of tags *vertical moisture flux at 50 mb AGL* (g*m^{-2}*s^{-1}) (top left panel), *vertical wind velocity at 700 mb (Omega)* (Pa/s) (top right panel), and *freezing level* (m) (bottom panel) in the circled areas of figures 4.25 and 4.26.

Moreover, the figure points out that the range of *vertical wind velocity at 700 mb (Omega)* allows a more narrow selection in the database.
This fact is confirmed by figure 4.29 which shows the scatterplot of *vertical moisture flux at 50 mb AGL* (vertical axis) and *vertical wind velocity at 700 mb (Omega)* (horizontal axis). The different selectivity is evident in the figure. Regarding the *freezing level*, it shows very small changes over the observed area (fig. 4.27, bottom panel). As mentioned in section 4.2.1, it can give an effective contribution to a preliminary selection of profiles in the database. For this reason it has been coupled with the other tags in all the tests carried out in this case study. A check on its effect on the selection procedure of CDRD profiles has shown a reduction of about 50% of the mean number of profiles selected, for a pixel.
In the following figures 4.30 – 4.32 the effects of the use of tags on surface rain rate and relative Bayesian variance are shown.

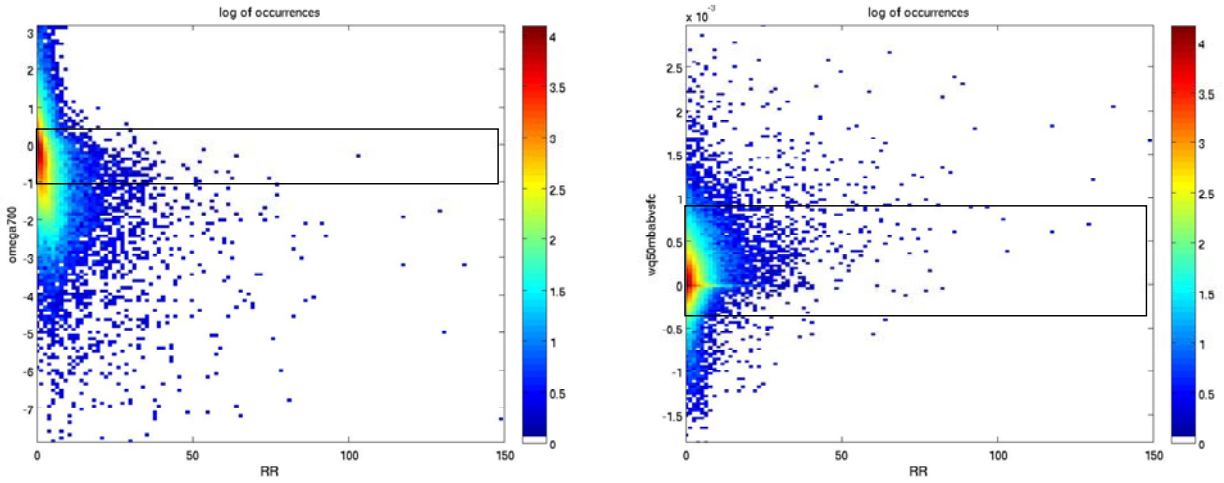

Fig. 4.28 – Scatterplot of *vertical wind velocity at 700 mb (Omega)* (Pa/s) and rain rate (mm/h) (left panel), and of *vertical moisture flux at 50 mb AGL* ($g*m^{-2}*s^{-1}$) and rain rate (mm/h) (right panel). On the vertical axes the rectangles show the ranges of the two tags in the selected areas of fig. 4.5.15.

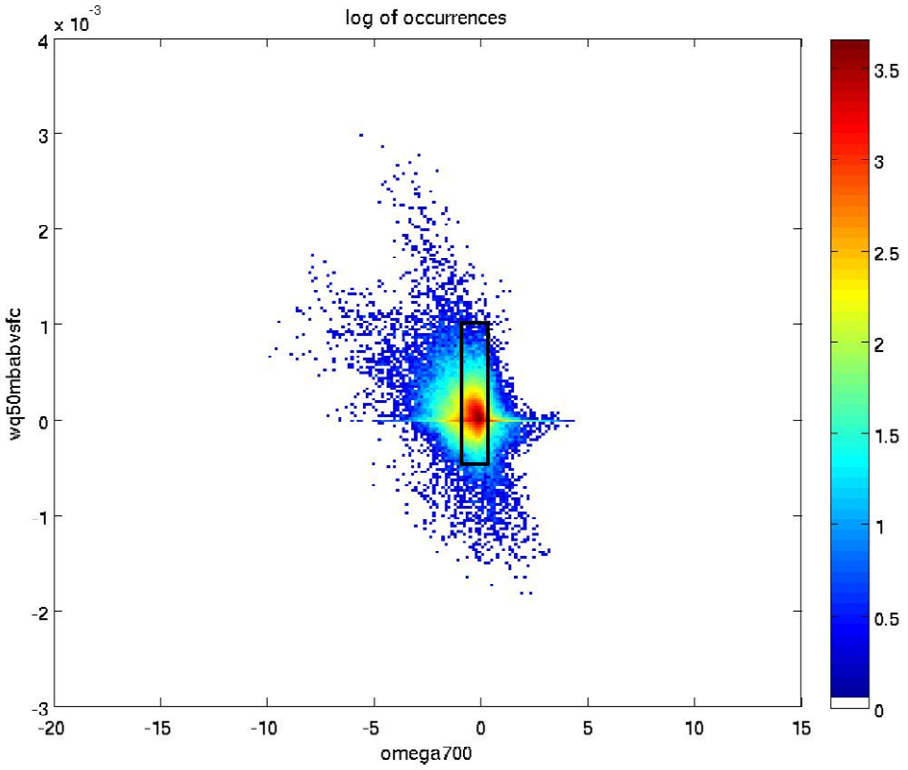

Fig. 4.29 – Scatterplot of *vertical moisture flux at 50 mb AGL* ($g*m^{-2}*s^{-1}$) (vertical axis) and *vertical wind velocity at 700 mb (Omega)* (Pa/s) (horizontal axis) for the profiles of CDRD. The common logarithm is used for the occurrences. The rectangle shows the ranges of the two tags in the selected area of fig. 4.5.15.

Figure 4.30 presents the scatterplots of rain rate values (left panel), and relative Bayesian variance values (right panel) without tags (horizontal axis) and with the use of the two tags *freezing level* and *vertical wind velocity at 700 mb (Omega)* (vertical axis). The effect of these tags, and substantially of *Omega,* is evident on both rain rate and variance. Rain rate values are slightly reduced, and the variance values are reduced in a more evident way. This result confirms the previous comments concerning the correct operation of this tag.

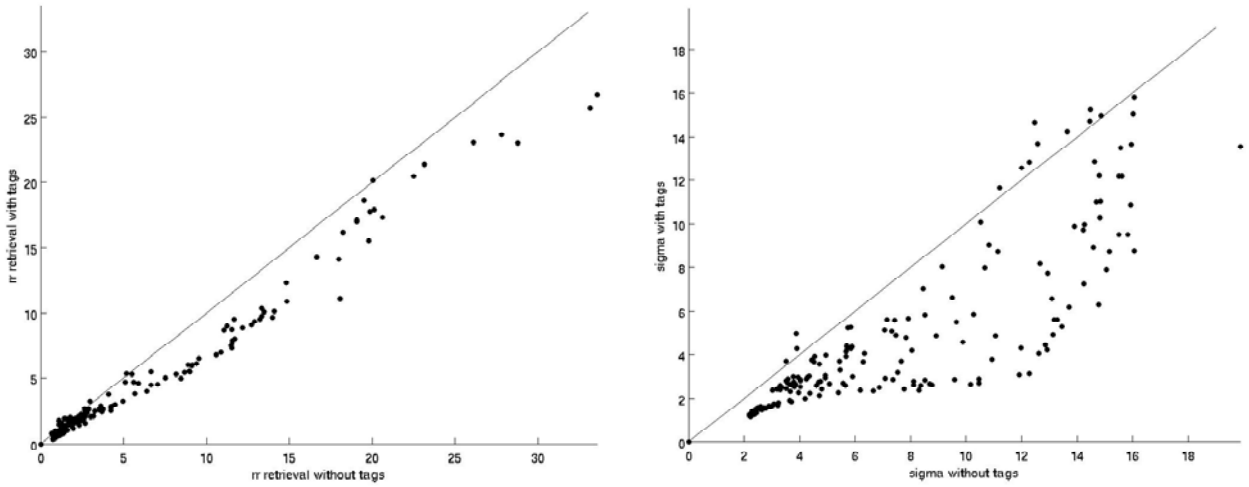

Fig. 4.30 – Case study over Lazio, November 4, 2008, 16.18 UTC. Scatterplots of rain rate values (mm/h) (left panel), and relative variance values (mm/h) (right panel), without tags (horizontal axis) and with the use of the tags *freezing level* and *vertical wind velocity at 700 mb (Omega)* (vertical axis).

Figure 4.31 presents the scatterplots as in the previous figure, but using the two tags *freezing level* and *vertical moisture flux at 50 mb AGL*. The effect is different from the previous figure. As expected from the analysis of images in figures 4.28 and 4.29, the *vertical moisture flux at 50 mb AGL* does not give a specific contribution to the retrieved values. There is an evident high spread of rain rate values; there is, however, also a reduction of the relative Bayesian variance.

Figure 4.32 shows the combined effect of the three tags *freezing level, vertical moisture flux at 50 mb AGL* and *vertical wind velocity at 700 mb (Omega)*. The result is the combination of the effects presented in previous figures 4.30 and 4.31. A reduction of the rain rate values emerges, less evident than in figure 4.30, with an increased spread, and a still manifest reduction of relative Bayesian variance.

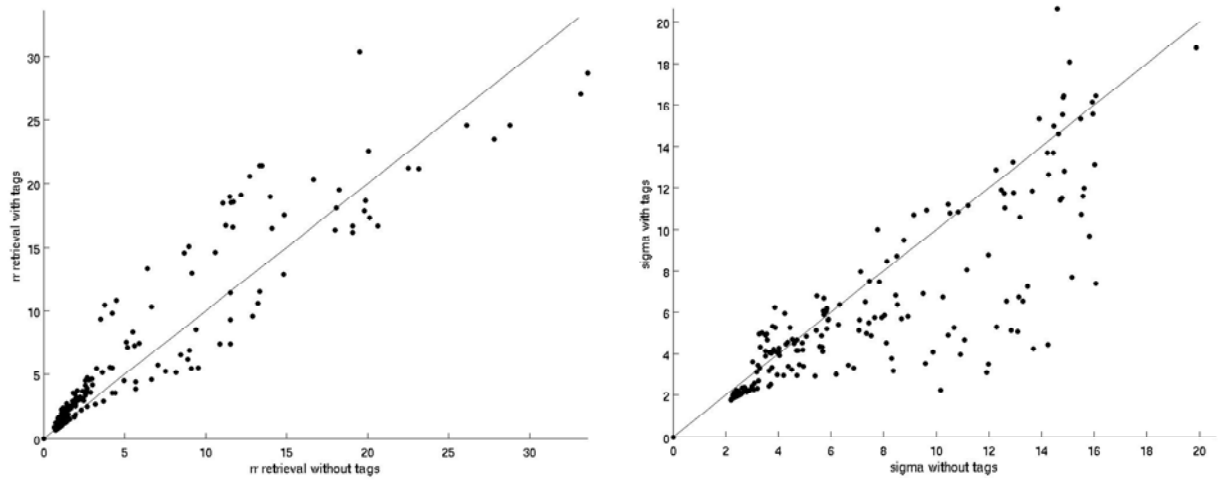

Fig. 4.31 – Case study over Lazio, November 4, 2008, 16.18 UTC. Scatterplot of rain rate values (mm/h) (left panel), and relative variance values (mm/h) (right panel), without tags (horizontal axis) and with the use of the tags *freezing level* and *vertical moisture flux at 50 mb AGL* (vertical axis).

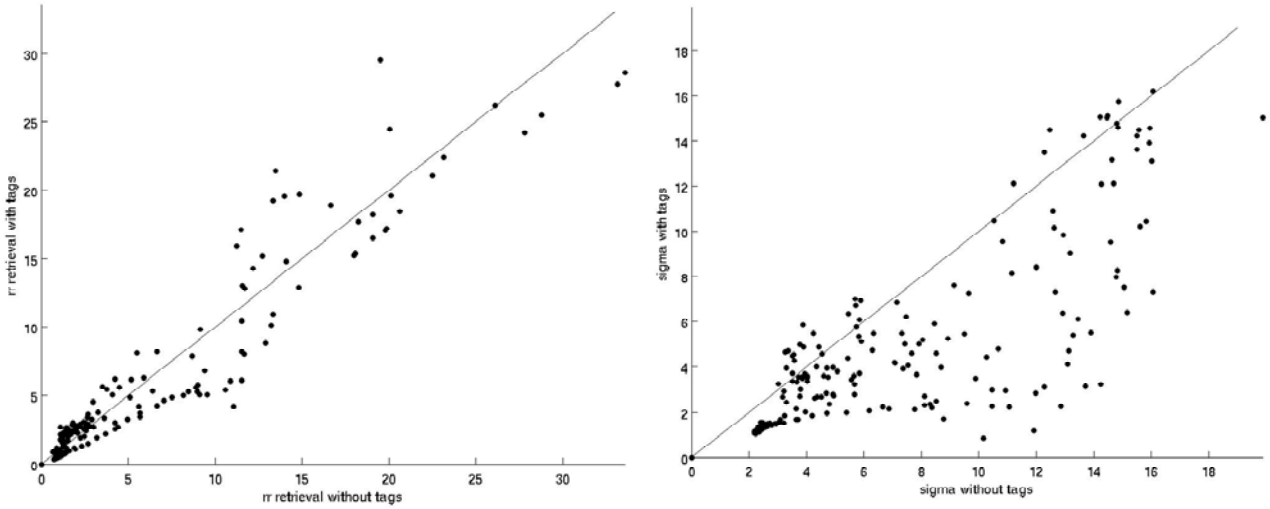

Fig. 4.32 – Case study over Lazio, November 4, 2008, 16.18 UTC. Scatterplot of rain rate values (mm/h) (left panel), and relative variance values (mm/h) (right panel), without tags (horizontal axis) and with the use of the tags *freezing level*, *vertical wind velocity at 700 mb (Omega)*, and *vertical moisture flux at 50 mb AGL* (vertical axis).

After all, based on these scatterplots, the addition of the *vertical moisture flux at 50 mb AGL*, has not given a favourable contribution to the retrieval procedure.

Figure 4.33 points out the effect of tags on the number of profiles selected from the CDRD database. In the figure the mean number of profiles selected, for a pixel, is shown when tags are not used, and when one (*freezing level)* or two (adding *vertical moisture flux at 50 mb AGL)* or three tags (adding *vertical wind velocity at 700 mb (Omega*) are used. The relevant effect on the screening of profiles produced by the *freezing level* (reduction of 50%) is clear in the figure. Altogether, the three tags cause a reduction of about 70% in the selection of profiles.

Figure 4.34 shows the comparison of the retrieval using two tags (*freezing level* and *vertical wind velocity at 700 mb (Omega)* with the radar, in a similar fashion as the previous figure 4.24. Only these two tags are used on the basis of the analysis presented in the previous part of this section. The better agreement with the radar measurements is clear in the figure.

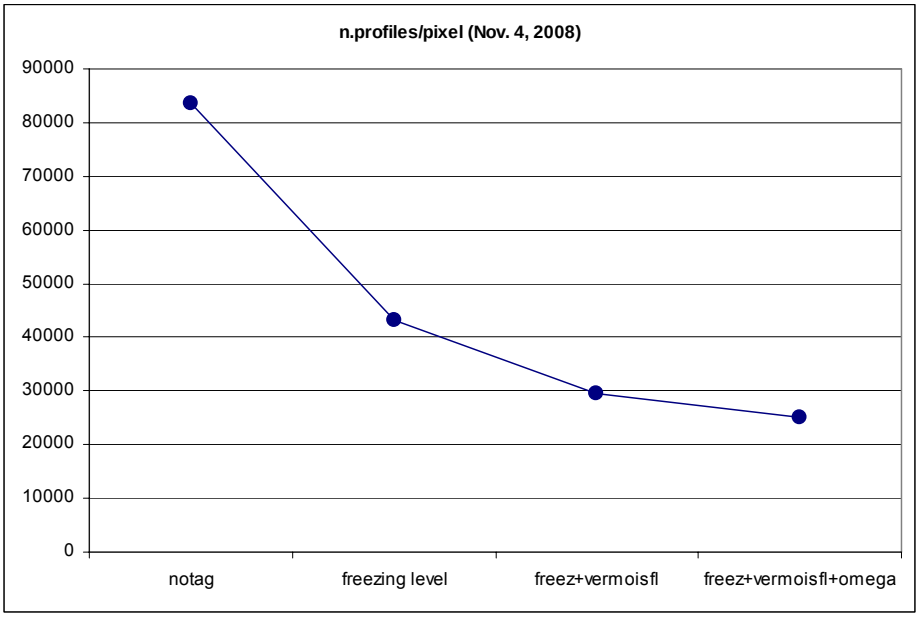

Fig. 4.33 – Case study over Lazio, November 4, 2008, 16.18 UTC. Decrease in the mean number of profiles, for a pixel, selected from the CDRD database using successively one tag (*freezing level*), two tags (adding the *vertical moisture flux at 50 mb AGL*), or three tags (adding *vertical wind velocity at 700 mb (Omega*)).

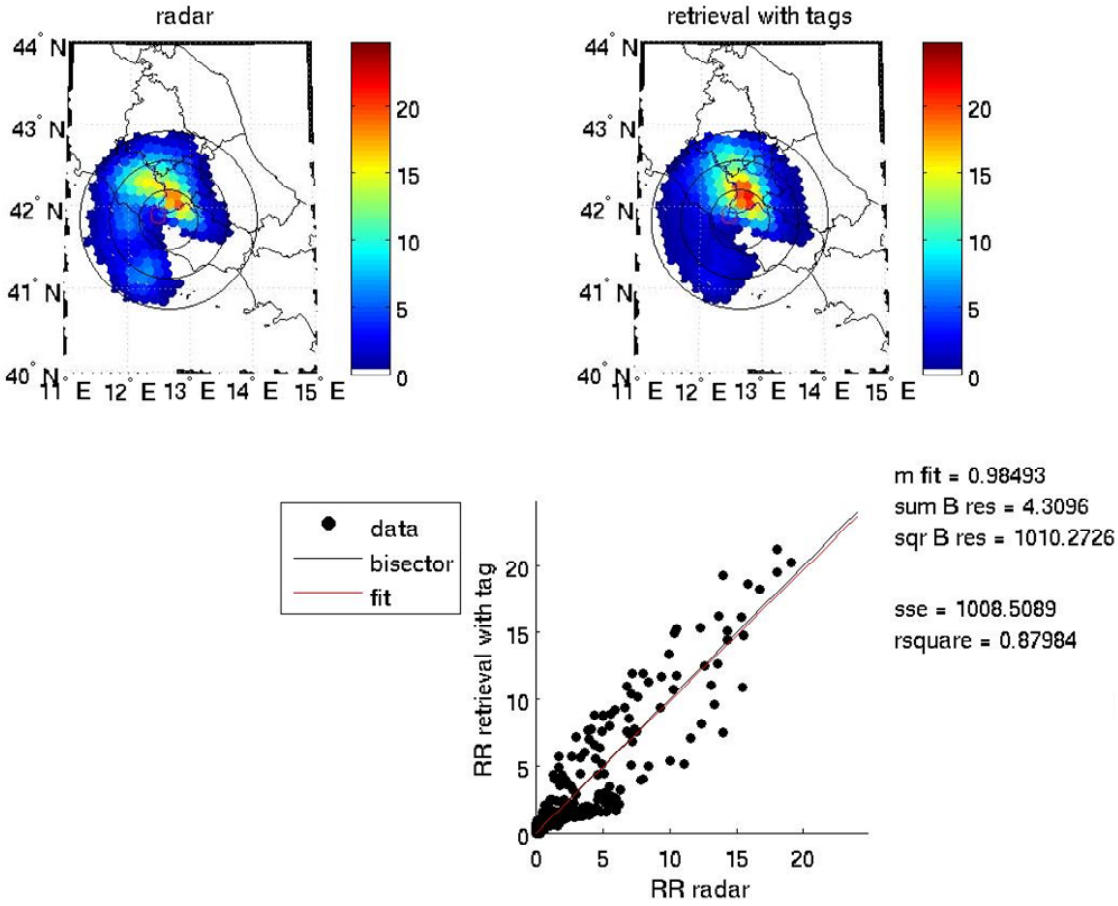

Fig. 4.34 - Case study over Lazio, November 4, 2008, 16.18 UTC. Same as figure 4.5.12, but using the tags *freezing level,* and *vertical wind velocity at 700 mb (Omega)* in the retrieval procedure (see text for more details).

The over estimation of previous retrieval is almost entirely removed and the spread of the data is significantly reduced. The angular coefficient of the fit (m fit parameter) has decreased from 1.1567 to 0.9849; the sum of squares due to error (sse index) has decreased from about 1507 to about 1008. The other statistical indexes confirm, similarly, the improvement in the retrieval.

In the end, the results of this case study confirm the possible improvement of the satellite retrieval by means of the CDRD approach.

4.4.3 Case study over the Rome area (July 2, 2009)

This case study concerns a heavy storm that hit the Lazio region, and particularly the area around the city of Rome, on 2 July 2009.

During the last days of June 2009, a cold pool descended from central Europe to the Balkans producing a cyclonic circulation over Eastern Europe. Consequently, an eastern flux developed over Italy carrying relatively cold air in the middle-level atmosphere.

More specifically, a cold tongue at 850 mb developed over the Balkans on June 29, that generated, two days later, a strong cold advection over Italy (fig. 4.35). In addition, the summer solar irradiation triggered strong and diffuse convection along the Apennine mountain chain. As a result, thunderclouds were carried toward the south-west by upper level winds, as shown in the Meteosat Second Generation (MSG) images of Figure 4.36. In the left panel, the High-Resolution Visible (HRV) image presents the situation at 11:00 UTC. On the right panel, the lighting activity as detected by the ZEUS network during the last 15 minutes is shown. The red circle in the right panel indicates the Rome area observed by the CNR ISAC Polar 55C radar.

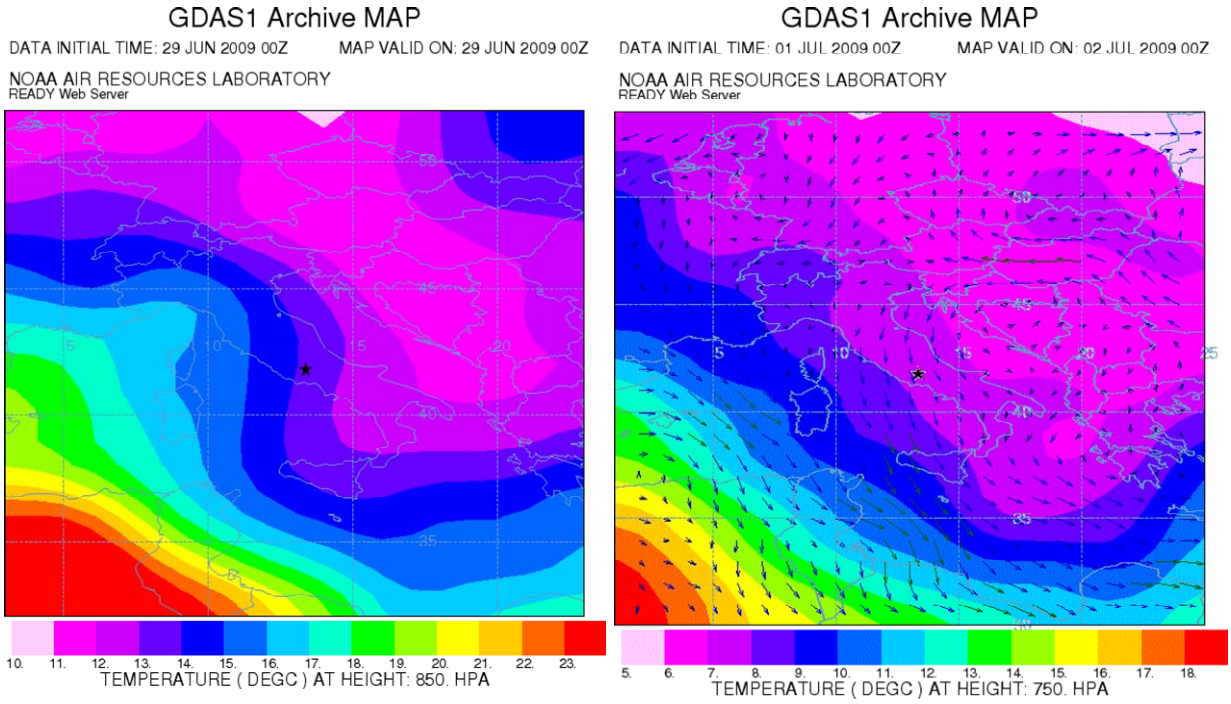

Fig. 4.35 – Synoptic scale evolution of the case study. Left panel: temperature at 850 mbar level at 00 UTC on 29th of June. Right panel: thermal advection at 750 mbar at 00 UTC of 2nd of July. The cold tongue has moved over Italy carried by eastern winds.

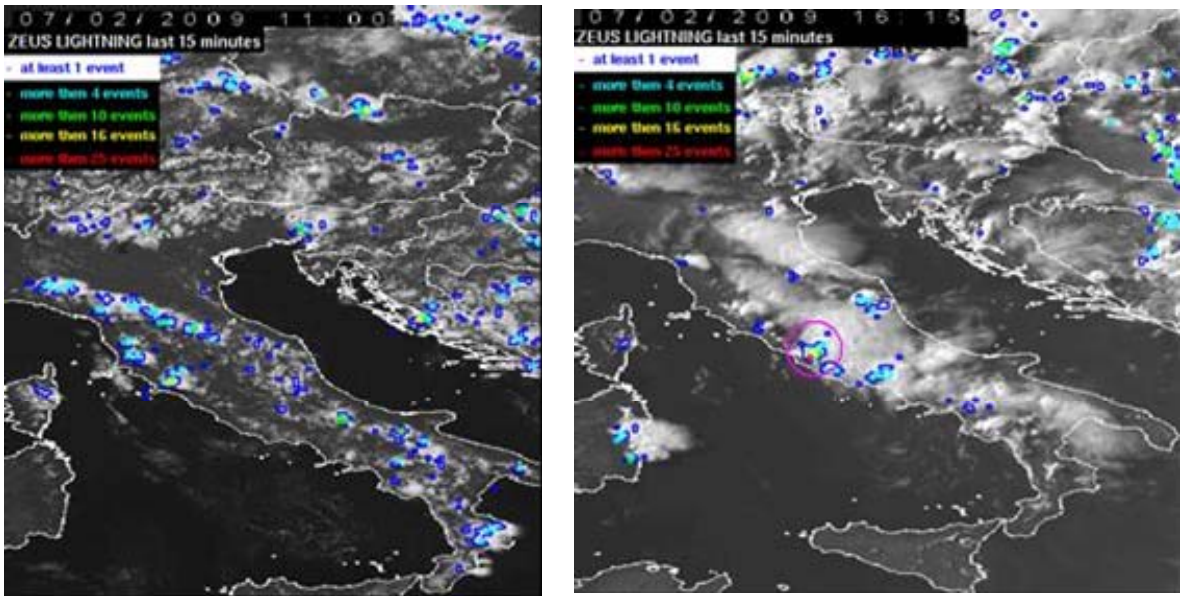

Fig. 4.36 - High-Resolution-Visible (HRV) MSG images of the Italian region on 02 July 2009, 11:00 UTC (left) and 16:15 UTC (right) with superimposed contours of lightning activity as detected by the ZEUS network during the last 15 minutes. The red circle in the right panel indicates the Rome area observed by the CNR ISAC Polar 55C radar

Figure 4.37 shows the rainfall map over the Rome area at 16:15 UTC, as measured by the Polar 55C radar, indicating the presence of a heavy storm over Rome.
There is a "head" of very high values of rainfall rates corresponding to the head of a well structured convective system. With the aid of the cloud resolving model UV-NMS, we have analyzed at CNR ISAC the structure of the storm. Figure 4.38 shows the result of the simulation We recognized a self-sustaining mesoscale system linked to a strong gust front. In the panel on the left, the mature stage of the event simulated by the Mesoscale Model, viewed from S-W, is presented. The cloud field (grey) and low level wind arrows are shown. There is a clear line of shear with strong convergence. The gust front moves west, forcing the lift of moist air carried by the sea breeze (westerly flow). The panel on the right presents the thermal field at ground level with winds and updraft (solid surfaces) viewed from S-E.
In conclusion, it was a very strong and well structured convective system; very heavy rainfall and hail were observed over Rome, with hailstones of big dimensions (some centimeters).

Figure 4.39 and 4.40 show the brightness temperatures at 85 and 37 GHz, horizontal and vertical polarization, obtained from SSM/I radiometer onboard satellite DMSP F-15, on the same day at 16:15 UTC. In both figures 4.37 and 4.39, the heavy storm over the Rome area is quite evident. The corresponding retrieval results of the BAMPR algorithm are shown in figures 4.41 and 4.42.

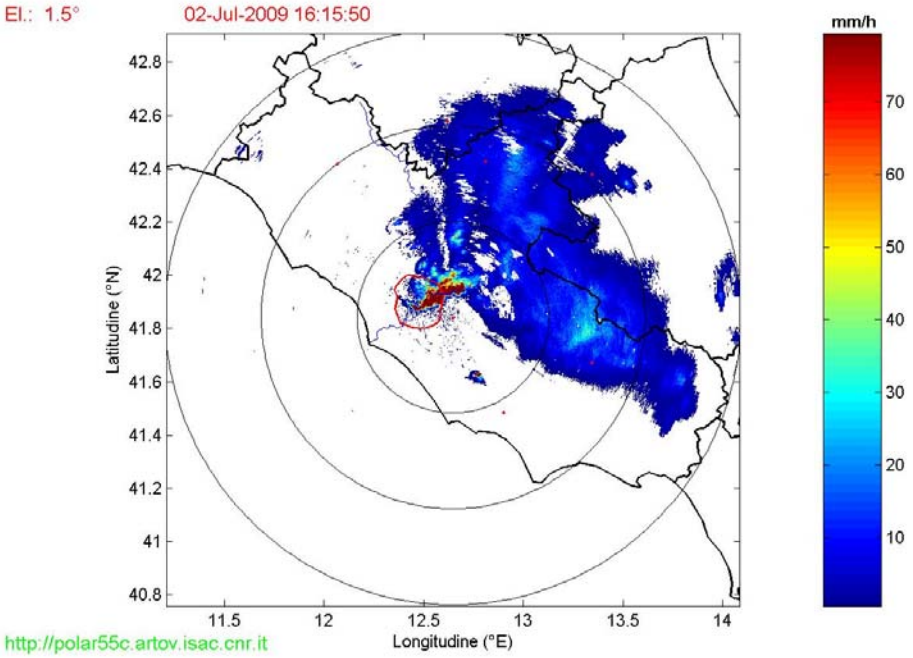

Fig. 4.37 - Rainfall rates measured on 2 July 2009 at 16:15 UTC by the CNR-ISAC C-band polarimetric Doppler radar Polar 55C – note that the Rome area is represented by the red circle.

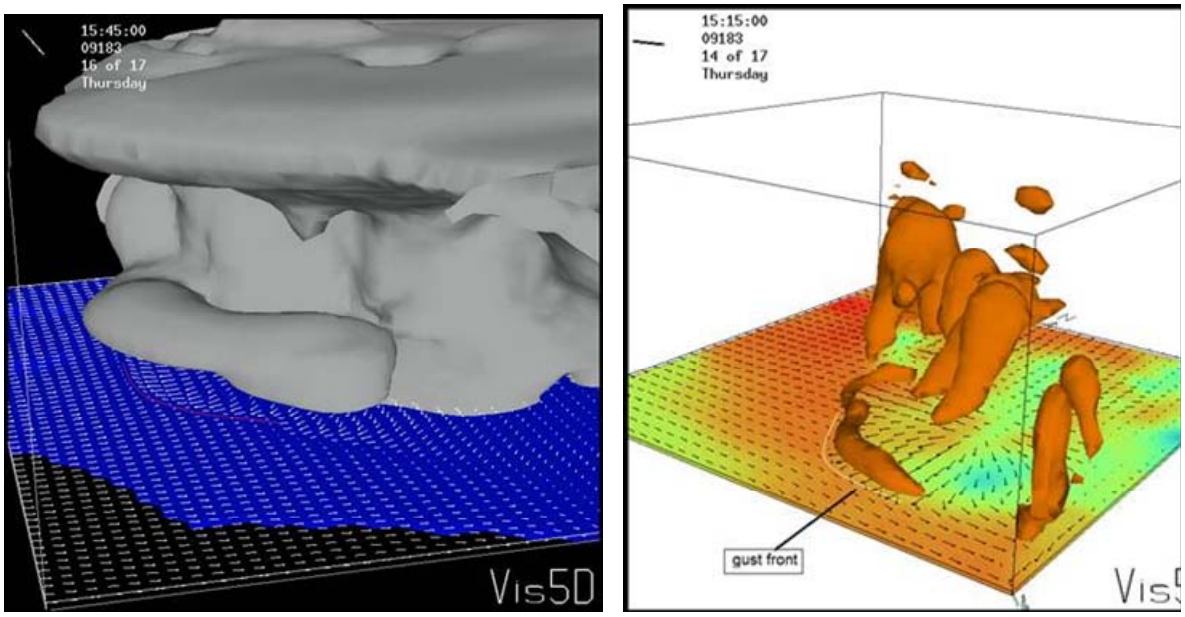

Fig. 4.38 – Model simulation of the event. Left panel: cloud field (grey) and low level wind arrows. The blue area shows the land. Right panel: thermal field, low level winds and updrafts (solid).

The CRD version of the database is used, i.e. the one without dynamical tags. Figure 4.41 shows the surface rain rate and points out the high values of rain rate (up to about 20-25 mm/h) over Rome area.

Figure 4.42 shows, in the left panel the number of profiles of CRD, for each pixel, contributing to the retrieval (common logarithm); in the right panel the relative variance (Bayesian variance to rain rate ratio) (mm/h). For each pixel a large number of profiles from the CRD database is selected for the Bayesian retrieval. A greater number of profiles are selected for low rain rates, depending on the structure of CRD that has a profile majority corresponding to low rain rate values. As a consequence, the retrieval uncertainty, as measured by the relative Bayesian variance, may be as large as the retrieved rain rate, thus calling for a more constrained retrieval (such as in the CDRD approach).

Figure 4.43 compares the satellite retrievals over Rome area with the corresponding radar measurements of figure 4.37. Note that to this end, it is found convenient to reduce radar measurements and satellite retrievals to a common resolution. A smoothing procedure (3x3 filter) has then been applied to the data. Evidently, there is a good agreement both in terms of precipitation path and rain rate values, even though BAMPR retrieval slightly under estimates the rain rate. Note, however, that while the fit of the scatterplot is close to the bisector, there is a high spread of the data.

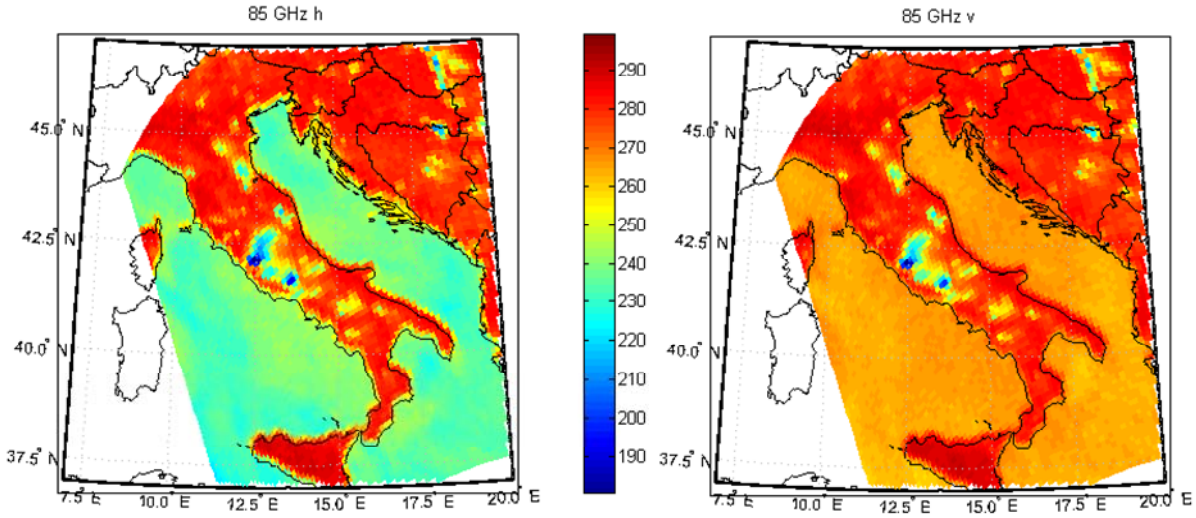

Fig. 4.39 – Case study Rome, 2 July 2009, 16:15 UTC. Microwave brightness temperatures (K) at 85 Ghz (H and V) as measured by the SSM/I radiometer onboard the DMSP F-15 satellite

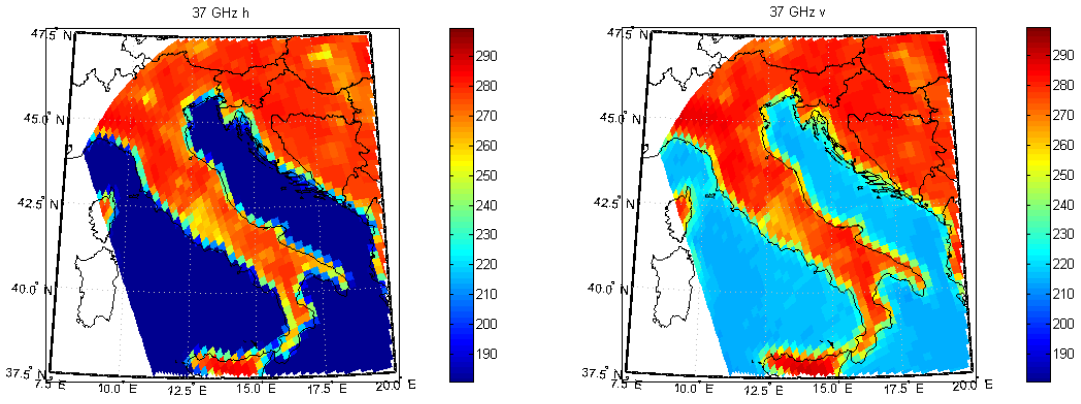

Fig. 4.40 – Case study Rome, 2 July 2009, 16:15 UTC. Microwave brightness temperatures (K) at 37 GHz (H and V) as measured by the SSM/I radiometer onboard the DMSP F-15 satellite

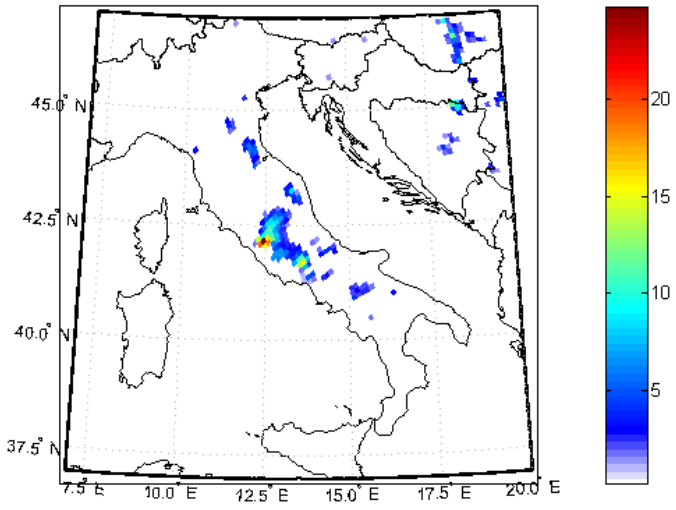

Fig. 4.41 - Case study Rome, 2 July 2009, h 16:15 (DMSP F-15): Surface rain rate (mm/h) obtained by BAMPR algorithm (CRD version).

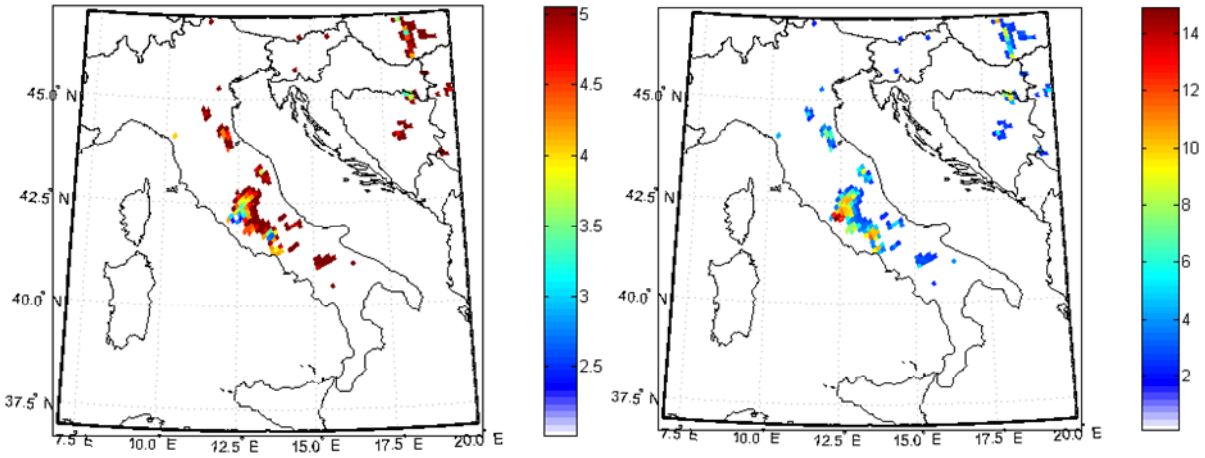

Fig. 4.42 - Case study Rome, 2 July 2009, h 16:15 (DMSP F-15). Outputs of BAMPR algorithm: the panel on the left shows the number of profiles of CRD that contributed to the retrieval (common logarithm). The panel on the right shows the Bayesian variance to rain rate ratio (mm/h).

In order to check the performance of the CDRD version of the retrieval algorithm, a new retrieval has been performed for this case study using the dynamical tags. Also for this case study the tags selected for a preliminary analysis are: *vertical moisture flux at 50 mb AGL*, *vertical wind velocity at 700 mb (Omega)*, the *Convective Available Potential Energy (CAPE)* in addition to the *freezing level*. As pointed out in the previous analysis of the event, using the UV-NMS model, the lift of moist air and the vertical winds were relevant components of the convective system analyzed. The use of *CAPE* is aimed at inspecting the level of instability at the time of the measurements. *Freezing level* can represent, as already specified, a more general tag, that can contribute to a more correct selection of CDRD profiles.

The following figures, 4.44 and 4.45, show the values of these tags during the event. The circles in the figures delimitate the area selected for the comparison with radar.

From both panels in figure 4.44, changes of tag values corresponding to the disturbance are evident. In figure 4.45, values of *CAPE* in the Rome area are quite low (1000-1400 J/kg) as a consequence of the gradual conversion of the potential energy into kinetic energy during the evolution of the event. A large area of reduced values of *freezing level* over the central Italy is evident in the right panel of this figure.

These variations of tag values are presented in a more detailed way in figure 4.46, which concerns only the circled areas of previous figures 4.44 and 4.45. In the figure, the values of the *vertical moisture flux at 50 mb AGL* (top left panel), the *vertical wind velocity at 700 mb (Omega)* (top right panel) and *freezing level* (bottom panel) are shown. The *CAPE* is not presented in the figure.

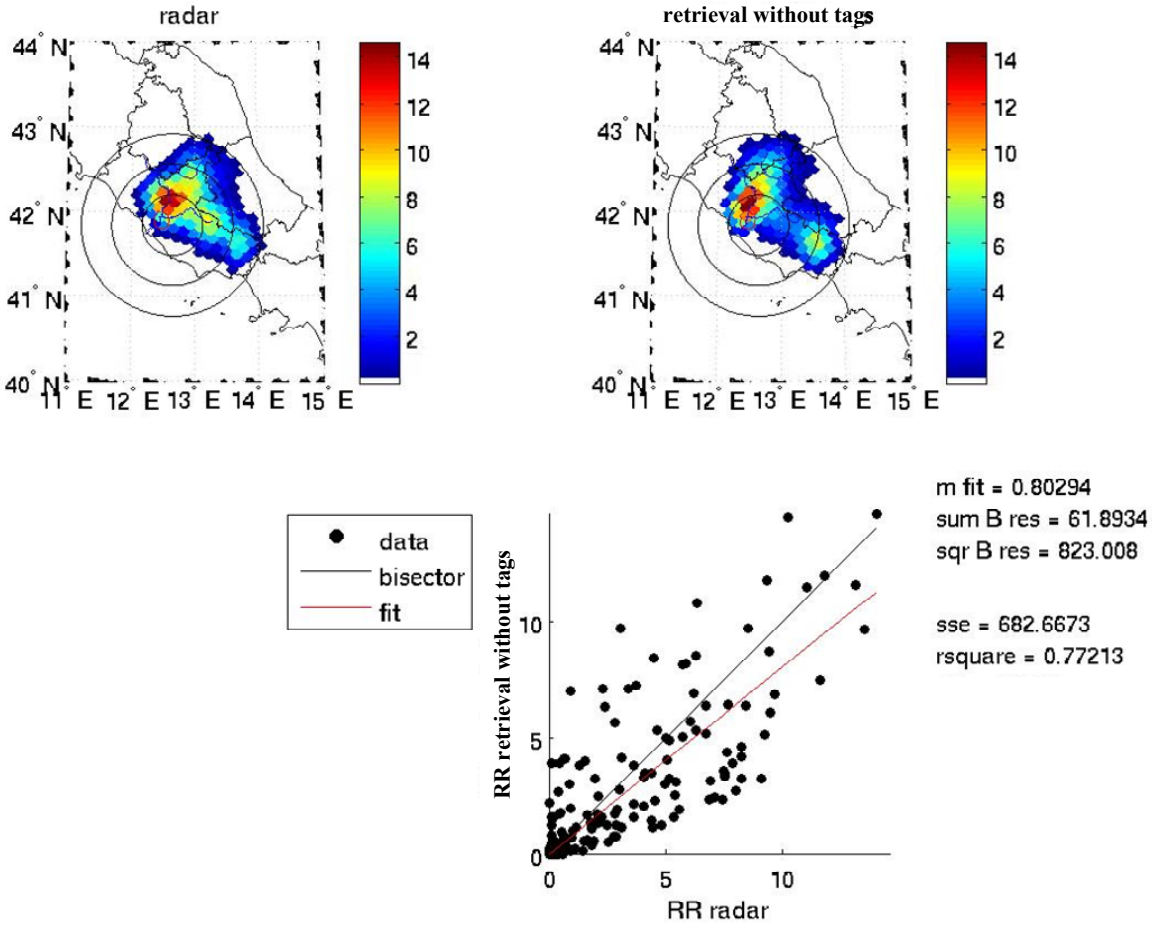

Fig. 4.43 – Average (see the text for more details) surface rain rates (mm/h) measured by the Polar 55C radar (top left) and estimated by the BAMPR algorithm (top right) for the case study of 2 July 2009, 16;15 UTC. Bottom panel: scatterplot of satellite rainfall retrievals of top-right panel vs. corresponding radar measurements of top-left panel, with some statistic indexes.

The details suggest that, in this strong and well structured convective system, the *vertical moisture flux at 50 mb AGL* and the *vertical wind velocity at 700 mb (Omega)* should play an important role in the retrieval procedure, allowing a more correct selection of profiles in the CDRD. This fact is confirmed by figures 4.47 and 4.48 that present three scatterplots concerning the distribution of the profiles of CDRD with respect to these tags and the rain rate.

Particularly, fig. 4.47 shows, in the panel on the left, the scatterplot of the *vertical wind velocity at 700 mb (Omega)* and the rain rate (the log of occurrences of profiles in CDRD is shown).

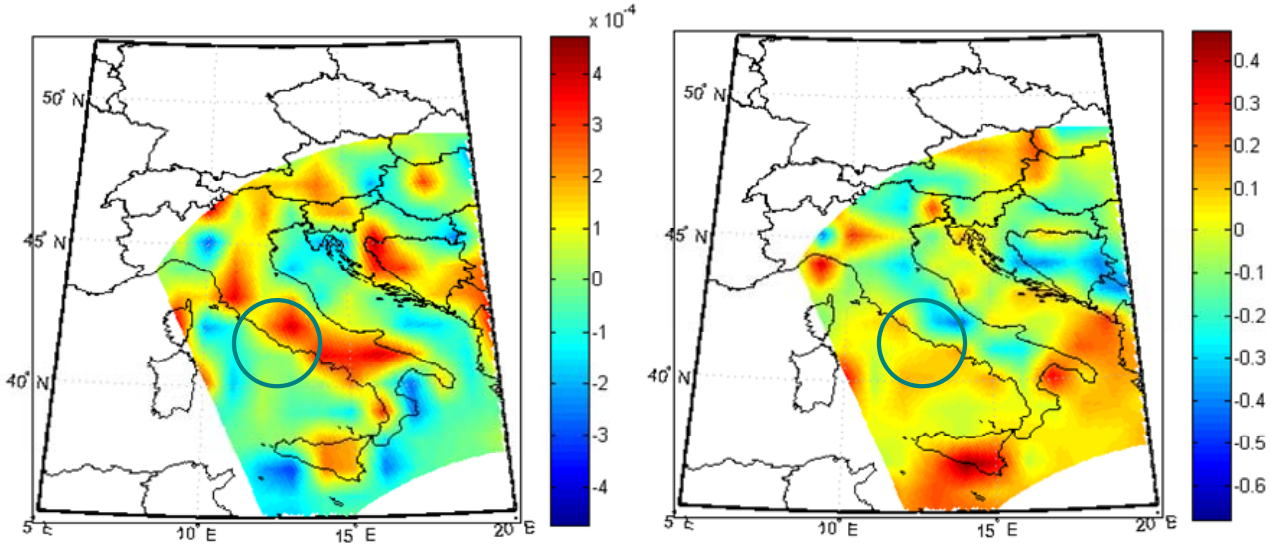

Fig. 4.44 – Values of *vertical moisture flux at 50 mb AGL* ($g*m^{-2}*s^{-1}$) (left panel), and *vertical wind velocity at 700 mb (Omega)* (Pa/s) (right panel), during the event of 2 July 2009 h 16:15. The circles show the area analyzed in the comparison with radar measurements.

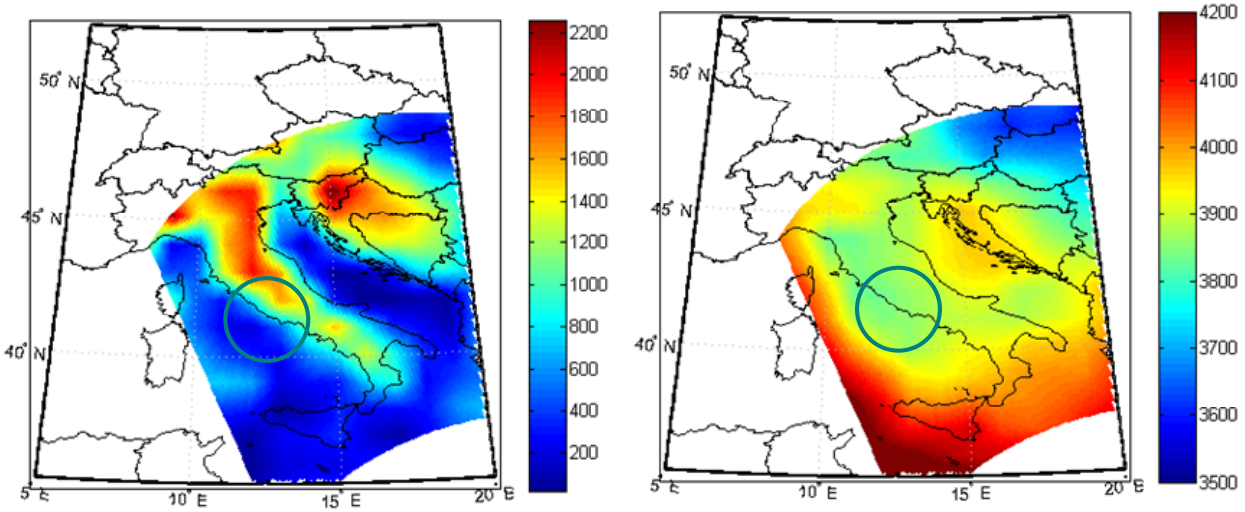

Fig. 4.45 - Values of the *Convective Available Potential Energy (CAPE)* (J/kg) (left panel), and *freezing leve*l (m) (right panel), during the event of 2 July 2009 h 16:15. The circles show the area analyzed in the comparison with radar measurements.

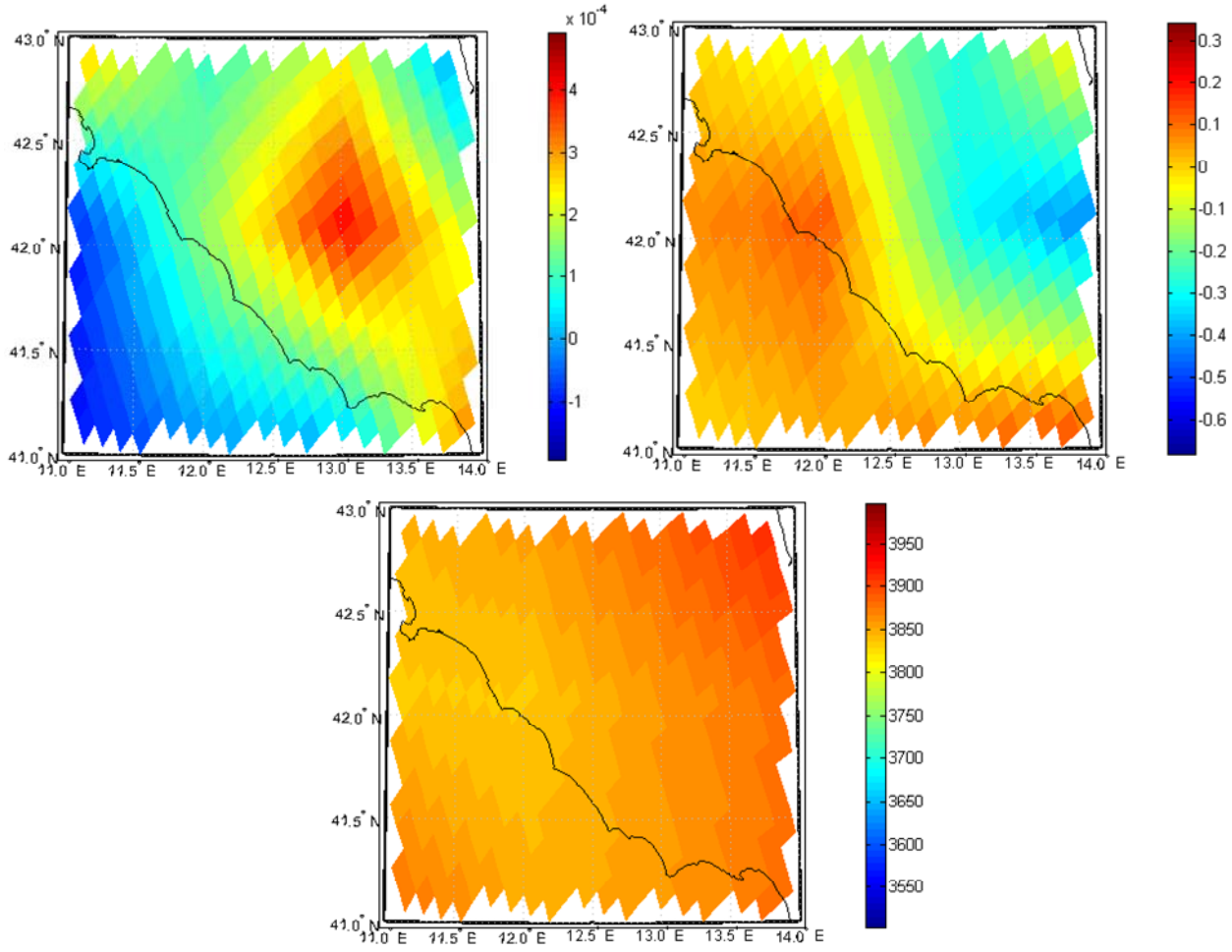

Figure 4.46 – Details of the values of tags *vertical moisture flux at 50 mb AGL* ($g*m^{-2}*s^{-1}$) (top left panel), *vertical wind velocity at 700 mb (Omega)* (Pa/s) (top right panel), and *freezing level* (m) (bottom panel) in the circled areas of figures 4.44 and 4.45.

In the panel, the range of this tag in the detailed area of figure 4.46 (top right panel) is also specified. In the panel on the right of figure 4.47 a similar scatterplot for the *vertical moisture flux at 50 mb AGL* is shown.

It is evident in the figure that both the ranges include the area with highest occurrences (red area) in the database. This means that the examined event is well represented in the CDRD. Moreover, the figure points out that both the tags can allow a narrow selection in the database. This fact is confirmed by figure 4.48, that shows the scatterplot of *vertical moisture flux at 50 mb AGL* (vertical axis) and *vertical wind velocity at 700 mb (Omega)* (horizontal axis). In the figure the good selectivity of the two tags is evident.

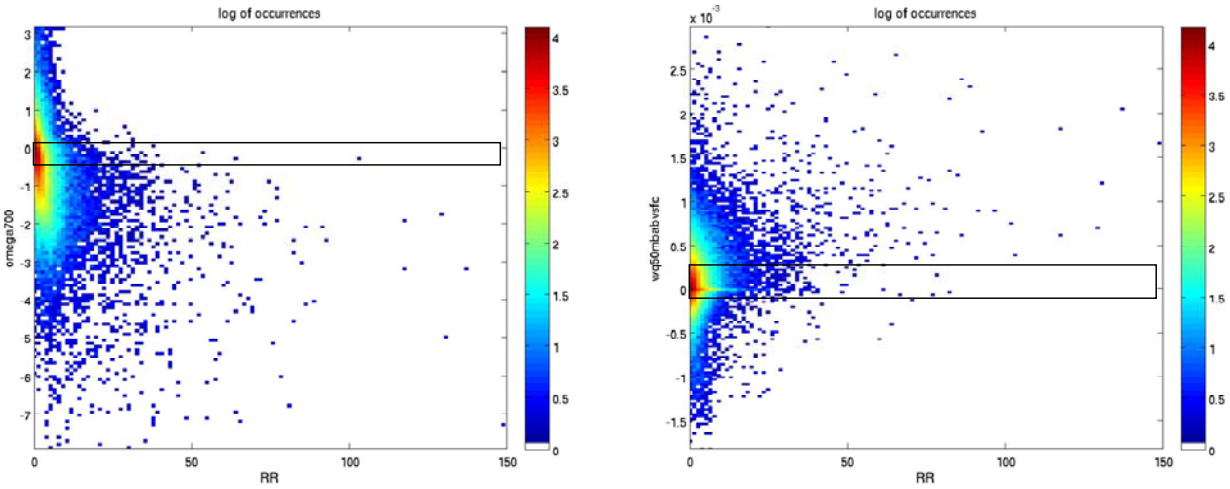

Fig. 4.47 – Scatterplot of *vertical wind velocity at 700 mb (Omega)* (Pa/s) and rain rate (mm/h) (left panel), and of *vertical moisture flux at 50 mb AGL* ($g*m^{-2}*s^{-1}$) and rain rate (mm/h) (right panel). On the vertical axes, the rectangles show the ranges of the two tags in the selected areas of fig. 4.46.

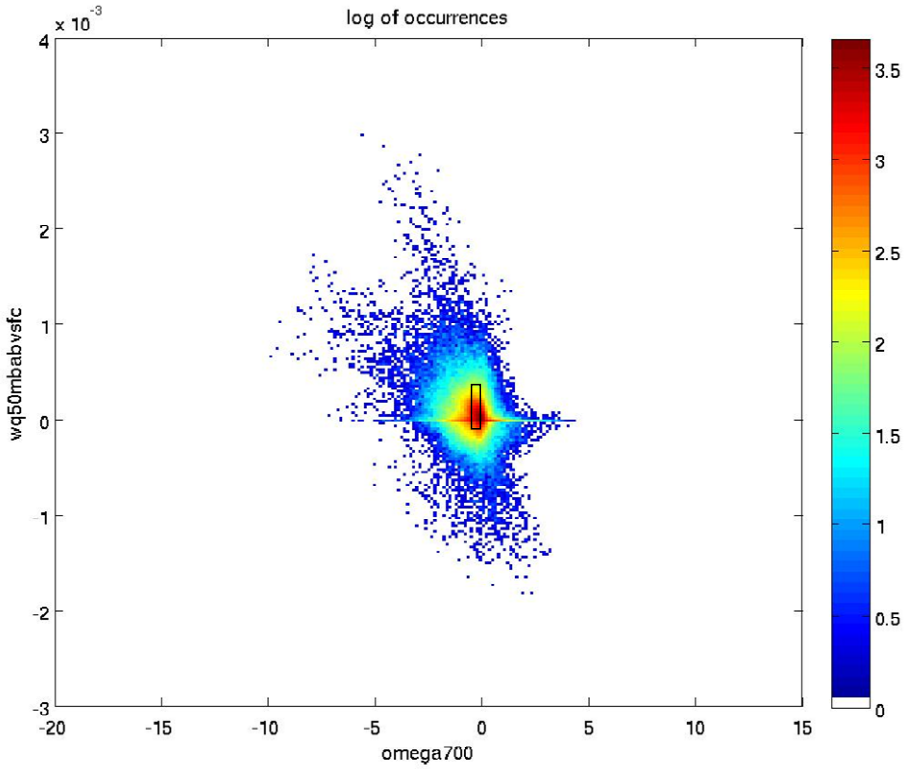

Fig. 4.48 – Scatterplot of *vertical moisture flux at 50 mb AGL* ($g*m^{-2}*s^{-1}$) (vertical axis) and *vertical wind velocity at 700 mb (Omega)* (Pa/s) (horizontal axis) for the profiles of CDRD. The common logarithm is used for the occurrences. The rectangle shows the ranges of the two tags in the selected area of fig. 4.46.

Also for this case study, the positive contribution of *freezing level* has been tested in a preliminary rough selection of profiles in terms of season and latitude of the event.

In the following figures 4.49 – 4.51 the effects of the use of tags on surface rain rate and relative Bayesian variance are shown.
Figure 4.49 presents the scatterplots of rain rate values (left panel), and relative variance values (right panel) without tags (horizontal axis) and with the use of the tags *freezing level* and *vertical wind velocity at 700 mb (Omega*) (vertical axis). With these tags, rain rate values are slightly reduced, and the relative variance values are reduced in a more evident way.
Figure 4.50 presents the scatterplots as in the previous figure, but using the tags *freezing level* and *vertical moisture flux at 50 mb AGL*. The effect is different from the previous figure.
Rain rate values are slightly increased, while variance values are reduced.

Figure 4.51 shows the combined effect of the three tags *freezing level, vertical moisture flux at 50 mb AGL* and *Omega.* The use of the three tags produces a slight increase of the rain rate and an evident reduction of the relative variance.

Figure 4.52 points out the effect of tags on the number of profiles selected from the CDRD database. In the figure the mean number of profiles selected for a pixel is shown when tags are not used, and when one (*freezing level)*, two (adding *vertical moisture flux at 50 mb AGL)* or three tags (adding *vertical wind velocity at 700 mb (Omega*) are used. The figure clearly shows the relevant effect on the screening of profiles produced by the *freezing level* (reduction of 60%). Altogether, the three tags cause a reduction of about 80% in the selection of profiles.

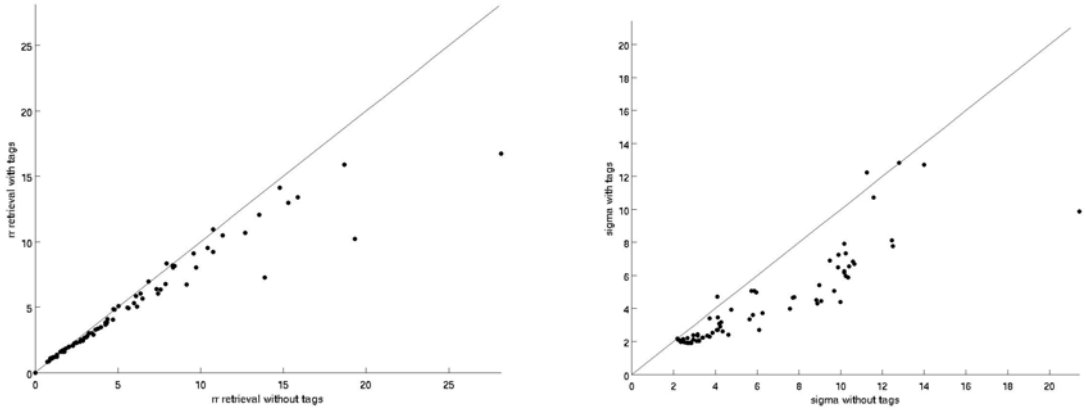

Fig. 4.49 – Case study Rome, 2 July 2009, h 16:15 (DMSP F-15). Scatterplot of rain rate values (mm/h) (left panel), and relative variance values (mm/h) (right panel), without tags (horizontal axis) and with the use of the tags *freezing level* and *vertical wind velocity at 700 mb (Omega)* (vertical axis).

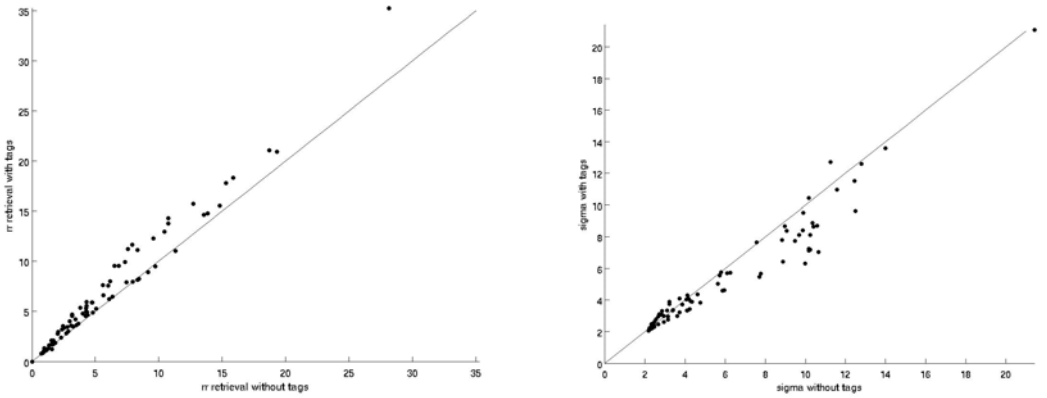

Fig. 4.50 – Case study Rome, 2 July 2009, h 16:15 (DMSP F-15). Scatterplot of rain rate values (mm/h) (left panel), and relative variance values (mm/h) (right panel) without tags (horizontal axis) and with the use of the tags *freezing level* and *vertical moisture flux at 50 mb AGL* (vertical axis).

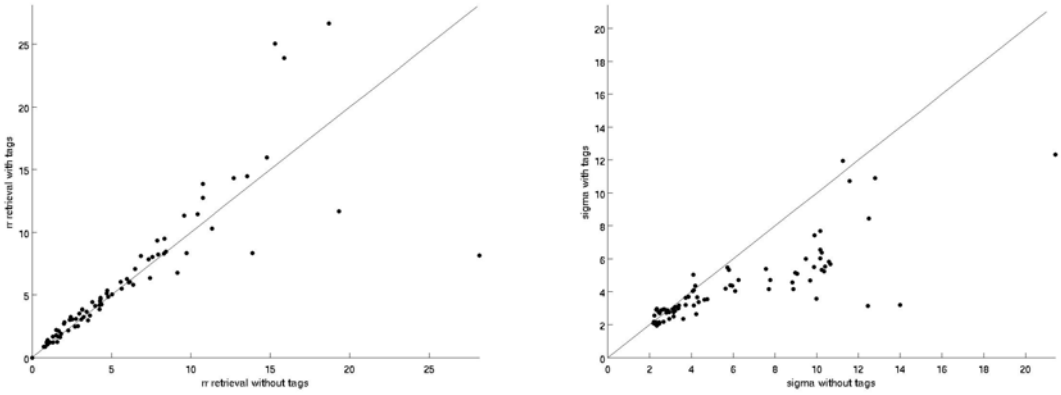

Fig. 4.51 – Case study Rome, 2 July 2009, h 16:15 (DMSP F-15). Scatterplot of rain rate values (mm/h) (left panel), and relative variance values (mm/h) (right panel), without tags (horizontal axis) and with the use of the tags *freezing level* , *vertical wind velocity at 700 mb (Omega)*, and *vertical moisture flux at 50 mb AGL* (vertical axis).

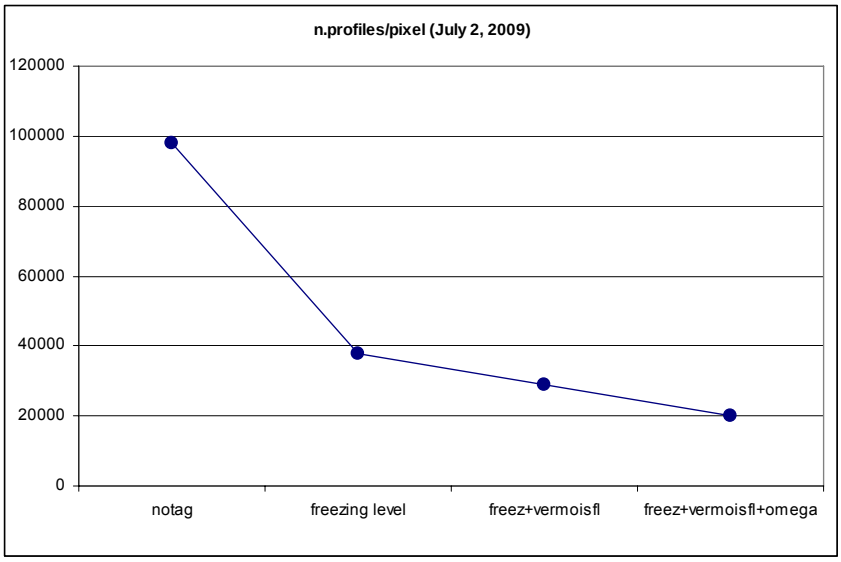

Fig. 4.52 – Case study Rome, 2 July 2009, h 16:15 (DMSP F-15). Decrease in the mean number of profiles for a pixel selected from the CDRD database using successively one tag (*freezing level*), two tags (adding the *vertical moisture flux at 50 mb AGL*), or three tags (adding *vertical wind velocity at 700 mb (Omega*)).

Figure 4.53 shows the comparison of the retrieval using three tags (*freezing level, vertical moisture flux at 50 mb AGL* and *vertical wind velocity at 700 mb (Omega))* with the radar, in a similar fashion to figure 4.43. There is clearly a closer agreement with the radar measurements with respect to fig. 4.43. The underestimation of previous retrieval is attenuated and the spread of the data is significantly reduced. The angular coefficient of the fit (m fit parameter) has increased from 0.8029 to 0.9306, the sum of square due to error (sse index) has decreased from about 682 to about 598, and the square of the correlation (rsquare index) has increased from about 0.772 to about 0.838.. The other statistical indexes confirm, similarly, the improvement in retrieval.

This result also confirms the positive effects of the tags on improving the screening of profiles, selecting the subset that really describes the analyzed event.

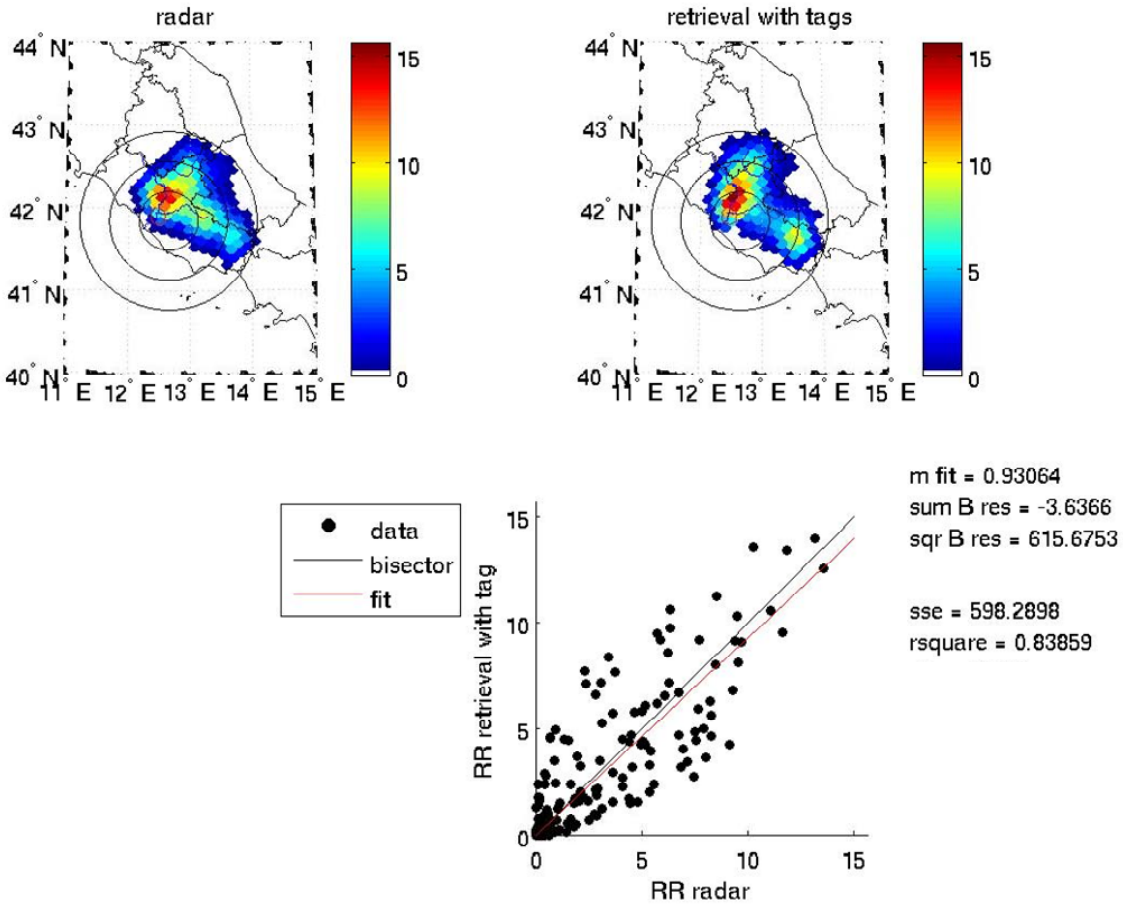

Fig. 4.53 – Case study Rome, 2 July 2009, h 16:15 (DMSP F-15). Same as figure 4.5.30 but using the tags *freezing level, vertical moisture flux at 50 mb AGL*, *and vertical wind velocity at 700 mb (Omega)* in the retrieval procedure (see text for more details).

4.4.4 POD and FAR

The evaluation of retrieval accuracy has also been performed using the indexes POD (Probability Of Detection) and FAR (False-Alarm Index) (Dixon and Wiener 1993). The definition of these indexes is based on the table of figure 4.54, which compares, for each area examined, the results (rain rate) of the BAMPR retrieval and the radar measurements. For a given range of rain rate (for example 0-5 mm/h) there is a "success (a)" in the comparison if both the results are in this range. There is a "failure (c)" if only the radar result is in this range, while the retrieval is out. There is a "false alarm (b)" if only the retrieval is in this range, while the radar measurement is out. The indexes POD and FAR are then computed as follows

		radar	
		yes	no
retrieval	yes	a	b
	no	c	d

Fig. 4.54 – Table for the comparison of BAMPR retrievals with radar measurements, used for the POD and FAR computation.

$$POD = \frac{n_a}{n_a + n_c} \qquad FAR = \frac{n_b}{n_a + n_b}$$

where n_a, n_b and n_c represent the numbers of "success", "false alarm", and "failure", respectively.
The following tables 4.2-4.5 show the values of POD and FAR obtained for the previously examined case studies. Each table presents: the ranges of rain rate in the first row, the values of the indexes in the study without tags in the second row, and the corresponding values of the indexes using tags in the third row.
The effect of the tags is evident in the tables; they increase the POD and reduce the FAR.

Tab. 4.2 November 4, 2009 – POD Index

0-5 mm/h	5-10 mm/h	10-15 mm/h	15-20 mm/h	20-25 mm/h	
0.25	0.20	0.35	0.35	0.40	no tags
0.25	0.50	0.60	0.70	0.60	with tags

Tab. 4.3 November 4, 2008 – FAR Index

0-5 mm/h	5-10 mm/h	10-15 mm/h	15-20 mm/h	20-25 mm/h	
0.30	0.40	0.30	0.35	0.50	no tags
0.26	0.25	0.20	0.15	0.40	with tags

Tab. 4.4 July 2, 2009 – POD Index

0-5 mm/h	5-10 mm/h	10-15 mm/h	15-20 mm/h	
0.40	0.40	0.45	0.65	no tags
0.50	0.75	0.65	0.70	with tags

Tab. 4.5 July 2, 2009 – FAR Index

0-5 mm/h	5-10 mm/h	10-15 mm/h	15-20 mm/h	
0.40	0.65	0.50	0.40	no tags
0.20	0.40	0.30	0.30	with tags

4.5 Comparison with the "NESDIS algorithm" of NOAA

In order to obtain a more complete evaluation of the results, a comparison between the CDRD algorithm and the operational algorithm of NOAA has been carried out. This algorithm, sometimes referred to as the "Ferraro algorithm" (Ferraro 1997), the "NESDIS algorithm" and the "FNMOC/EDR algorithm" (Fleet Numerical Meteorology and Oceanography Center, Environmental Data Record) is an 85 GHz scattering technique over land, and a combination 85 GHz scattering and 19/37 GHz emission approach over ocean. It is empirically tuned with ground based radar data. The algorithm has been available for about ten years, and it still serves as a benchmark algorithm that more advanced, and physically based approaches seek to improve upon. Moreover it is still utilized in many operational projects.

4.5.1 The "NESDIS algorithm"

The NOAA rain rate estimate is substantially based on two algorithms: an 85 GHz scattering-based algorithm (over land and ocean) and a 19/37 GHz emission-based algorithm (over ocean). The 85 GHz scattering-based algorithm uses the Scattering Index (SI) developed by Grody (1991) and described in chapter 2 (section 2.5) and chapter 3 (section 3.2.2). Two different Scattering Indexes are used for land (see formula (3.3.28)) and for ocean (formula 3.3.25). A value of SI greater than 10 K is considered as a good global indicator of rain. The following relationships are then used to calculate the rain rate (R)

Land $R = 0.00513 \cdot SI_L^{1.9468}$ (see chapter 2, formula (2.48))

Ocean $R = 0.00188 \cdot SI_O^{2.0343}$

where R is in mm/h.

Over ocean, an additional emission-based algorithm (the liquid water path – LWP) is used. The expressions utilized are (see Chapter 3, Section 3.2.2.1)

$$LWP_{19V} = -2.70[\ln(290 - Tb_{19V}) - 2.84 - 0.40 \ln(290 - Tb_{22V})]$$
$$LWP_{37V} = -1.15[\ln(290 - Tb_{37V}) - 2.99 - 0.32 \ln(290 - Tb_{22V})].$$

The rain is assumed present if either $LWP_{19V} > 0.60$ kg m^{-2} or if $LWP_{37V} > 0.20$ kg m^{-2}. A rain rate is then retrieved using the relationship (Ferraro and Marks 1995)

$$R = 0.001707\ (100\ LWP)^{1.7359}$$

where LWP value represents either the LWP_{19V} or the LWP_{37V} value.
Since the resulting rain rates (land and ocean) increase exponentially for higher SI values, R above 35 mm/h is set to 35 mm/h. However, it remains a tendency to overestimate, over land, in heavy rain events.

4.5.2 The comparison

To carry on the comparison, the events previously analyzed in sections 4.4.2 and 4.4.3 have been studied using the NOAA algorithm.
The results are shown in figures 4.55 and 4.56. In the figures, radar measurements and the satellite retrievals (CDRD and NOAA) are reduced to a common resolution of 25 km (NESDIS algorithm resolution).

Fig. 4.55, concerning the event of November 4, 2008 over Lazio, shows the rain rate (mm/h) as it results from CDRD estimate (top left), from NESDIS estimate (top right), and from radar (CNR-ISAC C-band polarimetric Doppler radar Polar 55C) measurements (bottom).
The close agreement between the CDRD and radar results is confirmed in the figure. The NESDIS algorithm shows some gaps in the detection of rain rate over coast and an overestimation over the heavy rain area.

While the overestimation is an expected result due to the expression used (2.48) to estimate the rain rate, as already underlined in section 4.5.1, the gaps at low rain rate values can be attributed to the particular processing procedure utilized by the NESDIS algorithm (Ferraro 1997, Ferraro et al. 1998) for pixels over coasts. In fact this algorithm analyses a 5x5 grid of SSM/I A-scan observations surrounding the pixel for which the retrieval is performed. Any coastline or land identified in this grid is classified as land. In other words, the NESDIS simply uses the ” land algorithm” over the coast and near coast FOVs. It follows that the sensitivity to emission-type rain is lost along the coast, and an underestimation of rain rate is then possible.

Figure 4.56, concerning the event over Rome on 2 July 2009, shows similar results to the previous figure. That is, it points out a close agreement between CDRD estimation of rain rate and radar measurements, and an overestimation of the NESDIS algorithm.

The following figures 4.57 and 4.58 present the scatterplots of CDRD and NESDIS rainfall retrievals vs. corresponding radar measurements. In the figures, radar measurements and CDRD retrievals have been reduced to the resolution of NESDIS retrieval (about 25 km). Figure 4.57 refers to the event over Lazio on 4 November 2008, and figure 4.58 to the event over Rome on 2 July 2009.

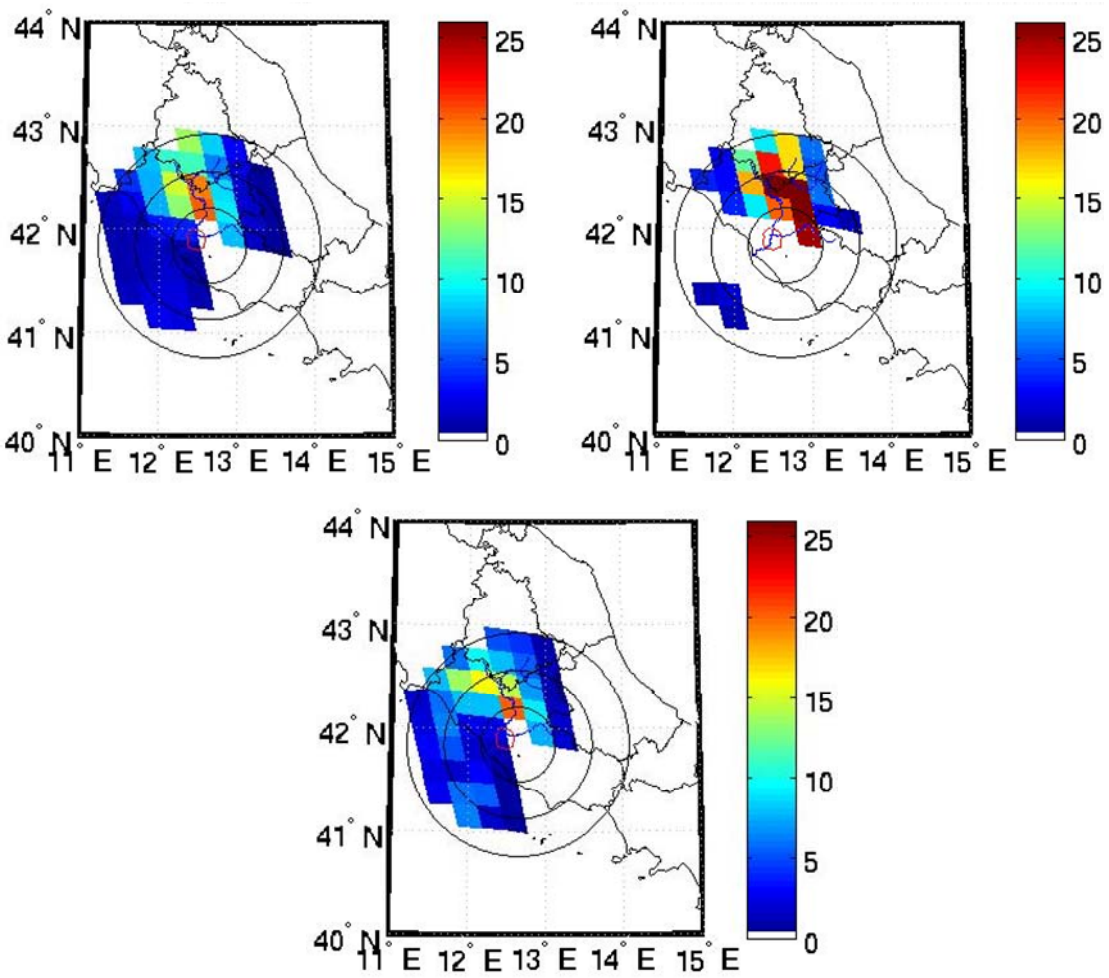

Fig. 4.55 - Case study over Lazio, November 4, 2008, 16.18 UTC. Surface rain rate values (mm/h) obtained using the CDRD algorithm (top left), NOAA (top right) algorithm, and radar (CNR ISAC) measurements (bottom).

In each figure, the left panel concerns the comparison of radar measurements with CDRD estimated rain rate, and the right panel concerns the comparison of radar measurements with NESDIS estimated rain rate.

Both the figures confirm the results that already came out from previous analysis of figures 4.55 and 4.56: there is a close agreement between radar and CDRD results, and some discrepancies between radar and NESDIS results, due to the overestimation and the gaps over coasts (case November 4, 2008).

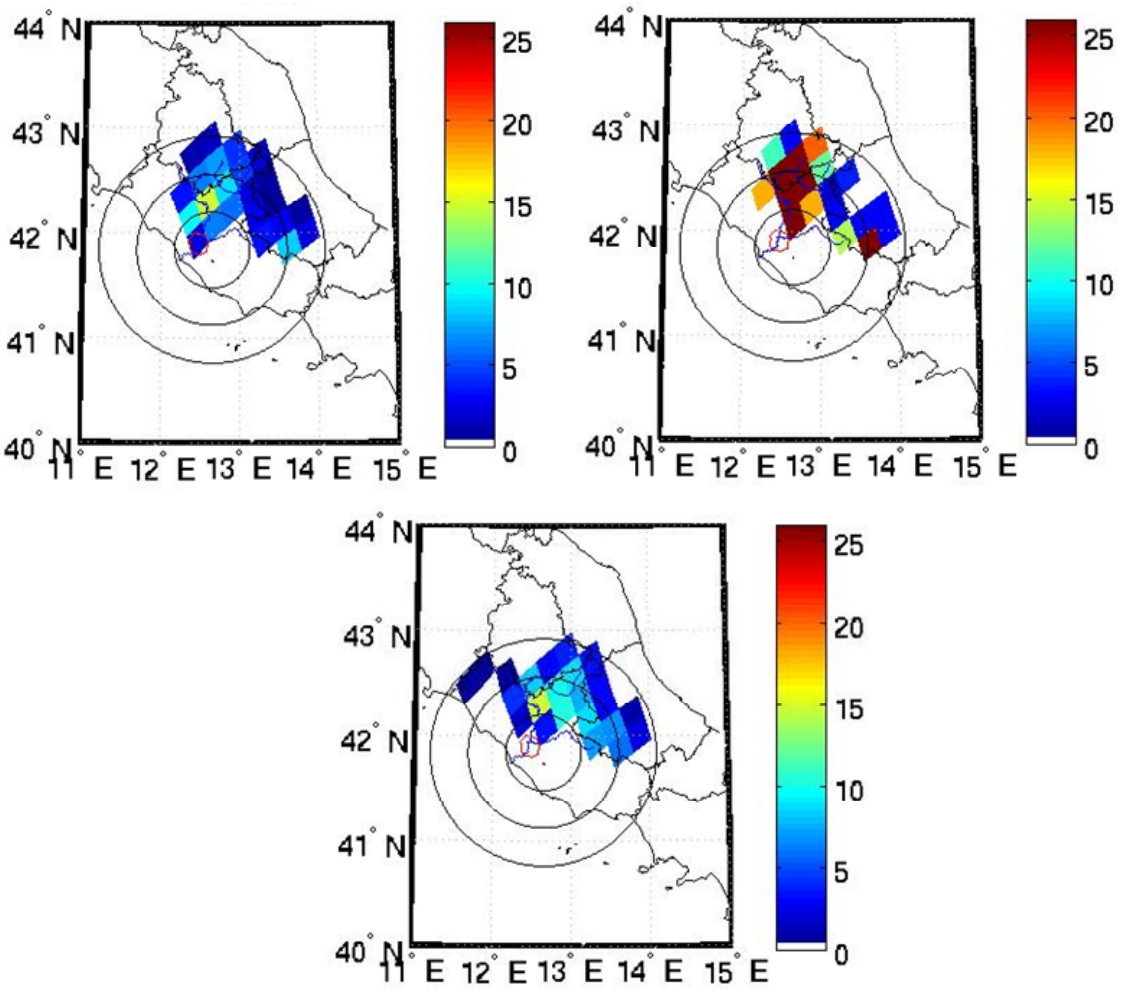

Fig. 4.56 – Case study Rome, 2 July 2009, 16:15 UTC. Surface rain rate values (mm/h) obtained using the CDRD algorithm (top left), the NOAA (top right) algorithm, and the radar (CNR ISAC) measurements (bottom).

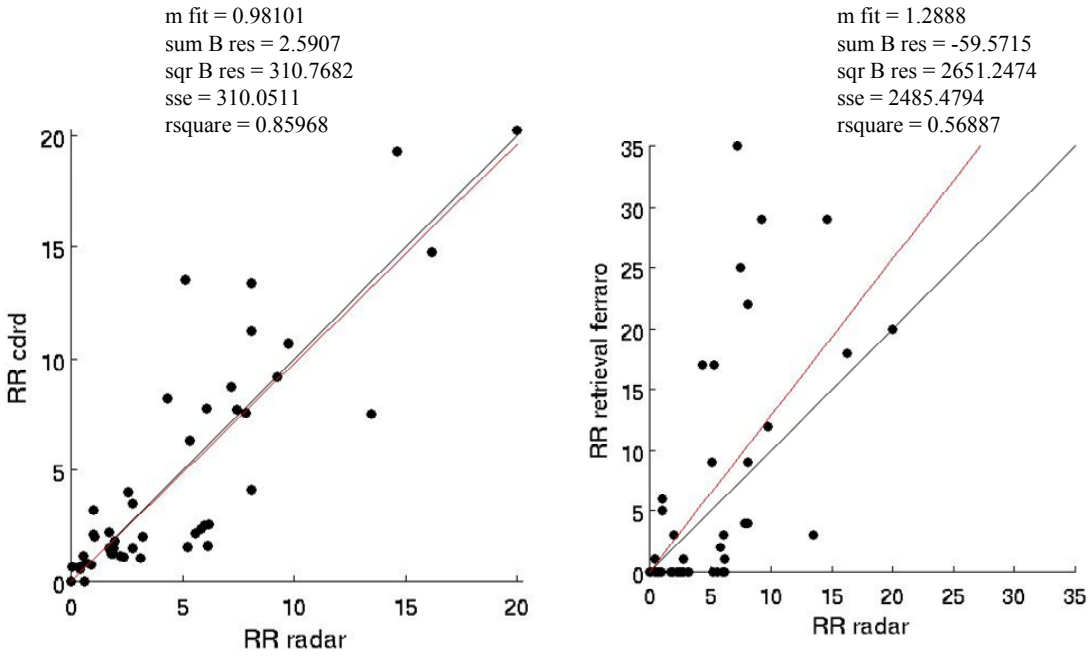

Fig. 4.57 – Case study over Lazio, November 4, 2008, 16.18 UTC. Scatterplot of rain rate (mm/h) of CDRD (left panel) and NESDIS (right panel) estimates vs. radar measurements.

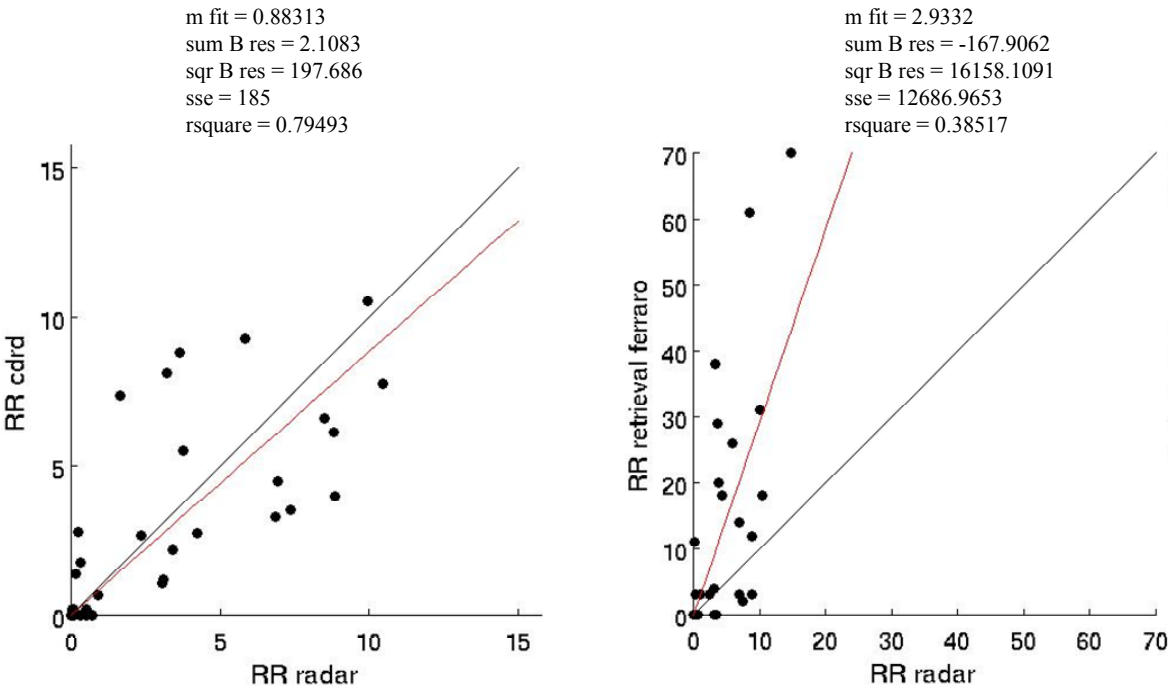

Fig. 4.58 – Case study Rome, 2 July 2009, 16:15 UTC. Scatterplot of rain rate (mm/h) of CDRD (left panel) and NESDIS (right panel) estimates vs. radar measurements.

CONCLUSIONS

In this thesis we have investigated some important issues regarding the retrieval of precipitation from satellite-based microwave measurements.
Although microwave radiometry retrieval techniques for the estimation of rainfall have advanced considerably over the past years, further developments are still necessary and some aspects of these techniques are currently being investigated in research activities.

The activity we have carried out in this thesis concerned first the implementation and the development of the complete BAMPR algorithm, based on the Bayesian estimation theory, for the SSM/I, SSMIS and AMSR-E data (brightness temperatures) processing. The algorithm is described in chapter 3, together with the screening procedures we have selected for the correct processing of pixels. In the chapter, the characteristics of the database used (Cloud Radiation Database), and some tests we have performed on it are also presented.
The activity was then focused on the introduction of the "dynamical tags" in the retrieval procedure of BAMPR, to be combined with brightness temperatures. This development we have carried out on the algorithm is aimed at reducing the "ambiguity" or the "non-uniqueness" of the database that is a severe limit for retrieval methodology. The new BAMPR algorithm and its utilization with three "dynamical tags" in two case studies over Lazio are presented in chapter 4.

The main results of our studies are summarized in the following points:

- We have studied in depth the "screening" problem, particularly over coasts, considering that rainfall retrieval over coasts is crucial for regions like Italy where a high portion of the region is considered to be "coastal". Moreover, the retrieval presents real difficulties because of the presence of sea and land areas in the same footprint, but with different emission signatures. We have analyzed and tested many possible screening procedures and we have defined those that optimize the retrieval of BAMPR. The results are reported in chapter 3.

- We have considered the problems of uncertainties in the retrieval procedure (forward-inverse problems) and the "non-uniqueness" of the database (CRD). The consequence of these problems is that precipitation and hydrometeor profiles obtained as a result of the retrieval algorithm were, in some cases, unrepresentative of the dynamical and thermodynamical state of the atmosphere under observation. Then we have recognized the need to introduce further information (dynamical tags), both in the retrieval procedure and in the database, about the "synoptic situation" of the considered event. We have implemented a new BAMPR algorithm, including tags and brightness temperatures in the Bayesian estimation procedure, to be used with the new database (CDRD – Cloud Dynamics and Radiation Database). The results are reported in chapter 4.

- We have tested the performance of the new algorithm in different studies (the results of two studies over Lazio are reported in chapter 4). The values of tags were obtained from the GFS of NOAA. In the tests only three tags were used (*vertical wind velocity at 700 mb*

(Omega), *vertical moisture flux at 50 mb AGL*, and *freezing level*), which were certainly related to the structure of the events considered in the studies. The use of tags raises, in fact, many difficulties related to their selection depending on various factors, such as the characteristics of the meteorological event, their processing, and their different possible simultaneous utilizations. To evaluate the performance of the new algorithm, the results of the case studies have been compared with simultaneous radar (CNR-ISAC Polar55 radar) measurements. The comparison has shown a positive effect of tags, in terms of enhancement of the agreement between the results (rain rate) of new BAMPR retrieval and radar measurements, and reduction of the variance of retrieved rain rates.

- In order to further check the performance of the new BAMPR, we have compared the results of the case studies with those obtained using the "NESDIS algorithm" of NOAA (chapter 4). The check has confirmed the good results of new BAMPR, which resulted in a better agreement than NESDIS results, with radar measurements.

The retrieval system we have developed in this thesis has been inserted among the deliverables of the international research projects described in chapter 1. For this reason the implementation of BAMPR has been subjected to specifications and standards defined in the projects. The system is now in the phase of validation with the contribution of other partners, and then it will be transferred to the users.

The results obtained in this thesis have proved the real effectiveness of the dynamical tags in reducing the "ambiguity" of the CRD. Further developments of the research can analyze the effect of the many different tags possible in different atmospheric environments, and can then give a more complete assessment of the potential contribution of tags. New tags, as for example the Convective Available Potential Energy (CAPE), the Positive Vorticity Advection (PVA) at 550 mb, Wind Shear at 300 mb, and Surface Height seem to be interesting in this direction.

REFERENCES

R.F. Adler, E.B. Rodgers, "Satellite-observed latent heat release in a tropical cyclone", *Monthly Weather Review*, vol. 105, issue 8, pp. 956–963, August 1977.

R.F. Adler, A.J. Negri, P.R. Keehn, I.M. Hakkarinen, "Estimation of monthly rainfall over Japan and surrounding waters from a combination of low-orbit microwave and geosynchronous IR data", *Journal of Applied Meteorology*, vol. 32, pp. 335-356, Feb.1993.

L.J. Allison, E.B. Rodgers, T.T. Wilheit , R.W. Fett, "Tropical cyclone rainfall as measured by the Nimbus Electrically Scanning Radiometer", *Bulletin of the American Meteorological Society*, vol. 55, pp. 1074-1090, 1974.

M. Barkat, "Signal detection and estimation", Artech House, 1991.

E.C. Barret, C. Kidd, "Rainfall monitoring by SSM/I in the midlatitudes", *Fifth Conf. Int. Satellite Meteor. Oceanog.*, London, England, Amer. Meteor. Soc., pp. 210-214, 1990.

A. Basist, D. Garrett, R. Ferraro, N. Grody, K. Mitchell, "A comparison between snow cover products derived from visible and microwave satellite observation", *Journal of Applied Meteorology*, Vol. 35, issue 2, pp. 163–177, February 1996.

A. Basist, N. C. Grody, T. C. Peterson, C. N. Williams "Using the special sensor microwave/imager to monitor land surface temperatures, wetness, and snow cover", *Journal of Applied Meteorology*, vol. 37, issue 9, pp. 888–911, September 1998.

A. Basist, C. Williams Jr., N. Grody, T.F. Ross, S. Shen, A.T.C. Chang, R. Ferraro, M. J. Menne, "Using the special sensor microwave imager to monitor surface wetness", *Journal of Hydrometeorology* , vol. 2, issue 3, pp. 297–308, June 2001.

P. Bauer, L. Schanz, L. Roberti, "Correction of the three-dimensional effects for passive microwave remote sensing of convective clouds", *Journal of Applied Meteorology*, vol. 37, pp. 1619–1632, 1998.

P. Bauer, "Over-Ocean rainfall retrieval from multisensor data of the tropical rainfall measuring mission. Part I: Design and evaluation of inversion databases", *Journal of Atmospheric and Oceanic Technology*, vol. 18, issue 8, pp. 1315–1330, August 2001.

P. Bauer, P. Amayenc, C. D. Kummerow, E. A. Smith, "Over-ocean rainfall retrieval from multisensor data of the tropical rainfall measuring mission. Part II: Algorithm implementation", *Journal of Atmospheric and Oceanic Technology*, vol. 18, Issue 11, pp.1838–1855, November 2001.

P. Bauer, J.F. Mahfouf, W.S. Olson, F.S. Marzano, S. Di Michele, A. Tassa, A. Mugnai,"Error analysis of TMI rainfall estimates over ocean for variational data assimilation", *Quarterly Journal of the Royal Meteorological Society*, vol. 128, issue 584, Part B, pp. 2129-2144, July 2002.

P. Bauer, E Moreau, S. Di Michele, "Hydrometeor retrieval accuracy using microwave window and sounding channel observations", *Journal of Applied Meteorology*, vol. 44, issue 7, pp. 1016–1032, July 2005.

W. Berg, R. Chase, "Determination of mean rainfall from the Special Sensor Microwave/Imager (SSM/I) using a mixed lognormal distribution", *Journal of Atmospheric and Oceanic Technology*, vol. 9, issue 2, pp. 129–141, April 1992.

W. Berg, W. Olson, R. Ferraro, S. J. Goodman, and F. J. LaFontaine, "An Assessment of the First- and Second-Generation Navy Operational Precipitation Retrieval Algorithms", *Journal of the Atmospheric Sciences*, vol. 55, issue 9, pp. 1558–1575, May 1998.

C.F. Bohren, D.R. Huffman, "Absorption and Scattering of Light by Small particles", John Wiley & Sons, 530 pp., 1983.

S.A.A. Boukabara, F. Weng, Q Liu, "Passive microwave remote sensing of extreme weather events using NOAA-18 AMSUA and MHS", *IEEE Transaction on Geoscience and Remote Sensing*, vol. 45, n. 7, pp. 2228-2246, July 2007.

D. Casella, P. Sanò, M. Formenton, A. Mugnai, "Microwave single-scattering quantities of randomly oriented soft ice hydrometeors", 9th EGU Plinius Conference: Mediterranean Storms, Varenna, Italy, 10-13 September, 2007.

D. Casella, P. Sanò, M. Formenton, W.-Y. Leung, A. Mehta, A. Mugnai, E.A. Smith, G.J. Tripoli, "Bayesian estimation of precipitation from space using the Cloud Dynamics and Radiation Database (CDRD) approach: Application to case studies of FLASH and H-SAF projects", 11th EGU Plinius Conference on Mediterranean Storms, Barcelona, Spain, 7-11 September, 2009.

F.W. Chen, A.M. Leckman, D.H. Staelin, "Satellite observations of polar precipitation using AQUA", American Meteorological Society, 7th Conference on Polar Meteorology and Oceanography on High-Latitude Climate Variations, Hyannis, MA, USA, May 2003.

J.C. Chiu, G.W. Petty, "Bayesian retrieval of complete posterior PDFs of oceanic rain rate from microwave observations", *Journal of Applied Meteorology and Climatology* , vol. 45, issue 8, pp. 1073–1095, August 2006.

M.D. Conner, G.W. Petty, "SSM/I brightness temperature deviations from gridded monthly means as a basis for over land precipitation estimation", Preprints, *Eighth Conference on Satellite Meteorology and Oceanography*, Atlanta, G.A. Amer. Meteor. Soc., pp. 295-298, 1996.

M.D. Conner, G.W. Petty, "Validation and intercomparison of SSM/I rain-rate retrieval methods over continental United States", *Journal of Applied Meteorology*, vol. 37, issue 7, pp.679–700, July 1998.

H. Czekala, P. Bauer, D. Jones, F. Marzano, A. Tassa, L. Roberti, S. English, J.P.V. PoiaresBaptista, A. Mugnai, C. Simmer, "Clouds and Precipitation Radiative Transfer Models for Microwave Radiometry" (C. Matzler, ed.), COST Action 712, Directorate-General for Research, European Commission, Brussels, Belgium, pp. 37-72, 2000.

S. Di Michele, F.K. Marzano, A. Mugnai, A. Tassa, J.P.V. Poiares Baptista, "Physically based statistical integration of TRMM microwave measurements for precipitatine profiling", *Radio Science*, vol. 38, n. 4, 8072, 12 p., 2003.

S. Di Michele, A. Tassa, A. Mugnai, F.K. Marzano, "The Bayesian algorithm for microwave preciptation retriva (BAMPR): potential and application to TRMM data", IEEE , 2003.

S. Di Michele, A. Tassa, A. Mugnai, F.K. Marzano, P. Bauer, J.P.V. Poiares Baptista, "Bayesian algorithm for microwave-based precipitation retrieval: description and application to TMI measurements over ocean ", *IEEE Transaction on Geoscience and Remote Sensing*, vol. 43, n. 4, pp. 778-791, 2005.

M. Dixon, G. Wiener, "TITAN: Thunderstorm identification, tracking, analysis, and nowcasting – a radar-based methodology", *Journal of Atmospheric and Oceanic Technology*, vol. 10, issue 6, pp. 785–797, December 1993.

S. English, T.J. Hewison, "A fast generic millimetre wave emissivity model" Proc.SPIE on Microwave Remote Sensing of the Atmosphere and Enviroment, pp. 22-30, 1998.

K.F. Evans, J. Turk, T. Wong, G.L. Sthephens, "A Bayesian approach to microwave precipitation profile retrieval", *Journal of Applied Meteorology*, vol. 34, pp. 260-279, January 1995.

K.F. Evans, S.J. Walter, A.J. Heimsfield, M. McFarquhar, "Submillimeter-wave cloud ice radiometer: simulations of retrieval algorithm performance", *Journal of Geophysical Research*, vol. 107, n. D3, 4028, 21 p., 2002.

M.R. Farrar, E.A. Smith, X. Xiang, "The impact of spatial resolution enhancement of SSM/I microwave brightness temperatures on rainfall retrieval algorithms", *Journal of Applied Meteorology*, vol. 33, issue 3, pp. 313–333, March 1994.

R.R. Ferraro, N.C. Grody, D. Forsyth, R. Carey, A. Basist, J. Janowiak, F. Weng, G. Marks, R. Yanamandra, "Microwave measurements produce global climatic, hydrologic data", *Eos. Trans. of Amer. Geophys. Union*, vol. 75, pp. 337-343, 1994.

R.R. Ferraro, G.F. Marks, "The Development of SSM/I Rain-Rate Retrieval Algorithms Using Ground-Based Radar Measurements", *Journal of Atmospheric and Oceanic Technology*, vol. 12, issue 4, pp. 755–770, August 1995.

R.R. Ferraro, N.C. Grody, F. Weng, A. Basist, "An Eight-Year (1987–1994) Time Series of Rainfall, Clouds, Water Vapor, Snow Cover, and Sea Ice Derived from SSM/I Measurements", *Bulletin of the American Meteorological Society* ,vol. 77, Issue 5, pp. 891–905, May 1996.

R.R. Ferraro, "Special sensor microwave imager derived global rainfall estimates for climatological applications", *Journal of Geophysical Research*, vol. 102, n. D14, pp. 16715–16735, 1997.

R.R. Ferraro, E.A. Smith, W. Berg, G.J. Huffman, "A Screening Methodology for Passive Microwave Precipitation Retrieval Algorithms", *Journal of the Atmospheric Sciences*, vol. 55, issue 9, pp. 1583-1600, May 1998.

G. Fiocco, "Il pianeta terra: Lezioni di fisica terrestre", Università di Roma "La Sapienza", 1998

M. Formenton, C. Adamo, D. Casella, A. Mugnai, P. Sanò, "Development of an algorithm for convection detection by means of IR observations from geosynchronous satellites and lighting data from VLF ground-based networks: Application to the FLASH project case studies over Italy", 9th EGU Plinius Conference: Mediterranean Storms, Varenna, Italy, 10-13 September, 2007.

G. Galati, A. Gilardini, "Tecniche e strumenti per il telerilevamento ambientale", Consiglio Nazionale delle Ricerche, Roma, 2000.

M. Grecu, E.N. Anagnostou, "Overland Precipitation Estimation from TRMM Passive Microwave Observations", *Journal of Applied Meteorology,* vol. 40, issue 8, pp. 1367–1380, Aug. 2001.

M. Grecu, W.S. Olson, E.N. Anagnostou, "Retrieval of precipitation profiles from multiresolution, multifrequency active and passive microwave observations", *Journal of Applied Meteorology*
volume 43, issue 4, pp. 562–575, April 2004.

M. Grecu, W.S. Olson, "Bayesian estimation of precipitation from satellite passive microwave observations using combined radar-radiometer retrieval", *Journal of Applied Meteorology and Climatology*, vol. 45, issue 3, pp.416-433, March 2006.

T.C. Grenfell, S.G. Warren, "Representation of a nonspherical ice particle by a collection of independent spheres for scattering and absorption of radiation", *Journal of Geophysical Research,* vol. 104, pp 31697-31709, 1999.

N.C. Grody, "Precipitation monitoring over land from satellite by microwave radiometry", *Int. Geoscience and Remote Sensing Symp.* (IGARSS '84), Strasbourg, France, ESA SP-215, pp. 417-523, 1984.

N.C. Grody, "Surface identification using satellite microwave radiometer", *IEEE Transaction on Geoscience and Remote Sensing*, vol. 26, pp. 850-859, 1988.

N.C. Grody, "Classification of snow cover and precipitation using the Special Sensor Microwave Imager", *Journal of Geophysical Research*, vol. 103, n. D4, pp. 7423–7435, 1991.

N.C. Grody, "Remote sensing of the atmosphere from satellite using microwave radiometry", *Atmospheric Remote Sensing by Microwave Radiometry*, M.A. Janssen, Ed., John Wiley and Sons., 310 pp., 1993.

N.C. Grody, A. Basist, "Global identification of snow cover using SSM/I measurements", *IEEE Transaction on Geoscience and Remote Sensing*, vol. 34, pp. 237-249, 1996.

G.N. Harris Jr., K.P. Bowman, Dong-Bin Shin, "Comparison of Freezing-Level Altitudes from the NCEP Reanalysis with TRMM Precipitation Radar Brightband Data", *Journal of Climate,*
v. 13, issue 23, pp. 4137–4148, December 2000.

T. Hewison, S. English, "Airborne retrievals of snow and ice surface emissivity at millimeter wavelengths", *IEEE Transaction on Geoscience and Remote Sensing*, vol. 37, issue 4, pp. 1871-1879, July 1999.

T. Hewison, S. English, "Fast models for land surface emissivity. Radiative Transfer Models for Microwave Radiometry" COST Action 712, Directorate-General for Research, European Commission, Brussels, Belgium, pp. 117-127, C. Matzler ed., 2000.

T. Hewison, "Airborne measurements of forest and agricultural land surface emissivity at millimeter wavelengths**",** *IEEE Transaction on Geoscience and Remote Sensing*, vol. 39, issue 2, pp. 393 – 400, Feb. 2001.

A.J. Heymsfield, L.M. Miloshevich, "Parameterizations for the cross-sectional area and extinction of cirrus and stratiform ice cloud particles", *Journal of the Atmospheric Sciences*, vol. 60, pp. 936-956, 2003.

J. Hollinger, "DMSP SSM/I calibration/validation", Naval Research Laboratory Final Report, Parts I and II, 419 pp., 1991.

H-SAF, "Product User Manual", ver. 2.0, H-SAF Consortium, June 2009.

J.A. Hoch, "The cloud dynamics and radiation database: a focus on orographic precipitation" Master of Science Thesis, University of Wisconsin-Madison, 2006.

J.A. Hoch, C.M. Medaglia, M. Kulie, C. O'Dell, G.J. Tripoli, A.V. Mehta, A. Mugnai, E.A. Smith, "Analysis of the global cloud dynamics and radiation database (CDRD) cloud scale parameter and radiation distribution", 2006.
J.R. Holton, "An introduction to dynamic meteorology", Academic Press Inc, International Geophysycs Series, vol.23, 1979.
R. Houze, "Cloud dynamics", Academic Press Inc., 1993.

Yimin Ji, E. Stocker, "Ground validation of TRMM and AMSU microwave precipitation estimates", IEEE , pp. 3157-3159, 2003.
J.H. Joseph, W.J. Wiscombe, and J.A. Weinman, "The Delta-Eddington approximation for radiative flux transfer", *Journal of the Atmospheric Sciences*, vol. 33, issue 12, pp. 2452–2459, December 1976.

C. Kidd, "On rainfall retrieval using polarization-corrected temperatures", *J. Remote Sensing*, vol. 19, n. 5, pp.981-996, 1998.
C. Kidd, D. Kniveton, E.C. Barrett, "The advantages and disadvantages of statistically derived-empirically calibrated passive microwave algorithms for rainfall estimation", *Journal of the Atmospheric Sciences*, vol. 55, pp. 1576-1582, 1998.
D.R. Kniveton, B.C. Motta, H.M. Goodman, M. Smith, F.J. LaFontaine, "The first Wetnet precipitation intercomparison project: Generation of results", *Remote Sensing Review*, vol. 11, pp. 243-302, 1994.
H.K. Kramer, "Observation of the Earth and its environment", Springer-Verlag, Berlin, 2002
C. Kummerow, R.A. Mack, I.M. Hakkarinen, "A self-consistency approach to improve microwave rainfall rate estimation from space", *Journal of Applied Meteorology*, vol. 28, pp. 869-884, Sept. 1989.
C. Kummerow, "On the accuracy of the Eddington-approximation for the radiative transfer in microwave frequencies", *Journal of Geophysical Research*, 98, pp. 2757–2765, 1993.
C. Kummerow, L. Giglio "A passive microwave technique for estimating rainfall and vertical structure information from space. Part II: applications to SSM/I Data", *Journal of Applied Meteorology*, vol. 33, issue 1, pp. 19–34, January 1994a.
C. Kummerow, L. Giglio "A passive microwave technique for estimating rainfall and vertical structure information from space. Part I: algorithm description", *Journal of Applied Meteorology*, vol. 33, issue 1, pp. 3–18, January 1994b.
C. Kummerow, W.S. Olson, L. Giglio, "A simplified scheme for obtaining precipitation and vertical Hydrometeor profiles from passive microwave sensors", ", *IEEE Transaction on Geoscience and Remote Sensing*, vol. 34, n. 5, pp. 831-846, pp. 1213-1232, Sept. 1996.
C. Kummerow, "Beamfilling errors in passive microwave rainfall retrievals", *Journal of Applied Meteorology* , vol. 37, issue 4, pp. 356–370, April 1998.
C. Kummerow, J. Simpson, O. Thiele, W. Barnes, A.T.C. Chang, E. Stocker, R.F. Adler, A. Hou, R. Kakar, F. Wentz, P. Ashcroft, T. Kozu, Y. Hong, K. Okamoto, T. Iguchi, H. Kuroiwa, E. Im, Z. Haddad, G. Huffman, B. Ferrier, W.S. Olson, E. Zipser, E. A. Smith, T. T. Wilheit, G. North, T. Krishnamurti, K. Nakamura, "The status of the Tropical Rainfall Measuring Mission (TRMM) after two years in orbit", *Journal of Applied Meteorology* vol. 39, issue 12, pp. 1965–1982, December 2000.
C. Kummerov, Y. Hong, W.S. Holson, S. Yang, R.F. Adler, J. McCollum, R. Ferraro, G.Petty, D,-B. Schin, T.T. Wilheit, "The evolution of the Goddard profiling algorithm (GPROF) for

rainfall estimation from passive microwave sensors", *Journal of Applied Meteorology,* vol. 40, pp. 1801-1820, 2001.
C. Kummerow, P. Poyner, W. Berg, J. Thomas-Stahle, "The effects of rainfall inhomogeneity on climate variability of rainfall estimated from passive microwave sensors", *Journal of Atmospheric and Oceanic Technology*, vol. 21, issue 4, pp. 624–638, April 2004.
C. Kummerow, W. Berg, J. Thomas-Stahle, H. Masunaga, "Quantifying global uncertainties in a simple microwave rainfall algorithm", *Journal of Atmospheric and Oceanic Technology*, vol. 23, issue 1, pp. 23–37, January 2006.

K. Lagouvardos, V. Kotroni, H.-D. Betz, K. Schmidt, "A comparison of lightning data provided by ZEUS and LINET networks over Western Europe", *Natural Hazards and Earth System Sciences*, vol. 9, pp. 1713-1717, 2009.
Landolt-Börnstein, "Observed global climate", Group V Geophysics, vol. 6, Springer Berlin Heidelberg, 2006.
T.S. L'Ecuyer, G.L. Stephens, "An uncertainty model for Bayesian Monte Carlo retrieval algorithm: Application to the TRMM observing system", *Q. J. Royal Meteorological Society*, vol. 128, pp. 1713-1737, 2002.
Q. Li, R. Ferraro, N. Grody, "Detailed analysis of the error associated with the rainfall retrieved by the NOAA/NESDIS SSM/I algorithm: 1. Tropical oceanic rainfall", *Journal of Geophysical Research*, 103(D10), 11, 419–11, 427, 1998.
Hyo-Suk Lim, C.E. Graves, G.R. North, T. Wilheit "Rainfall Estimation from ESMR-5 Measurements and Application to El Niño" *Journal of Applied Meteorology*, vol. 34, issue 2, pp. 391–403, February 1995.
X. Lin, A:Y. Hou, "Evaluation of coincident passive microwave estimates using TRRM PR and ground measurements as references", *Journal of Applied Meteorology and Climatology*, vol.47, pp. 3170-3187, December 2008.
G. Liu, J.A. Curry, "An investigation of the relationship between emission and scattering signals in SSM/I data", *Journal of the Atmospheric Sciences*, vol. 55, pp. 1628-1642, 1998.
G. Liu, C. Simmer, E. Ruprecht, "Three-dimensional radiative transfer effects of clouds in the microwave spectral range", *Journal of Geophysical Research*, 101, pp. 4289-4298,1996.
A.C. Lorenc, "Analysis methods for numerical weather prediction", *Quarterly Journal of the Royal Meteorological Society*, vol. 112, pp. 1177-1194, 1986.

V. Marecal, J.F. Mahfouf, "Variational retrieval of temperature and humidity profiles from TRMM precipitation data", *Monthly Weather Review*, vol. 138, pp. 3853-3866, Nov.2000.
V. Marecal, J.F. Mahfouf, "Four-dimensional variational assimilation of total column water in rainy areas", *Monthly Weather Review*, vol. 130, pp. 43-58, 2002.
F.S. Marzano, A. Mugnai, E.A. Smith, X. Xiang, J. Turk, J. Vivekanandan, "Active and passive remote sensing of precipitating storm during CaPE. Part II: Intercomparison of precipitation retrieval from AMPR radiometer and CP-2 radar", *Meteorology and Atmospheric Physics*, vol. 54, n. 1-4, pp. 29-51, March 1994.
F.S. Marzano, A. Mugnai, G. Panegrossi, N. Perdicca, E.A. Smith, J. Turk, "Bayesian estimation of precipitating cloud parameters from combined measurements of spaceborne microwave radiometer and radar", *IEEE Transaction on Geoscience and Remote Sensing*, vol. 37, n. 1, pp. 593-613, 1999.

F.S. Marzano, S. Di Michele, A. Mugnai, A. Tassa, "Bayesian techniques for precipitation profile retrieval from spaceborne microwave radiometric sensors", *Proceedings of the 5th Pacific Remote Sensing Conference (PORSEC)*, Natl. Inst. of Oceanogr., Goa, India, 5-8 Dec. 2000, pp. 221-228, 2001.

H. Masunaga, T. Iguchi, R. Oki, M. Kachi, "Comparison of rainfall products derived from TRMM microwave imager and precipitation radar", *Journal of Applied Meteorology*, vol. 41, issue 8, pp. 849–862, August 2002.

J.R. McCollum, R.R. Ferraro, "Next generation of NOAA/NESDIS TMI, SSMI/S, and AMSE-E microwave land rainfall algorithms", *Journal of Geophysical Research*, vol. 108, n. D8, 8382, doi:10.1029/2001JD001512, 2003.

J.R. McCollum, R.R. Ferraro, "Microwave rainfall estimation over coast", *Journal of Atmospheric and Oceanic Technology*, vol. 22, pp. 497-512, May 2005.

A. Mugnai, W.J. Wiscombe, "Scattering of Radiation by Moderately Nonspherical Particles", *Journal of the Atmospheric Sciences*, vol. 37, issue 6, pp. 1291–1307, June 1980.

A. Mugnai, E.A. Smith, "Radiative transfer to space through a precipitating cloud at multiple microwave frequencies. Part I: Model description", *Journal of Applied Meteorology*, vol. 27, issue 9, pp. 1055–1073, September 1988.

A. Mugnai, H.J. Cooper, E.A. Smith, G.J. Tripoli, "Simulation of microwave brightness temperatures of an evolving hailstorm at SSM/I frequencies", *Bulletin of the American Meteorological Society*, vol. 71, n. 1, pp. 2-13, 1990.

A. Mugnai, E.A. Smith, G.J. Tripoli, "Foundations for statistical physical precipitation retrieval from passive microwave satellite measurement. Part II : Emission-source and generalized weighting-function properties of a time-dependent cloud-radiation model", *Journal of Applied Meteorology*, vol. 32, n. 1, pp. 17-39, 1993.

A. Mugnai, S. Di Michele, F.S. Marzano, A. Tassa, "Cloud-model based Bayesian techniques for precipitation profile retrieval from TRMM microwave sensors", Proc. ECMWF/EuroTRMM Workshop on Assimilation of Clouds and Precipitation, ECMWF,Reading, U.K., pp. 323-345, 2001.

A. Mugnai, "Modeling and retrieval of precipitation in the microwave spectral region", SHMI-EUMETSAT Workshop on "MSG Applications in Nowcasting, Precipitation Detection & Forecasting, Vinicne, Slovak Republik, June 2006a.

A. Mugnai, D. Casella, P. Sanò, S. Dietrich, F. Di Paola, L. Levizzani, E. Cattani, F. Torricella, B. Bizzarri, F. Prodi, E.A. Smith, A. Metha, S. Yang, G.J. Tripoli, J. Hoch, W.-Y. Leung, "The EUMETSAT satellite application facility in support to operational hydrology and water management /H-SAF): precipitation retrieval algorithm and precipitation products", 6th GPM International Workshop, Annapolis, Maryland, USA, November 6-8, 2006b.

A. Mugnai, F. Baordo, J. Hoch, C.M. Medaglia, A. Metha, E.A. Smith, G.J. Tripoli, "Precipitation retrieval and analysis of severe storm events based on Cloud Dynamics and Radiation Database (CDRD) approach", *Geophysical Research Abstract*, vol. 8, ISSN:1029-7006, EGU General Assembly 2006, Vienna, Austria, 2-7 April 2006c.

A. Mugnai, "The EUMETSAT satellite application facility in support to operational Hydrology and Water management (H-SAF): precipitation retrieval algorithms and precipitation products", *Geophysical Research Abstracts*, vol. 9, pg. 11091, 2007a.

A. Mugnai, "Precipitation retrieval and analysis by means of combined satellite observations, lightning data and cloud model simulations", *Geophysical Research Abstracts*, vol. 9, pg. 11116, 2007b.

A. Mugnai, D. Casella, M. Formenton, W.-Y. Leung, A. Metha, P. Sanò, E.A. Smith, G.J. Tripoli, S. Yang, "Investigating contrasts between continental and maritime precipitation over Mediterranean basin based on CDRD Algorithm methodology", 9th EGU Plinius Conference: Mediterranean Storms, Varenna, Italy,10-13 September, 2007c.

A. Mugnai, Bizzarri B., Casella D., Capacci D., Cattani E., Di Paola F., Dietrich S., Formenton M., Levizzani V., Porcù F., Prodi F., Sanò P., Torricella F, "precipitation retrieval algorithms and precipitation products for the EUMETSAT satellite application facility in support to operational Hydrology and Water Management (H-SAF)", *2007* EUMETSAT Meteorological Satellite Conference and the 15th American Meteorological Society (AMS) Satellite Meteorology & Oceanography Conference, Amsterdam, The Netherlands, 24 – 28 September 2007d.

A. Mugnai, D. Casella, M. Formenton, P. Sanò, E.A. Smith, A. Mehta, S. Yang, G.J. Tripoli, W.-Y. Leung, "Algorithms for precipitation retrieval: PR-OBS-1 development status precipitation rate at ground by MW conical scanners", presented at the Hydrology SAF 4th project team Meeting, Istanbul, Turkey, May 14-16, 2007e.

A. Mugnai, R. Bennartz, D. Casella, T. Hashino, P. Sanò, E.A. Smith, G.J. Tripoli, "Precipitation retrieval by means of passive-microwave satellite observations and cloud model simulations: Impact of ice microphysics parameterization", *Geophysical Research Abstracts*, vol.9, p. 11099, EGU 2007f.

A. Mugnai, E.A. Smith, G.J. Tripoli, S. Dietrich, V. Kotroni, K. Lagouvardos, C.M. Medaglia, "Explaining discrepancies in passive microwave cloud-radiation database in microphysical context from two different cloud-resolving models", Meteorology and Atmospheric Physics, vol. 101, pp. 127-145, 2008.

C.M.U. Neale, M.J. McFarland, K. Chang, "Land surface classification using microwave brightness temperatures from the Special Sensor Microwave/Imager", *IEEE Transaction on Geoscience and Remote Sensing*, vol. 28, pp. 829-838, 1990.

S. Neshyba, T.C. Grenfell, S.G. Warren, "Representation of a nonspherical ice particle by a collection of independent spheres for scattering and absorption of radiation: 2. Hexagonal columns and plates", *Journal of Geophysical Research*, vol. 108, n. D15, 4448, 2003.

W. S. Olson, C. D. Kummerow, G. M. Heymsfield, L. Giglio "A method for combined passive–active microwave retrievals of cloud and precipitation profiles", *Journal of Applied Meteorology*, vol. 35, issue 10, pp. 1763–1789, October 1996.

W.S. Olson, P. Bauer, N.F. Viltard, D.E. Johnson, W.K. Tao, R. Meneghini, L. Liao, "A melting layer model for passive/active microwave remote sensing applications. Part II: simulation of TRMM observations", *Journal of Applied Meteorology*, vol. 40, pp. 1164–1179, 2001

G. Panegrossi, S. Dietrich, F.K. Marzano, A. Mugnai, E.A. Smith, X. Xiang, G.J. Tripoli, P.K. Wang, J.V.P. Poiares Baptista, "Use of cloud model microphysics for passive microwave-based precipitation retrieval: Significancee of consinstency between model and measurement manifolds", *Journal of the Atmospheric Sciences*, vol. 55, pp. 1644-1673, 1998.

N. Perdicca, F.S. Marzano, G. d'Auria, P. Basili, P. Ciotti, A. Mugnai, "Precipitation retrieval from spaceborne microwave radiometers based on maximum a posteriori probabilità estimation", *IEEE Transaction on Geoscience and Remote Sensing*, vol. 34, n. 4, pp. 831-846, 1996.

N. Pierdicca, L. Pulvirenti, C. Bignami, M. Chini, F. Ticconi, "Retrieval and analysis of land surface microwave emissivity from SSMI/S data", *Rivista Italiana di Telerilevamento*, vol. 40, n. 2, pp. 15-25, 2008.

G.W. Petty, K.B. Katsaros, "Precipitation observed over the south China sea by the Nimbus-7 scanning multichannel microwave radiometer during winter MONEX", *Journal of Applied Meteorology*, vol. 29, pp. 273–287, April 1990.

G.W. Petty, "Frequencies and characteristics of global oceanic precipitation from shipboard present-weather reports", *Bulletin of the American Meteorological Society*, vol. 76, n. 9, pp. 1593-1616, Sept.1995.

G.W. Petty, "Physical and microwave radiative properties of precipitating clouds. Part I: Principal component analysis of observed multichannel microwave radiances in tropical stratiform rainfall", *Journal of Applied Meteorology*, vol. 40, pp. 2105–2114, Dec. 2001.

C. Prabhakara, H.D. Chang, A.T.C. Chang, "Remote sensing of precipitable water over the oceans from Nimbus 7 microwave measurements", *Journal of Applied Meteorology*, vol. 21, issue 1, pp. 59–68, January 1982.

L. Roberti, J. Haferman, C. Kummerow, "Microwave radiative transfer through horizontally inhomogeneous precipitating clouds", *Journal of Geophysical Research.*, vol. 99, pp. 707-716, 1994

P. Sanò, D. Casella, M. Formenton, A. Mugnai, E.A. Smith, G.J. Tripoli, S. Yang, "Bayesian estimation of precipitating cloud parameters: Application to case studies of FLASH and RISKMED projects", 9th EGU Plinius Conference: Mediterranean Storms, Varenna, Italy, 10-13 September, 2007.

C. Schär, D. Lüthi, U. Beyerle, E. Heise "The soil–precipitation feedback: a process study with a regional climate model", *Journal of Climate*, vol. 12, issue 3, pp. 722–741, March 1999.

G. Schiavon, P. Ferrazzoli, D. Solimini. P. de Maagt, J.V.P. Poiares Baptista, "A global high-resolution microwave emission model for the Earth", *Radio Science*, vo. 33, pp. 753-766, May-June 1998.

P. Schluessel, H. Luthardt, "Surface Wind Speeds Over the North Sea From Special Sensor Microwave/Imager Observations", *Journal of Geophysical* Research, vol. 96, n. C3, pp. 4845–4853,

E.K. Seo, G. Liu, "Retrievals of cloud ice water path by combining ground cloud radar and satellite high-frequency microwave measurements near the ARM SGP site", *Journal of Geophysical Research – Atmospheres*, 110, D14203, doi 10.1029/2004JD005727, July 2005.

D.B. Shin, C. Kummerow, "Parametric rainfall retrieval algorithm for passive microwave radiometers", *Journal of Applied Meteorology,* vol. 42, Issue 10, pp. 1480-1496, Oct. 2003.

J.R. Simpson, R.F. Adler, G.R. North, "A proposed tropical rainfall measuring mission (TRMM) satellite", *Bulletin of the American Meteorological Society*, vol. 69, pp. 278-295, 1988.

G.M. Skofronic-Jackson, A.J. Gasiewski, "A nonlinear multispectral statistical CLEAN-based precipitation parameter-retrieval algorithm", *IEEE Transaction on Geoscience and Remote Sensing*, vol. 38, n. 1, pp. 226-236, 2000.

D.M. Smith, D.R. Kniveton, E.C. Barrett, "A statistical modelling approach to passive microwave rainfall retrieval", *Journal of Applied Meteorology,* vol. 37, pp. 135-154, February 1998.

E.A. Smith, A. Mugnai, "Radiative transfer to space through a precipitating cloud at multiple microwave frequencies. Part II: Results and analysis", *Journal of Applied Meteorology*, vol. 27, issue 9, pp. 1074–1091, September 1988.

E.A. Smith, A. Mugnai, H.J. Cooper, G.J. Tripoli, X.W. Xiang, "Foundations for statistical physical precipitation retrieval from passive microwave satellite measurement. I : Brightness-temperature properties of a time-dependent cloud-radiation model", *Journal of Applied Meteorology*, vol. 31, n. 6, pp. 506-531, 1992.

E.A. Smith, C.Kummerow, A. Mugnai, "The emergence of inversion-type profile algorithms for estimation of precipitation from satellite passive microwave measurements", *Remote Sensing Reviews*, vol.11, pp. 211-242, 1994a.

E.A. Smith, X.W. Xiang, A. Mugnai, G.J. Tripoli, "Design of an inversion-based precipitation profile retrieval algorithm using an explicit cloud model for initial guess microphysics", *Meteorology and Atmospheric Physics*, vol. 54, n. 1-4, pp. 53-78, 1994b.

E.A. Smith, X. Xiang, A. Mugnai, R.E. Hood, R.W. Spencer, "Behavior of an Inversion-Based precipitation Retrieval Algorithm with High-Resolution AMPR Measurements Including a Low-Frequency 10.7-GHz Channel", *Journal of Atmospheric and Oceanic Technology*, vol. 11, issue 4 pp. 858–873, August 1994c.

E.A. Smith, F.J. Turk, M.R. Farrar, A. Mugnai, X.W. Xiang, " Estimating 13.8 GHz path-integrated attenuation from 10.7 GHz brightness temperature for the TRMM combined PR-TMI precipitation algorithm", *Journal of Applied Meteorology,* vol. 36, n. 4, pp. 365-388, 1997.

E. A. Smith, J. E. Lamm, R. Adler, J. Alishouse, K. Aonashi, E. Barrett, P. Bauer, W. Berg, A. Chang, R. Ferraro, J. Ferriday, S. Goodman, N. Grody, C. Kidd, D. Kniveton, C. Kummerow, G. Liu, F. Marzano, A. Mugnai, W. Olson, G. Petty, A. Shibata, R. Spencer, F. Wentz, T. Wilheit, E. Zipser, "Results of WetNet PIP-2 Project", *Journal of the Atmospheric Sciences*, vol. 55, Issue 9, pp.1483–1536, May 1998.

R.W. Spencer, "Satellite passive microwave rain rates measurement over croplands during spring, summer and fall", *Journal of Climate and Applied Meteorology*, Vol. 23, pp. 1553–1562, November 1984.

R.W. Spencer, "A satellite passive 37-GHz scattering-based method for measuring oceanic rain rates", *Journal of Climate and Applied Meteorology*, Vol. 25, pp. 754–766, June 1986.

R.W. Spencer, H.M. Goodman, R.E. Hood, "Precipitation retrieval over land and ocean with the SSM/I: identification and characteristics of the scattering signal", *Journal of Atmospheric and Oceanic Technology*, vol. 6, pp. 254-273, April 1989.

G.L. Stephens, C.D. Kummerow, "The remote sensing of clouds and precipitation from space: a review", *Journal of the Atmospheric Sciences*, vol. 64, iss. 11, pp. 3742-3765, Nov. 2007.

A. Tassa, S. Di Michele, A. Mugnai, "Cloud model-based Bayesian technique for precipitation profile retrieval from the Tropical Rainfall Measuring Mission Microwave Imager", *Radio Science*, vol. 38, n. 4, 8074, 13 p., 2003.

A. Tassa, S. Di Michele, A. Mugnai, F.S. Marzano, P. Bauer, J.P.V. Poiares Baptista, "Modeling uncertainties for passive microwave precipitation retrieval: evaluation of a case study", *IEEE Transaction on Geoscience and Remote Sensing*, vol. 44, n. 1, pp. 78-89, 2006.

M.C. Todd, J.O. Bailey, "Estimates of rainfall over the United Kingdom and surrounding seas from SSM/I using the polarization corrected temperature algorithm", *Journal of Applied Meteorology*, vol. 34, pp. 1254-1265, June 1995.

G.J. Tripoli, "A nonhydrostatic mesoscale model designed to simulate scale interaction", *Monthly Weather Review*, vol. 120, issue 7, pp. 1342-1359, July 1992.

G.J. Tripoli, C.M. Medaglia, S. Dietrich, A. Mugnai, G. Panegrossi, S. Pinori, E. A. Smith, "The 9–10 November 2001 Algerian Flood: A Numerical Study", *Bulletin of the American Meteorological Society*, vol. 86, issue 9, pp. 1229–1235, September 2005.

J. Turk, F.S. Marzano, A. Mugnai, "Effects of Degraded Sensor Resolution upon Passive Microwave Precipitation Retrievals of Tropical Rainfall", *Journal of the Atmospheric Sciences*, vol. 55, issue 9, pp. 1689–1706, May 1998.

F.T: Ulaby, R.K. Moore, A.K. Fung, "Microwave remote sensing: Active and passive, Vol. III, From theory to applications", Artech House, Norwood, Mass., 1986.

J.W. Wallace, P.V. Hobbs, "Atmospheric Science: An introductory survey", 1977.

J.W. Waters, K.F. Kunzi, R.L. Pettyjohn, R.K.L. Poon, D.H. Staelin, "Remote Sensing of Atmospheric Temperature Profiles with the Nimbus 5 Microwave Spectrometer", *Journal of the Atmospheric Sciences*, vol. 32, issue 10, pp. 1953–1969, October 1975.

J.A. Weiman, M.-J. Kim, "A simple model of the Mn-wave scattering parameters of randomly oriented aggregate of finite cylindrical ice hydrometeors", *Journal of the Atmospheric Sciences*, 2006.

F. Weng, N.C. Grody, "Retrieval of cloud liquid water using the special sensor microwave imager (SSM/I)", *Journal of Geophysical Research*, vol. 99, n. D12, pp. 25535-25551, December 1994.

F. Weng, N.C. Grody, R. Ferraro, A. Basist, D. Forsyth, "Cloud liquid water climatology from Special Sensor Microwave/Imager", *Journal of Climate*, vol. 10, pp.1086-1098, May1997.

F. Weng, N. C. Grody "Retrieval of ice cloud parameters using a microwave imaging radiometer", *Journal of the Atmospheric Sciences*, vol. 57, issue 8, pp. 1069–1081, April 2000.

F. J. Wentz, R.W. Spencer, "SSM/I rain retrievals within a unified all-weather ocean algorithm", *Journal of the Atmospheric Sciences*, vol. 55, issue 9, pp. 1613–1627, May 1998.

Ed R. Westwater, W. Zhenhui, N.C. Grody, L.M. McMillin, "Remote Sensing of Temperature Profiles from a Combination of Observations from the Satellite-Based Microwave Sounding Unit and the Ground-Based Profiler", *Journal of Atmospheric and Oceanic Technology*, vol. 2, issue 2, pp. 97–109, June 1985.

T. Wilheit, A.T.C. Chang, M.S.V. Rao, E.B. Rodgers, J.S. Theon, "A satellite technique for quantitatively mapping rainfall rates over the ocean", *Journal of Applied Meteorology*, vol. 16, issue 5, pp. 551-560, May 1977.

T. Wilheit, A.T.C. Chang, J.L. King, E.B. Rodgers, R.A. Nieman, B.M. Krupp, A.S. Milman, J.S. Stratigos, H. Siddalingaiah, "Microwave Radiometric Observations Near

19.35, 92 and 183 GHz of Precipitation in Tropical Storm Cora", *Journal of Applied Meteorology* , vol. 21, issue 8, pp. 1137–1145, August 1982.

T. Wilheit, "Some comments on passive measurements of rain", *Bulletin of the American Meteorological Society*, vol. 67, issue 10, pp. 1226-1232, October 1986.

T. Wilheit, A.T.C. Chang, L.S. Chiu, "Retrieval of monthly rainfall indices from microwave radiometric measurements using probability distribution functions", *Journal of Atmospheric and Oceanic Technology*, vol. 8, issue 1, pp. 118–136, February 1991.

T. Wilheit, R. Adler, S. Avery, E. Barret, P. Bauer, W. Berg, A. Chang, J, Ferriday, N. Grody, S. Goodman, C. Kidd, D. Kniveton, C. Kummerow, A. Mugnai, W. Olson, G. Petty, A. Shibata, E. Smith, "Algorithms for the retrieval of rainfall from passive microwave measurements", *Remote Sensing Reviews*, vol.11, pp. 163-194, 1994.

T. Wilheit, C.D. Kummerow, R. Ferraro, "Rainfall algorithms for AMSR-E", *IEEE Transaction on Geoscience and Remote Sensing*, vol. 41, n. 2, pp. 204-214, Feb. 2003.

W.J. Wiscombe, "Improved Mie scattering algorithms", *Appl. Opt*., vol. 19, pp. 1505-1509, 1980.

C.P. Woods, "The study of snow particles in Pacific Northwest winter precipitation: observations and mesoscale modelling", Dissertation for the degree of Doctor of Philosophy, University of Washington, 2006.

ACRONYMS

AMPR – Advanced Microwave Precipitation Radiometer
AMSR-2 - Advanced Microwave Scanning Radiometer - 2 (on GCOM-W)
AMSR-E – Advanced Microwave Sounding Radiometer - EOS
AMSU- Advanced Microwave Sounding Unit (on NOAA and MetOp)
AMSU-A/B - Advanced Microwave Sounding Unit – A/B
ASAR - Advanced Synthetic Aperture Radar (on Envisat)
ASCAT - Advanced Scatterometer (on MetOp)
ATMS - Advanced Technology Microwave Sounder (on NPP and NPOESS)
AVHRR - Advanced Very High Resolution Radiometer (on NOAA and MetOp)
BAMPR – Bayesian Algorithm for Microwave-based Precipitation Retrieval
BUFR - Binary Universal Form for the Representation of meteorological data
CAPE – Convective Available Potential Energy (J/kg)
CDRD – Cloud Dynamics and Radiation Database
CIN – Convective Inhibition (J/kg)
CMIS - Conical-scanning Microwave Imager/Sounder (on NPOESS starting from NPOESS-2)
CNMCA - Centro Nazionale di Meteorologia e Climatologia Aeronautica (in Italy)
CNR - Consiglio Nazionale delle Ricerche
CRD – Cloud Radiation Database
CrIS - Cross-track Infrared Sounder (on NPP and NPOESS)
CRM – Cloud Resolving Model
DMSP – Defense Meteorological Satellite Program
DoD - Department of Defence (in the USA)
DPR - Dual-frequency Precipitation Radar (on the GPM "core" satellite)
ECMWF - European Centre for Medium-range Weather Forecasts
EGPM – European Global Precipitation Mission
Envisat - Environmental Satellite
EOS – Earth Observing System
ERS - European Remote-sensing Satellite (1 and 2)
ESA - European Space Agency
ESMR – Electrically Scanning Microwave Radiometer
EUMETSAT European Organisation for the Exploitation of Meteorological Satellites
FAR – False Alarm Ratio
FNMOC – Fleet Numerical Meteorology and Oceanographic Center
FOV – Field of view
GCOM-W Global Change Observation Mission - Water
GEO - Geostationary Earth Orbit
GFS – Global Forecasting System
GIS - Geographical Information System
GMI - GPM Microwave Imager (on the GPM "core" satellite)
GNSS - Global Navigation Satellite System
GPCP – Global Precipitation Climatology Project
GPM - Global Precipitation Measurement mission
GPROF – Goddard Profiling Algorithm
GSCAT – Goddard Scattering Algorithm

HIRS - High-resolution Infrared Radiation Sounder (on NOAA and MetOp 1/2)
H-SAF - SAF on Support to Operational Hydrology and Water Management
IASI - Infrared Atmospheric Sounding Interferometer (on MetOp)
IFOV – Instantaneous Field of View
IR - Infra Red
ISAC - Istituto di Scienze dell'Atmosfera e del Clima (of CNR)
ISCCP – International Satellite Cloud Climatology Project
LEO - Low Earth Orbit
LIS - Lightning Imaging Sensor (on TRMM)
LST - Local Solar Time (of a sunsynchronous orbit)
MAP – Maximum A posteriori Probability
MetOp - Meteorological Operational satellite
MHS - Microwave Humidity Sounder (on NOAA 18 and 19, and on MetOp)
MMS – Minimum Mean Square
MSG - Meteosat Second Generation
MVIRI - Meteosat Visible and Infra Red Imager (on Meteosat up to 7)
MW - Micro Wave
NASA – National Aeronautical and Space Administration
NATO - North Atlantic Treaty Organization
NCEP - NOAA National Centers for Environmental Prediction
NEΔT - Noise Equivalent Differential Temperature
NESDIS – National Environmental Satellite, Data and Information System
NESR - Noise-Equivalent Spectral Radiance
NMS – Non-hydrostatic Modelling System
NOAA - National Oceanic and Atmospheric Administration (Agency and satellite)
NPOESS - National Polar-orbiting Operational Environmental Satellite System
NWP - Numerical Weather Prediction
PCT – Polarization-Corrected Temperature
PIP-2 – Precipitation Intercomparison Project 2
Pixel - Picture element
PM – Passive Microwave
POD – Probability Of Detection
PR - Precipitation Radar
QPF - Quantitative Precipitation Forecast
RTM – Radiative Transfer Model
SAF - Satellite Application Facility
SAR - Synthetic Aperture Radar
SEVIRI - Spinning Enhanced Visible and Infra-Red Imager
SMMR – Scanning Multichannel Microwave Radiometer
SSM/I – Special Sensor Microwave/Imager
SSMIS - Special Sensor Microwave Imager/Sounder
Tb or T_B - Brightness Temperature
T_{BB} - Equivalent black body temperature
TMI - TRMM Microwave Imager (on TRMM)
TRMM – Tropical Rainfall Measuring Mission
UTC - Universal Coordinated Time

UW NMS – University of Wisconsin – Non-hydrostatic Modeling System
VIS - Visible
VWSH – Vertical Speed Shear (1/s)
WRCP – World Climate Research Program